NANOSTRUCTURED WO_3 FOR ELECTROCHROMIC AND PHOTOCATALYTIC APPLICATIONS

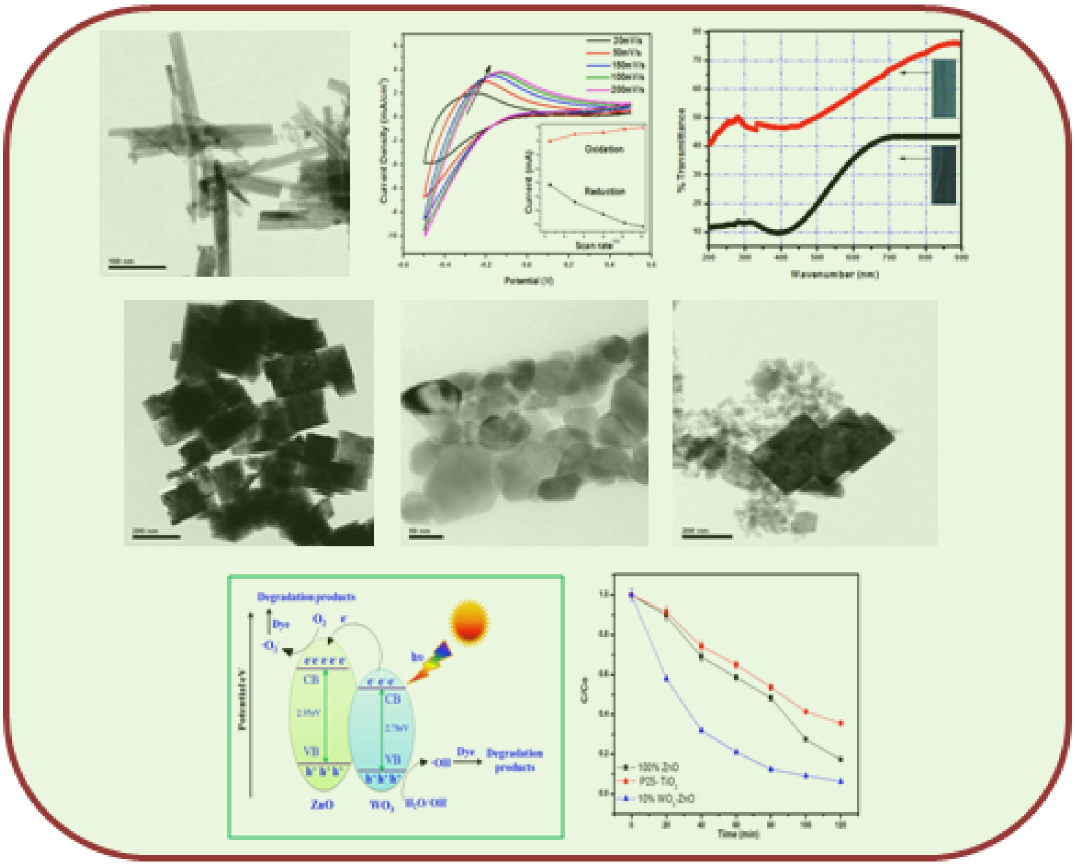

SANGEETA ADHIKARI

Nanostructured WO_3 for Electrochromic and Photocatalytic Applications

A THESIS SUBMITTED
IN FULFILMENT OF THE REQUIREMENT
FOR THE DEGREE OF

Doctor of Philosophy

in

Ceramic Engineering

By
Sangeeta Adhikari
(511CR301)

Supervisor:
Prof. Debasish Sarkar

Department of Ceramic Engineering
National Institute of Technology
Rourkela

November 2015

DEDICATED TO

MY PARENTS

CERTIFICATE

This is to certify that the thesis entitled “**Nanostructured WO_3 for Electrochromic and Photocatalytic Applications**” submitted by **Miss Sangeeta Adhikari** in partial fulfilment of the requirement for the award of Doctor of Philosophy Degree in Ceramic Engineering at the National Institute of Technology, Rourkela is an authentic work carried out by her under my supervision and guidance.

To the best of my knowledge, the matter embodied in the thesis has not been submitted in any other University/Institute for the award of any Degree or Diploma.

30/11/15

Prof. Debasish Sarkar
Department of Ceramic Engineering
National Institute of Technology
Rourkela-769008

DECLARATION

I declare that this thesis is my own work and has not been submitted in any form for another degree or diploma at any university or other institution of tertiary education. Information derived from the published or unpublished work of others has been acknowledged in the text and a list of references given.

Sangeeta Adhikari
30/11/15

Date : **Sangeeta Adhikari**

Signature

Acknowledgements

I wish to express my deep sense of gratitude and indebtedness to Prof. Debasish Sarkar, Department of Ceramic Engineering, N.I.T Rourkela for assigning me the project “Nanostructured WO_3 for Electrochromic and Photocatalytic Applications” and for his inspiring guidance, constructive criticism and valuable suggestion throughout this research work.

I am thankful to INAE Distinguished Professor H.S. Maiti, Department of Ceramic Engineering, for his valuable suggestions and encouragement.

I am thankful to all faculty members of Ceramic Engineering Department, NIT Rourkela for their constructive suggestions and encouragement at various stages of the work. I am thankful to Prof. D. Mangalaraj, Department of Nanoscience and Nanotechnology, Bharathiar University for providing the thin film characterization facility. I am also thankful to Prof. Bikramjit Basu and Prof. Giridhar Madras, Material Research Centre, Indian Institute of Sciences, Bangalore, for permitting me to carry out photocatalytic experiments and other material characterizations funded by NRCM, IISc. Bangalore. I am also thankful to Director, PSG College of Technology, Coimbatore for permitting to carry out TEM analysis.

I express my sincere thanks to Mr. Shubhabrata Chakraborty, Department of Ceramic Engineering for helping with the micrsoscopy facility required for the completion of the thesis.

I am also thankful to Mr. Sanjaya kumar Swain, Mr. Raju Mula, Mr. B. S. Reddy, Mr. Sarat Chandra and all the research scholars in the Department of Ceramic Engineering for their kind help and providing all joyful environments throughout this work.

Last but not least, my sincere thanks to all my friends who have patiently extended all sorts of help for accomplishing this undertaking.

Sangeeta Adhikari
Ceramic Engineering

Abstract

Transition metal oxide semiconductors are known to be a smart category of materials with extensive demand for large scale production at lower costs. Facts in the present technologies remains with tunable and altering material properties that make them efficient for wide ranging applications such as smart windows, sensors, photoelectrics, solar cells, photocatalysis and etc. Their physical and chemical properties are influenced by the invariant surface structures affecting the surface energy and bonding that can be controlled by various synthesis approaches. Thus, in perspective of energy storage system, ion holding capacity and efficient use of solar energy, WO_3 and ZnO are the most researched materials due to its simple and viable construction with effective visible light harvesting ability other than TiO_2.

In the present research work, selective synthesis of two different transition metal oxide semiconductor nanostructures namely, WO_3 and ZnO has been developed for assessment of electrochromic and photocatalytic application. Four different classes of morphologies i.e., spherical, rod, cuboid and fiber WO_3 nanoparticles are prepared through co-precipitation and hydrothermal techniques. Low temperature co-precipitation is an excellent approach to prepare spherical WO_3 nanoparticles and rod shaped nanoparticles. Hydrogen peroxide concentration and temperature directs the phase, crystallinity and highest surface area of monoclinic spherical nanoparticles in comparison to CTAB directed rod shaped particles. Hydrothermal process favours in confined growth of nanocuboids and nanofibers under particular reaction conditions. In the present study, fluoroboric acid (HBF_4) and sodium chloride (NaCl) has been chosen as structure directing reagents (SDR). Molar concentrations of SDR, time and temperature have prime importance to control the morphology and phase during the hydrothermal reactions. Cuboid morphology has an intermediate metastable hexagonal phase which is subsequently transformed to monoclinic phase at specific processing condition. A stable hexagonal phase is recorded for nanofibers with predominant (001) plane. Phase and morphology has no significant effect on the band gap energy. On the other hand, quasi-fibrous zinc oxide (ZnO) is prepared using oxalic acid fuel with zinc nitrate oxidizer through solution-combustion synthesis method.

Commercially viable methods such as drop-coating and dip-coating of nanostructured WO_3 onto ITO glass substrates have been explored in light of efficient electrochromism performance. High surface continuity without any cracks and flaws after drying exhibits high current density for dip-coated electrodes. WO_3 nanofiber electrode with micro thin uniformity exhibits high current density in comparison to electrode fabricated for other nanostructures. An excellent electrochromic property is observed for WO_3 nanofiber coated ITO than WO_3 nanocuboids due to high structural openness and tunneling zone to hold ions through its hexagonal crystal structure. However, pure WO_3 shows negligible photocatalytic activity towards the organic dyes. The photocatalytic degradation of dyes becomes effective upon coupling with ZnO. Monoclinic WO_3 nanocuboid shows enhanced photocatalysis in presence of both UV and visible light. Combustion synthesized quasi-fibrous ZnO enhances the photocatalytic performance than commercial ZnO. In addition, the quasi-fibrous ZnO coupled with WO_3 has better photocatalytic efficacy in comparison to individual quasi-fibrous ZnO only. High photocatalytic activity is achieved for methylene blue and orange G dye solution with 10 wt% loading of monoclinic WO_3 nanocuboids in ZnO matrix under visible light irradiation due to suppressed rate of electron-hole recombination. The hexagonal WO_3 nanofibers and nanocuboids WO_3 coupled with ZnO is found as an invaluable source for electrochromic and photocatalytic application, respectively.

Keywords: Nanoparticles, WO_3, Electrochromism, ZnO, Photocatalysis

Table of Contents

List of Publications

List of Figures:

List of Tables:

Chapter 1

INTRODUCTION

1.1. Background of Invention

In the past decades, supply of fossil fuels has decreased enormously and numerous environmental problems are exploited in hunt of a sustainable and renewable energy supply [1]. However, the strong dependence on the supply of non-renewable fossil fuels causes threat of global warming along with energy crises [2]. The statistical growth of world population and the unregulated industrial growth have accelerated the consumption of energy with release of unwanted agents into the environment that deteriorates the overall ecological balance [3]. A highlighted review by world energy statistic depicts the total energy consumption world wide as shown in Figure 1.1 [4]. The trend of dramatic technologies with personal and mobile electronics application for environmental monitoring and communication uses huge amount of power [5]. Powering of these requires batteries but challenge arises with recycling and replacement of these electronics. A worldwide effort has begun towards development of technologies that will make use of energy harvested from environment [6]. The exploration of alternative sources is one of the major challenging tasks.

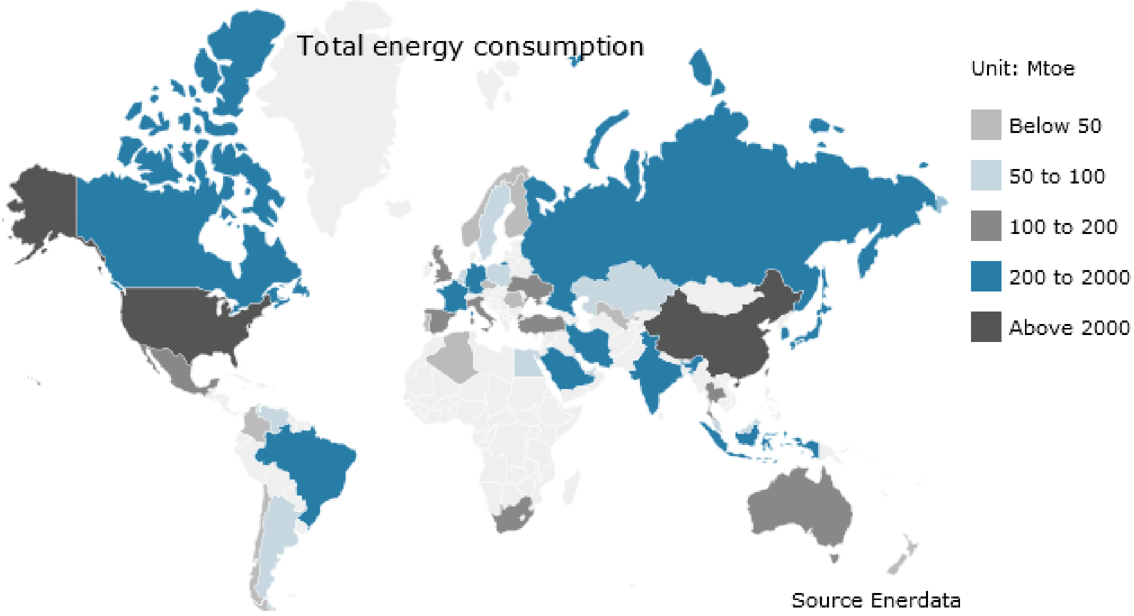

Figure 1.1. World’s total primary energy consumption statistics-2013 [4]

Solar energy is solitarily the largest and cleanest alternative energy form, but its consumption and utility is still very rare [7]. Recent research focuses on the development of a sustainable and lucrative manner to harvest solar energy with minimum global damage and that can satisfy the growing energy demand [8]. The global energy consumption by different sources has been presented in Figure 1.2 [9]. The use of most sustainable energy is almost negligible. A scientific understanding along with technology development of energy harvesting for empowering future is the ultimate requirement. Thus, the goal is to develop materials that can contribute to the progress of environment harmony, ecologically clean, sustainable and chemical technologies with high energy efficiency using the abundant energy [8].

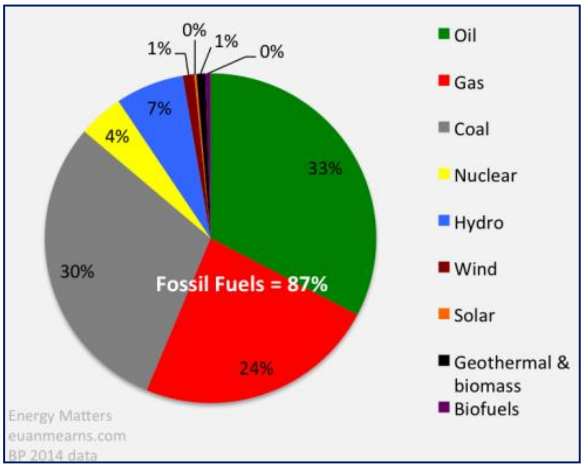

Figure 1.2. Global energy consumption – 2013 [9]

Today, the technological world using nanomaterials advocate ‘Nanotechnology’ for reduced use of energy and resources [9]. Theoretically it has been proved that nanomaterials have more potential over bulk conventional materials because of its reduced sizes. A new working definition to the word ‘nanomaterials’ has been given by US EPA in April 2010 as “an ingredient that contains particles that have been intentionally produced to have at least one dimension measurable between approximately 1 and 100 nanometers” for facilitation of its use in products commercially. The high expectations on nanomaterials is due to their unique properties like optical, electrical, thermal, mechanical, magnetic and catalytic properties that make them special ingredients for number of applications [10, 11]. As the world is looking forward to the miniaturization, light-weight and less energy consuming materials are more explored [12, 13]. The global market for nanotechnology did not match the hype initially but several permeable products in consumer areas have grown the market. However, the manufacturing of these nanomaterials has an unexpected footprint over the ecological system that relates to the specialized production environments, high water and energy demands with low yield of product and highly generated wastes [14-16]. These nanomaterials are liable to be used in smaller quantities than substances used conventionally such that over all life-cycle assessment of the products would contribute to an accurate impression of total energy and environmental impacts [17]. The possibility in successful commercialization of nanomaterials is only when production and application development proceeds in parallel with each other.

Estimation for energy saving made by International Energy Agency (IEA) corresponds to almost one fifth of the current energy consumption worldwide. This can be achieved by improvement in the energy efficiency through nanotechnology that enables huge energy and saving the cost especially through transportation, buildings and large scale manufacturing industries. The windows in these concrete structures creates a connection to the fantasy world outside that adds a verge of natural lighting but critically affects the energy balance of the buildings. ‘Nanotechnology based-Smart windows’ has outweighed the problem of energy saving and conversion. ‘Smart glass windows’ outbreak can be dated back to late 1990’s. These windows are capable of changing colour at the flick of a switch, i.e., through application of voltage that optically changes electrochromic glass from transparent to translucent and vice-versa. This associates migration of electrons from counter electrode to an electrochromic electrode layer. Management of heat and light can efficiently and optimally balance the cooling and lighting of the indoors. This phenomenon of reversible color change is explained through ‘electrochromism’. Figure 1.3 presents a typical comparison between smart glass and normal glass windows with light transmission percentage as advantages during climatic changes [18].

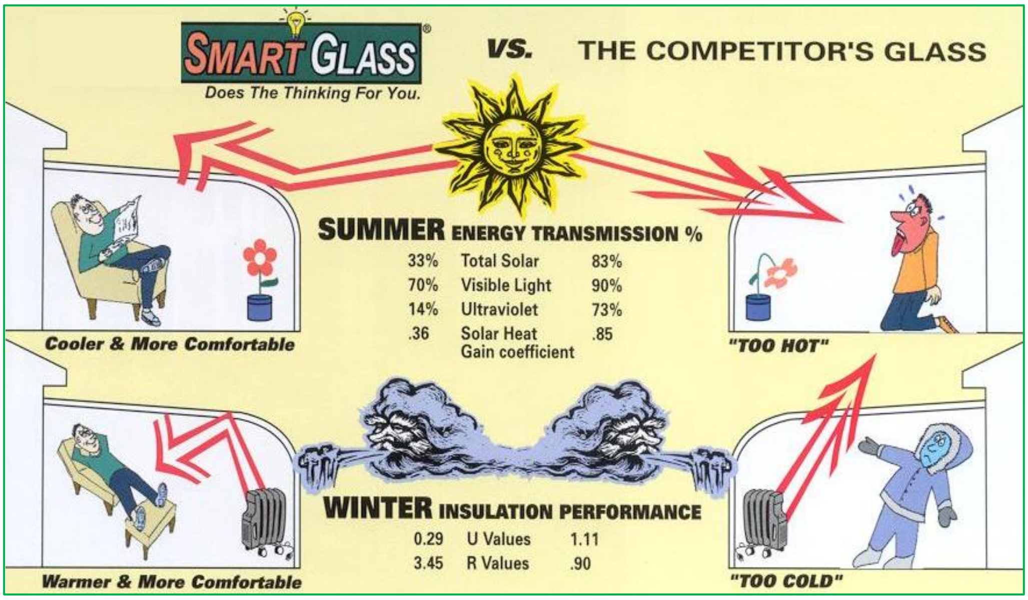

Figure 1.3. Advantages of Smart glass vs. normal glass windows.

Another emerging and serious problem in most of the developing and developed nations is the environmental pollution. Anthropogenic activities contribute to the major imbalance of ecosystem via pollution made by air, water and solid waste like plastics. Most of the common pollutants include highly toxic organic pollutants like aliphatic and aromatic compounds with chlorine, agro-wastes like pesticides and insecticides, disinfection by products and etc. Apart from these pollutants untreated dyes, surfactants and detergents are directly disposed into the water. Inorganic compounds like heavy metals, obnoxious gases like SO_x, NO_x, CO and pathogens contribute to pollution of the environment [19]. With escalating revolution in science and technology, demand for newer chemicals is rising, which could be used in various industrial processes. Organic textile dyes came up as one of the many new chemicals which could be used in many industrial activities [20]. Extensive use of these dyes in industries has become an integral part of industrial effluent. Country side people are supposed to continuous use of this water for their daily household needs. Sometimes, due to scarcity of water people also use this water for drinking and irrigation purposes. Figure 1.4 shows release of dyes directly to water bodies with people using it for their convenience purpose. There are legislations relating to the safe disposal with clean and green processes for pollutant degradation for prolonged future but lack in implementation may cause havoc later in the environment. Thus, scientists are searching for methods that can treat these dyes before releasing to the environments. In this perspective, photodegradation of textile dyes using advanced oxidation process in presence of degrading media using nanoparticles is one of the best options [21-23].

Figure 1.4. Untreated textile dyes from industries into water bodies.

In recent the metal oxide semiconductors are potential candidate and most researched for both electrochromic smart glass and photo-oxidation of dye under influence of natural or artificial source of light [24, 25]. In this chapter, brief insight of metal oxide semiconductors, electrochromism and photodegradation in view point of energy and environmental impact have been discussed.

1.2. Metal Oxide Semiconductors

Metal oxide semiconductors are known to be an attractive category of materials that can be produced at large scale with low cost to meet the extensive demand [26]. Metal oxide semiconductors composed of transition metals such as are ZnO, TiO_2, SnO_2, WO_3, V_2O_5 and etc are highly explored for various applications [27]. The common utilization of metal oxide depends on the oxygen atoms that are bound to the transition metals but are commonly utilized for their semiconductive and catalytic properties. Their application is not limited to the pigments in plastics and paints but also in other advanced electro-optical devices [28]. The chemical properties of these transition metal oxides are influenced by the invariant surface structures affecting the surface energy and bonding. The coordination of the ions of metal and oxygen affects the metal oxide surface atoms by changing the relative acidity and basicity [29]. The properties of these compounds are greatly influenced by the defects in the structure of transition metal oxides. Metal oxide surface containing active acidic and basic sites are commonly known via analytical techniques like calorimetry and infrared spectroscopy [30]. It is due to the versatile transition states, they can also undergo certain photons assisted reactions that are controlled by their semiconductive nature. Response towards the electromagnetic radiation is one of the most researched properties of these metal oxides [31]. This property provides space for complex redox reactions, specialized surface & intercalation reactions, isotope exchange and also exploration of other application is being carried.

1.3. Electrochromism- A Brief History

As defined widely, 'Electrochromism is the phenomenon being displayed by some materials that can reversibly change color upon application of burst of charge' [32]. Metal oxides containing transition metal possesses versatile interesting properties that are explored in the field of electrochromism. They are one of the prime branches of the chromic materials that can sustain reversible and continual changes to the optical properties like reflectance, absorbance and transmittance under alternate applied voltages. During the last decade, electro-optic devices made of these materials have acquired tremendous attention because of its probable applications in the area of optical displays, rear view mirrors and smart windows [33]. However, commercialized development and practical application of these are seriously restricted by the adequate conjugate of electrochromic materials and subsequent fabrication technology. These devices show evidence of low consumption of power with good memory effect, long term stability and high contrast. The configuration that is mostly used in electrochromic devices is the sandwich structure as shown in Figure 1.5.

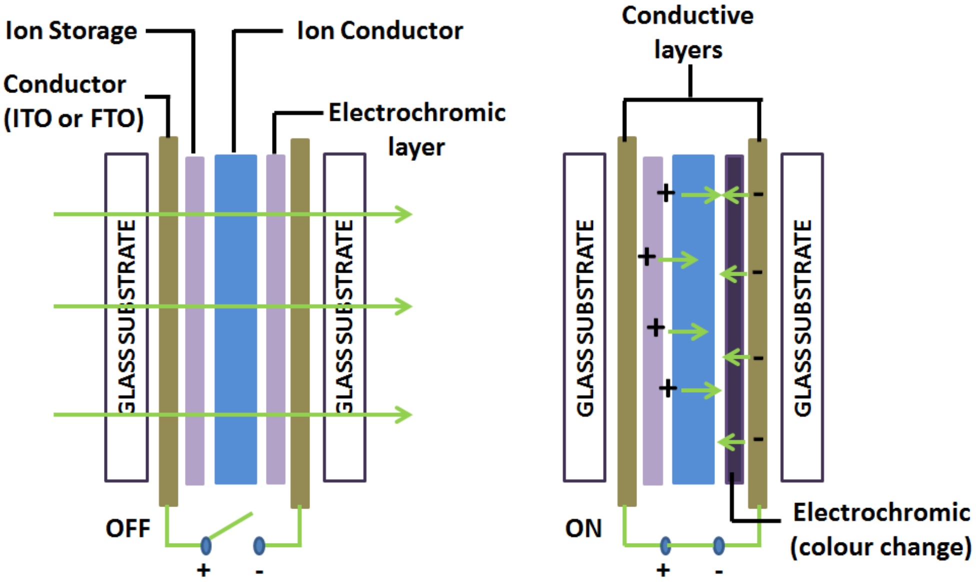

Figure 1.5. Typical sandwich structure of electrochromic material layer.

The sandwich structure includes a layer of electrochromic material, an electrolyte for storage of ion, and two transparent conductors that are utilized for establishing electrical contacts. With the application of voltage, ions drive into the layer getting intercalated into the sites causing chromic effect. Upon the reverse of voltage, the ions intercalated are withdrawn from the layer matrix and returns to the electrolyte. The electrolytes used are rich in small cations such as Na^+, H^+, Li^+, and etc [34, 35]. There are certain techniques to fabricate electrochromic films using magnetron sputtering, electrodeposition, plasma-enhanced chemical vapor deposition, lithography and etc. Although, these are traditional techniques but they have rigorous experimental condition, expensive equipments with complicated operation and multiple steps for processing [36-38]. Bulk particles for electrochromism are not conventional candidates as they are prone towards crack and getting detached from the substrate after repetitive cycles due to strain that relates to the poor material adhesion to the substrate [39]. Commercially, tungsten based materials are used for fabrication of smart glass windows [40]. However, they depend on the shape, size and crystal structure of the electrochromic material used. Therefore, it is a great challenge for scientists to synthesize novel electrochromic materials and develop economic fabrication techniques for electrochromic devices with enhanced performance.

1.4. Photocatalysis-Advanced Oxidation Process

With significant advancements made in the synthesis and fabrication of novel materials and nanostructures, the process of photocatalysis has witnessed a huge change over the decades. Designing of efficient processes for effective degradation of pollutants with less energy consumption has become the exclusive research area with publication and knowledge growing exponentially. The word ‘Photocatalysis’ refers to the acceleration in rate of chemical reactions like reduction/oxidation activated in presence of a catalyst (generally metal oxide semiconductors) under influence of the visible or ultraviolet radiation [41]. History dated back to 1972 when discovery of water splitting using TiO_2 single crystal electrode was explored by Fujishima and Honda explaining simultaneous oxidation to oxygen and reduction to hydrogen under an illuminated external bias as applied potential [42]. This incredible discovery has marked the onset of the redox reactions on the surface of the semiconductor through photonic phase. Soon realization was made that such processes could be a key point for environmental tidying application, when in 1977 Frank and Bard photocatalytically oxidized $CN^-$and SO_3^- using different transition metal oxide semiconductor materials like TiO_2, ZnO, Fe_2O_3 and WO_3. These transition metal oxide semiconductors are chosen depending on this band gap they posses as shown in Figure 1.6 [43]. There have been several standard review articles that are dedicated to the principles and mechanism of photocatalysis, with extraordinary emphasis on the electron transfer processes, surface chemistry of semiconductor oxides, lattice and electronic structures, reactive radicals generation, chemisorption of small and large molecules, surface modification by doping, photo-oxidation of organic and inorganic substrates, organic compounds via green synthesis, and also generation of hydrogen [44]. Hence, it can be regarded a well explicit field but still enormous challenges and opportunities exist in realization for large scale practical applications for decontamination of the environment and generation of clean energy.

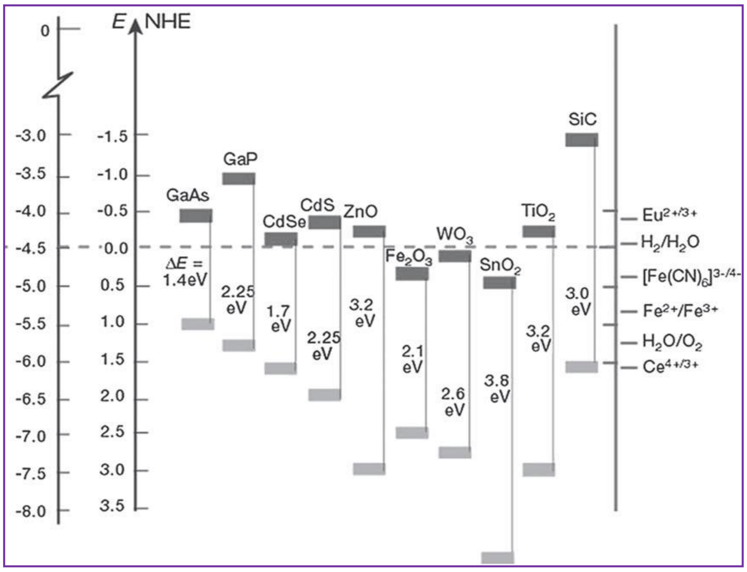

Figure 1.6. Band gap and energy levels of different semiconductors. [43]

It is worthy to mention that the photocatalysis is one of the fundamental part of the advanced oxidation processes (AOPs) that employs oxidizing agents like hydrogen peroxide (H_2O_2), Fenton's reagent (H_2O_2 + Fe^{2+}) and ozone (O_3) for effective detoxification of the pollutants. The working of the catalyst has been shown in Figure 1.7 [45]. During the process, the above oxidants are used in combination with ultra-violet (UV) radiation in order to step up the degradation rate of the pollutants. A common characteristic that oxidation process follow is the generation of reactive hydroxyl radicals (OH•), which acts as base precursors for degradation of any organic or inorganic compounds [46].

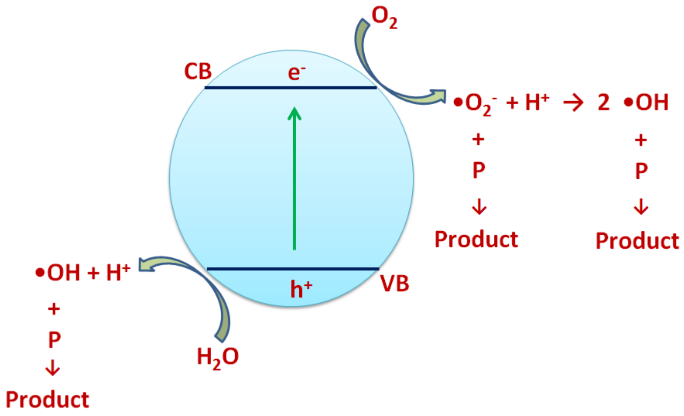

Figure 1.7. Schematic mechanism of catalyst under influence of energy.

However, one of the major lacuna in this process is recombination of the photoinduced electron-hole pairs. Nanostructured form of the photocatalysts can bear the potential to improve this phenomena because of their short charge transfer distances, reactant adsorption and product desorption enhancement due to the high surface area and electron density.

1.5. Aims and Purposes

The aim of this thesis is to synthesize two prime metal oxide semiconductors preferentially, WO_3 and ZnO, and optimization of their opto-electronic properties in perspective of highly efficient electrochromism phenomenon and photonic properties for effective textile dye degradation.

1.6. Thesis Structure

This dissertation has been elaborated in five different chapters. Essential background of all the important fields has been briefly described in introduction to know the basic and market importance of this research as discussed in **Chapter-1**. A detailed literature review on nanostructured tungsten oxide (WO_3) and zinc oxide (ZnO) has been discussed in **Chapter-2** describing the crystal structure, different synthesis methodologies through wet chemical methods by investigators in different aspects. A detailed mechanism of electrochromism and photocatalysis has also been described along with objective of the thesis at the end of this chapter. Synthesis of different morphologies of tungsten oxide with different synthesis methods likely acid co-precipitation and hydrothermal method has been explained in details followed by exploration of combustion synthesis of zinc oxide and also preparation of mixed oxide composites. Fabrication processes of electrodes for electrochemical testing has been described in **Chapter-3**. Basic theory and applicability of different analytical techniques used for characterizing synthesized materials and a brief description of experimental processes for carrying photocatalytic experiments is also discussed. **Chapter-4** represents the results and discussion of the above processes and characterizations. There are nine subsections under this section, which illustrates preparation of different morphologies of WO_3 nanoparticles using acid co-precipitation method with respect to pH, temperature and directing agents for optimization of process conditions followed by electrochemical testing of the fabricated electrodes of these nanoparticles. Hydrothermal approach is followed for easy synthesis of other morphologies of WO_3 and their electrochemical testing has been carried simultaneously. Morphology and crystal structure effect on electrochromism of WO_3/ITO electrodes has been discussed. Similar effect has been discussed for WO_3-ZnO nanocomposites for methyl orange degradation with an illustration of different mechanism under both UV and Visible light. Photocatalytic degradation of methyl orange and its kinetics in presence of combustion synthesized zinc oxide nanopowders under both UV and Visible light followed by stability test of the synthesized powders with respect to light irradiation has been studied. Comparative study on degradation of methyl orange under visible light for both commercial and synthesized ZnO formed WO_3-ZnO nanocomposites has been detailed. Cationic and anionic dye has been photodegraded under visible light irradiation using the WO_3-ZnO nanocomposites formed from synthesized WO_3 and ZnO. **Chapter-5** summarizes the research findings from the carried work and also extends the pathway towards possible future work. A complete record of references has been provided at the end of the dissertation.

References:

[1] M. Zach, C. Haglund, D. Chakarov, B. Kasemo, Nanoscience and nanotechnology for advanced energy systems, Curr Opin Solid State Mater Sci, 2006, 10, 132-143.

[2] M. Grätzel, Photoelectrochemical cells, Nature 2001, 414, 338-344.

[3] P. Harrop, R. Das, Wireless Sensor Networks 2011 – 2021, IDTechEX, 2011.

[4] https://yearbook.enerdata.net/

[5] Z. L. Wang, W. Wu, Nanotechnology enabled energy harvesting for self powered micro/nanosystems, Angew Rev, 2012, 51, 2-24.

[6] B. Z. Tian, X. L. Zheng, T. J. Kempa, Y. Fang, N. F. Yu, G. H. Yu, J. L. Huang, C. M. Lieber, Coaxial silicon nanowires as solar cells and nanoelectronic power sources, Nature, 2007, 449, 885 – 889.

[7] Z. L. Wang, Progress is piezotronics and piezo-phototronics, Adv Mater, 2012, 24, 4632 – 4646.

[8] N. S. Lewis, D. G. Nocera, Powering the planet:chemical challenges in solar energy utilization, Proc Natl Acad Sci USA, 2007, 104, 20142 – 20142.

[9] http://euanmearns.com/global-energy-trends-bp-statistical-review-2014/

[10] J. R. Szczech, J. M. Higgins, S. Jin, Enhancement of the thermochromics properties in nanoscale and nanostructured materials, J Mater Chem 2011, 21, 4037 – 4055.

[11] G. Q. Zhang, Q. X. Yu,W.Wang, X. G. Li, Nanostructures for thermochromics applications: synthesis, growth mechanism and property studies, Adv Mater, 2010, 22, 1959 – 1962.

[12] V. Leonov, T. Torfs, P. Fiorini, C. Van Hoof, Thermoelectric converters of human warmth for self-powered wireless sensor nodes, IEEE Sens J, 2007, 7, 650 – 657.

[13] V. Leonov, R. J. M. Vullers, Wearable electronics self-powered by using human heat: the state of the art and the perspective, Renewable Sustainable Energy Rev, 2009, 1, 062701-062714.

[14] L. D. Hicks, M. S. Dresselhaus, Effect of quantum well structures on the thermoelectric figure of merit, Phys. Rev. B 1993, 47, 16631 –16634.

[15] F. Zhou, J. Szczech, M. T. Pettes, A. L. Moore, S. Jin, L. Shi, Determination of transport properties in chromium disilicide nanowires via combined thermoelectric and structural characterizations, Nano Lett, 2007, 7, 1649 – 1654.

[16] A. I. Hochbaum, R. Chen, R. Diaz Delgado, W. Liang, E. C. Garnett, M. Najarian, A. Majumdar, P. Yang, Enhanced thermoelectric performance of rough silicon nanowires, Nature 2008, 451, 163 – 167.

[17] C. E. Chang, V. H. Tran, J. B. Wang, Y. K. Fuh, L.W. Lin, Direct-write piezoelectric polymeric nanogenerator with high energy conversion efficiency, Nano Lett, 2010, 10, 726 – 731.

[18] N. Gershenfeld, R. Krikorian, D. Cohen, The internet of things, Sci Am, 2004, 291,76 – 81.

[19] O.Legrini, E. Oliveros, A. M. Braun, Photochemical processes for water treatment, Chem Rev, 1993, 93, 671-698.

[20] C. Y. Hsiao, C. L. Lee, D. F. Ollis, Heterogeneous photocatalysis: degradation of dilute solutions of dichloromethane, chloroform and carbon tetrachloride with illuminated TiO_2 photocatalyst, J Catal, 1983, 82, 418‑423.

[21] D. R.Kennedy, M. Ritchie, J. Mackenzie, The photosorption of oxygen anf nitric oxide on titanium dioxide, J Trans Faraday Soc, 1958, 54, 119-129.

[22] G. Palmisano, V. Augugliaro, M. Pagliaro, L. Palmisano, Photocatalysis: a promising route for 21st century organic chemistry, Chem Comm, 2007, 3425‑3437.

[23] Y. Wada, H. Yin, S. Yanagida, Environmental remediation using catalysis driven under electromagnetic irradiation, Catal Sur Japan, 2002, 5, 127‑138.

[24] T. Aarthi, G. Madras, Photocatalytic degradation of Rhodamine dyes with nano TiO_2, Ind Eng Chem Res, 2007, 46, 7‑14.

[25] R. Vinu, S. U. Akki, G. Madras, Investigation of dye functional group on the photocatalytic degradation of dyes by nano-TiO_2, J Hazard Mater, 2010, 176, 765‑773.

[26] G. R. Patzke, F. Krumeich, R. Nesper, Oxidic nanotubes and nanorods- anisotropic modules for a future nanotechnology, Angew Chem Int Ed, 2002, 41, 2446-2461.

[27] G. R. Patzke, Y. Zhou, R. Kontic, F. Conrad, Oxide nanomaterials: synthetic developments, mechanistic studies and technological innovations, Angew Chem Int Ed, 2011, 50, 826-859.

[28] G. Buxman, G. Pfaff, Industrial Inorganic Pigments, Wiley-VCH Verlag GmbH & Co. KGaA , Weinheim, 2005.

[29] M. Kong, Y. Z. Li, X. Chen, T. T. Tian, P. F. Fang, F. Zheng, X. J. Zhao, Tuning the relative concentration ratio of bulk defects to surface defects in TiO_2 nanocrystals leads to high photocatalytic efficiency, J Am Chem Soc, 2011 , 133 , 16414-16417.

[30] X. B. Chen, L. Liu, Z. Liu, M. A. Marcus, W. C. Wang, N. A. Oyler, M. E. Grass, B. H. Mao, P. A. Glans, P. Y. Yu, J. H. Guo, S. S. Mao, Properties of disorder-engineered black titanium dioxide nanoparticles through hydrogenation, Sci Rep 2013, 3, 1510-1516.

[31] A. Ikesue, Y. L. Aung, Ceramic laser materials, Nat Photon, 2008 , 2 , 721-727.

[32] D. T. Gillaspie, R. C. Tenant, A. C. Dillon, Metal oxide films for electrochromic applications: present technology and future directions, J Mater Chem, 2010, 20, 9585-9592.

[33] M. Li, A. Patra, Y. Sheynin and M. Bendikov, Hexyl-derivatized Poly(3,4-ethylenedioxyselenophene): novel highly stable organic electrochromic material with high contrast ratio, high coloration efficiency, and low-switching voltage, Adv Mater, 2009, 21, 1707-1711.

[34] S. Ahmed, I. A. I. Hassan, H. Roy, F. Marken, Photoelectrochemical transients for chlorine/hypochlorite formation at "roll-on" nano-WO_3 film electrodes, J Phys Chem C, 2013, 117, 7005-7012.

[35] S. H. Lee, H. M. Cheong, J.-G. Zhang, A. Mascarenhas, D. K. Benson, S. K. Deb, Electrochromic mechanism in a-WO_{3-y} thin films, Appl. Phys. Lett., 1999, 74, 242-244.

[36] S. Osono, M. Kitazoe, H. Tsuboi, S. Asari, K. Saito, Development of catalytic chemical vapour deposition apparatus for large size substrates, Thin Solid Films, 2006, 501, 61-64.

[37] V. Sirtori, P. Cavallotti, R. Rognoni, X. Xu, G. Zangari, G. Fratesi, M.I. Troni, M. Bernasconi, Unusually large magnetic anisotropy in electrochemically deposited Co-rich Co-Pt films, ACS Appl Mater Interf, 2011, 3, 1800-1803.

[38] A. Azens, E. Avendano, J. Backholm, L. Berggren, G. Gustavsson, R. Karmhag, G. A. Niklasson, A. Roos and C. G. Granqvist, Flexible foils with electrochromic coatings: science, technology and applications, Mater Sci Eng B, 2005, 119, 214-223.

[39] http://plastics.dupont.com/plastics/pdflit/americas/rynite/H72128.pdf.

[40] E. L. Runnerstrom, A. Llordes, S. D. Lounis, D. J. Milliron, Nanostructured electrochromic smart windows: traditional materials and NIR selective plasmonic nanocrystals, Chem Comm, 2014, 50, 10555-10572.

[41] J. C. Colmenares, R. Luque, J. M. Campelo, F. Colmenares, Z. Karpinski, A. A. Romero, Nanostructured photocatalysts and their applications in the photocatalytic transformation of lignocellulosic biomass: an overview, Materials, 2009, 2, 2228-2258.

[42] T. Inoue, A. Fujishima, S. Konishi, K. Honda, Photoelectrocatalytic reduction of carbon dioxide in aqueous suspensions of semiconductor powders, Nature 1979, 277, 637–638.

[43] A. Fujishima, T. N. Rao, D. A. Tryk, Titanium dioxide photocatalysis, J Photochem Photobiol C, 2000, 1, 1–21.

[44] Y. Nakato, A. Tsumura, H. Tsubomura, Photo-and electroluminescence spectra from an n-titanium dioxide semiconductor electrode as related to the intermediates of the photooxidation reaction of water, J Phys Chem, 1983, 87, 2402–2405.

[45] U. I. Gaya, A. H. Abdullah, Heterogeneous photocatalytic degradation of organic contaminants over titanium dioxide: a review of fundamentals, progress and problems, J Photochem Photobiol C, 2008, 9, 1–12.

[46] D. Bahnemann, Photocatalytic water treatment: solar energy applications, Solar Energy, 2004, 77, 445–459.

Chapter 2

LITERATURE REVIEW

2.1. WO_3 Nanostructures

The development of advanced functional materials and smart devices through nanostructuring has emerged as one of the best tools to unlock their full potential. A rigorous study on tungsten oxide has been done for its unique properties contributed through chromism, photocatalysis and its sensing capabilities. Tungsten oxide (WO_3) is an n-type transition metal oxide with wide ranging applications. Initial study of WO_3 dated back to 17th century when the synthesis techniques for $LiWO_3$ and $NaWO_3$ were studied [1]. Researchers renewed their interest in WO_3 with the emergence of its efficient electrochromic (EC) effect. The synthesis and analysis of WO_3 nanostructures has become increasingly prominent with the advent of nanotechnologies [2]. Enhancement in the performance of the functional materials was achieved through nanostructuring of WO_3 that do not exist in the bulk form. In comparison with the bulk material, nanostructuring provides the following fascinating features: i) an increased surface-to-volume ratio, which provide more surface area for both chemical and physical interactions; ii) significantly altered surface energies that allow tuning and engineering of the material's properties, as atomic species near the surface have different bond structures than those embedded in the bulk; and iii) quantum confinement effects, due to their inherently small size, that significantly influence charge transport, electronic band structure and optical properties [3, 4].

The tungsten oxides consist of WO_6-octahedra arranged in various sharing (corners, edges, planes) configurations. The phases obtained by corner sharing are: monoclinic II (ε-WO_3), triclinic (δ-WO_3), monoclinic I (γ-WO_3), orthorhombic (β-WO_3), tetragonal (α-WO_3), and cubic WO_3 as shown in the polyhedral representation in Figure 2.1. Experimentally, cubic WO_3 is not commonly observed [5].

The main differences between the phases are the position alteration of W atom within the octahedra and variation in W—O bond lengths. Since, it has the defect perovskite structure; its simplest form has composition WO_3 or $LiWO_3$. As shown in Figure 2.2a, W ions occupy the corners of a primitive unit cell, and O ions bisect the unit cell edges. The vacant central atom acts as a conducting medium upon intercalation by ions like Li or Na in symmetry. Each W ion is surrounded by six equidistant oxygen ions. The stable monoclinic WO_3 can have a ReO_3 type structure (corner-sharing arrangement of octahedra) [6].

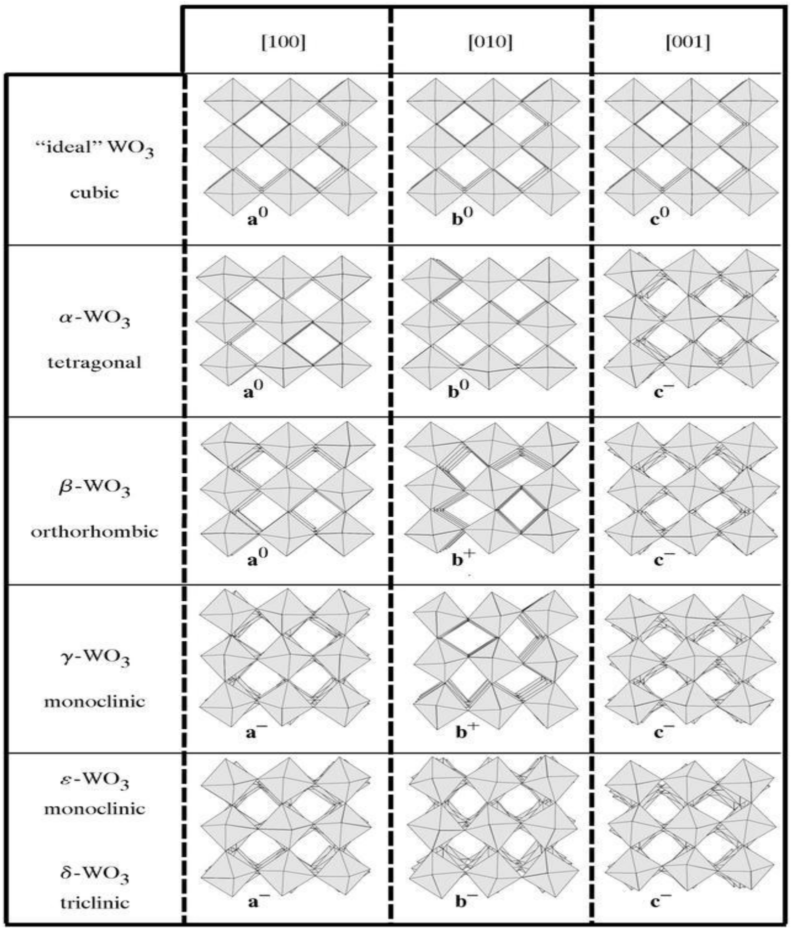

Figure 2.1. Tilt patterns of different polymorphs of WO_3 [5].

An infinite array of corner sharing WO_6 octahedral is formed as shown in Figure 2.2b. These octahedras are in planes perpendicular to the [001] hexagonal axis and it form four membered rings in the xy or (001) plane. These layers are stacked in arrangement and are held together by weak vander Waal's forces. The stacking of such planes along the z axis leads to the formation of tunnels between these octahedras. Figure 2.2c shows the conduit tunnel upon stacking. In the extended small tunnel, small ions can stay or move in case of an exterior force. This may present the possibility of ionic transport, intercalation in the structure, and also mechanism for electrochromic (EC) materials [7].

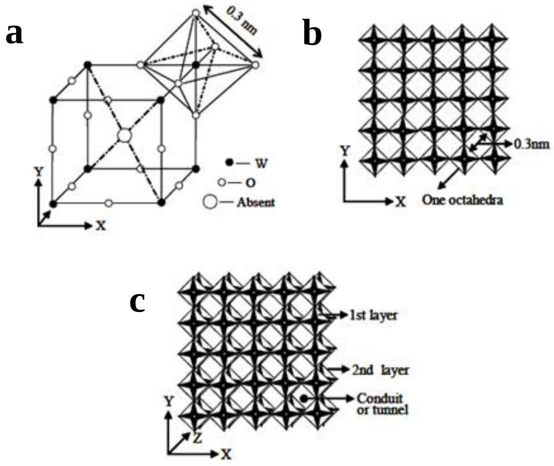

Figure 2.2. (a) Unit cell of the perovskite lattice; (b) One layer of the monoclinic WO_3 structure in the corner sharing arrangement of octahedral; (c) Layer stacking to form monoclinic WO_3 structure.

The widely reported crystal phase transitions for WO_3 in its bulk form occur in the following sequence: monoclinic II (ε-$WO_{3,}$ < - 43^{o}C) to triclinic (δ-$WO_{3,}$ - 43^{o}C to 17^{o}C) to monoclinic I (γ-$WO_{3,}$ 17^{o}C to 330^{o}C) to orthorhombic (β-$WO_{3,}$ 330^{o}C to 740^{o}C) to tetragonal (α-$WO_{3,}$ >740^{o}C). These transitions are partially reversible, with monoclinic I (γ-WO_3) as the most stable phase at room temperature [8]. A quite complex behavior is observed upon nanostructuring that depends on the morphology and dimension of the material. As proposed by Gibbs-Thomson expression, the size reduction of WO_3 crystallite enhances the surface energy that affects the material property by decreasing the melting and sublimation temperature [9, 10]. Thus, in nanostructured WO_3 phase transition occurs at lower temperature than that compared to bulk WO_3. In general, the tetragonal and orthorhombic phases of WO_3 are found during high temperature annealing. Apart from the crystal phases mentioned, another more specious metastable hexagonal WO_3 is reported by several groups of researchers [11, 12].

WO_3 is also known for its non-stoichiometric properties as its lattice withstand a considerable amount of oxygen deficiency [13]. Its electronic band structure is affected by a partial loss of oxygen content [14]. Reduction of WO_3 is accompanied by structural changes forming nonstoichiometric WO_x compositions such as $W_{20}O_{58}$, $W_{18}O_{49}$ and

$W_{24}O_{68}$. Such oxides are formed when WO_6 octahedras establish themselves alternately by partial edge sharing. [13].

Tungsten oxide is a wide band-gap n-type semiconductor, with the bandgap of nanostructured WO_3 blue shifted having the reported values as E_g = 2.60 to 3.25eV. The electronic band structure corresponds to the difference between the energy levels of the valence band that results from filled 2p orbitals of O and the conduction band formed by empty 5d orbitals of W [15, 16]. Normally, amorphous WO_3 with the most distorted structure possesses a relatively large E_g ~3.25eV, but typically 2.62eV has been reported for monoclinic WO_3 in bulk form [15]. Nanostructuring WO_3 increases the band gap due to reduction in the particle size. The band gap phenomenon could be well explained by a statistical formula of Fermi function, *f*(E) which explains the probability of finding a free electron in a given energy state. The expression for Fermi function is given below:

$$f\ (E) = \frac{1}{e^{\frac{(E-E_F)}{k_B T}}+1} \qquad (1)$$

Where, E_F is the Fermi energy, k_B is the Boltzmann's constant and T is the absolute temperature of the solid. According to the above function, the Fermi energy is present in the middle of the highest occupied band in conductors. However, Fermi energy is given by band gap energy in semiconductors and insulators. Figure 2.3 shows the plots of Fermi energy versus temperature (when T= 0 K and T= 500 K).

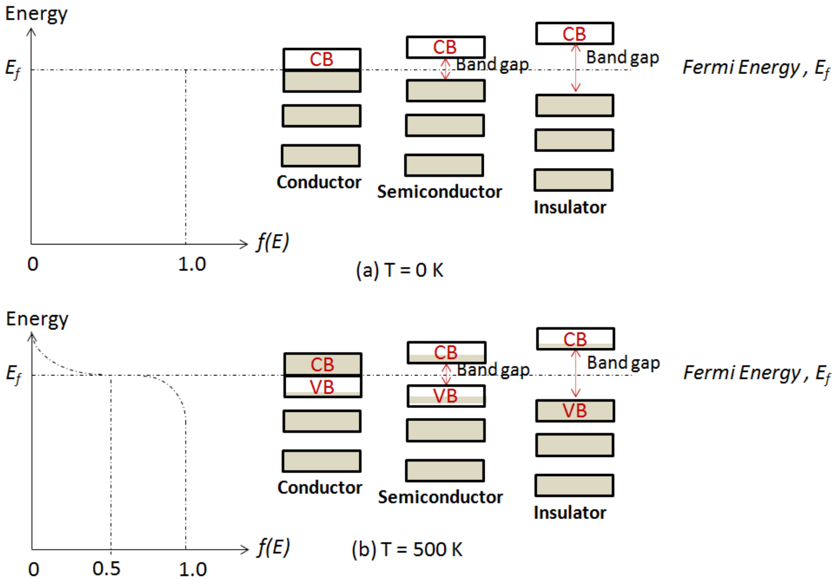

Figure 2.3. Fermi energy and corresponding band diagrams for conductor, semiconductor and insulator under (a) T= 0 K and (b) T= 500 K.

There is a drop in the probability of finding free electron in valence band as seen in the figure. The increment temperature allows the electron jump to the conduction band. The overlapping band structure in conductors does not have any barrier for free electron movement. However, in case of semiconductors, electrons have enough energy to cross the band gap but only few electrons can only overcome the band gap in insulators [17]. Band gap in nanomaterials differ from that of the bulk material. The presence of few atoms in the band structure of material causes the spreading of energy states and widens the band gap of semiconductors and also insulators. For example, when the atoms are arranged in atomic level, their sublevels split and band broadens with addition of more atoms. Band gap gets smaller as band broadens as shown in Figure 2.4. Therefore, quantum dots have the bigger band gap energy [18].

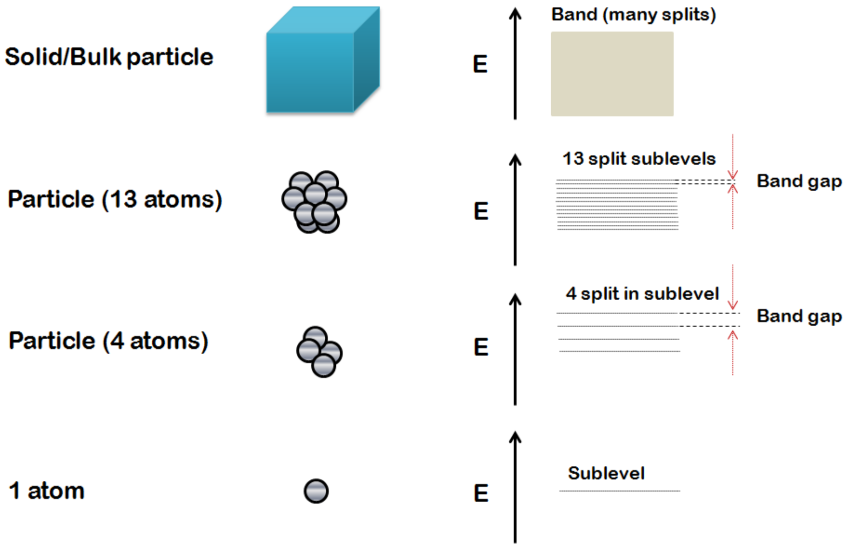

Figure 2.4. Band gap tuning with respect to particle size.

When we talk of changing the band gap of material by nanostructuring, we change the wavelength of electromagnetic radiation it emits. In perspective of nanostructuring, this causes blue shift in the optical absorption as the visible region is dominated by the absorption threshold defined as the band gap energy of the material [19]. Most of the visible wavelength is essentially transparent for stoichiometric form of WO_3. Thus, photon energies greater than the band gap energy, the light absorption α can be approximated by the equation: [20]

$$\varepsilon\alpha \propto (\varepsilon - E_g)^{\eta} \qquad (2)$$

Where ε is the photon energy and $\eta=2$, indicating allowed indirect transitions for WO_3. The observed blue shift is widely accepted as the quantum confinement (QC) effect [21]. Quantum confinement can be described as when the material diameter is similar to the magnitude of de Broglie wavelength of the electron wave function. More precisely, smaller materials have tendency to deviate their opto-electronic properties than those of bulk materials. The QC effect is divided into two categories namely strong and weak. When the crystal size is reduced to much smaller than the Bohr radius (3nm for WO_3) of the material, it is having the strong QC effect [22]. This causes direct changes to the electron wave functions and affects the band gap energy. The weak QC effect occurs when the crystal size is larger than the Bohr radius of the material. This affects the band gap energy by the indirect perturbation caused to the electron wave function [23]. For n-type semiconductor materials, electrical conduction relies on a significant concentration of free electrons being present in the conduction bands. The concentration of free electrons in such materials is determined by the concentration of stoichiometric defects in the form of oxygen vacancies [24]. Adding to the above factors, structural factors such as grain size, grain boundary, morphology, crystal phase and dopants have a great influence on the material conductivity. Depending on the stoichiometry, electrical conductivity of single crystal WO_3 ranges from 10 to 10^{-4} S cm^{-1} [25, 26]. Synthesis techniques and the growth condition play a pivotal role for development of such properties. Nanostructured WO_3 allows effective intercalation to achieve optimum band structures, while it is more difficult for dopants to diffuse into bulk WO_3.

2.2. Synthesis Techniques of WO_3 Nanostructures

Many different approaches have been disclosed for the synthesis of WO_3 nanostructures via different wet chemical methods following the predefined processing. Wet chemical method specifically includes sol-gel, acid precipitation, hydrothermal, solvothermal and combustion method, etc [27-29]. The above methods offer a better control of the material morphology through hydrolysis, condensation, etching and oxidation during the reaction. Some of the synthesis processes in the perspective of project objective are discussed below in details.

2.2.1. Acid Precipitation Method

Synthesis of WO_3 nanostructures from peroxo-tungstic acid precursor is most commonly reported under wet chemical process using acid for precipitation [30, 31]. This method demonstrates dissolution of tungsten metal in concentrated hydrogen peroxide solution to produce peroxo-complexes. Addition of organic or mineral acids to this complex at 50-60°C produces $WO_3.nH_2O$ gel that upon calcination forms WO_3 [32-34].

Nogueira et al followed thermal decomposition of precursor tungstic acid to form nanopowders. The yellowish precursor was synthesized by interactive mixing of $Na_2WO_4.2H_2O$ and HCl and variable parameter including concentration of W(VI) species, H^+ concentration, temp and time has significant influence on the resultant morphologies and size after calcination at 500°C for 1 hour. Different set of morphologies such as round plates, micrometric rectangular plates and also nanosized WO_3 were reported [35].

Another researcher uses tetrabutylammonium decatungstate as the precursor material for the precipitation by addition of aqueous tetrabutyl ammonium bromide (TBABr) solution to tungstic acid solution. It forms a white precipitate that is recrystallized in hot dimethyl formamide to give yellow crystals of precursor material that is loaded inside the tubular furnace at temperature 450°C under Ar atmosphere for 3 hours. Monoclinic WO_3 nanorod was obtained after calcination having rods length in the few hundred nanometres and width of 20-60 nm [36].

A highly crystalline orthorhombic WO_3 nanoparticle was obtained from tungsten hexachloride precursor via low temperature hydrolysis method followed by water in oil sucrose ester micelle emulsion and cetyl-tri-methyl-ammonium-bromide (CTAB). Here, CTAB act as co-surfactant to stabilize the particles in the emulsion. Spherical shape particles were obtained with size ranging from 10-50 nm [37].

Acidification of aqueous sodium tungstate to form tungstic acid base precursor is another widely accepted processing technique [38]. This precursor solution undergoes hydrolysis and condensation to form hydrate of crystalline WO_3 particles followed by calcination at 400^oC to 500^oC to produce nanoparticles of WO_3 [39]. Fabrication of films uses this base precursor for deposition of particles but the resultant films prepared consists of large crystallites. Thus, control over the precursor preparation methodology can produce many interesting morphologies.

As seen in above methodologies developed by different researchers, surfactants are also used as directing agents to produce different morphologies during the sol-gel process. Either cetyl-tri-methyl-ammonium-bromide, $C_{19}H_{42}BrN$ (CTAB) or tetrabutylammonium bromide (TBABr) has been used as the directing agent during a sol–gel technique to prepare films with plate like morphology [40, 41]. Post annealing of WO_3 at temperatures less than 500^oC retains it hydrated structure after annealing. Difficulties have been observed to produce different directional morphologies through these methods. Investigation of the application potentiality depends on the development of low dimension morphology to enhance the electrical and optical performance for tuning modern device properties.

2.2.2. Hydrothermal Method

In the above backdrop, hydrothermal technique is a facile and cost effective method that has the capability to develop different WO_3 nanostructures at an elevated temperature ($120\text{-}300^oC$) for a certain period of time, allowing the nucleation and growth of the crystallites [42]. Addition of sulphates and some organic acids to the tungstic acid precursor produces a high aspect ratio WO_3 nanostructure that includes nanofibers, nanorods, nanobelts, etc. These additives act as directing or dispersing agents that control the growth.

Song et al. fabricated pure orthorhombic tungsten oxide nanobelts through hydrothermal route using tungstic acid as base precursor. Sodium sulfate and cetyltrimethylammoniumbromide (CTAB) were found promising directing agent for WO_3 nanobelts [43]. A comparative study was carried by Jiao et al. where the formation of plate, wedge and sheet-like orthorhombic WO_3 nanostructures were synthesized by using capping agents Na_2SO_4, $(NH_4)_2SO_4$ and CH_3COONH_4 to oxidize the methanol and split water. The highest photoconversion efficiency of 0.3% under simulated solar illumination was found for sheet-like WO_3 prepared using CH_3COONH_4 [44].

Su et al. synthesized both uniform orthorhombic and monoclinic WO_3 square plates with the assistance of tartaric and citric acid by hydrothermal process, respectively [45]. Synthesis of highly crystalline tungsten oxide nanorods through solution based method using tungsten hexacarbonyl as the base precursor was carried by Lee et al. The possible stoichiometry of the compound formed is tungsten oxide hydrate ($W_{18}O_{49}$). Oleylamine was used to control the size of the nanorods. Longer nanorods were formed at 270^{o}C with 12 equivalent of oleylamine whereas the shorter nanorods were formed at 250^{o}C with 16 equivalents [46]. Time optimized hydrothermal synthesis of one dimensional hexagonal WO_3 nanorods was achieved through autoclaving the aqueous solution of sodium tungstate dihydrate and sodium chloride in acid media at 180^{o}C. The morphology change along with particle size was determined. The nanorods were found to be 2-3 micron in length and 100-200nm in diameter after 3 hours of hydrothermal duration [47].

Highly purified hexagonal WO_3 nanowire was synthesized using oxalic acid and potassium sulfate as structure directing agents. Hydrothermal duration of 48h at 180^{o}C was provided for the formation of nanowires. Nanowire suspension was deposited onto Au/Ti finger electrode for NH_3 sensing. It was found that there are electrons being trapped or released on varying the bias voltage upon ultraviolet and NH_3 gas exposure. Furthermore, the chromic properties were induced by the injection/extraction of hydrogen ions upon ultraviolet light irradiation [48]. One-third hydrate of orthorhombic tungsten oxide nanorods were prepared by ion-exchange method combined with hydrothermal treatment. A strong acidic ion exchange resin was used to form yellow tungstic acid sol from sodium tungstate. The sol was kept for hydrothermal treatment for 24 hours. Diameter of nanorods obtained were 20-60 nm and 0.15-2μm in length. The product morphology changes from rod to bundle like and irregular shapes upon prolonged hydrothermal duration [49].

Recently, p-aminobenzoic acid has been used as a facile structure directing agents to synthesize hexagonal WO_3 nanorods hydrothermally [50]. In another research, growth of tetragonal nanobrick WO_3 has been done through acidified solution of sodium tungstate precursor [51]. Thiourea is another interesting directing agent to synthesis WO_3 microtubes followed by pyrochlore crystal structure of WO_3. The growth was under the influence of thiourea and hydroxylamine hydrochloride as viscosity regulator to form uniform tubular morphology [52]. Directional growth along [001] crystal direction was found using Na_2SO_4 as directing agent by hindering growth along (200) crystal plane to form hexagonal phase WO_3 nanorods that exhibited high photoactivity under visible light irradiation [53]. Hexagonal WO_3 hydrate nanowire netted-spheres having uniform diameter of 4-6nm were synthesized by using WCl_6, triblock copolymer Pluronic F127 and glycol as surfactant for sensing NH_3 showing a rapid response to 100ppm NH_3 gas. Reaction time, solvent and surfactant loading played an important role for WO_3 nanowire formation [54]. Some of the interesting FESEM images of different morphology have been shown in Figure 2.5.

Hong et al. investigated the size effect of monoclinic WO_3 nanoparticles from ammonium metatungstate using CTAB surfactant for photo-oxidation of water and achieved a maximum photocurrent density of $0.6mA/cm^2$ for the sample calcined at 600^oC [55]. Zhang et al. studied the electrochromic behavior of hydrothermally prepared monoclinic WO_3 nanotree films. The annealed film exhibited 30% optical reflectance with coloration efficiency value of 43.6 cm^2/C [56]. A brief summary of the WO_3 nanostructures synthesized from hydrothermal method using additives has been presented in Table 2.1.

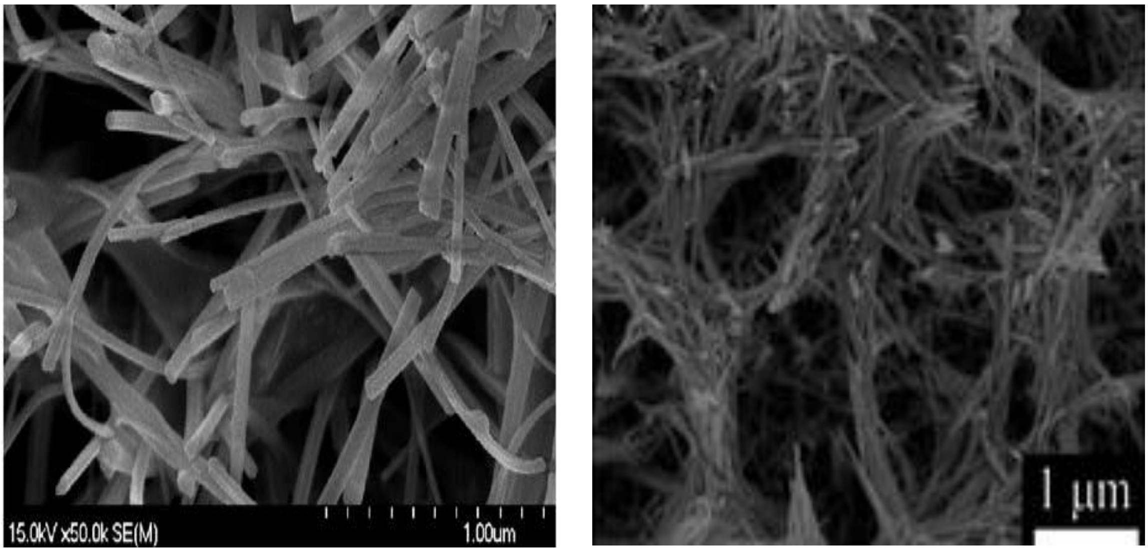

WO_3 Nanobelts

WO_3 Nanowire arrays

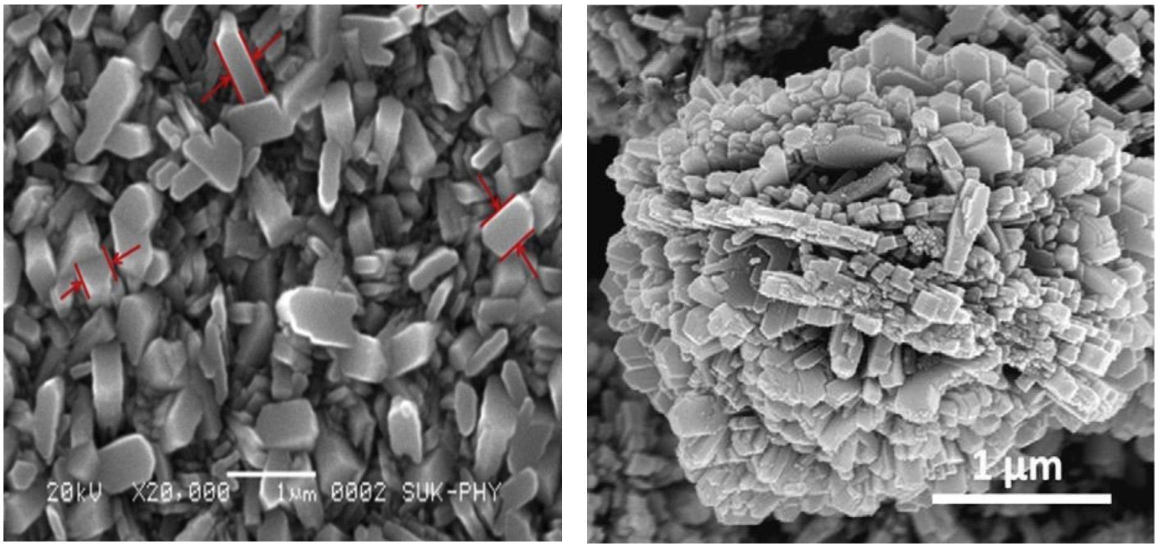

WO_3 Nanobricks

WO_3 Self assembled architechtures

Figure 2.5. FESEM images of different morphology of WO_3 (a) Nanobelts [43], (b) Nanowire arrays [57], (c) Nanobricks [51] and (d) Self assembled architectures [58].

Thorough literature survey depicts; no trial has been conducted to prepare different aspect ratio of morphologies from identical precursors following acid precipitation and hydrothermal techniques by control over their concentration, solution pH and temperature. Hence, this challenging task has been considered as one of the objectives in this research work. Morphological and crystal structure effect has been studied in respect of electrochromism and photocatalysis.

Table 2.1. Synthesis of WO_3 nanostructures using hydrothermal process.

Morphology	Precursor	Additives	Temp. (^oC)	Duration (h)	Crystal Phase	Ref.
Nanorods	H_2WO_4	$(NH_4)_2SO_4$	180	8	h-WO_3	[59]
Nanosheets	$Na_2WO_4.2H_2O$	Nitric acid	180	3	m-WO_3	[60]
Hierarchical spheres	$Na_2WO_4.2H_2O$	Citric acid	120	24	m-WO_3	[61]
3D Sphere-like architectures	H_2WO_4	Malic acid	120	24	m-WO_3 or h-WO_3	[58]
Nanorods	$Na_2WO_4.2H_2O$	Oxalic acid Poly acid	180	3	h-WO_3	[62]
Nanotube bundles	H_2WO_4	$KHSO_4$ $NaHSO_4$	180	24-48	h-WO_3	[63]
Nanotube WO_3	WCl_6	Urea	180	12	m-WO_3	[64]
Nanorods	$Na_2WO_4.2H_2O$	Oxalic acid & NaCl	170	2	m-WO_3	[65]

2.3. WO_3 Nanostructures for Electrochromism

Most investigation of electrochromism was focussed on the amorphous form of WO_3 films [66 - 69]. Problem with the amorphous structure relies with the stability of the films following dissolution of film in electrolyte making them unfit for potential use. In this perspective, crystalline WO_3 has been found much more stable due to its dense crystal structure and slow dissolution rate in acid electrolytes. However, bulk form of crystalline WO_3 usually shows slow switching response. Hence, achievement of enhanced switching behaviour is done through nanocrystalline WO_3 for fabrication of electrochromic (EC) materials and devices in recent years. An EC material is sustained by reversible changes in optical properties upon application of voltage.

2.3.1. Electrochromic Mechanism

Tungsten oxide is described as a defect perovskite structure formed by corner sharing of WO_6 octahedra that consist of cubical tunnel. This cubical tunnel has considerable empty spaces to avail interstitial sites of large number where the foreign ions can be cleaved. The film of tungsten trioxide with tungsten (VI) state electrochemically reduces to tungsten (V) to give electrochromic effect (color changes to blue) [70]. This color change is globally known as bronze type tungsten compound that forms through successive chemical and physical reactions taking place simultaneously. The detailed mechanism of coloration is still controversial. WO_3 act as cathode material for ionic insertion. The injection and extraction of electrons and protons like Li^+, H^+ etc play pivotal role during the electrochemical process. The coloration of the WO_3 films can be reversibly changed to original through electrochemical oxidation. In case of H^+ cations, the electrochemical reaction can be presented using equation:

$$WO_3 + xH^+ + xe^- \text{ (transparent)} \rightarrow H_xWO_3 \text{ (blue)} \qquad (3)$$

The amount of protons filled into the fractional number of site is designated as subscript x in the general formula H_xWO_3. At lower value of x, the film exhibits an intense blue color formed by photoeffected intervalence charge transfer between adjacent W(V) and W(VI) sites but at higher x value, ‘metallic bronze’, red/golden in color is irreversibly formed [71]. The induction of ions and electron injection due to promotion of cathodic polarization expands the lattice of the host oxide. The reversible coloration process is based on the double injection of light ions and electrons to form the tungsten bronze. WO_3 in its pristine state is pale yellow in color and a poor conductor of electricity whereas the intercalated H_xWO_3 state becomes highly conducting with blue color having absorption spectra around 0.5-0.6 μm. Figure 2.6 represents the schematic of the electrochromic device.

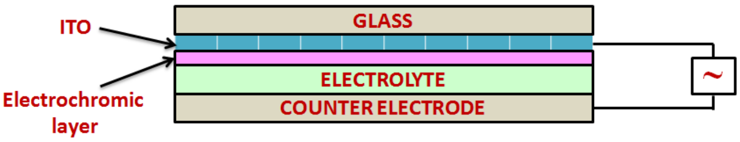

Figure 2.6. Schematic of the five layer design of electrochromic device.

The prototype of the electrochromic device (ECD) consists of five layers where the electrochromic material is sandwiched between an electrolyte and conducting glass substrate. The glass substrates are used for deposition of conducting material. Generally, indium-doped tin oxide (ITO) and fluorine-doped tin oxide (FTO) coated glass is used to make ECD. The device includes an electrochromic layer, transparent conductors for establishment of electrical conduction and an electrolyte for ion storage. The electrolyte is an ionic conductor kept at the middle of the construction is either a polymeric laminate material or a thin film exhibiting good conduction through intercalation of small ions H^+ or Li^+. The electrolyte is sandwiched between counter electrode and electrochromic material coated onto ITO. The counter electrode should be a material that provides a reversible electrochemical reaction in devices [72-74].

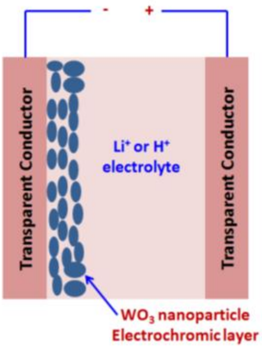

Figure 2.7. Schematic of electrolytic cell with WO_3 nanoparticle coated ITO electrode.

However, the small scale ECD testing is done in an electrolytic cell consisting of WO_3 coated ITO as working electrode/cathode, Pt as counter electrode and solution electrolyte as shown in Figure 2.7. The electrolytes used for testing are usually H_2SO_4, $HClO_4$ and HCl, where H^+ likes to serve as an intercalation ion, similarly for Li^+ insertion $LiClO_4$ serves as good electrolyte [75]. The applied voltages drive ions into the electrolyte causing chromic effect upon intercalation. The ions from the matrix of WO_3 returns back to the electrolyte upon reversing the applied voltage. In recent, films of nanostructured WO_3 has been utilised to overcome the backdrops of crystalline WO_3 for electrochromic applications.

2.3.2. Electrode Fabrication

Fabrication of nanostructured films on a particular substrate is another broad area of research. There are two types of film fabrication methods namely vapour phase and liquid phase methods. Vapour phase fabrication techniques include sputtering, thermal evaporation and spray pyrolysis that requires highly sophisticated instrumental operations. These methods provide high degree of dimension stability all along the matrix with expensive equipment set-up. However, favourable control of morphology and their dimension is limited by vapour phase. In this context, the liquid phase methods include sol-gel, template based film fabrication, drop-coating, dip-coating and hydrothermal techniques are economically popular and to achieve the morphology influenced properties of ECD. The sol gel film fabrication widely uses peroxotungstic acid as precursor due to its excellent stability [38]. The WO_3 films are formed by immersing the ITO substrate inside the precursor solution. The precursor obtained through dissolution of tungsten metal in hydrogen peroxide solution produces complexes followed by gelation taking place after aging for 24-48 hours. The films are then annealed at prerequisite temperatures to obtained WO_3 films [33]. In this process the structural morphology is affected by the humidity during aging process [76]. More humid environment can lead to formation of different structure morphology and mixed phase after annealing as shown in Figure 2.8 [39]. Annealing of the films is another factor that affects the film, morphology and its electrochemistry.

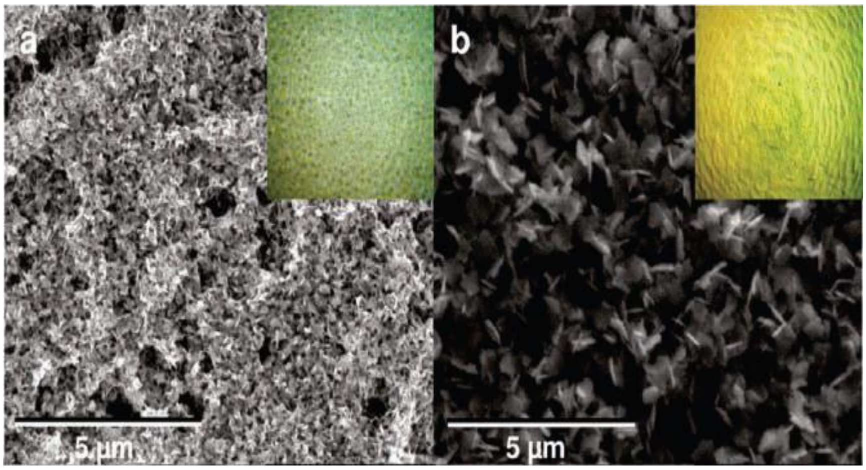

Figure 2.8. SEM images of hydrates of WO_3 (a) dried at low humidity and (b) dried at humid environment.

In similar fashion, removal of templates at elevated temperature is another restricting condition in template based film fabrication where by precursor template requires aging that needs to be controlled through slow hydrolysis [77-80]. Templates used are carbon based structures in the form of organic compounds such as polyethylene glycol (PEG), block copolymers, polymethyl methacrylate (PMMA), etc. The morphologies of the film obtained after soft templating using PMMA followed by heat treatment is shown in Figure 2.9 [81]. The integrity of the film is degraded through phase separation and dissociation due to rapid crystallization.

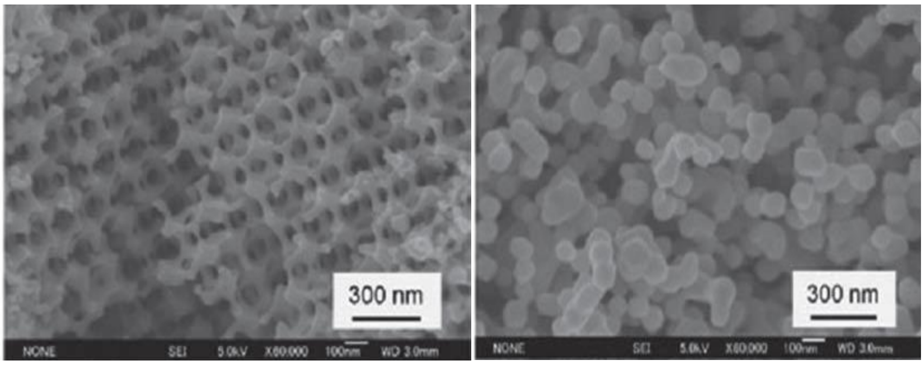

Figure 2.9. SEM images of WO_3 films using PMMA (a) 500°C and (b) 600°C.

Biswal et al fabricated WO_3 films by a simple dip coating technique. The precursor used for dip-coating was prepared by dissolution of tungstic acid powder in hydrogen peroxide to form peroxotunsgtic acid. The precursor was deposited onto Fluorine doped tin oxide (FTO) substrate [82]. This method has been further explored by Sharbatdaran et al to fabricate dip-coated electrochromic films [83]. In another research, mesoporous tungsten oxide films were prepared by using similar peroxotungstic acid precursor. In order to form mesoporous films non-ionic surfactant Brij 56 was mixed slowly into the precursor and dip coated onto Indium doped tin oxide (ITO) substrate followed by heat treatment of films at temperatures ranging between 100-450^{o}C [84]. Drop-casting is another economic technique for electrode fabrication, where a suspension of synthesized WO_3 nanoparticles is prepared followed by drop-coating onto substrate. Lu et al. synthesized uniform hexagonal WO_3 nanorods via hydrothermal process followed by preparation of a stable suspension of nanorods for dropping onto ITO substrate and drying at room temperature [85].

However, hydrothermal technique is another well studied technique to grow WO_3 nanostructures directly onto ITO/FTO or other metal substrate. Nanotree like WO_3 arrays were grown on tungsten metal substrate hydrothermally using oxalic acid, rubidium sulphate and nitric acid as other directing agents. The films obtained after hydrothermal treatment were annealed at 700^{o}C for 2 hours in air to develop crystalline monoclinic WO_3 that exhibited current density of ~5 mA/cm^2 [86]. In another research hydrothermally grown monoclinic WO_3 plate like structures on to fluorine doped tin oxide substrates were fabricated from peroxotungstic acid solution prepared after hydrogen peroxide treatment to tungstic acid obtained after acidification of sodium tungstate. High electrochromic stability with coloration efficiency of 38.2cm^2/C was obtained at 632.8nm [87].

The factors that influence the property of electrochemical device performance are cyclic stability/reversibility, optical modulation, coloration/bleaching time and coloration efficiency. The details summarization of some morphology, crystal structure with their electrochemical properties is tabulated in Table 2.2. The devices fabricated using WO_3 nanostructures showed significant impact with respect to morphology and crystal structure in optical modulation, switching time and coloration efficiency. Although, we can get versatile morphologies through hydrothermal method but removal of the conducting substrate and smaller size device fabrication restricts the applicability. Therefore, favourable growth of nanostructures using hydrothermal method followed by fabrication of films using dip-coating and drop-casting method for electrochemical measurements is one of the objectives in this work, which eventually assist to make large piece of electrode for electrochromic device.

Table 2.2. The electrochemical performance of WO_3 based nanostructures.

Surface morphology	Crystal structure	Optical modulation (%)	Color/bleach time (s)		Coloration efficiency	Ref
Nanowires (l ~5μm)	Monoclinic	65%	3	1.5	61.3 cm^2/mC	[88]
Nanorod (l ~2μm)	Hexagonal	66%	42	38	N/A	[89]
Nanorod (l ~2μm)	Hexagonal	34%	25	18	37.6 cm^2/mC	[90]
Vertically aligned WO_3	Hexagonal	66%	6.7	3.4	106.8 cm^2/C	[91]
Nanobrick	Monoclinic	76%	9.7	6.9	39.24 cm^2/C	[51]

2.4. WO_3 Nanostructures for Photocatalysis

In case of electrochromism, electrical energy supplied to the semiconductor causes conduction of electrons by changing the transition state of the material via changes in the crystal lattice. However, photocatalysis of a semiconductor material is through illumination of the material in a solvent medium usually water to convert energies equal to or larger than the semiconductor to photons [92]. Consequently, generation of electron-hole pairs takes place which further undergoes reactions to form free radicals that actively take part in photocatalysis/photodegradation. The positions of the conduction band and valence band edge makes WO_3 an efficient material for photo-oxidizing a versatile range of organic compounds, bacterial pollutants and textile dyes. In comparison to well known photocatalyst TiO_2, the advantage that makes WO_3 favourable photocatalyst is its narrow energy band gap of ~2.6 eV that allows irradiation of the blue region of the visible solar spectrum [93]. Another promising factor is its remarkable stability under acidic environments and possible treatment of water contaminated by organic acids. Enhancement of the photocatalytic ability is done by nanostructuring of WO_3 due to increased surface to volume ratio that increases the surface area of the particles and provides enough sites for photochemical reaction to occur [94]. The WO_3 nanoparticles having different dimensions exhibit photocatalytic performances differently. Moreover, separation of charge carriers and transport mechanism of nanocrystalline material is different from the bulk material.

2.4.1. Photocatalyst Mechanism

The mechanism that follows the photodiscoloration/degradation of dye is in accordance to the following mechanism: the catalyst is allowed to expose under light radiation following promotion of electrons from valence band to the conduction band resulting in generation of electron-hole pair.

$$\text{Catalyst} + h\upsilon \rightarrow e^-_{cb} + h^+_{vb} \tag{4}$$

Where, e^-_{cb} and h^+_{vb} is the electron in the conduction band and hole in the valence band, respectively. These entities can migrate to the catalyst surface, where they participate in redox reaction with foreign species present on the surface. Mostly, h^{+}_{vb} can easily react with surface bound H_2O to produce ${}^{\cdot}OH$ radicals, whereas, e^{-}_{cb} can react with O_2 to produce superoxide radical anion of oxygen.

$H_2O + h^{+}_{vb} \rightarrow {}^{\cdot}OH + H^{+}$ (5)

$O_2 + e^{-}_{cb} \rightarrow O_2^{-\cdot}$ (6)

These reaction forming free radicals prevents the recombination of the electron and the hole that are produced in the first step. The ${}^{\cdot}OH$ and $O_2^{-\cdot}$ radicals produced can then react with the dye to form other species and is thus responsible for the discoloration/degradation of the dye.

$O_2^{-\cdot} + H_2O \rightarrow H_2O_2$ (7)

$H_2O_2 \rightarrow 2\,{}^{\cdot}OH$ (8)

${}^{\cdot}OH + dye \rightarrow dye_{ox}$ (9)

$Dye + e^{-}_{cb} \rightarrow dye_{red}$ (10)

The generation of oxidative species during photocatalysis has been represented in a mechanistic way as shown in Figure 2.10 [95].

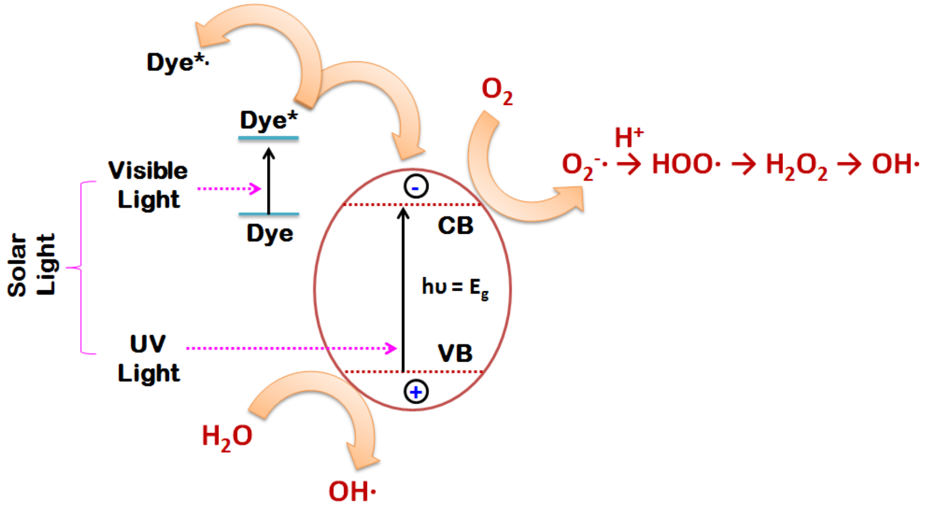

Figure 2.10. Schematic diagram showing the mechanism during photocatalysis.

The suggested mechanism of heterogeneous photocatalysis can be better described using Langmuir-Hinshelwood process on the basis of electrons and holes produced during photoexcitation of the catalyst. The dye molecules adsorbed on the catalyst surface forms reactive species through hole trap that decays as a result of recombination with an electron. Langmuir‑Hinshelwood (L‑H) is expressed in the form given below:

$$1/r = 1/k_r + 1/(k_r k_a C) \qquad (11)$$

Where, r is the reaction rate for the oxidation of reactant, k_r is the specific reaction rate constant for the oxidation of the reactant; k_a is the equilibrium constant of the reactant and C is the dye concentration.

However, when the chemical concentration C_o is a millimolar solution (C_o is small) the equation can be simplified to an apparent first order equation:

$$\ln(C_o/C) = k\mathrm{K}t = k_{\mathrm{app}}t \text{ or } C = C_o \exp(-k_{\mathrm{app}}t) \qquad (12)$$

A plot of ln C_o/C versus time represents a straight line, the slope of which upon linear regression equals the apparent first-order rate constant k_{app}. In general, first-order kinetics is appropriate for the entire concentration range up to few parts per million (ppm) and several studies have been reasonably well fitted by this kinetic model [96, 97]. Literature also illustrates the model dye degradation using different WO_3 nanostructures.

2.4.2. Dye degradation using WO_3 Nanostructures

Versatile WO_3 morphologies is synthesized and studied with respect to evaluation of the photocatalytic degradation of dyes using nanopowders. He et al. used hydrothermal method to synthesize multi structural tungsten oxide in presence of metal salts like Na_2SO_4 and $CaCl_2$ [98]. The obtained hierarchical nanonetwork structures were investigated for photodegradation of methylene blue under simulated solar irradiation. The nanostructures exhibited orthorhombic phase. The photodegradation of methylene blue took 7-8 hours for photochemical reaction. In another study, plate shaped monoclinic WO_3 nanostructures were used for degradation of alizarin yellow GG using Nd:YAG laser as an irradiation source [99]. Different morphologies of orthorhombic tungsten oxide were prepared successfully using conventional and microwave assisted methods. High surface acidity of WO_3 bundles efficiently degraded methylene blue after 5 hours of UV irradiation [100]. Another researcher, Bamwenda et al. prepared tungsten oxide powders by air annealing of different tungsten precursors. The precursors annealed at 700^{o}C showed highest photocatalytic activity after 20 hours of UV lamp irradiation [101]. WO_3 nanoparticles were synthesized using microwave assisted hydrothermal process without any additives and calcined at different temperature to obtain different polymorphs of WO_3 namely monoclinic and hexagonal structures. The photocatalytic activity of these WO_3 polymorphs were evaluated with respect to degradation of rhodamine B (rhB), indigo carmine (IC) and tetracycline hydrochloride (TC) under UV-Vis illumination. The samples treated at 700^{o}C showed highest photocatalytic activity. In this study, the percentage degradation of the organic dyes were found as 95% for rhB, 65% IC and 65% for TC after 96 hours of UV light irradiation [102].

Although WO_3 is a visible light absorber but degradation of organic dyes under UV & Vis light irradiation takes more time with individual WO_3. Individual backdrop is compensated by the presence of other semiconductor [103-105]. As we know, heterogeneous photocatalysis is the process that follows generation of electron-hole pairs on the semiconductor surface through absorption of light energy. This is the key factor for rapid degradation of organic dyes but the recombination of electron and hole pairs due to its narrow band gap structure is one of the detrimental factors. In order to prevent the recombination rate of individual WO_3, surface modification is required to enhance the photocatalytic degradation efficiency in minimal time [106]. The surface modification can be done by the given following four processes:

1) Metal or non-metal doping in semiconductor [107-109],
2) Metal impregnation on the surface of semiconductor nanoparticles [110-112],
3) Sensitization by dye to absorb high solar energy [113-115], and
4) Composite or coupled semiconductor nanoparticles [116-118].

Coupling of the semiconductors is one of the probable surface modifications that enhances the photocatalytic activity by synergistically combining two semiconductor materials to compensate the individual backdrop. Moreover, tuning of band gap to absorb both UV and visible is easier in case of coupled semiconductors. Material sensitivity during photocatalysis is another restrictive factor that mainly occurs when semiconductor is doped with metal ions and also noble metals are expensive. Light absorbing dyes are used for sensitization but they need efficient charge separating semiconductors. Thus, surface modification by semiconductor coupling is effective and chosen for photocatalysis [99].

2.4.3. Surface Modification of WO_3 Nanostructures

Literature has reported numerous semiconductor composites like WO_3/AgBr, WO_3/Ag/ZnO, WO_3/TiO_2, WO_3/fullerene-TiO_2 and other WO_3-carbon composites. Researchers are also trying to use the blue region visible absorption of WO_3. Recently, WO_3/Ag/ZnO was synthesized by precipitation-decomposition method and used against degradation of Napthol Blue Black in aqueous solution under solar light for 40 min. The described photochemical reaction was depended on pH, dye concentration and catalyst dosage [98]. Similar precipitation deposition method was followed by Cao et al. to synthesize AgBr loaded WO_3. Methyl orange was degraded using the photocatalyst with addition of H_2O_2 in photochemical slurry for efficient trapping of electrons and improve catalytic efficiency. The mineralization of methyl orange was carried till 3 hours [119]. Photochemical degradation of versatile dyes was carried using WO_3-TiO_2 mixed oxide composite under both UV and visible light irradiation for 2 hours. Herein, TiO_2 loaded with 15% WO_3 showed highest photocatalytic activity [120]. In another research WO_3-TiO_2 photocatalyst was prepared in a vacuum evaporator by impregnation of TiO_2 with WO_3 dissolved in H_2O_2 solution followed by calcination at certain temperatures. Low amount of WO_3 in 1-5% showed high adsorption of Acid red dye on surface enhancing the photocatalytic activity under UV light for 90 min [121]. The WO_3 used for coupling to form composite for photocatalytic degradation are mostly monoclinic in nature. However, the photocatalytic activities of different polymorphs of WO_3 along with morphological influence are very rare. Thus, this is one of the prime objectives of this thesis. Among the mentioned semiconductors, ZnO is a suitable alternative for coupling as it has similar band gap (~3.2 eV) and absorbs solar spectrum in larger fraction than TiO_2 [122]. The detail information of ZnO semiconductor material is discussed in the next section.

2.5. ZnO Nanostructures

ZnO is one of the key technological semiconductor materials. ZnO nanostructured material is known for its distinguished performance in electronics, optics and photonics. ZnO is a wide band gap ~3.2eV semiconductor suitable for short wavelength optoelectronic applications. It is also transparent to visible light and can be made highly effective by doping/coupling. It possesses a hexagonal wurtzite structure as shown in Figure 2.11. The crystal structure of ZnO can be described as tetrahedral coordination of O^{2-} and Zn^{2+} ions with number of alternating planes and stacked along c-axis alternately. ZnO in tetrahedral coordination results in non-central symmetric structure that contributes to the piezoelectric and pyroelectric properties [123-125].

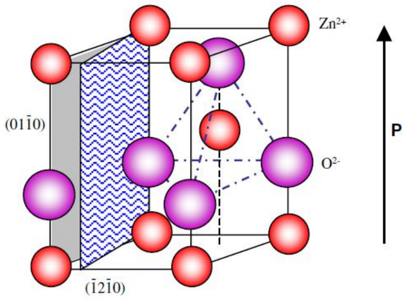

Figure 2.11. Tetrahedral coordinated Zn-O wurtzite model.

The interesting properties like piezoelectricity, large photoconductivity, semiconducting properties, wide energy band gap and high excitonic binding energy makes it suitable for various applications in the field of photoelectrics, UV-light emitters, window materials, solar blind photodetectors, transparent power electronics, displays etc. [126-128]. Moreover, its ability to harvest solar energy greater than that of TiO_2 makes it useful in the field of photocatalysis [122]. In the above mentioned applications, the parameters that play a key role are the morphology, grain size and surface area of the particles. There are several methods such as precipitation [129], hydrothermal [130], template based growth [131], sol-gel [132], solvothermal [133], combustion synthesis [134] for the synthesis of nanosized ZnO. Combustion synthesis (CS) has many advantages such as high production rate, energy efficiency, low processing cost and easy tailoring of the properties. This method requires low cost starting materials with no requirement of high temperature facilities. The self-propagating exothermic redox reaction during combustion is the major advantage that takes place with environmental friendly by-products [135]. The major advantage of combustion synthesis is that this method yields highly porous structures that could be beneficial for photochemical applications.

2.5.1. Combustion Synthesis of ZnO

The combustion synthesis is also known as low temperature self combustion, auto-ignition/self propagation method where metal salt solution is auto ignited in presence of the fuel to undergo thermal decomposition to metal oxide. This method follows an exothermic and self sustaining thermally favoured redox reaction from aqueous solution as shown in Figure 2.12. The calculation of proportions is carried in accordance to the valences of the reacting elements to fulfil the relation of oxidizer by reductant. In general, the nitrate salts are considered as precursors due to its high water soluble nature and release of nitrates at low temperature during synthesis. Moreover, metal nitrates are hygroscopic and can easily absorb moisture thus intensive stirring and heating can easily mix the reactants without addition of water. During the combustion process, large volume of gases accompanied by great mass loss due to rapid reaction is observed [136].

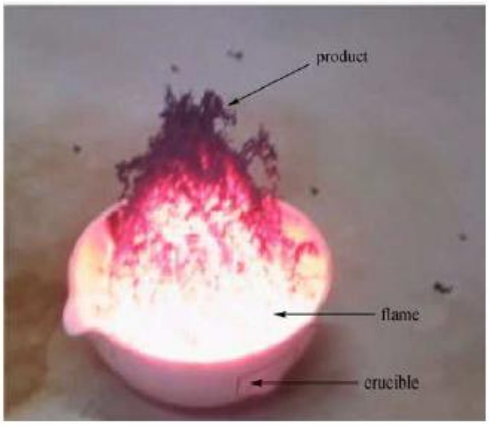

Figure 2.12. Combustion reaction in reactant mixture.

Many researchers followed this method to achieve their desired perspective. The influence of zinc nitrate to glycine ratio has been studied by Hwang et al. [137]. Fuels such as valine, β-alanine, zinc acetate and acrylamide have been successfully tested for the synthesis of ZnO nanopowders, where the smallest crystallite size was obtained with acrylamide fuel [138]. Lin et al. prepared ZnO particles, rod like structures and tetra-pod whiskers using metallic zinc and glycine in the presence of zinc nitrate as oxidant [139]. A pure mesoporous nanosized ZnO powder has been synthesized using various fuels like citric acid, dextrose, glycine, oxalyl dihydrazide, oxalic acid and urea. The photocatalysis of ZnO nanopowders obtained from oxalic acid showed highest activity for the degradation of orange G dye [140]. The thermal decomposition of zinc acetate in the presence of oleic acid as fuel was studied to fabricate size dependent ZnO nanocrystals for enhanced photocatalytic activity [141]. Directional growth of nanoparticles is an important factor in perspective of surface based application that provides high surface area with active surface sites for reaction to take place. Literature reports very few information about the directional growth of ZnO nanostructures by combustion method. This backdrop has been taken as one of the objectives to develop ZnO nanostructures in a confined direction.

2.6. WO_3-ZnO Nanocomposites

Several synthetic methods have been attempted to prepare WO_3-ZnO nanocomposites but evaluation of their cumulative photocatalytic efficiency of these mixed oxides is limited in recent literature [142, 143]. WO_3 – ZnO mixed oxide is prepared in one step aqueous solution route at low temperature with different loading of WO_3. These powders were used to investigate the photocatalytic and energy storage ability of the as prepared composites in comparison with the pure ZnO and Degussa P25 under UV-Vis light irradiation. The photocatalytic efficiency for degradation of methyl orange with 5 mol% loaded WO_3 is around 17.2% in dark for 3 hours only [144]. Another methodology explored for synthesis of WO_3-ZnO nanocomposite is flame spray pyrolysis. Different mol% of WO_3 was varied to fabricate different compositions of the nanocomposite. The precursor solution used was a mixture of zinc naphthenate and tungsten ethoxide in presence of ethanol. The precursor was sprayed followed by combustion to obtain the nanocomposites and characterized their physio-chemical properties [145].

WO_3-ZnO nanocomposite was prepared by hydrothermal – deposition method. Hydrothermally prepared ZnO nanorods were dispersed and mixed with ammonium metatungstate at pH ~6.5. The mixture formed precipitate after 12 hours and isolated for calcination at different temperatures. The composites prepared was used for photodegradation of an organic acid 2,4 -dichlorophenoxyacetic acid under the influence of natural sunlight. The WO_3-ZnO composite having 2.0% WO_3 and calcined at 400^oC showed highest photocatalytic activity after 7 hours under natural sunlight [146]. Recently, surface decoration of ZnO nanorods (commercially available) by WO_3 nanoparticles was synthesized by hydrothermal technique followed with chemical solution process. The endocrine disrupting chemicals like resorcinol, bisphenol A and methylparaben were successfully degraded under 55W compact fluorescence lamp irradiation. The photocatalytic degradation of methylparaben was 44% within 3 hours [142]. However, only around 50% efficiency has been achieved for WO_3 – ZnO in time period greater than 3 hours. In another research work, a series of WO_3/ZnO composites were prepared through co-precipitation-grinding method followed by calcination at different temperatures. These samples were evaluated for photocatalytic degradation of acid orange II under UV light irradiation. Highest photocatalytic efficiency of 53% was achieved through 2 at% doping of WO_3 in 5 hours which is highest till date. Effective suppression of recombination of photo generated electron and holes was achieved with 2% WO_3 calcined at 600°C which was found twice as active as pure ZnO [143]. Thus, further increasing the photocatalytic efficiency of WO_3 – ZnO nanocomposites in reduced time period is one of the objectives of this thesis.

2.7. Summary of Contribution

The extensive literature survey shows different morphology particles using different structure directing agents and control over the concentration of the precursor; solution pH and temperature are limited. The reaction and growth mechanism in specific hydrothermally synthesized WO_3 nanopowders with respect to combination of time, temperature and reaction concentration of the directing agents is also not reported. Moreover, no detail trial has been conducted in understanding the nanoparticle growth through different directing agents like HBF_4 and NaCl in respect of morphology and crystal structure.

The influences over different morphologies like spherical, cuboid and fiber nanostructures on electrochemical response are not available in recent literature. Furthermore, electrochemical response is also affected by the method of coating and electrochemical parameters. Comparison of two different coating methods namely drop-coating and dip-coating have also not been explored followed by coating thickness effect over electrochromism. Effect of both crystal structure and morphology of nanoparticles coated onto substrate have also not been compared in perspective of electrochromic phenomena.

Since, different crystal structure and morphology can affect the electrochemical properties, thus, no reports on the photocatalytic properties of WO_3-ZnO nanocomposites with morphology and crystal structure is assessed. Enhancement in the photocatalytic properties with different WO_3 loading content has not been reported for methyl orange in respect of crystal structure under both UV and visible light irradiation. No trial has been recorded for dimensional growth of ZnO nanocrystals through solution-combustion method. The activity of WO_3-ZnO nanocomposites in comparison to the commercial ZnO prepared nanocomposite has also not been investigated. The assessment to increase the efficiency under visible light irradiation particularly for a cationic and anionic dye has also not been documented for WO_3-ZnO mixed oxide nanocomposites. Based upon the above findings the objective of the present investigation has been summarized.

2.8. Thesis objectives

a) To optimize directional growth of WO_3 and ZnO nanostructures through wet chemical methods.

b) To compare the electrochemical properties of the synthesized nanoparticles with respect to different crystal structure and morphologies under different proton concentration and scan rate.

d) To estimate the photon assisted cationic and anionic dye degradation efficiency of nanostructured WO_3 coupling with semiconductor ZnO under UV and visible light irradiation.

References:

[47] S. K. Deb, Opportunities and challenges in science and technology of WO_3 for electrochromic and related applications, Sol Energy Mat Sol, 2008, 92, 245-258.

[48] C. G. Granqvist, Electrochromic materials: microstructure, electronic bands, and optical properties Appl. Phys. A, Mater. Sci. Process, 1993, 57, 3-12.

[49] A. S. Zoolfakar, R. A. Rani, A. J. Morfa, A. P. O’Mullane, K. K. Zadeh, Nanostructured copper oxide semiconductors: a perspective on materials, synthesis methods and applications, J Mater Chem C, 2014, 2, 5247-5270.

[50] Q. Zhang, K. Zhang, D. Xu, G. Yang, H. Huang, F. Nie, C. Liu, S. Yang, CuO nanostructures: Synthesis, characterization, growth mechanisms, fundamental properties, and applications, Prog Mater Sci, 2014, 60, 208–337.

[51] P. Roussel, P. Labbe, D. Groult, Symmetry and twins in the monophosphate tungsten bronze series $(PO_2)_4(WO_3)_{2m}$ ($2 \leq m \leq 14$), Acta Crystallogr B, 2000, 56, 377-391.

[52] E. K. H. Salje, S. Rehmann, F. Pobell, D. Morris, K. S. Knight, T. Herrmannsdorfer, M. T. Dove, Crystal structure and paramagnetic behaviour of ε-WO_{3-x}, J Phys Condens Mater, 1997, 9, 6563-6577.

[53] E.K.H. Salje, Polarons and bipolarons in tungsten oxide WO_{3-x}, Eur J Solid State Inorg Chem, 1994, 31, 805-821.

[54] T. Vogt, P. M. Woodward, B. A. Hunter, The high temperature phases of WO_3, J Solid State Chem, 1999, 144, 209-215.

[55] P. J. Desre, A thermodynamic model for the nanocrystal to glass transition of intermetallic compounds subjected to high deformation by mechanical attrition– application to $L1_2$ phases, Nanostruct Mater, 1997 8, 687-701 .

[56] M. Boulova, G. Lucazeau , Crystallite nanosize effect on the structural transitions of WO_3 studied by raman spectroscopy, J Solid State Chem, 2002, 167, 425-434.

[57] B. Gerand, G. Nowogrocki, J. Guenot, M. Figlarz, Structural study of a new hexagonal form of tungsten trioxide, J Solid State Chem, 1979, 29, 429-434.

[58] S. Balaji, Y. Djaoued, A. S. Albert, R. Z. Ferguson, R. Bruning, Hexagonal tungsten oxide based electrochromic devices: spectroscopic evidence for the Li ion occupancy of four-coordinated square windows, Chem Mater, 2009, 21, 1381-1389.

[59] A. Polaczek, M. Pekala, Z. Obuszko, Magnetic susceptibility and thermoelectric power of tungsten intermediary oxides, J Phys Condens Mater, 1994, 6, 7909-7919.

[60] V. O. Makarov, M. Trontelj, Sintering and electrical conductivity of doped WO_3, J Eur Ceram Soc, 1996, 16, 791-794.

[61] M. Gillet, K. Aguir, C. Lemire, E. Gillet, K. Schierbaum, The structure and electrical conductivity of vacuum-annealed WO_3 thin films, Thin Solid Films, 2004, 467, 239-246.

[62] S. K. Gullapalli, R. S. Vemuri, C. V. Ramana, Structural transformation induced changes in the optical properties of nanocrystalline tungsten oxide thin films, Appl. Phys. Lett. 2010, 96, 171903-171909.

[63] B. Rogers, S. Pennathur, J. Adams, Nanotechnology: Understanding small systems, CRC Press, Taylor & Francis group, 2008.

[64] Z. Guo, L. Tan, Fundamentals and applications of nanomaterials, Artech House, 2014.

[65] M. T. Chang, L. J. Chou, Y. L. Chueh, Y. C. Lee, C. H. Hsieh, C. D. Chen, Y. W. Lan, L. J. Chen, Nitrogen-doped tungsten oxide nanowires: low-temperature synthesis on Si, and electrical, optical, and field-emission properties, Small, 2007, 3, 658-664.

[66] A. Hjelm, C. G. Granqvist, J. M. Wills, Electronic structure and optical properties of WO_3, $LiWO_3$, $NaWO_3$, and HWO_3, Phys Rev B, 1996, 54, 2436-2445.

[67] A. D. Yoffe, Low-dimensional systems: quantum size effects and electronic properties of semiconductor microcrystallites (zero-dimensional systems) and some quasi-two-dimensional systems, Adv Phys, 1993, 42, 173-262.

[68] R. A. May, L. Kondrachova, B. P. Hahn, K. J. Stevenson, Optical constants of electrodeposited mixed molybdenum−tungsten oxide films determined by variable-angle spectroscopic ellipsometry, J. Phys. Chem. C 2007, 111, 18251- 18257.

[69] T. Ihn, Semiconductor nanostructures: quantum sates and electronic transport, OUP Oxford, 2009.

[70] K. Aguir, C. Lemire, D. B. B. Lollman, Electrical properties of reactively sputtered WO_3 thin films as ozone gas sensor, Sens Actuators B, 2002, 84, 1-5.

[71] G. A. De Wijs, P. K. de Boer, R. A. de Root, G. Kresse, Anomalous behaviour of the semiconducting gap in WO_3 from first principle calculations, Phys Rev B, 1999, 59, 2684-2693.

[72] R. S. Vemuri, K. K. Bharathi, S. K. Gullapalli, C. V. Ramana, Effect of structure and size on the electrical properties of nanocrystalline WO_3 films, ACS Appl Mater, 2010, 2, 2623-2628.

[73] Z. Gu, Y. Ma, W. Yang, G. Zhang, J. Yao, Self-assembly of highly oriented one-dimensional h-WO_3 nanostructures, Chem Comm, 2005, 16, 3597-3599.

[74] Z. Gu, H. Li, T. Zhai, W. Yang, Y. Xia, Y. Ma, J. Yao, Large-scale synthesis of single-crystal hexagonal tungsten trioxide nanowires and electrochemical lithium intercalation into the nanocrystals, J Solid State Chem, 2007, 180, 98-105.

[75] K. K. Zadeh, A. Vijayaraghavan, M. H. Ham,H. Zheng, M. Breedon, M. S. Srano, Synthesis of atomically thin WO_3 sheets from hydrated tungsten trioxide, Chem Mater, 2010, 22, 5660-5666.

[76] T. Nishide, F. Mizukami, Crystal structures and optical properties of tungsten oxide films prepared by a complexing-agent-assisted sol-gel process, Thin Solid Films, 1995, 259, 212-217.

[77] Y. Zhang, Y. Chen, H. Liu, Y. Zhou, R. Li, M. Cai, X. Sun, 3D Hierarchical structure of single crystalline tungsten oxide nanowires: construction, phase transition and voltammetric behavior, J Phys Chem C, 2009, 113, 1746-1750.

[78] M. Deepa, A. G. Joshi, A. K. Srivastava, S. M. Shivaprasad, S. A. Agnihotry, Electrochromic nanostructured tungsten oxide films by sol-gel: structure and intercalation properties, J Electrochem Soc, 2006, 153, C365-C576.

[79] B. Yang, Y. J. Zhang, E. Drabarek, P. R. F. Barnes, V. Luca, Enhanced photoelectrochemical activity of sol−gel tungsten trioxide films through textural control, Chem Mater, 2007, 19, 5664-5672 .

[80] A. K. Srivastava, S. A. Agnihotry, M. Deepa, Sol–gel derived tungsten oxide films with pseudocubic triclinic nanorods and nanoparticles, Thin Solid Films, 2006, 515, 1419-1423.

[81] H. I. S. Nogueira, A. M. V. Cavaleiro, J. Rocha, T. Trindade, J. D. P. Jesus, Synthesis and characterization of tungsten trioxide powders prepared from tungstic acids, Mater Res Bull, 2004, 39, 683-693.

[82] J. Rajeshwari, P. S. Kishore, B. Vishwanathan, T. K. Varadarajan, Facile hydrogen evolution reaction on WO_3 nanorods, Nanoscale Res Lett, 2007, 2, 496-503.

[83] N. Asim, S. Radiman, M. A. B. Yarmo, Synthesis of WO_3 in Nanoscale with the usage of sucrose ester microemulsion and CTAB micelle solution, Mater Lett, 2007, 61, 2652-2657.

[84] J. Livage, D. Ganguli, Sol-Gel electrochromic coatings and devices: A review, Sol.Energy Mater Sol C, 2001, 68, 365-381.

[85] M. Breedon, P. Spizzirri, M. Taylor, J. du Plessis, D. McCulloch, J. M. Zhu, L. S. Yu, Z. Hu, C. Rix, W. Wlodarski, K. Kalantar-Zadeh, Synthesis of nanostructured tungsten oxide thin films: a simple, controllable, inexpensive, aqueous sol−gel method, Cryst Growth Des, 2010, 10, 430-439.

[86] S. Kim, I. Hwang, J. Choi, J. Lee, Gas sensing characteristics of WO_3 nanoplates prepared by acidification method, Thin Solid Films, 2011, 519, 2020-2024.

[87] D. S. Martinez, C. G. Solis, L. M. T. Martinez, CTAB assisted ultrasonic synthesis, characterization and photocatalytic properties of WO_3, Mater Res Bull, 2015, 61, 165-172.

[88] H. Kominami, K. Yabutani, T. Yamamoto, Y. Kara, B. Ohtani, Synthesis of highly active tungsten (VI) oxide photocatalysts for oxygen evolution by hydrothermal treatment of aqueous tungstic acid solutions, J Mater Chem, 2001, 11, 3222-3227 .

[89] X. Song, Y. Zhao, Y. Zheng, Hydrothermal synthesis of tungsten oxide nanobelts, Mater Lett, 2006, 60, 3405-3408.

[90] Z. Jiao, X. Wang, L. Ke, H. V. Demir, T. V. Koh, X. W. Sun, Efficient synthesis of plate like crystalline hydrated tungsten trioxide thin films with highly improved electrochromic performance, Chem Comm, 2012, 48, 365-367.

[91] X. Su, F. Xiao, Y. Li, J. Jian, Q. Sun, J. Wang, Synthesis of uniform WO 3 square nanoplates via an organic acid-assisted hydrothermal processMater Lett, 2010, 64, 1232-1234.

[92] K. Lee, W. S. Seo, J. T. Park, Synthesis and optical properties of colloidal tungsten oxide nanorods, J Am Chem Soc, 2003, 125, 3408-3409.

[93] H. Hassani, E. Marzbanrad, C. Zamani, B. Raissi, Effect of hydrothermal duration on synthesis of WO_3 nanorods, J Mater Sci: Mater Electron, 2011, 22, 1264-1268.

[94] Y. H. Jun, C. Y. Qi, Y. Fang, P. Y. Hua, H. X. Wu, Z. Ding, T. D. Sheng, Hydrothermal synthesis and chromic properties of hexagonal WO_3 nanowires, Chin Phys B, 2011, 20, 036103 (1-6).

[95] R. F. Mo, G. Q. Jin, X. Y. Guo, Morphology evolution of tungsten trioxide nanorods prepared by an additive free hydrothermal route, Mater Lett, 2007, 61, 3787-3790.

[96] Q. Sun, F. Xiao, S. Ren, Z. Dong, J. Wang, X. Su, Hydrothermal synthesis of WO_3 nanorods and their performance in the adsorption of Rhodamine B and the synthesis of adipic acid, Ceram Int, 014, 40, 11447-11451.

[97] V. V. Kondalkar, R. R. Kharade, S. S. Mali, R. M. Mane, P. B. Patil, P. S. Patil, S. Choudhary, P. N. Bhosale, Nanobrick like WO_3 thin films: hydrothermal synthesis and electrochromic application, Superlattices & Microstructures, 2014, 73, 290-295.

[98] X. Wang, X. Meng, M. Zhong, F. Wu, J. Li, Hydrothermal synthesis of $WO_3.0.5H_2O$ microtubes with excellent photocatalytic properties, Appl Surf Sci, 2013, 282, 826-831.

[99] T. Peng, D. Ke, J. Xiao, L. Wang, J. Hu, L. Zan, Hexagonal phase WO_3 nanorods: hydrothermal preparation, formation mechanism and its photocatalytic O_2 production under visible light irradiation, J Solid State Chem, 2012, 194, 250-256.

[100] A. Yan, C. Xie, D. Zeng, S. Cai, M. Hu, Synthesis, formation mechanism and sensing properties of WO3 hydrate nanowire netted spheres, Mater Res Bull, 2010, 45, 1541-1547.

[101] S. J. Hong, Y. S. Gao, H. Y. Lin, S. J. Chen, Synthesis of tungsten trioxide nanowires by a solvothermal process, J. Engg. Technology and Education, 2010, 7, 192–197.

[102] J. T. Zhang, X. Wang, X. H. Xia, C. Gu, J. Tu, Electrochromic behaviour of WO_3 nanotree films prepared by hydrothermal oxidation, Sol Energy Mater Sol C, 2011, 95, 2107-2112.

[103] J. Zhang, J. Tu, X. Xia, X. Wang, C. Gu, Hydrothermally synthesized WO_3 nanowire array with highly improved electrochromic performance, J Mater Chem, 2011, 21, 5492-5498.

[104] H. Zhang, T. Liu, L. Huang, W. Guo, D. Liu, W. Zeng, Hydrothermal synthesis of assembled sphere like WO_3 architectures and their gas sensing properties, Physica E, 2012, 44, 1467-1472.

[105] Z. J. Gu, T. Y. Zhai, B. F. Gao, X. H. Sheng, Y. B. Wang, H. B. Fu, Y. M , J. N. Yao, Controllable assembly of WO_3 nanorods/nanowires into hierarchical nanostructures, J Phys Chem B, 2006, 110, 23829-23836.

[106] G. Zhang, W. Gu, H. Shen, X. Zhang, W. Fan, C. Lu, H. Bai, L. Xiao, W. Gu, W. Shi, Organic additives free hydrothermal synthesis and visible light driven photodegradation of tetracycline of WO3 nanosheets, Ind Eng Chem Res, 2014, 53, 5443-5450.

[107] S. Bai, K. Zhang, X. Shu, S. Chen, R. Luo, D. Li, A. Chen, Carboxyl-directed hydrothermal synthesis of WO_3 nanostructures and their morphology-dependent gas sensing properties, Cryst Eng Comm, 2014, 16, 10210-10217.

[108] J. R. G. Navarro, A. Mayence, J. Andrade, F. Lerouge, F. Chaput, P. Pleynikov, L. Bergstrom, S. Parola, A. Pawlicka, WO_3 nanorods created by self assembly of highly crystalline nanowires under hydrothermal conditions, Langmuir, 2014, 30, 10487-10492.

[109] J. Li, X. Liu, Q. Han, X. Yao, X. Wang, Formation of WO_3 nanotube based bundles directed by $NaHSO_4$ and its application in water treatment, J Mater Chem A, 2013, 1, 1246-1253.

[110] K. Hara, Z. G. Zhao, Y. Cui, M. Miyauchi, M. Miyashita, S. Mori, Nanocrystalline electrodes based on nanoporous walled WO_3 nanotubes for organic dye sensitized solar cells, Langmuir, 2011, 27, 12730-12736.

[111] F. Zheng, H. Lu, M. Guo, M. Zhang, Effect of substrate pre-treatment on controllable synthesis of hexagonal WO_3 nanorod arrays and their electrochromic properties, Cryst Eng Comm, 2013, 15, 5828-5837.

[112] J. Wang, X. W. Sun, Z. Jiao, Application of nanostructures in electrochromic materials and devices: recent progress, Materials, 2010, 3, 5029-5053.

[113] A. Georg, W. Graf, R. Neumann, V. Wittwer, Mechanism of the gasochromic coloration of porous WO_3 films, Solid State Ionics 2000, 127, 319-328.

[114] S. H. Lee, H. M. Cheong, P. Liu, D. Smith, C. E. Tracy, A. Mascarenhas, J. R. Pitts, S. K. Deb, Raman spectroscopic studies of gasochromic a-WO_3 thin films, Electrochim Acta, 2001, 46, 1995-1999.

[115] J. Y. Luo, S. Z. Deng, Y. T. Tao, F. L. Zhao, L. F. Zhu, L. Gong, J. Chen, N. S. Xu, Evidence of localized water molecules and their role in the gasochromic effect of WO_3 nanowire films, J Phys Chem C, 2009, 113, 15877-15881.

[116] G. A. Niklasson, L. Berggren, A. Larsson, Electrochromic tungsten oxide: the role of defects, Sol Energy Mater Sol C, 2004, 84, 315-328.

[117] R. Baetens, B. P. Jelle, A. Gustavsen, Properties, requirements and possibilities of smart windows for dynamic daylight and solar energy control in buildings: A state-of-the-art review, Solar Energy Mater Solar C, 2010, 94, 87-105.

[118] C. G. Granqvist, Handbook of Inorganic Electrochromic Materials; Elsevier: Amsterdam, The Netherlands, 1995.

[119] S. K. Deb, Reminiscences on the discovery of electrochromic phenomena in transition metal oxides, Solar Energy Mater Solar C, 1995, 39, 191-201.

[120] P. Andersson, R. Forchheimer, P. Tehrani, M. Berggren, Printable all-organic electrochromic active-matrix displays, Adv Funct Mater 2007, 17, 3074-3082.

[121] C. G. Granqvist, P. C. Lansaker, N. R. Mlyuka, G. A. Niklasson, E. Avendaño, Progress in chromogenics: New results for electrochromic and thermochromic materials and devices, Solar Energy Mater Solar C, 2009, 93, 2032-2039.

[122] M. Deepa, P. Singh, S. N. Sharma, S. A. Agnihotry, Effect of humidity on structure and electrochromic properties of sol‐gel-derived tungsten oxide films, Sol. Energy Mater Sol C, 2006, 90, 2665-2682.

[123] J. A. Li, Q. L. Zhao, G. Y. Zhang, J. Z. Chen, L. A. Zhong, L. Li, J. Huang, Z. Ma, Synthesis of monoclinic WO_3 nanosphere hydrogen gasochromic film via a sol‐gel approach using PS-b-PAA diblock copolymer as template, Solid State Sci, 2010, 12, 1393-1398.

[124] Y. Z. Zhang, J. G. Yuan, J. Le, L. X. Song, X. F. Hu, Structural and electrochromic properties of tungsten oxide prepared by surfactant-assisted process, Sol Energy Mater Sol C, 2009, 93, 1338-1344 .

[125] J. G. Yuan , Y. Z. Zhang , J. Le , L. X. Song , X. F. Hu , New templated method to synthesize electrochromic mesoporous tungsten oxides, Mater Lett, 2007, 61, 1114-1117 .

[126] T. Brezesinski, D. Fattakhova-Rohlfing, S. Sallard, M. Antonietti, B. M. Smarsly, Highly crystalline WO_3 thin films with ordered 3D mesoporosity and improved electrochromic performance, Small, 2006, 2, 1203-1211.

[127] M. Sadakane , K. Sasaki, H. Kunioku, B. Ohtani, W. Ueda, R. Abe, Preparation of nano-structured crystalline tungsten(VI) oxide and enhanced photocatalytic activity for decomposition of organic compounds under visible light irradiation, Chem Comm, 2008, 6552-6554.

[128] P. K. Biswas, N. C. Pramanik, M. K. Mahapatra, D. Ganguli, J. Livage, Optical and electrochromic properties of sol-gel WO_3 films on conducting glass, Mater Lett, 2003, 57, 4429-4432.

[129] M. Sharbatdaran, A. Novirooz, H. Noorkojouri, Preparation and characterization of WO_3 electrochromic films obtained by the sol-gel process, Iran J Chem Chem Eng, 2006, 25-29.

[130] W. Wang, Y. Pang, S. N. B. Hodgson, On key factors for the fabrication of mesoporous tungsten oxide films from tungstic acid, J Sol Gel Sci Technol, 2011, 58, 135-141.

[131] C. Lu, M. H. Hon, C. Kuan, I. Leu, Preparation of WO_3 nanorods by a hydrothermal method for electrochromic device, Jpn J Appl Phys, 2014, 53, 1-5.

[132] M. Shibuya, M. Miyauchi, Efficient electrochemical reaction in hexagonal forests with a hierarchical nanostructure, Chem Phys Lett, 2009, 473, 126-130.

[133] Z. Jiao, X. W. Sun, J. Wang, L. Ke, H. V. Demir, Hydrothermally grown nanostructured WO_3 films and their electrochromic characteristics, J Phys D: Appl Phys, 2010, 43, 285501-285506.

[134] C. C. Liao, F. R. Chen, J. J. Kai, Annealing effect on electrochromic properties of tungsten oxide nanowires, Sol Energy Mater Sol C, 2007, 91, 1258-1266.

[135] J. M. Wang, E. Khoo, P. S. Lee, J. Ma, Synthesis, assembly, and electrochromic properties of uniform crystalline WO_3 nanorods, J Phys Chem C, 2008, 112, 14306-14312.

[136] J. M. Wang, E. Khoo, P. S. Lee, J. Ma, Controlled synthesis of WO_3 nanorods and their electrochromic properties in H_2SO_4 electrolyte, J Phys Chem C, 2009, 113, 9655-9658.

[137] D. Ma, G. Shi, H. Wang, Q. Zhang, Y. Li, Morphology tailored synthesis of vertically aligned 1D WO_3 nanostructure films for highly enhanced electrochromic performance, J Mater Chem A, 2013, 1, 684-691.

[138] R. Doherty, Photocatalysis: water is the solution, Nature Chemistry, 2014, 6, 168-169.

[139] M. Bhaskaran, S. Sriram, K. Iniewski, Energy harvesting with functional materials and microsystems, CRC Press, Taylor & Francis, 2014.

[140] M. Balandeh, A. Mezzetti, A. Tacca, S. Leonardi, G. Marra, G. Divitini, C. Ducati, L. Meda, F. D. Fonzo, Quasi 1D hyperbranced WO_3 nanostructures for low voltage photoelectrochemical water splitting, J Mater Chem A, 2015, 3, 6110-6117.

[141] R. Vinu, G. Madras, Environmental remediation by photocatalysis- Review, J Ind Inst Sci, 2010, 90, 189-230.

[142] G. Sivalingam, K. Nagaveni, M. S. Hegde, G Madras, hotocatalytic degradation of various dyes by combustion synthesized nano anatase TiO_2, Appl Catal B: Environ, 2003, 45, 23‑38.

[143] D. F. Ollis, E. Pelizzetti, N. Serpone, Photocatalyzed destruction of water contaminants, Environ Sci Technol, 1991, 25, 1522‑1529.

[144] X. He, C. Hu, Q. Yi, X. Wang, H. Hua, X. Li, Preparation and improved photocatalytic activity of $WO_3.0.33H_2O$ nanonetworks, Catal Lett, 2012, 142, 637-645.

[145] M. A. Gondal, K. Hayat, M. Khaled, Z. H. Yamani, S. Ahmed, Photocatalytic removal of hazardous dye from water using nanostructured WO_3, Int J Nanoparticles, 2011, 4, 53-63.

[146] J. Li, J. Huang, J. Wu, L. Cao, Q. Li, K. Yanagisawa, Microwave assisted growth of $WO_3.0.33H_2O$ micro/nanostructures with enhanced visible light photocatalytic properties, Cryst Eng Comm, 2013, 15, 7904-7913.

[147] G. R. Bamwenda, H. Arakawa, The visible light induced photocatalytic activity of tungsten trioxide powders, Appl Catal A: Gen, 2001, 210, 181-191.

[148] D. B. H. Uresti, D. S. Martinez, A. M. Cruz, S. S. Guzman, L. M. T. Martinez, Characterization and photocatalytic properties of hexagonal and monoclinic WO_3 prepared via microwave assisted hydrothermal synthesis, Ceram Int, 2014, 40, 4767-4775.

[149] K. Y. Song, M. K. Park, Y. T. Kwon, H. W. Lee, W. J. Chung, W. I. Lee, Preparation of transparent particulate MoO_3/TiO_2 and WO_3/TiO_2 films and their photocatalytic properties, Chem Mater, 2001, 13, 2349-2355.

[150] Y. Li, L. Chen, Y. Guo, X. Sun, Y. Wei, Preparation and characterization of WO_3/TiO2 hollow microsphere composites with catalytic activity in dark, Chem Engg J, 2012, 181, 734-739.

[151] L. J. Zhang, S. Li, B. K. Liu, D. J. Wang, T. F. Xie, Highly efficient CdS/WO_3 photocatalysts, z-scheme photocatalytic mechanism for their enhanced photocatalytic H_2 evolution under visible light, ACS Catal, 2014, 4, 3724-3729.

[152] A. L. Linsebigler, G. Lu, J. T. Yates, Photocatalysis on TiO_2 surfaces: principles, mechanisms and selected results, Chem Rev, 1995, 95, 735-758.

[153] Y. Miseki, H. Kusama, H. Sugihara, K. Sayama, Cs-modified WO_3 photocatalyst showing efficient solar energy conversion for O_2 production and Fe(III) ion reduction under visible light, J Phys Chem Lett, 2010, 1, 1196-1200.

[154] A. Hameed, M. A. Gondal, Z. H. Yamani, Effect of transition metal doping on photocatalytic activity of WO_3 for water splitting under laser illumination: role of 3d-orbitals, Catal Comm, 2004, 5, 715-719.

[155] Y. C. Nah, I. Paramasivam, R. Hahn, N. K. Shrestha, P. Schmuki, Nitrogen doping of nanoporous WO_3 layers by NH_3 treatment for increased visible light photoresponse, Nanotech, 2012, 21 105704.

[156] A. Hameed, I. M. I. Ismail, M. Aslam, M. A. Gondal, Photocatalytic conversion of methane into methanol: performance of silver impregnated WO_3, Appl Catal A: Gen, 2014, 470, 327-335.

[157] Y. Li, W. Wu, P. Dai, L. Zhang, Z. Sun, G. Li, M. Wu, X. Chen, C. Chen, WO_3 and Ag nanoparticle co-sensitized TiO_2 nanowires: preparation and the enhancement of photocatalytic activity, RSC Adv, 2014, 4, 23831-23837.

[158] T. Samerjai, C. Liewhiran, A. Wisitsoraat, A. Tuantranont, C. Khanta, S. Phanichphant, Highly selective hydrogen sensing of Pt-loaded WO_3 synthesized by hydrothermal/impregnation methods, Int J Hyd Energy, 2014, 39, 6120-6128.

[159] S. Suhaimi, M. M. Shahimin, Z. A. Alahmed, J. Chysky, A. H. Reshak, Materials for enhanced dye sensitized solar cell performance: electrochemical application, Int J Electrochem Sci, 2015, 10, 2859-2871.

[160] S. C. T. Lau, J. Dayou, C. S. Sipaut, R. F. Mansa, Development of photoanode materials for highly efficient dye sensitized solar cells, Int J Renew Energy Res, 2014, 4, 665-674.

[161] J. Luo, M. Xu, R. Li, K. Huang, C. Jiang, Q. Qi, W. Zeng, Jie. Zhang, C. Chi, P. Wang, J. Wu, N-annulated perylene as an efficient electron donor for porphyrin based dyes: enhanced light harvesting ability and high efficiency Co(II/III) based dye sensitized solar cells, J Am Chem Soc, 2014, 136, 265-272.

[162] X. Liu, Y. Yan, Z. Da, W. Shi, C. Ma, P. Lv, Y. Tang, G. Yao, Y. Wu, P. Huo, Y. Yan, Significantly enhanced photocatalytic performance of CdS coupled WO_3 nanosheets and the mechanism study, Chem Engg J, 2014, 241, 243-250.

[163] S. J. Theerthagiri, R. A. Senthil, A. Malathi, A. Selvi, J. Madhavan, M. Ashokkumar, Synthesis and characterization of a CuS-WO_3 composite photocatalyst for enhanced visible light photocatalytic activity, RSC Adv, 2015, 5, 52718-52725.

[164] H. Widiyandari, A. Purwanto, R. Balgis, T. Ogi, K. Okuyama, CuO/WO_3 and Pt/WO_3 nanocatalyst for efficient pollutant degradation using visible light irradiation, Chem Engg J, 2012, 180, 323-329.

[165] J. Cao, B. Luo, H. Lin, S. Chen, Photocatalytic activity of novel AgBr/WO_3 composite photocatalyst under visible light irradiation for methyl orange degradation, J Hazard Mater, 2011, 190, 700-706.

[166] S. A. Singh, G. Madras, Photocatalytic degradation with combustion synthesized WO_3 and WO_3-TiO_2 mixed oxides under UV and visible light, Separ Pur Technol, 2013, 105, 79-89.

[167] B. Tryba, M. MIszcz, A. W. Morawski, Photocatalytic activity of TiO_2-WO_3 composites, Int J Photoenergy, 2009, 1-7.

[168] A. Fujishima, K. Honda, Electrochemical photolysis of water at a semiconductor electrode, Nature, 1972, 238, 37-38.

[169] H. Cao, J. Y. Xu, D. Z. Zhang, S. H. Chang, S. T. Ho, E. W. Seeling, X. Liu, R.P.H. Chang, Spatial confinement of laser light and photonic atoms, Phys. Rev. Lett., 2000, 84, 5584-5587.

[170] E. Ohshima, H. Ogino, I. Niikura, K. Maeda, M. Sato, M. Ito, T. Fukuda, Growth of the 2-in-size bulk ZnO single crystals by the hydrothermal method, J. Cryst. Growth, 2004, 260, 166-170.

[171] S. Park, D. W. Lee, J. C. Lee, J. H. Lee, Photocatalytic silver recovery using ZnO nanopowders synthesized by modified glycine-nitrate process, J. Am. Ceram. Soc., 2003, 86, 1508-1512.

[172] J. H. Jun, H. Seong, K. Cho, B. Moon, S. Kim, Ultraviolet photodetectors based on ZnO nanoparticles, Ceram Int, 2009, 35, 2797-2801.

[173] Y. Liao, H. Li, Y. Liu, Z. Zou, D. Zeng, C. Xie, Characterization of photoelectric properties and composition effect of TiO_2/ZnO/Fe_2O_3 composite by combinatorial methodology, J Comb Chem, 2010, 12, 883-889.

[174] X. Fang, Y. Bando, U. K. Gautum, T. Zhai, H. Zeng, X. J. Xu, ZnO and ZnS nanostructures: ultraviolet light emitters, lasers and sensors, Critical Rev Solid State Mater Sci, 2009, 34, 190-223.

[175] R. Ullah, J. Dutta, Photocatalytic degradation of organic dyes with manganese-doped ZnO nanoparticles, J. Hazard. Mater., 2008, 156, 194-200.

[176] M. A. Mahmood, S. Baruah, J. Dutta, Enhanced visible light photocatalysis by manganese doping or rapid crystallization with ZnO nanoparticles, Mater. Chem. Phys., 2011, 130, 531-535.

[177] Y. Li, G. W. Meng, L. D. Zhang, F. Phillip, Ordered semiconductor ZnO nanowires arrays and their photoluminescence properties, Appl. Phys. Lett., 2000, 76, 2011-2013.

[178] R. Slama, F. Ghribi, A. Houas, C. Barthou, L. E. Mir, Visible photocatalytic properties of vanadium doped zinc oxide aerogel nanopowder, Thin Solid Films, 2011, 519, 5792-5795.

[179] C. Yu, K. Yang, Y. Xie, Q. Fan, J. C. Yu, Q. Shu, C. Wang, Novel hollow Pt-ZnO nanocomposite microspheres with hierarchical structure and enhanced photocatalytic activity and stability, Nanoscale, 2013, 5, 2142-2151.

[180] R. Nagaraja, N. Kottam, C. R. Girija, B. M. Nagabhushana, Photocatalytic degradation of Rhodamine B dye under UV/solar light using ZnO nanopowder synthesized by solution combustion route, Powder Technol , 2012, 215, 91-97.

[181] A. J. Reddy, M. K. Kokila, H. Nagabhushana, J. L. Rao, C. Shivakumara, B. M. Nagabhushana, R. P. S. Chakradhar, Combustion synthesis, characterization and raman studies of ZnO nanopowders, Spectrochim Acta A, 201, 1, 53–58.

[182] K. Manjunath, T. N. Ravishankar, D. Kumar, K. P. Priyanka, T. Varghese, H. R. Naika, H. Nagabhushana, S. C. Sharma, J. Dupont, T. Ramakrishnappa, G. Nagaraju, Facile combustion synthesis of ZnO nanoparticles using cajanus cajan (L) and its multidisciplinary applications, Mater Res Bull, 2014, 57, 325-334.

[183] C. C. Hwang, T. Y. Wu, Synthesis and characterization of nanocrystalline ZnO powders by a novel combustion synthesis method, Mater Sci & Eng B, 2004, 111, 197-206.

[184] R. Ianos, I. Lazau, C. Pacurariu, P. Sfirloaga, Aqueous combustion synthesis and characterization of ZnO powders, Mater Chem Phys, 2011, 129, 881-886.

[185] C. S. Lin, C. C. Hwang, W. H. Lee, W. Y. Tong, Preparation of zinc oxide (ZnO) powders with different types of morphology by a combustion synthesis method, Mater Sci & Eng B, 2007, 140, 31-37.

[186] P. R. Potti, V. C. Srivastava, Comparative studies on structural , optical, and textural properties of combustion derived ZnO prepared using various fuels and their photocatalytic activity, Ind Eng Chem Res, 2012, 51, 7948-7956.

[187] A. Mclaren, T. V. Solis, G. Li, S. C. Tsang, Shape and size effects of ZnO nanocrystals on photocatalytic activity, J. Am. Chem. Soc., 2009, 131, 12540-12541.

[188] S. Lam, J. Sin, A. Z. Abdullah, A. R. Mohamed, ZnO nanorods surface decorated by WO_3 nanoparticles for photocatalytic degradation of endocrine disruptors under a compact fluorescent lamp, Ceramics International, 2013, 39, 2343-2352.

[189] C. Yu, K. Yang, Q. Shu, J. C. Yu, F. Cao, X. Li, Preparation of WO_3/ZnO composite photocatalyst and its photocatalytic performance, Chinese J. of Catalysis, 2011, 32, 555-565.

[190] J. Xei, Z. Zhou, Y. Lian, Y. Hao, X. Liu, M. Li, Y. Wei, Simple preparation of WO_3-ZnO composites with UV-Vis photocatalytic activity and energy storage ability, Ceramics International, 2014, 40, 12519-12524.

[191] C. Siriwong, N. Wetchakun, C. Liewhiran, S. Phanichphant, Characterization of WO_3/ZnO nanocomposite synthesized by flame spray pyrolysis, Spray Pyrolysis, 2009, 1151, 13-16.

[192] S. Lam, J. Sin, A. Z. Abdullah, A. R. Mohamed, Transition metal oxide loaded ZnO nanorods: preparation, characterization and their UV-Vis photocatalytic studies, Separation Pur Technol, 2014, 132, 378-387.

Chapter 3

MATERIALS & METHODS

The purpose of this chapter is to describe detail experimental procedure in relation to the thesis work. At the initial stage, different WO_3 nanostructures were prepared following co-precipitation and hydrothermal method. Furthermore, different physicochemical characterization methods are utilized that includes X-ray diffraction (XRD), field emission scanning electron microscopy (FESEM), transmission electron microscopy (TEM), FT-IR Spectroscopy, Raman spectroscopy and BET surface area analysis, etc. Following that the electrochemical properties of the drop-coated and dip-coated nanoparticles are measured with respect to electrochromism phenomenon. Finally, photocatalytic experiments are carried in respect of morphology and crystal structure of WO_3 in the form of synthesized WO_3-ZnO composites to degrade different grade of dyes. In this perspective, ZnO nanocrystals has been synthesized through a solution combustion method and used in preparation of nanocomposite.

All the reagents used were of analytical grade and no further purification was done before using it for the synthesis processes.

3.1. Co-precipitation Method

A simple wet chemical process namely co-precipitation was employed for the synthesis of spherical and rod-shaped WO_3 nanoparticles.

3.1.1. Synthesis of Spherical WO_3 Nanoparticles

Synthesis of spherical WO_3 nanoparticles (designated as SW) was carried out through acid catalyzed reaction between solid tungstic acid and hydrogen peroxide solution. The analytical grade H_2WO_4 powder was taken in a dry glass vessel attached with a Pt-temperature sensor and heated to 90 ± 5^oC. This was followed by simultaneous addition of hydrogen peroxide solution (30%, w/w) and concentrated nitric acid to conduct an acid catalyzed reaction. The pH of the solution was ~1. This exothermic reaction led to the formation of a pale greenish yellow precipitate, which was later found to be amorphous spherical WO_3 and accordingly designated as ASW. The precipitate was washed twice in a centrifuge at 14,000 rpm followed by freeze-drying at-52^oC with a vacuum of 20 torr. The dried powder was flash heated at 500^oC for 5 minutes. By flash heating, we mean direct insertion of the sample inside a preheated furnace followed by isothermal heating for a requisite length of time. Subsequently, the sample was taken out for normal cooling under the ambient condition. The crystallization temperature was confirmed by thermal analysis prior to flash heating of as-synthesized nanoparticles. A schematic of the process methodology has been shown in Figure 3.1.

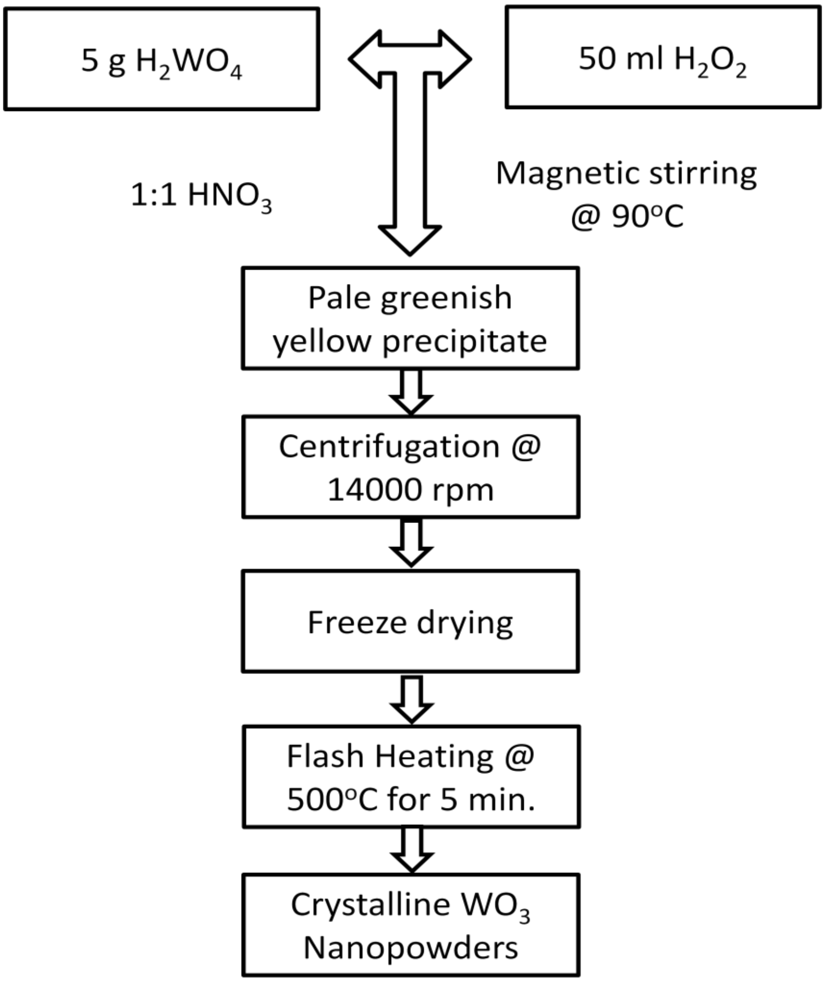

Figure 3.1. Flow diagram for preparation of spherical WO_3 nanoparticles.

3.1.2. Synthesis of Rod-shaped WO_3 Nanoparticles

Rod-shaped WO_3 nanoparticles (designated as RW) were prepared by a similar acid precipitation method from a different base precursor $Na_2WO_4.2H_2O$ with addition of a structure directing agent CTAB (cetyl-trimethyl-ammonium-bromide, $C_{19}H_{42}BrN$) at pH of ~3. There was a clear solution formed after mixing the two reagents. Acidification of the reaction led to the formation of a white precipitate that was later confirmed as amorphous nanoparticles designated as ARW. The precipitate was finally flash heated at 500°C for 5 minutes. Starting precursors and solution pH were the prime parameters to control the morphology of the prepared powders. A schematic of the process methodology for synthesis has been shown in Figure 3.2.

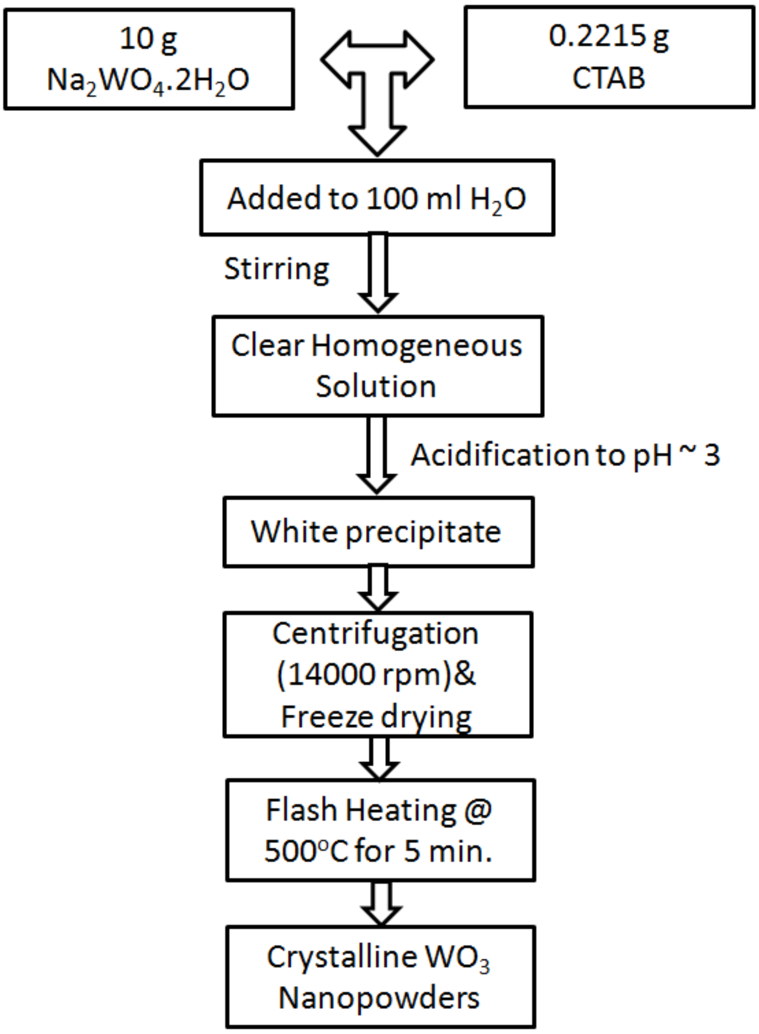

Figure 3.2. Flow diagram for preparation of rod-shaped WO_3 nanoparticles.

3.2. Hydrothermal Method

One step hydrothermal process was conducted for the synthesis of WO_3 nanocuboids and nanofibers using different structure directing reagents and their process optimization was also carried. An image of the hydrothermal set up is shown in Figure 3.3.

Figure 3.3. A typical hydrothermal setup or high pressure metal bomb.

3.2.1. Synthesis of WO_3 Nanocuboids

Sodium tungstate ($Na_2WO_4.2H_2O$) was used as base precursor along with fluoroboric acid as a structure-directing agent to synthesize WO_3 nanocuboids. Prior to hydrothermal treatment, fluoroboric acid (HBF_4, 50% w/w) solution was added to a sodium tungstate aqueous solution and was constantly stirred on a magnetic stirrer at 300 rpm for 30 minutes to transform into a yellowish green precipitate. The solution together with the precipitate was then transferred to a 50 ml teflon beaker, placed inside an autoclave (high-pressure metal bomb) that was sealed tightly and kept at certain temperature for a predetermined time in a hot air oven. After autoclaving, the precipitate together with the solvent was centrifuged at 14000 rpm to remove the excess HBF_4. Hot water followed by isopropanol was used for washing the precipitate. The residue after centrifuging was freeze-dried at a temperature of -52°C and a vacuum of 20 torr. Solute concentration and effective volume of the reaction chamber were also important considerations for the aforementioned process. The experiments were performed by varying the concentration of HBF_4, time duration and reaction temperature to optimize the crystal structure and morphology. A series of experiments were conducted at various solute concentrations with constant temperature of 180°C and at a constant time of 4 hours. Similarly, additional experiments were performed to determine the effect of hydrothermal duration and temperature. A typical hydrothermal process for synthesis of WO_3 nanocuboid is shown in Figure 3.4.

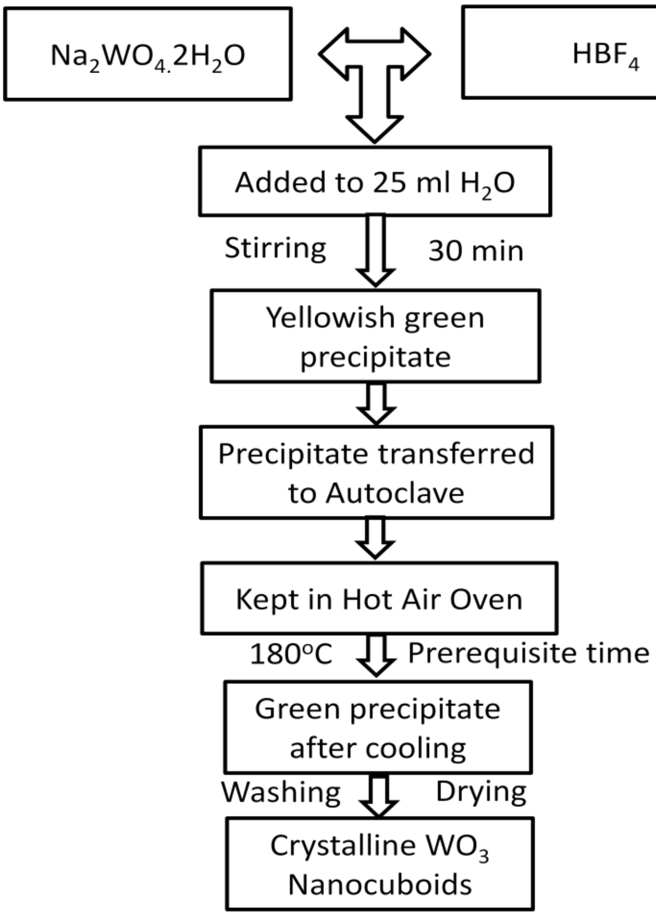

Figure 3.4. Flow diagram for synthesis of WO_3 nanocuboids.

3.2.2. Synthesis of WO_3 Nanofibers

In the present methodology, base precursor sodium tungstate ($Na_2WO_4.2H_2O$), structure directing agent sodium chloride (NaCl) and catalyst HCl were used to synthesize WO_3 nanofibers. Before the hydrothermal treatment, anhydrous sodium chloride was added to sodium tungstate aqueous solution and constantly stirred on a magnetic stirrer at 300 rpm for 30 minutes so as to prepare a clear transparent solution. Concentrated hydrochloric acid solution (1:1) was added dropwise to achieve solution pH ~ 2. The solution was then transferred to a 50 ml Teflon beaker, placed inside an autoclave (high pressure metal bomb), which was sealed tightly and kept at a set temperature for a predetermined time in a hot air oven. Excess NaCl and impurities content in the precipitated solvent were removed by centrifuging at 14000 rpm, and subsequently washed by hot water and isopropanol, respectively. The collected residue was freeze-dried at temperature of −52°C and a vacuum of 20 torr. The similar experiments were carried out by varying the NaCl molar concentration, hydrothermal duration and reaction temperature to optimize the morphology and crystal structure. Moreover, several experiments were conducted to understand the effect of NaCl concentration at constant temperature 180°C for 12 hours duration. Additional experiments with selective parameters were also conducted to understand the effect of hydrothermal temperature and time similar to synthesis to WO_3 nanocuboids. A typical flow diagram for synthesis of WO_3 nanofiber is shown in Figure 3.5.

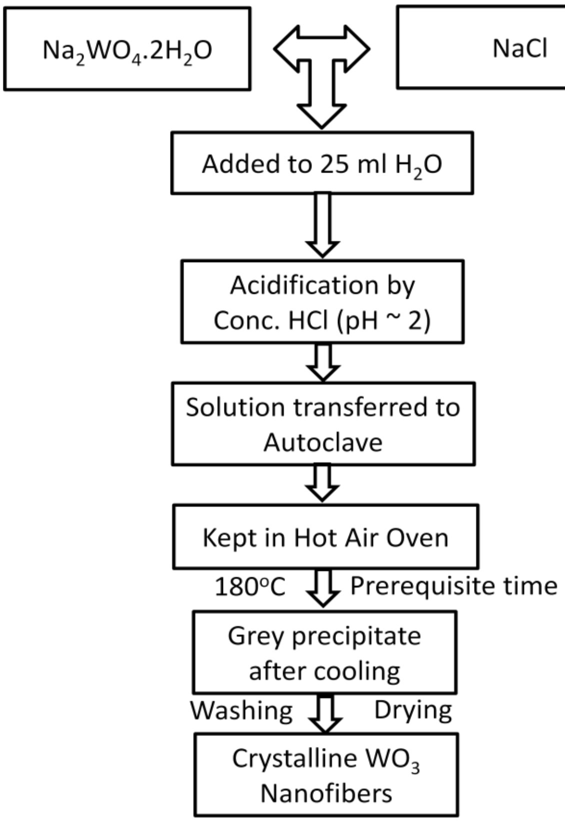

Figure 3.5. Flow diagram for synthesis of WO_3 nanofibers.

3.3. Combustion Method

One step combustion process was conducted for synthesis of ZnO quasi-fiber using oxalic acid as fuel. The process optimization for quasi fiber ZnO was also carried out. An image of the combustion process has been shown in Figure 3.6.

Figure 3.6. A typical combustion reaction taking place in a muffle furnace.

3.3.1. Synthesis of ZnO Quasi-fibers

Zinc oxide (ZnO) quasi-fiber was formed by the solution combustion synthesis method. According to this method, stoichiometric composition of oxalic acid as fuel and zinc nitrate hexahydrate as oxidizer was dissolved in minimal amount of water in a beaker to form a solution. The prepared solution was kept in a preheated muffle furnace at 450 ± 10^{o}C until complete combustion. Higher temperature was required for complete decomposition of the intermediates formed during the combustion reaction. After complete combustion, a white colored porous material was formed. The stoichiometric composition of both fuel and oxidizer was calculated based on the concepts of propellant chemistry of solution combustion synthesis by taking oxidizing and reducing valences, respectively. The experiments were carried out by varying the oxidizer by fuel ratio, time and combustion temperature to optimize the crystal structure and morphology. A series of experiments were conducted at various ratios at 450^{o}C with 30 minutes duration. Similarly, additional experiments were carried out to determine the effect of time and temperature on crystallinity, crystal structure, and morphology characterized through different physicochemical techniques. A flow diagram is shown in Figure 3.7 for synthesis of ZnO quasi-fibers.

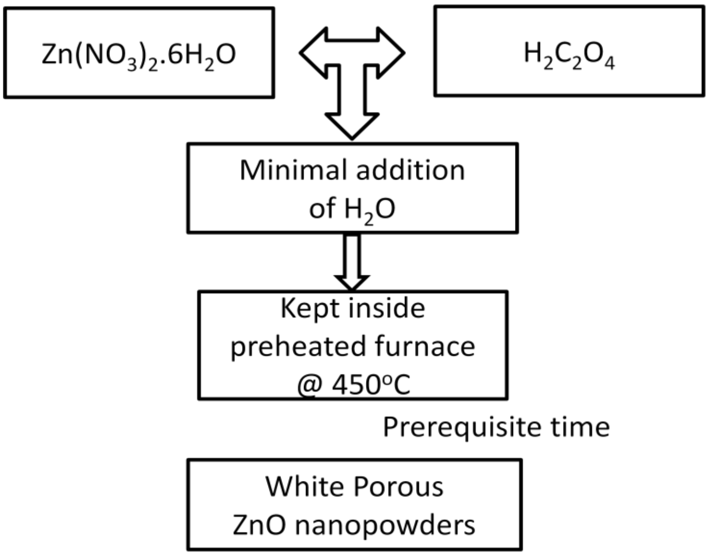

Figure 3.7. Flow diagram for synthesis of ZnO Quasi-fibers.

3.4. Fabrication of WO_3/ITO electrodes

Fabrication of electrode is an important part for electrochemical assessment. Herein, a homogeneous dispersion of WO_3 nanopowders in ethanol was prepared and coated onto a transparent conducting oxide (TCO) substrate and 2cm^2 area (dimensions: 2cm x 1cm) evaluated the electrochromic effect of WO_3/ITO electrode. Prior to coat the electrode, the homogeneous suspension was prepared from an optimum solid content of 0.5gm of WO_3 in 3 ml ethanol through ultrasonication for 30 min. Commercial grade 84% optically transparent conducting Sn-doped indium oxide (ITO) glass substrate was used as the TCO substrate to fabricate the working electrode. The conductive ITO glass substrate was cleaned by ultrasonication through successive immersion in distilled water, acetone and ethanol prior to WO_3 coating.

The WO_3 nanopowders obtained from two step co-precipitation method was drop coated onto TCO substrate. The WO_3 suspension was dropped on ITO substrate followed by drying at 60^{o}C for 20 minutes and was repeated twice. However, same suspension was dip-coated onto the substrate and a comparative study was carried between WO_3 spherical and rod-shaped particles fabricated electrodes.

Since, dip-coated samples showed better electrochromic performance, thus, the suspensions of hydrothermally synthesized WO_3 nanopowders were dip coated onto ITO substrate and considered as working electrode for electrochemical measurements. Similar suspension preparation was followed and WO_3 dip-coating was carried for a prerequisite time and speed. Additionally, in case of WO_3 nanofibers, the coating thickness was further enhanced through sequential four times of dip-coating and designated as S–1 (original), S–2, S–3, S–4, S–5, respectively to evaluate electrochemical effect in respect of coating thickness. The dip coated samples were dried at 80^{o}C for 30 minutes.

3.5. Preparation of WO_3-ZnO Nanocomposites

Different weight ratios of WO_3 was added to ZnO to prepare a physical mixture of WO_3-ZnO mixed oxide nanocomposites by taking down known amounts of both the powders. Uniform mixing of the composite was carried by fine grinding followed by ultrasonication and heat treatment at 450^{o}C for 2 hours to prepare a photoactive catalyst. High frequency ultrasonication lead to formation of colloidal particles with homogeneous distribution of particles and heat treatment was given for better interaction between WO_3 and ZnO particles. These photocatalysts were successfully used for photocatalytic experiments without any further modification. A flowchart for preparation of WO_3-ZnO nanocomposites for photocatalysis of dye is shown in Figure 3.8.

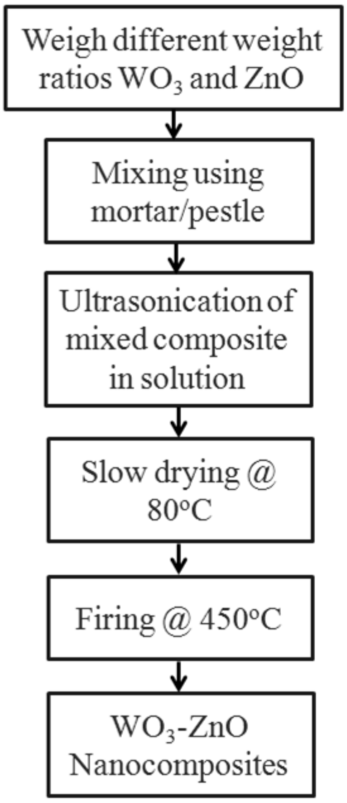

Figure 3.8. Flowchart for preparation of WO_3-ZnO nanocomposites for photocatalysis of dye.

3.6. Physicochemical Characterizations

The characteristic property of the synthesized nanopowders and mixed oxide nanocomposites was determined following the different analytical techniques. A brief working principle and their utilization for the aforesaid materials are given systematically.

3.6.1. Phase Analysis by X-ray diffraction

X-ray diffractions are produced based on the constructive interference between monochromatic x-ray radiations and a crystalline sample. X-ray diffraction works on the principle of Bragg's Law. Mathematically, let us assume an X-ray beam incident on a pair of parallel planes P1 and P2 that is separated by an interplanar spacing'd'. The incident rays 1 and 2 makes an angle of theta with these planes. As a result, maximum intense reflection of beam is observed if the waves observed remain in phase and also the path length of each of these waves equals the integral multiple 'n' of the wavelength 'λ'.

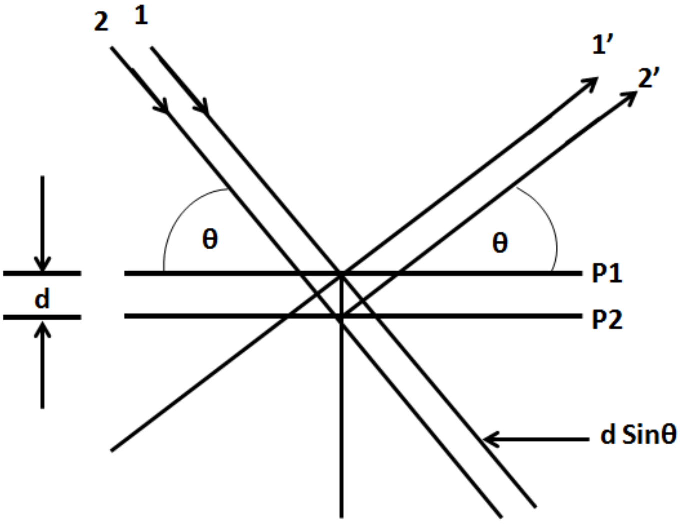

Figure 3.9. Schematic representation of constructive interference in Bragg's Law.

The intensity of interference is due to the cumulative effect of reflections onto crystallographic planes of the crystal lattice denoted as Miller indices (h, k, l). A schematic representation of Bragg's Law has been shown in Figure 3.9 that describes the condition on θ to be strongest for constructive interference. The mathematical expression of this is given as follows: $2d \sin \theta = n \lambda$. Basically, this law relates to the wavelength of the X-ray radiation and the interplanar spacing in a crystalline sample. The samples are scanned through a range of 2θ angles to attain all possible directions of diffraction due to random orientation. These diffraction peaks are converted for mineral identification through unique d-spacing. Phase, crystallinity and crystal structure of WO_3, ZnO nanopowders and WO_3-ZnO mixed oxide nanocomposites were analysed using room temperature powder X-ray diffraction (Rigaku (Japan) Ultima-IV X-Ray Diffractometer) with an attachment of Ni-filter 0.154 nm and Cu K-α radiation as source. The diffractometer was operated at 35 kV and 30A. All powder samples were scanned in a continuous mode over a 2θ range from 10 to 80^o with a scanning rate of 0.05^o/sec. The reference powder diffraction data from JCPDS (Joint Committee on Powder Diffraction Standards) was compared and matched for relevant peak position, phase purity, peaks of different atomic planes and the relative intensities of the powder pattern.

3.6.2. Rietveld Refinement

Rietveld refinement was carried for WO_3 nanostructured particles to evaluate their probable crystal pattern, crystal structure, lattice parameter, cell volume as for reference. The pattern obtained after powder X-ray diffraction was considered for Rietveld Refinement using FullProf.2k program. Analysis of WO_3 nanoparticles was carried from room temperature X-ray diffraction with Ni-filtered Cu-Kα radiation source, and data were collected in continuous mode having 2θ range from 10 to 80^o with a scanning rate of 0.05^o/sec. Rietveld structure refinement method was corresponded to the general guideline as adopted by the International Union of Crystallography Commission on Powder Diffraction. At the first step, scale factors, zero shift, line profile parameters, lattice parameters, preferential orientations and asymmetry parameters were refined. Atomic displacement factors, as well as atomic coordinates from the WO_3 structure were refined in the second step. Occupancies of cations and anions were also systematically checked in the last run.

3.6.3. Thermal Analysis

It is a characteristic material property that represents the stability of the material as a function of temperature. The crucial parameters for this experiment includes the atmosphere, gas flow rate, sample vapour pressure, heating rate, thermal contact to the sample crucible and sensor, etc. As an effect of temperature, the sample undergoes physical transformation such as phase transitions that requires more/less heat flow in comparison to reference to maintain same temperature in both working and reference. The flow of heat depends on the exothermic or endothermic nature during the process. When the sample undergoes absorption of heat followed by phase transitions, it is endothermic process. On the other hand, heat required is less during exothermic processes to raise the sample temperature. The heat flow difference between the reference and the sample measures the amount of heat released and absorbed. Thermogravimetry (TG) and differential scanning calorimetric (DSC) analyses of the WO_3 nanopowders were carried out upto 600^oC in a Netzsch (Germany) model STA449C/4/MFC/G thermal analyzer with a heating rate of 10^oC/min.

3.6.4. Field Emission-Scanning Electron Microscopy (FE-SEM)

This analytical technique is used to investigate the surface structures using electrons instead of light. The electrons are liberated from a field emission source and accelerated in a high electrical field gradient called primary electrons. These electrons are allowed to focus and deflected by electronic lenses to produce a beam for bombardment with the object that emits secondary electrons as shown in Figure 3.10. The nature of the secondary electrons is related to the surface of the object. These secondary electrons are caught to produce electronic signal that is amplified to a scan image and saved. The EDAX (Energy dispersive X-ray analysis) along with elemental mapping system provides the qualitative and quantitative analysis of elements in a sample where the matter interacts with the electromagnetic radiation. As each of the elements has unique atomic structure, thus, X-rays distinguish each element in a distinctive manner. FESEM images for all WO_3 and ZnO nanoparticles were carried out using NOVA NANOSEM FEI 450 system. The powder was mounted on a double-sided carbon tape attached to an

SEM stub and sputter coated with gold for 2min.The EDAX elemental mapping has been done for WO_3-ZnO mixed oxide nanocomposites.

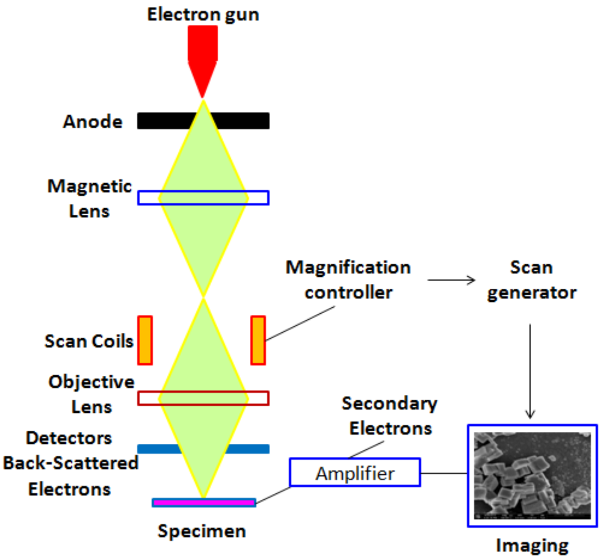

Figure 3.10. Working principle of Field Emission-Scanning Electron Microscopy.

3.6.5. Transmission Electron Microscopy (TEM)

Transmission electron microscopy (TEM) is an analytical technique that helps in studying the high resolution morphology, lattice fringe and crystallinity of materials. In this, a beam of electrons is allowed to transmit through the ultra-thin specimen where the specimen interacts with the electrons. An image is developed from interaction of electrons transmitted through the specimen. It works like a slide projector, where a beam of electrons shine from a projector that gets transmitted through the slide. The patterns on the slide allow certain parts of the light beam to pass through. As a result, the replicated pattern from the slide forms an enlarged image upon falling on the phosphor screen as shown in Figure 3.11. The particle size, morphology, particle growth direction and lattice parameters like d-spacing of the as synthesized nanopowder and nanocomposite were studied by TEM, HR-TEM and SAED pattern, respectively. The TEM sample preparation was carried out by dispersing a small amount of powder in acetone using 20 kHz and 500W ultrasonic energy for 30 min. A carbon coated copper grid was used as substrate. A well dispersed suspension was dropped onto the substrate and dried for evaporation of the solvent. The powder morphology was observed under bright field mode transmission electron microscope (JEOL JEM-2100, TEM).

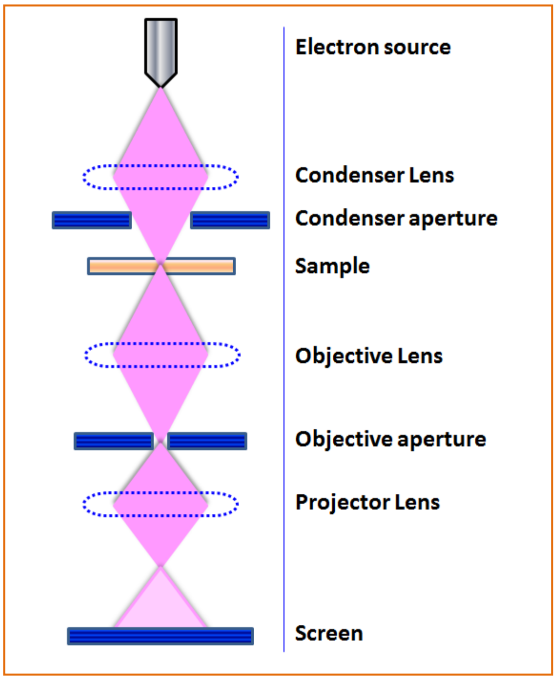

Figure 3.11. Working principle of Transmission Electron Microscopy.

3.6.6. FT-IR Spectroscopy

FTIR spectroscopy was used to understand the formation of major functional group of intermediate and resultant compounds formed during different state of reactions. The FT-IR spectrum is from molecular vibrational when sample molecules selectively absorb specific wavelength radiation and changes their dipole moment. Consequently, there is vibrational energy gap due to transfer from ground state to excited state. The absorption peak intensity relates to the dipole moment change and possible energy level transition. The production of beam occurs via interferometer. Michelson interferometer is the core of IR spectrophotometer that splits a single beam into two such that paths of both the beams are different. However, these beams further recombine but path length difference creates constructive and destructive interferences forming an interferogram. Interferogram is basically a function of time. Moreover, the output values as a function of time is said to make a time domain. This time domain is transformed mathematically using Fourier transformation that undergoes deconvulation to produce a spectrum. Figure 3.12 shows the transformation of an interferogram of the polychromatic light to its respective spectrum.

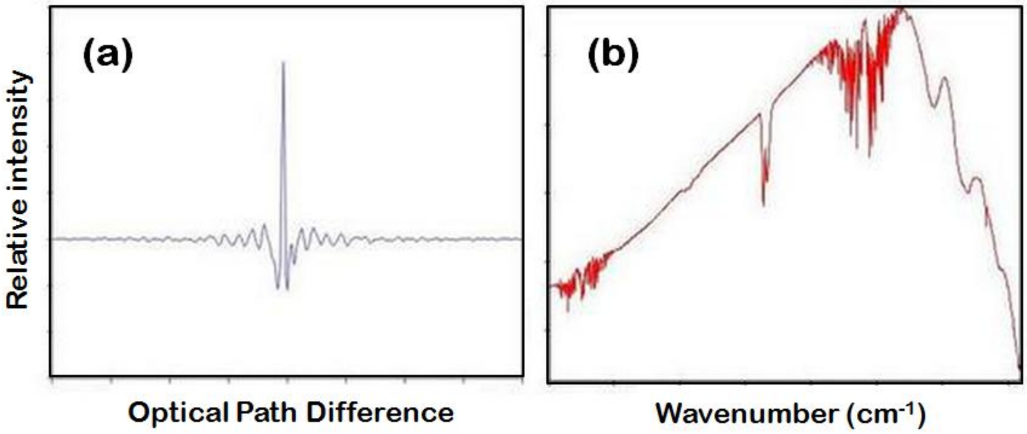

Figure 3.12. (a) Interferogram from a monochromatic light and (b) FT-IR Spectrum.

Fourier Transform Infra-Red (FT-IR) spectrums were formed using Perkin Elmer RXI, Spectrum, USA. From infrared spectrum, we can obtain information about the structure of the specimen. In general, mid-infrared region is selected in the wavenumber range of 4000 – 400 cm^{-1} for measuring the transmittance of the sample with KBr as reference. The specimen discs of WO_3 and ZnO nanopowders were prepared by pressing the mixture of 5 mg of nanoparticles with 100 mg of KBr at pressure of 3 ton.

3.6.7. Raman Spectroscopy

Raman spectroscopic technique uses vibrational, rotational and other frequency modes in a system. It uses a laser in the visible, near infrared and near ultraviolet region. A distinction in crystal structure could also be done due to the vibrations that occur due to change in polarizability of the molecules from laser beam. The molecular vibrations are made to interact with the laser beam causing inelastic scattering to change the resultant energy of the laser photons shifting up or down. The scattering from a molecule has certain components such as Rayleigh scattering, Stokes and Anti-stokes scattering.

Rayleigh scattering deals with the scattering without any change in the frequency. However, change in the light frequency accounts for the raman scattering. The photons of the light energy shifts Raman scatter. This energy shift provides the information about the different vibrational modes in the system. The possible frequency shifts are Stokes-raman scattering where the scattered light has frequency lower than the incident light and Anti-stokes raman scattering where frequency is higher than the incident light as shown in Figure 3.13. As number of molecules present in the higher vibrational level will be less thus, Stokes scattering is stronger among two processes due to high population in the ground vibrational state.

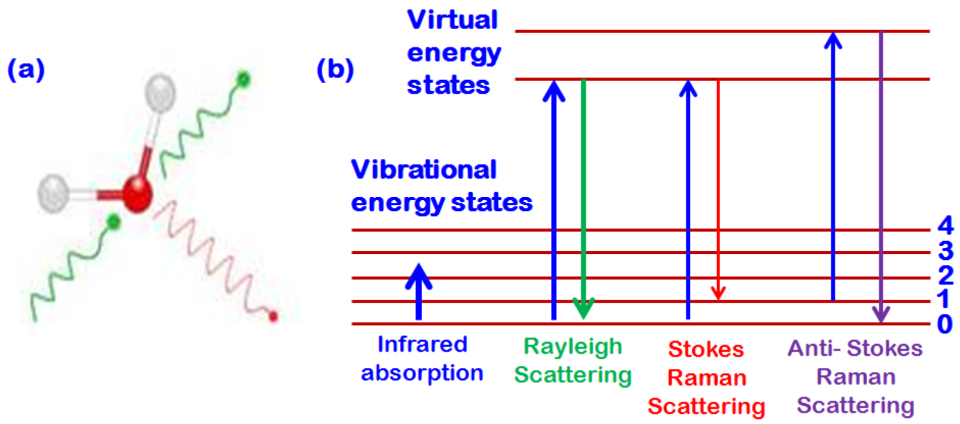

Figure 3.13. (a) Light scattered from a molecule and (b) Energy level diagram of Raman Scattering.

The Raman measurements were carried out in backscattering geometry with a triple grating spectrometer equipped with a cooled charge coupled device detector (Horiba Jobin, LabRAM HR). For excitation, the 488 nm line of Ar^+/Kr^+ mixed gas laser was used.

3.6.8. UV-Vis Diffuse Reflectance Spectroscopy (UV-DRS)

It uses the light from UV, visible and other near infrared region to detect the transitions taking place due to excitation from ground state to excited state. The basic principle is that the easy electron excitation causes longer wavelength absorbance due to lower energy gap between the highest occupied molecular orbital (HOMO) and lowest occupied molecular orbital (LUMO) of the material. This suggests that the sample may absorb light energy in order to move electrons from valence band having filled energy level to an empty conduction band causing relative decrease in the amount of light energy with respect to a reference source. In this experiment, the light is allowed to scatter in all directions from the sample followed by collection of scattered light by an optical detector. Surface reflectance is measured by scanning the sample over a range of wavelengths. In other way, the relative change in the amount of light reflected from surface is being measured as shown in Figure 3.14. Diffuse reflectance measurements were carried out in a Shimadzu Spectrophotometer (UV-2450) to evaluate band gap energy for WO_3, ZnO nanopowders and WO_3-ZnO nanocomposites. Room temperature diffuse reflection percentage was measured in the wavelength region 200-800nm. Barium sulphate was used as the reference for this measurement.

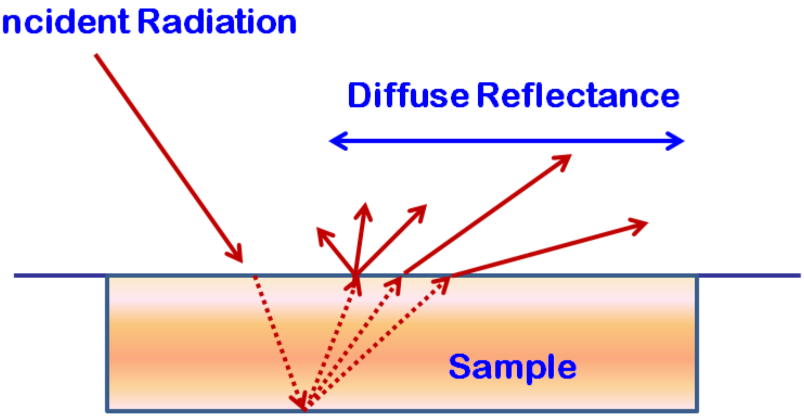

Figure 3.14. Diffuse Reflectance of a sample upon incident radiation.

3.6.9. BET (Brunauer, Emmett and Teller) Surface area studies

The phenomena of BET theory were to explain the physical adsorption of gas molecules on the solid surface for measurement of the specific surface area of the material. The theory was a joint invention by Stephen ***B***runauer, Paul ***E***mmett and Edward ***T***eller in 1938, who perused the surface phenomena of a powder or porous body with the help of gas adsorption method. This theory is an extension of Langmuir theory which explains monolayer or multilayer adsorption following certain hypotheses. Low pressure adsorption isotherm provides a mean to take the mass of adsorption corresponding to a single gas molecule layer and calculated the surface area from it. BET surface area is then calculated from adsorption behaviour under a range of partial pressures. The BET equation is represented as:

$$\frac{P}{X(P_o - P)} = \frac{1}{X_m C}\left[1 + \frac{P}{P_o}\,(C-1)\right] \qquad (13)$$

Where,

P = Measured partial pressure of adsorbate,

P_o = Saturation or equilibrium pressure of adsorbate (depends on the gas and temperature),

X = Mass of the gas adsorbed at pressure P,

X_m = Adsorption capacity of the powder (the mass of gas necessary to form a saturated surface coating one atomic layer thick), and

C = Constant relating to the adsorption enthalpy.

BET equation is a linear equation and valid for measuring the surface area of a powder when the pressure range P/P_o varies from 0.05 to about 0.35. The SBET equation can be represented in a general form as:

$$S_{BET} = \frac{X_m N_O A_O}{WM} \qquad (14)$$

Where,

M = Molecular weight of the adsorbate,

A_o = Average occupational area of an adsorbate molecule (nitrogen is the most popular adsorbate gas and it has an average occupational area of 16×10^{-20} m^2),

N_o = Avogadro’s number, and

W = Mass of the sample.

BET specific surface area is explained with consideration of equivalent spherical diameter of monosized spheres. The BET equivalent for spherical diameter particle is calculated from surface area as follows.

$$S_{BET} = \frac{X_m N_O A_O}{WM} \qquad (15)$$

$$D_{BET} = \frac{6}{S_{BET}\rho_t} \qquad (16)$$

Where,

S_{BET} = Specific surface area of the powder measured in m^2/g,

ρ_t = Theoretical density of the powder, and

D_{BET} = Particle size measured in micrometer.

The BET surface area is calculated from the slope of the linear plot as shown in Figure 3.15. The BET specific surface area of synthesized WO_3 nanopowders and WO_3-ZnO nanocomposites were taken using nitrogen as adsorbate in BET instrument (Quantachrome Autosorb, USA). The sample powders were degassed at 100^oC and measurement was performed at five different points for specific surface area. At approximate, 40 mg of powder was taken to remove contaminant water vapour and adsorbed gases from the samples at 100^oC in nitrogen atmosphere.

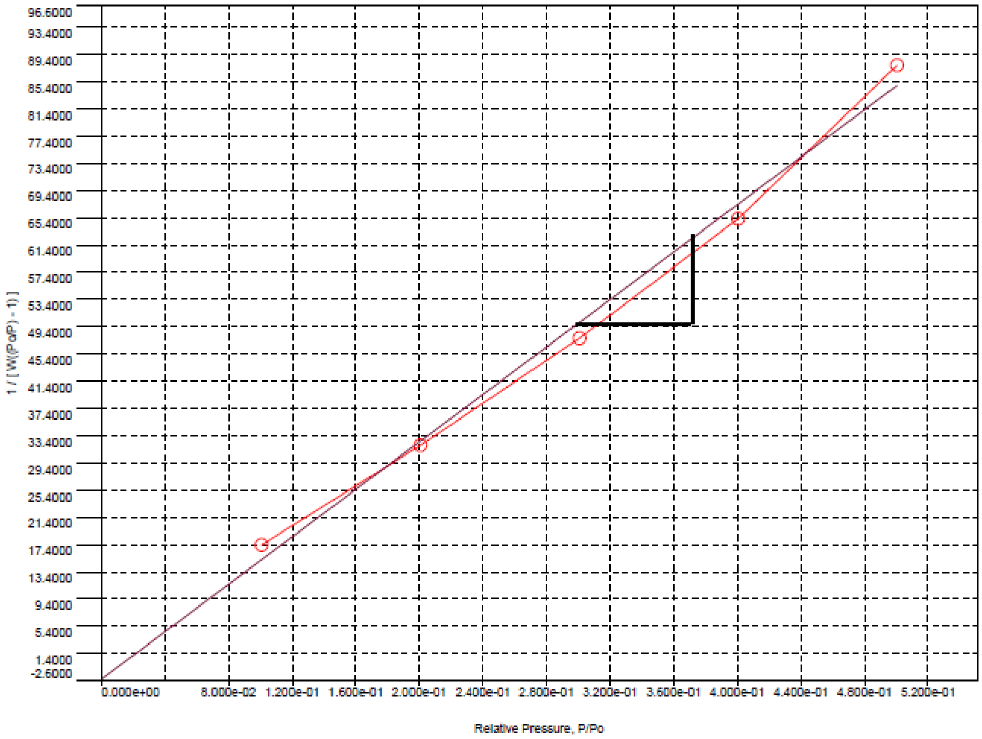

Figure 3.15. Multipoint BET surface area plot.

3.7. Electrochemical Measurements

Cyclic Voltammetry (CV), Chronoamperometry (CA) and Chronocoulometry (CC) techniques were used to investigate the electrochemical properties for fabricated WO_3/ITO electrodes. The electrochemical protonation and deprotonation was carried out using Biologic Science Instruments SP-50 controlled by EC-lab software.

3.7.1. Cyclic Voltammetry (CV) of WO_3/ITO electrodes

It is a potentiodynamic electrochemical technique that measures the current developing in an electrochemical cell when voltage is excess in the system. In general it is performed by cycling the potential of working electrode and measuring the resulting current/current density. The qualitative information about the electrochemical processes under conditions of varying voltage range, scan rate and concentration of electrolyte, the presence of intermediates in a redox system and reversibility of a reaction is known.

In the current experimental set up, the system consists of an electrolytic cell, a potentiostat, current to voltage converter, and a data acquisition system. Electrolytic cell is an assembly of the three electrode cell consisted of Platinum (Pt) as a counter electrode, saturated Ag/AgCl as a reference electrode and as prepared WO_3 films as the working electrode in H_2SO_4 electrolyte solution. Linear variation of potential with respect to time is carried, while the reference electrode maintains a constant potential. The counter electrode draws electricity from the source to the working electrode. Moreover, the electrolytic solution provides ions to the electrodes during oxidation and reduction processes. Potentiostat uses the direct current (dc) power source to produce a potential which can be maintained while allowing small currents to be drawn into the system without changing the voltage. The converter measures the resulting current and data acquisition system generates the resulting voltammograms. A cyclic voltammogram results from the measurement of the current at the working electrode during the potential sweeps.

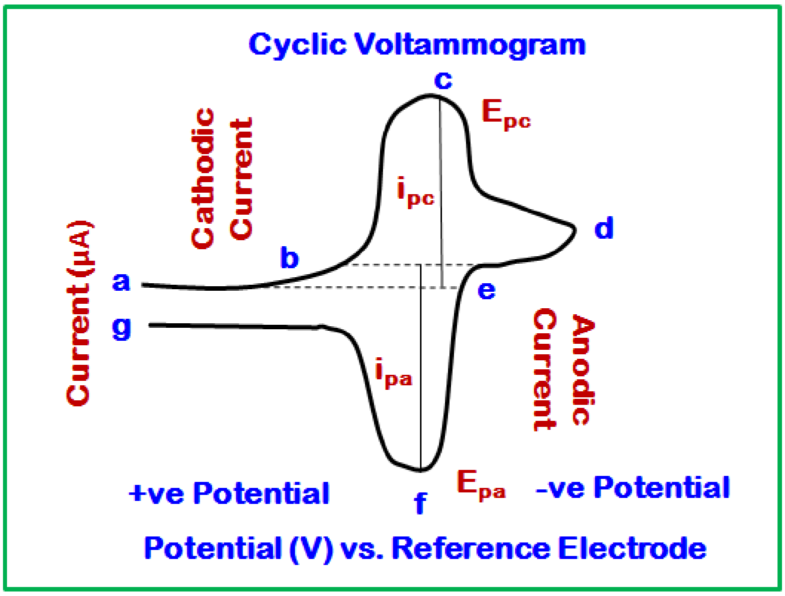

Figure 3.16. Single electron reduction/oxidation forming a voltammogram.

Figure 3.16 shows a typical cyclic voltammogram resulting due to single electron reduction/oxidation. In the figure, the reduction process occurs when the potential is sweeped negatively from initial potential (a) to switching potential (d). The resultant current is called a cathodic current denoted as 'i_{pc}'. Highest peak position at c represents the cathodic peak potential (E_{pc}). This attributes that all the surface of the electrode has been reduced. In reverse, positive potential scan occurs from (d) to (g) as a result of oxidation and the resultant current is known as anodic current denoted as 'i_{pa}'. Highest peak potential at (f) is reached upon oxidation of surface of the electrode and called as anodic peak potential (E_{pa}).

3.7.2. Chronoamperometry (CA) of WO_3/ITO electrodes

It is an electrochemical technique in which the working electrode potential is stepped and the current resulting from the faradaic processes is monitored as a function of time. Unlike CV, it is single potential step experiment. This experiment gives the current-time response of the WO_3/ITO working electrode.

3.7.3. Chronocoulometry (CC) of WO_3/ITO electrodes

In this the potential of the working electrode is sweeped to obtain the total charge that passes through the working electrode as a function of time. Thus, this experiment provides the charge-time transients of the WO_3/ITO working electrode.

3.7.4. Optical Transmittance measurements

The direct optical transmittance of the electrodes was measured using UV-Vis spectrophotometer. Bare ITO glass substrate was taken as a reference electrode for transmittance measurement. The transmittances of colored and bleached samples were also measured for calculation of coloration efficiency of the WO_3/ITO electrode.

3.8. Photocatalytic Set-Up and Measurements

Initially, experiments were carried using a model dye, Methyl Orange (MO). Based on the experiments performed using the model dye, monoclinic WO_3-ZnO nanocomposites showed better results in comparison to hexagonal WO_3-ZnO composites. Therefore, WO_3-ZnO nanocomposites prepared using monoclinic WO_3 nanocuboids and ZnO quasi-fibers were used to degrade a cationic and anionic dye, namely, methylene blue and Orange G. Structures of different dyes are shown in Table 3.1.

Table 3.1. Structure of different dyes.

Name	Structure
Methyl Orange	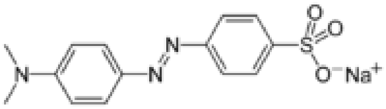
Methylene Blue	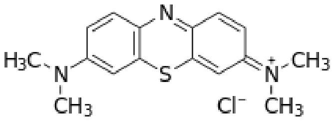
Orange G	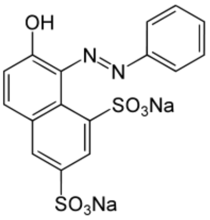

3.8.1. UV light irradiated Photocatalytic Reaction

The photocatalytic activities of WO_3-ZnO nanocomposite towards the degradation of different dyes was carried under high pressure mercury vapour lamp (125W, Philips India) for all the UV experiments. The reactor set up consists of lamp jacketed in a quartz tube and was placed inside the slurry reactor maintaining the height between lamp and reaction slurry enclosed in a rectangular hard wood casing. The slurry reactor was pyrex jacketed with constant supply of water channels through the jacket to maintain the temperature at 29 ±2^{o}C.

3.8.2. Visible light irradiated photocatalytic reaction

For visible light reaction similar set up was used with a metal halide lamp (400W, Phillips India) and the position between the lamp and solution was maintained.

3.8.3. Photocatalytic Degradation

A standard stock solution of dye having concentration 20mg/l was prepared. The dye solution along with the catalyst was kept in dark environment through continuous stirring to establish adsorption – desorption equilibrium. For each experiment, a 50 mg of catalyst was dispersed in a 50 ml aqueous solution of the dye followed by irradiated with proper intensity of light. Each time ~5 ml aliquot containing dye and powder catalyst was taken out followed by centrifugation at 3000 rpm for 10 min. After the catalyst separation, change in concentration was determined through change in absorbance using a UV-Vis spectrophotometer. After the measurement, the aliquot along with the powder was shaken and poured back to the reaction slurry to maintain the concentration of both dye and catalyst. Each experiment was repeated thrice and percentage error was found to be ± 3%.

3.8.4. UV-Vis Absorbance Measurements

The dye absorbance after experiment was determined using UV-Vis spectroscopy under wavelength region 300-800 nm. The quantitative analysis of concentration of absorbing species in dye solution was calculated using Beer-Lambert’s Law. The law states that absorbance of a solution is directly proportional to the concentration of absorbing species and their path length. The schematic of Beer-Lambert’s law is given in Figure 3.17. Mathematically, it is represented as given below:

$$\text{Log } I_o/I = abc \equiv A \qquad (17)$$

Where,

I_o = Intensity of the incident light,

I = Intensity of the transmitted light,

A = Absorbance,

b = Path length in cm (the distance that light pass through the material),

c = Concentration of the solution, and

a = Absorption coefficient (L $mol^{-1}cm^{-1}$)

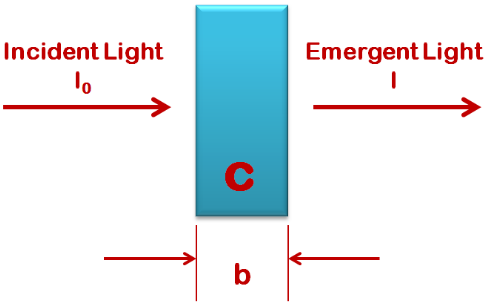

Figure 3.17. Schematic of Beer-Lambert's Law.

3.8.5. Photoluminescence Spectroscopy

It is a spectroscopic technique that absorbs electromagnetic radiation in the form of photons and then re-radiates the photons to different transition states. The basic principle relies on the excitation of electron to higher energy state and then return to lower energy state with emission of photon as described by Jablonski diagram in Figure 3.18. This diagram helps to predict the type of transitions to take place in a particular system. The allowed transitions are generally very slow with the electron staying in the same multiple manifolds. Transitions are observed between the first excited state and the ground state of a molecule as at higher energies, dissipation may occur due to internal conversion and vibrational relaxation. Initially, at first excited state, non-radiative processes occur in regard to timescale and the photons emitted have the energy less than that of the exciting photons. As there are large number of vibrational levels that couples into transition between electronic states and the emission is measured over a range of wavelengths. It allows us to predict the charge separation of the material on application of light. Photoluminescence spectrums of the prepared photocatalysts were measured using Hitachi F-4500 spectrofluorimeter.

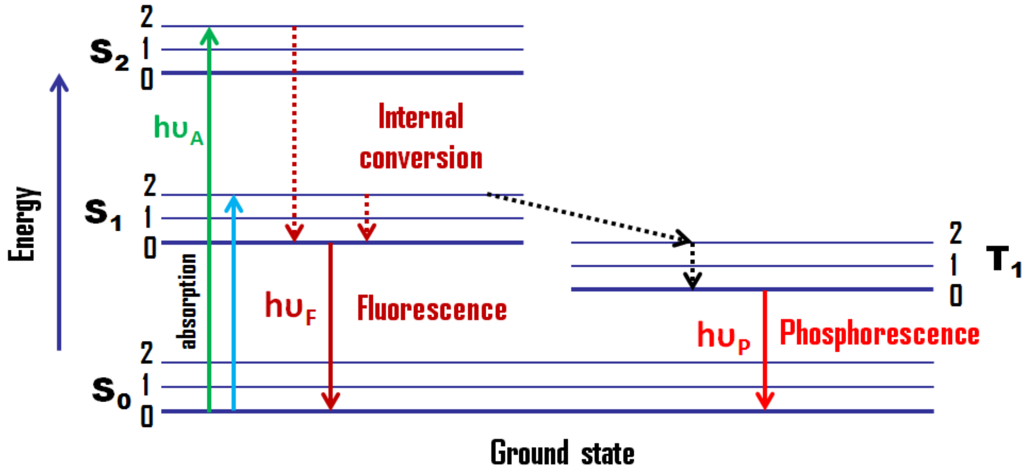

Figure 3.18. Jablonski diagram for Flourescence spectroscopy.

Chapter 4

RESULTS
&
DISCUSSION

4.1. Physicochemical Properties of Nanoparticles

Technological interest in WO_3 nanostructured material focuses on the high surface area, mesoporous and transparent films for their prospective use in energy harvesting devices [1, 2]. The potentiality and properties of material relies on the control over the size/shape, morphology, size distribution of nanoparticles, crystal structure and degree of crystallization, owing significant importance towards application [3-5]. Synchronization of above factors is carried through optimization of temperature gradient, solution pH and structure directing reagent. In the present section, a detailed discussion on the different properties of synthesized WO_3 nanostructures through two different precursors has been emphasized to understand the nature of confinement growth. Moreover, a detailed parametrical study has been carried for synthesis of ZnO nanostructures. The detail synthesis routes are discussed in Chapter 3.

4.1.1. Co-precipitation assisted Spherical and Rod-shaped WO_3 Nanoparticles

4.1.1.1. Thermal Analysis of Amorphous WO_3

In the first case, acid catalyzed exothermic reaction of tungstic acid forms an intermediate pale greenish yellow precipitate, which was later found to be amorphous spherical WO_3 and accordingly designated as ASW. Similar intermediate in the form of white precipitate, designated as ARW is obtained after acid precipitation of sodium tungstate in presence of CTAB as structure directing reagent. The crystallization temperature is confirmed by thermal analysis of ASW and ARW prior to flash heating of the as-synthesized nanoparticles. The thermal analysis of amorphous samples ASW and ARW are presented in Figure 4.1. High instability of the compound is observed in ASW due to presence of both physisorbed and chemisorbed water as shown in Figure 4.1a [6]. Thermogravimetric weight loss at 100°C is close to 3 wt% associated with loss of physisorbed water and additional ~7 wt% weight loss is due to removal of chemisorbed water molecule from $WO_3.H_2O$. Beyond 300°C no further weight loss has been measured. In DSC, two endothermic peaks are attributed to the loss of physisorbed and chemisorbed water. The exothermic peak at 450°C represented the conversion of amorphous to crystalline WO_3 under a dynamic condition. These results suggest that the amorphous

WO_3 is formed at around 300°C with the removal of both the forms of water molecules. The same is crystallized at a temperature of 450°C with a distinct exothermic peak. This analysis confirms that the flash calcination at a temperature of more than 450°C favours formation of crystalline and phase-pure WO_3.

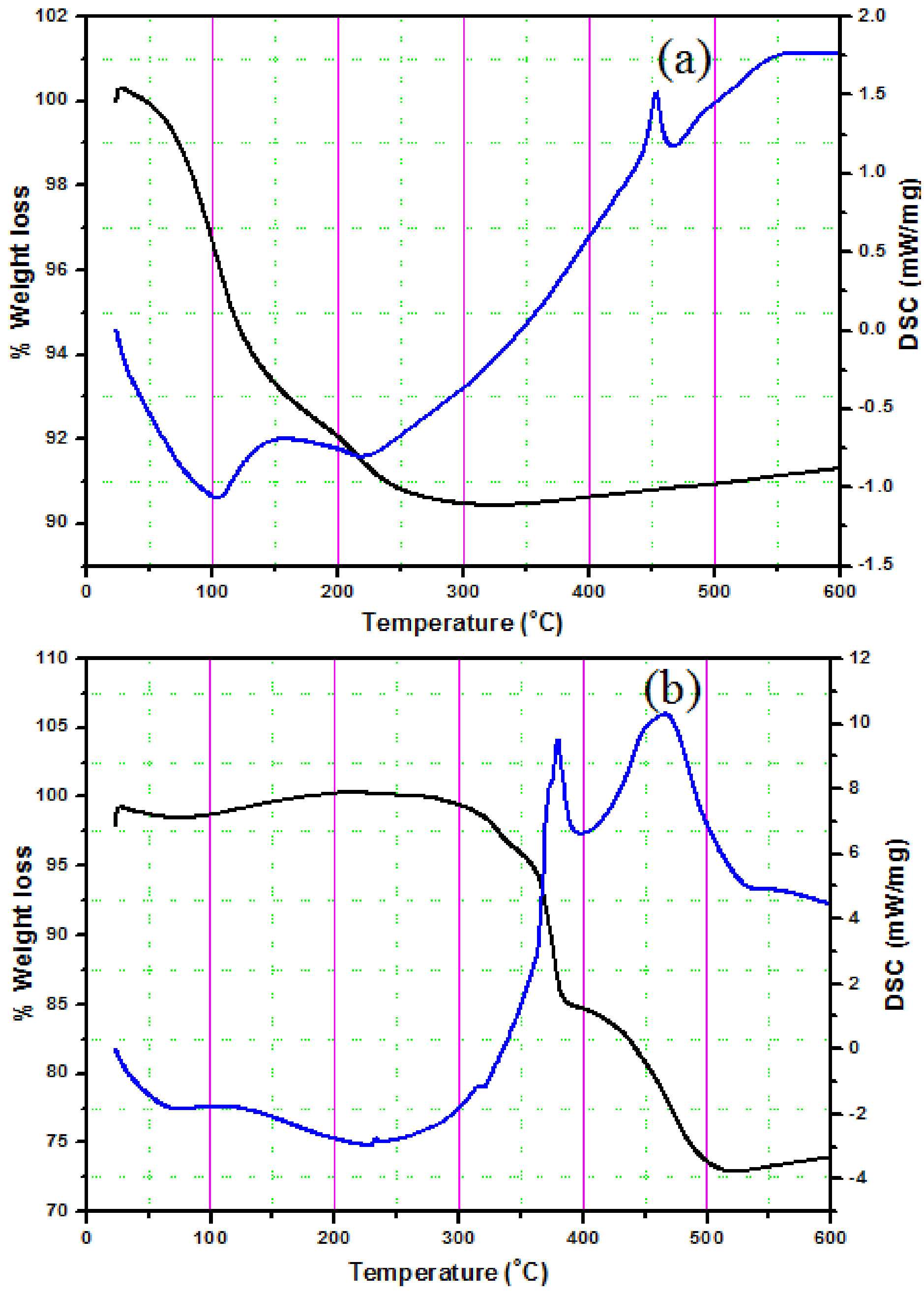

Figure 4.1. Thermogravimetric-Differential Scanning Calorimetry of (a) ASW and (b) ARW.

On the other hand, the thermogram of ARW in Figure 4.1b shows greater stability of the compound till 300^{o}C, indicating that there is no presence of either physisorbed or chemisorbed water. However, the overall weight loss is much larger (~27%) compared to that in ASW (<10%). The DSC plot indicates that there are two exothermic peaks, a sharp one at 380^{o}C and a broad peak at 460^{o}C corresponding to weight losses of ~15% and ~12%, respectively. Even though there is negligible quantity of water molecules associated with this sample, considerable quantity of organic species resulting from CTAB (structure directing agent) must have been associated with this sample. The weight loss of ~15% at a relatively low temperature is presumed to be due to partial removal of sterically hindered methyl groups. The presence of the organic compounds in ARW has been further discussed through FTIR spectral analysis in a latter part of this section. The second weight loss of ~12% which occurs between 380 and 500^{o}C can be assigned to desorption and/or decomposition of the remaining organic molecules, presumably the surfactant species, associated with the WO_3 particles [7]. Comparing the sharpness of the DSC peaks between the Figure 4.1a, amorphous to crystalline transition for the ARW specimen appears to take place at a slightly lower temperature of 380^{o}C (the first peak in Figure 4.1b) and not at 450^{o}C observed for the ASW specimen.

4.1.1.2. Phase and Crystallinity of WO_3 Nanopowders

Phase analysis is carried out to understand the crystallinity and phase purity of the nanopowders. The x-ray diffraction (XRD) patterns of four nanopowders namely ASW, SW, ARW and RW is plotted in Figure 4.2. As designated earlier, ASW and ARW corresponds to the powders obtained immediately after freeze-drying and are observed to be amorphous in nature due to the broad humps observed in the crystalline region (2θ – 22 to 25^{o}). However, SW and RW are the nanopowders obtained after flash calcination of the ASW and ARW specimens, respectively. The indexed XRD patterns of these nanopowders confirm their crystallinity with apparently monoclinic structure having a = 7.29Å, b =7.53Å and c =7.68Å having space group: P21/n (JCPDS No. 43-1035), which has been further confirmed from Raman spectroscopic data presented later [8]. XRD pattern and the peak intensities depict that rod-shaped WO_3 (RW) is better crystalline than the spherical WO_3 nanoparticles. The measured specific BET surface areas for SW and RW are found to be 9.91 m^2/g and 5.16 m^2/g, respectively. Both crystallite size and surface area data reconfirm better crystal growth for the RW specimen.

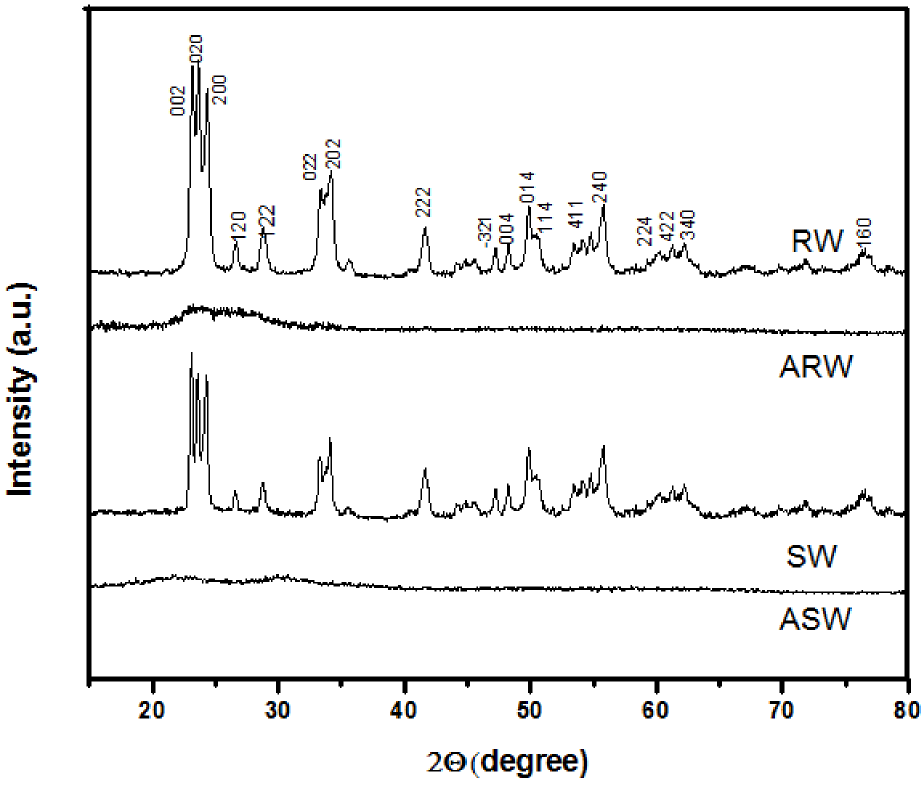

Figure 4.2. X. Ray diffraction (XRD) pattern of ASW, SW, ARW and RW Nanopowders.

4.1.1.3. Morphological Analysis of WO_3 Nanopowders

Investigation of morphology, crystallinity and particle size is carried through TEM and SAED techniques. TEM micrographs of TEM micrographs with SAED pattern and HRTEM images for both SW and RW nanoparticles is represented in Figure 4.3. Figure 4.3a shows the distinct spherical morphology of WO_3 nanoparticles with an average particle size of around ~50 nm. Although the particles are partially agglomerated, there is no sign of the formation of hard agglomerates or neck formation. Figure 4.3b shows the rod-shaped morphology of the WO_3 nanoparticles with an average particle length of ~140 nm and width of ~40 nm.

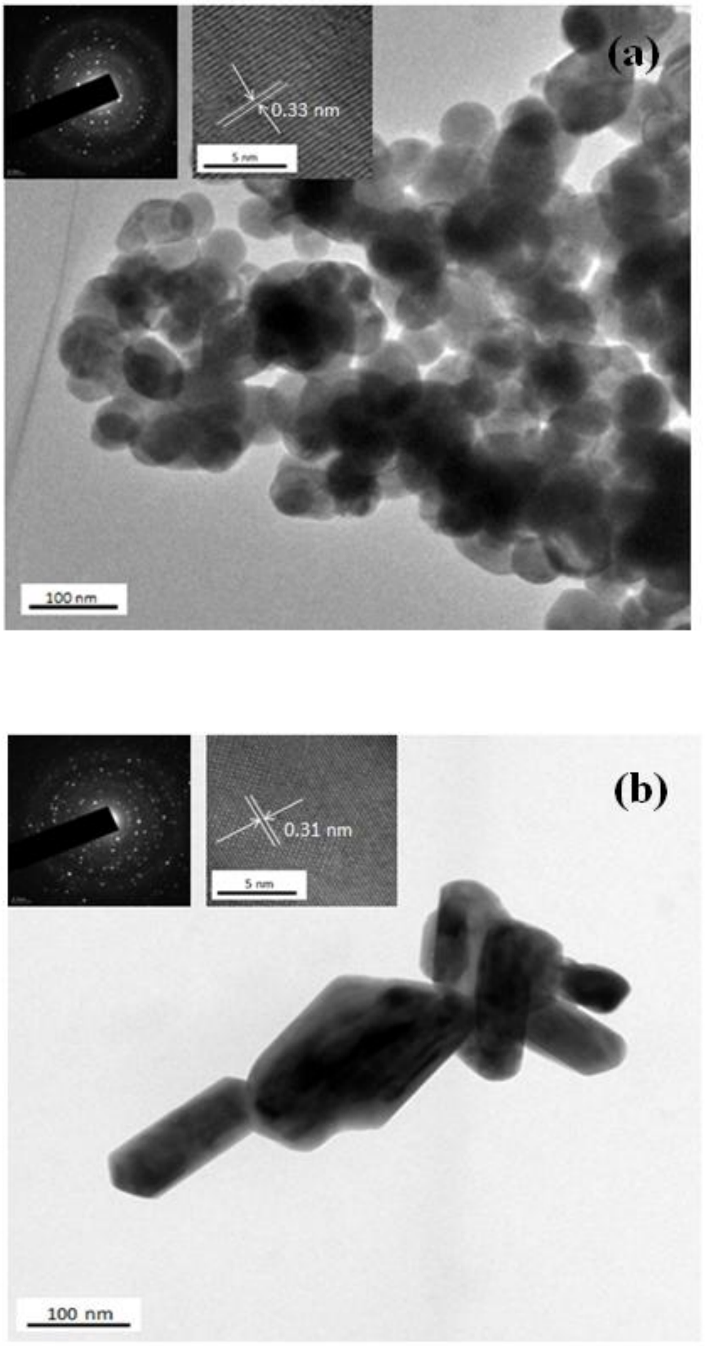

Figure 4.3. TEM images for (a) Spherical and (b) Rod - shaped WO_3 Nanoparticles.
(Inset represents the HRTEM images and SAED patterns)

In spite of the fact that spherical and rod shaped WO_3 nanoparticles have different shapes; they possess the same crystal structure. The inset represents the selected area electron diffraction (SAED) patterns and HRTEM images of the WO_3 nanoparticles, which clearly indicates relatively high crystallinity of the rod shaped WO_3 nanoparticles than the spherical WO_3 nanoparticles. The spacing of the lattice fringes has been found to be about 0.33 nm of (0 0 2) plane for SW and 0.31 nm for RW which confirms that the rod prefers to grow along [0 0 2] direction. The above d-spacing also compares well with the d-spacing calculated from X-ray diffraction patterns.

4.1.1.4. Functional group of WO_3 Nanopowders

The presence of functional groups before and after flash heating has been confirmed from FTIR spectral analysis. The infrared transmittance spectrum has been recorded for the same four nanopowders namely ASW, ARW, SW and RW to understand the chemical purity and the nature of ligands associated with these nanopowders (Figure 4.4). The spectra of ASW and SW specimens are shown in Figure 4.4a. ASW exhibits a small absorption peak at 1611.29 cm^{-1}, corresponding to O–H stretching mode vibration of the water molecules adsorbed on the surface of the particles, the evidence of which also came from thermal analysis (Figure 4.1a). In conformity with the thermal analysis data, this absorption peak disappears on calcination at 500°C (specimen SW) together with the formation of crystalline spherical particles. The peaks observed at 890.49 cm^{-1} in ASW and at 844.90 cm^{-1} in SW can be assigned respectively to W–O–O–W stretching vibration [9]. Similar spectra for ARW and RW specimens are presented in Figure 4.4b.

Unlike that of ASW, the spectra of the ARW exhibits a number of absorption peaks throughout the range of wave number, most of which arise from the organic ligands present in this nanopowders. The peaks at 2921.12 cm^{-1} and 2950.31 cm^{-1} are identified with the anti-symmetric stretching vibrations of $–CH_2–$ and $–CH_3$ group present in the carbon chain of the CTAB [10]. Similar to ASW, ARW shows less hydrated sharp O–H stretching and bending peaks at 1626.90 cm^{-1} and 1466.69 cm^{-1}, respectively. Further, peaks at low wave numbers have been found to be at 958.84 cm^{-1} for W=O terminal stretching, 892.99 cm^{-1} for O–O stretching and 797.93 cm^{-1} for W–O–W asymmetric intra-bridge stretching that indicates the amorphous nature of the powders [11]. Both SW and RW reveal nearly similar spectra in both low as well as high wave number regions. Similar W–O–W stretching peak is also observed at 850.92 cm^{-1} for RW.

In general, tungsten atom is known to have six-fold coordination in crystalline WO_3, whereas in amorphous form it becomes five or four fold coordination due to deficiency of oxygen ions giving rise to distortion in the structure and leading to amorphous nature of the particles [12]. The distinct feature in crystallography and long-range periodicity of regular planes attributes to the difference in stretching vibration behavior of amorphous and crystalline nanoparticles.

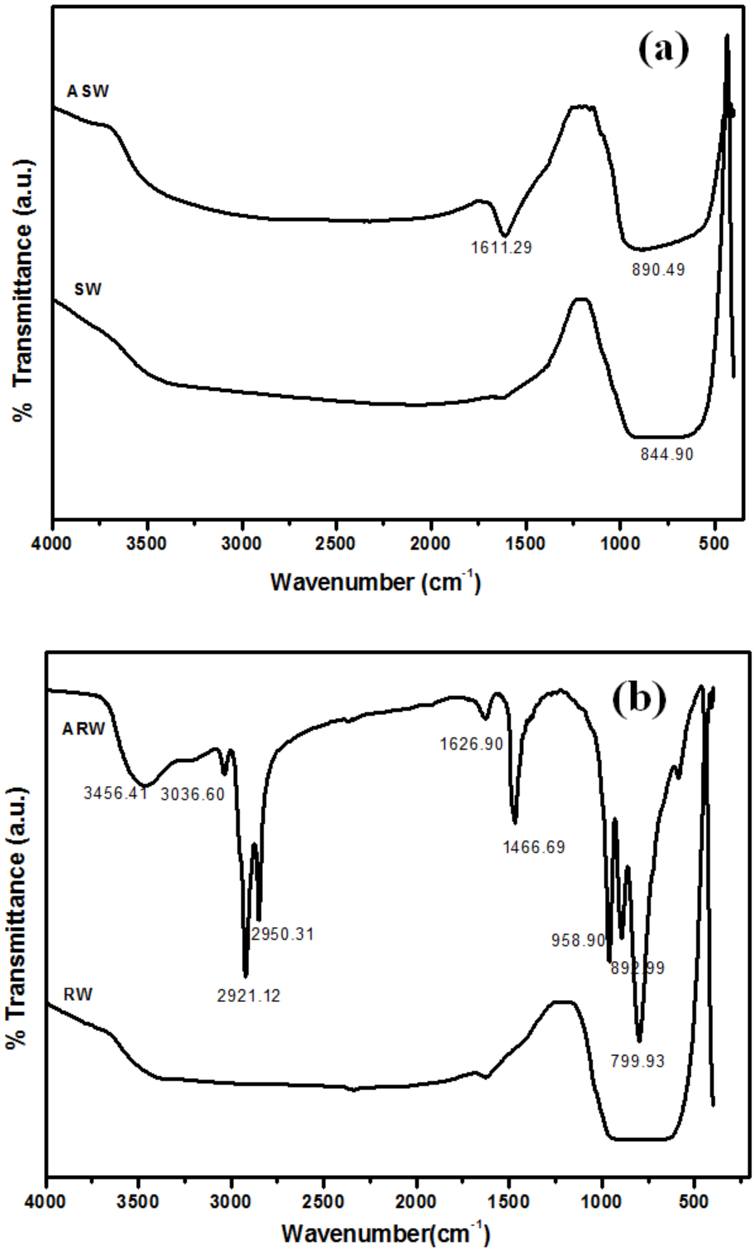

Figure 4.4. FTIR spectra of (a) Spherical (ASW and SW) and (b) Rod-shaped (ARW and RW) nanoparticles.

4.1.1.5. Bonding behaviour of WO_3 Nanopowders

Figure 4.5 represents the Raman spectra of spherical and rod-shaped WO_3 nanopowders to better understand the phase and bond characteristics of WO_3 nanoparticles. Raman spectrum of both SW and RW supports the formation of crystalline WO_3 monoclinic phase as supported by available literature [13]. Both the powders reveal very similar wavenumber in the wide spectra zone. The W– W bond is identified near to 187 cm^{-1} wave number, however, the intensity varies because of crystallinity of WO_3 nanoparticles. Raman peaks observed at low wave numbers 268 and 327 cm^{-1} relates to the bending vibration of W–O–W bond. The higher wave number peaks at 716 cm^{-1} is due to the O–W–O vibration and 808 cm^{-1} corresponding to the crystalline WO_3 stretching vibration of the bridging oxygen of W–O–W. These two peaks clearly attributes to the monoclinic structure of WO_3.

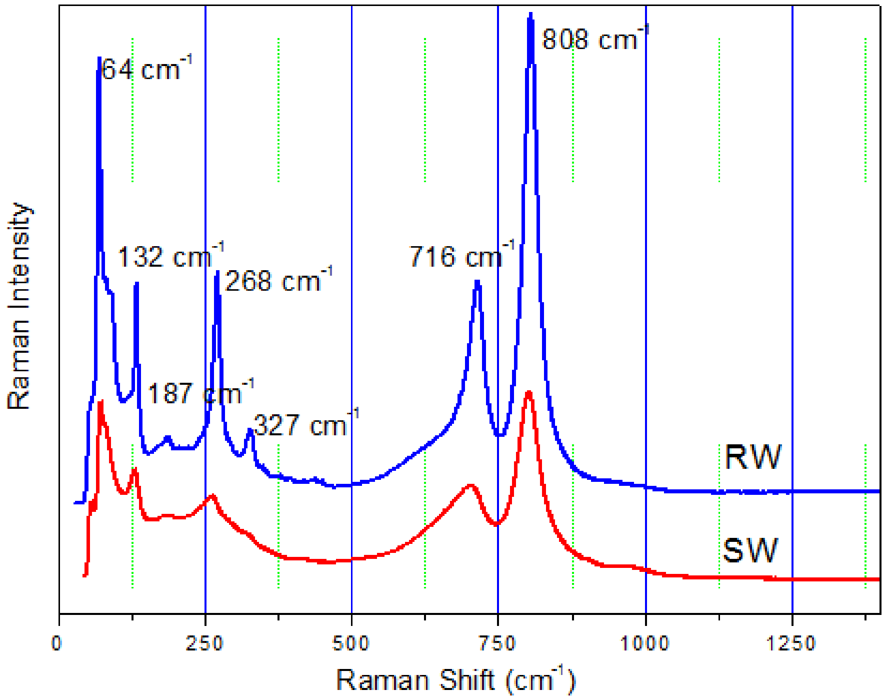

Figure 4.5. Raman Spectra of spherical (SW) and rod-shaped (RW) WO_3 nanoparticles.

4.1.1.6. Proposed Reaction Mechanism

For synthesis of spherical particles, the two most important parameters are found to be temperature and pH of the reaction media in presence of hydrogen peroxide solution. The exothermic nature of the reaction could possibly be due to spontaneous decomposition of H_2O_2 leading to the formation of water vapour and nascent oxygen above the critical temperature of 95°C and pH > 5 [14, 15]. On the other hand, a temperature less than 95°C together with a low solution pH of < 5 prevent spontaneous loss of H_2O_2 and therefore are expected to cause the stoichiometric reaction with tungstic acid. However, in this investigation, the preheated pot temperature of 90 ± 5°C initiates the decomposition of H_2O_2 and accelerates the reaction between nascent oxygen atom and H_2WO_4 to form peroxotungstic acid ($WO_3.xH_2O_2$). The value of x varies in the range of 1–2, whereas for hydrated WO_3, the value of x is in the range of 0–2 depending on the reaction conditions [16, 17]. Simultaneous addition of nitric acid favours the dehydroxylation by the acid catalyst oxidation reaction and $WO_3.xH_2O_2$ transforms to insoluble pale yellowish precipitate (ASW). Thus, the overall reaction sequence can be summarized as follows:

$$H_2O_2 \xrightarrow{\quad} 2H_2O + 2\ddot{O} \qquad (18)$$

$$H_2WO_4 + 2\ddot{O} \xrightarrow{\quad} WO_3.xH_2O_2 \text{ (peroxo-tungstic acid (PTA))} \qquad (19)$$

$$WO_3.xH_2O_2 + 2HNO_3 \xrightarrow{\quad} WO_3.xH_2O + 2NO_2 + O_2 \qquad (20)$$

$$WO_3.xH_2O \xrightarrow{500^oC} WO_3 + xH_2O \qquad (21)$$

The values of 'x' in Eqn. (20) and (21) is found to be 1 as confirmed from the thermogravimetric data presented in Figure 4.1a.

On the other hand, synthesis of WO_3 with rod like morphology (RW) follows acidification of $Na_2WO_4.2H_2O$ forming anionic WO_4^{2-} and cationic H^+ under acidic condition and finally to form hydrated WO_3. However, an optimum amount of CTAB ($H_3C–(CH_2)_{15}– N^+(CH_3)_3 Br^-$) provides encapsulation to form a confined reaction zone where the nuclei prefers an anisotropic growth leading to the development of a rod like structure as reported by Brust et al. [18]. The probable reaction inside the reverse micelle formed by CTAB encapsulation is found similar to the nanorod formation as reported by

Shen et al. [19]. Thus, the details of the various reactions inside the confined reaction zone arising from the presence of the structure directing agent CTAB may be summarized as follows:

$$Na_2WO_4.2H_2O + 2HNO_3 + H_2O \longrightarrow WO_3.xH_2O + 2NaNO_3 \qquad (22)$$

$$WO_3.xH_2O \xrightarrow{500^{o}C} WO_3 + H_2O \qquad (23)$$

The value of ‘x’ in the intermediate compound $WO_3.xH_2O$ is reported to vary in the range 1–2 when CTAB surfactant is used for the synthesis of WO_3 nanoparticles or other morphologies. The degree of ionization of the parent solute such as sodium tungstate and the degree of aggregation of the surfactant depends on the cationic and anionic interaction, which in turn controls the growth phenomena of the particular compound [20, 21]. DSC analysis presented earlier indicates the decomposition of the organic component through a couple of distinctly different exothermic reactions together with the conversion of amorphous to crystalline WO_3 supported by presence of organic groups from CTAB with the hydrated WO_3.

4.1.1.7. Band Gap of WO_3 Nanopowders

The UV–Vis diffuse reflectance spectrum has been used to determine the band gap energy for both of the samples. The measured diffuse reflectance spectra (Figure 4.6) have been used for Tauc plot, in which square root of Kubelka–Munk function multiplied by the photon energy is plotted against the photon energy ($E_{photon} = h\upsilon$) as shown in the inset of Figure 4.6. The Kubelka–Munk unit of absorption is calculated from the equation; $KMU = (1 - R)^2/2R$, where, R = reflectance [22]. The band gap energy is calculated as ~2.82 eV and ~2.75 eV for SW and RW nanopowders, respectively. Similar band gap energy of 2.62 eV has been reported for monoclinic WO_3 films prepared by spray pyrolysis but higher value of 3.4 eV has been observed for orthorhombic WO_3 films prepared by sol–gel method [23, 24].

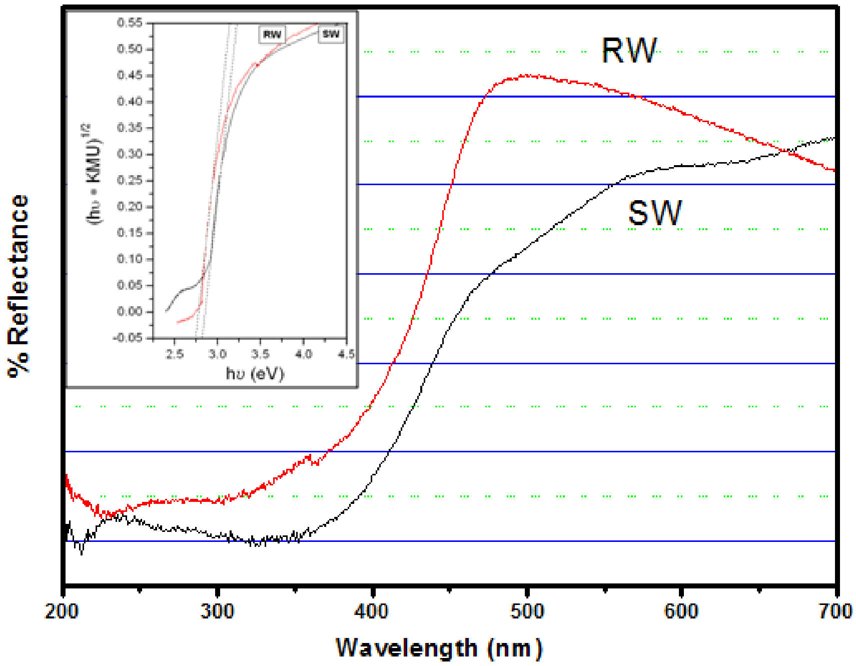

Figure 4.6. UV-DRS for Spherical (SW) and Rod-shaped (RW) nanoparticles.
(Inset shows the Tauc plot for the two specimens for the purpose of band gap calculation)

4.1.1.8. Summary

Crystalline WO_3 nanoparticles having monoclinic crystal structure but with two distinctly different morphologies such as spherical and rod shaped are successfully synthesized through wet chemical precipitation using two different precursors namely H_2WO_4 and $Na_2WO_4.2H_2O$ via control over solution pH and temperature. For the first case, acid catalyzed exothermic reaction under low pH (~1) and low temperature (95^oC) favours isotropic non-confined spherical WO_3 nanoparticle formation through an intermediate amorphous phase. On the other case, anisotropic growth of rod-shaped particles using CTAB as structure directing reagent is favoured. Vibrational spectra of amorphous powders reflect the presence of adsorbed water molecules and organic species from CTAB, respectively. Flash calcination forms the pure phase crystalline monoclinic WO_3 nanoparticles. Approximate particle size of spherical nanoparticle is 50 nm, whereas, the average dimensions of the nanorods are 140 nm/40 nm (length/ width). Rod-shaped nanoparticle has high crystallinity and specific surface area compare to spherical nanoparticles of WO_3. Thus, the prepared morphologies of WO_3 nanoparticles have been considered for the fabrication of electrodes for electrochemical measurements and studied their electrochemistry for efficient electrochromism in later.

However, this co-precipitation process does not able to develop low temperature ($<500^oC$) pure monoclinic phase as well as hexagonal structure which has theoretical more intercalation space in crystal structure in comparison to monoclinic crystal of WO_3. In this context, another method namely hydrothermal technique has been adopted and their significant results are discussed in the following section.

4.1.2. Hydrothermal assisted WO_3 Nanocuboids

The complex three-dimensional (3D) nanostructures have also attracted much attention since this nanostructure possesses features of nanometer-scale building blocks and novel properties [25]. In general cuboid morphology with equal volume of sphere and cylinder has high surface area [26]. Hydrothermal method is one of the economic wet chemical routes over physical deposition techniques to prepare different morphologies of nanostructured WO_3 in the presence of structure directing reagents such as acids, surfactants and metal sulphates, chlorides and sulphides [27, 28]. In the present study, fluoroboric acid (HBF_4) has been used as structure directing reagent for growth of WO_3 nanocuboids using hydrothermal method. A plausible reaction process is also studied that optimizes the critical processing parameters to control the pure-phase crystal structure and morphology.

4.1.2.1. Influence of processing conditions on the crystal structure

The powder x-ray diffraction pattern confirms the phase content, crystal structure and crystallinity of the WO_3 nanopowders. Initially, experiments are designed chiefly to determine the primary crystal structure and phase of the products formed upon changing the HBF_4 molar concentration (M) from stoichiometric 2 M to the higher concentration of 5 M. The other parameters such as temperature (180^{o}C) and time (4 hours) are kept constant during this experiment. The XRD pattern of synthesized powders under these conditions is shown in Figure 4.7. The stoichiometric HBF_4 concentration (2M) begins to form the triclinic tungsten oxide phase mixed with the partial monoclinic phase (JCPDS card no. 830949 and 431035). The pure triclinic tungsten oxide (JCPDS card no. 830949) phase is recorded with increasing concentration of 2.5 M HBF_4. There are no peaks of a monoclinic phase found in this concentration. A pure hexagonal tungsten oxide phase (JCPDS card no. 752187) starts to form at 3 M HBF_4 concentration. In the later stage, coexistence of hexagonal and monoclinic phases is found for the 3.5 M concentration. This depicts the plausible conversion of hexagonal to monoclinic phase. The pure monoclinic crystalline tungsten oxide (JCPDS card no. 720677) phase is observed upon further increasing the concentration (4 M to 5 M), as shown in the Figure. The above investigation shows that WO_3 transition follows triclinic to hexagonal followed by monoclinic, which is similar to the observation of researchers [1, 29]. Both stable triclinic and monoclinic WO_3 phases are formed by varying the HBF_4 concentration in the present studied system. However, the hexagonal phase occurs as only a metastable phase and has a tendency to form a stable monoclinic phase with further HBF_4 concentration increments, particularly beyond 4 M [30].

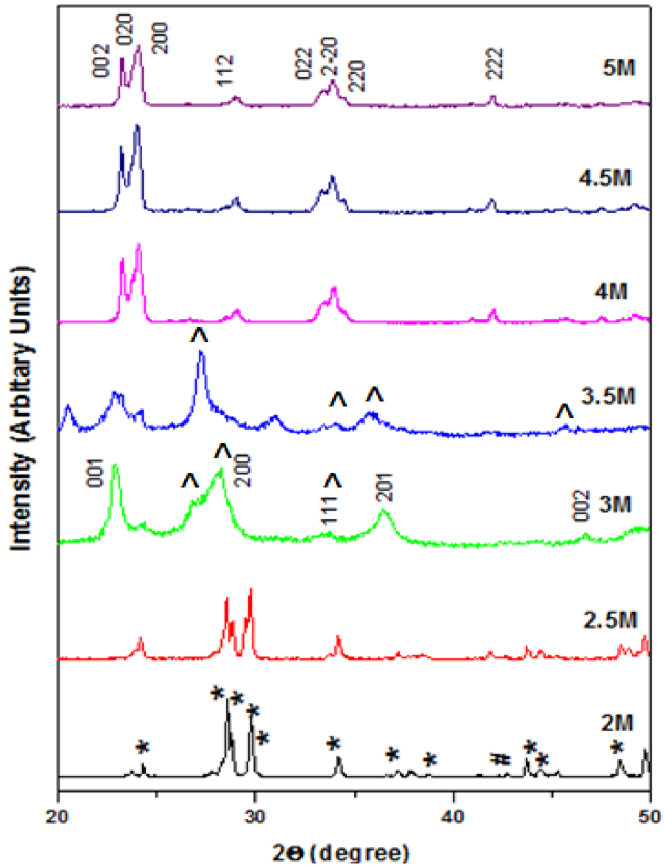

Figure 4.7. XRD patterns for the effect of HBF_4 molar concentration at 180°C for 4 hours. (Symbols: * = triclinic, # = monoclinic and ^ = hexagonal crystal structure)

The growth phenomenon depends on time under isothermal conditions irrespective of any process condition [31]. Hence, it is necessary to understand the effect of time on the formation of the pure phase along with the desired morphology. A time variation is done starting from 0–8 hours while keeping the other parameters such as HBF_4 concentration (4 M) and temperature (180°C) constant, as shown in Figure 4.8. The molar concentration of HBF_4 is chosen to be 4 M as formation of only the monoclinic phase is favoured for HBF_4 concentrations greater than 4 M. Zero hour is defined as before insertion of the closed vessel in the hydrothermal process chamber. Immediate HBF_4 addition results in orthorhombic tungstic acid (Tungstite, JCPDS card no. 840886) along with some impurity peaks. The pure orthorhombic tungstite (Tungstite, JCPDS card no. 840886) phase is formed at only 2 hours duration. Interestingly, the crystalline monoclinic phase has been detected for the duration of 4 hours and the phase remains constant beyond this time limit. This result depicts the periodic formation of orthorhombic tungstite (H_2WO_4) and monoclinic WO_3 crystal structures by varying the hydrothermal duration. Process control variables suggest that the optimized conditions for obtaining pure monoclinic tungsten oxide is 4 M HBF_4 concentration, 4 hours duration and 180 ^{o}C temperature. However, these conditions provide low crystalline cuboid morphology and subsequent band-gap energy due to the content of crystalline water [32]. The presence of water content is further confirmed by thermal analysis in the next section. In this result, 6 hours processing time is again considered as the optimum hydrothermal time. However, no significant change in the crystallinity is observed after the hydrothermal duration of 6 hours.

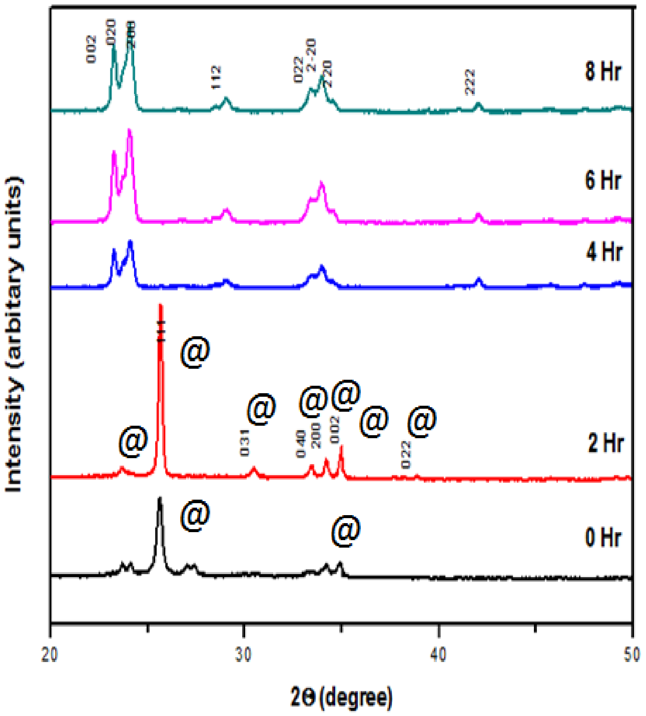

Figure 4.8. XRD patterns for the effect of time at 180^{o}C with 4 M HBF_4 concentration (Symbol: @ = orthorhombic tungstite crystal structure)

Every synthesis requires a minimum thermal energy to overcome the potential energy barrier for the completion of the targeted reaction. To optimize this, additional studies on varying the reaction temperature (160°C to 200°C) have also been carried out at constant conditions such as 4 M HBF_4 concentration and 6 hours reaction duration. Figure 4.9 clearly represents orthorhombic tungstic acid at 160°C. However, a mixture of orthorhombic tungstic acid and monoclinic tungsten oxide results at 170°C, which indicates the initialization of monoclinic crystal phase at such temperature. Additionally, incrementing the temperature up to 200°C only enhances the crystallinity of a monoclinic phase or in another sense decreases the surface area. Thus, optimized conditions for the synthesis of WO_3 nanocuboids from $Na_2WO_4.2H_2O$ and HBF_4 include temperature of 180°C, time of 6 hours and HBF_4 concentration of 4 M.

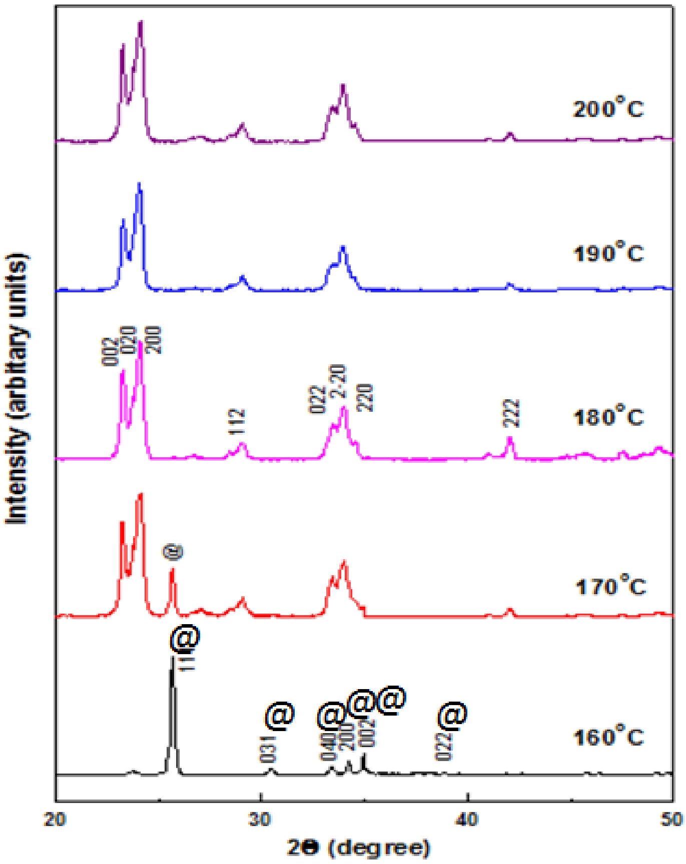

Figure 4.9. XRD patterns for the effect of temperature for 6 hours at 4 M HBF_4 concentration (Symbol: @ = orthorhombic tunsgtite crystal structure)

4.1.2.2. Thermal analysis of WO_3 Nanocuboids

The necessary thermal analysis is carried to understand the stability of the synthesized material. Thermal analysis of WO_3 nanocuboids for both 4 hours and 6 hours is presented in Figure 4.10a and 4.10b, respectively. The thermogram of 4 hours illustrates the instability of the compound until 280^{o}C. A total of 3.5% weight loss is observed from room temperature to 280^{o}C which corresponds to the presence of water molecules in the WO_3 nanocuboid crystal system. In the DSC plot, the endothermic peak near 80^{o}C corresponds to the loss of physisorbed water. A broad exothermic peak at around 550^{o}C is associated with the further crystallization of WO_3. However, the thermogram of 6 hours reveals high thermal stability of the compound until 600^{o}C as there is no weight loss, although plausible crystallization at high temperature has been depicted by a small exothermic hump. This study predicts that the synthesized particles have a tendency to a high degree of crystallinity at high temperature as the powder synthesized at low temperature has a tendency to form a semi-crystalline structure [33]. Phase changes of specific cuboid WO_3 morphology during hydrothermal reaction follows orthorhombic tungstite to monoclinic WO_3 transformation, which has already been confirmed through crystal phase and thermal analysis at optimum HBF_4 molar concentration. The aforementioned process conversion can be represented through Eqn. 24-26:

$$Na_2WO_4.2H_2O + 2HBF_4 \rightarrow H_2WO_4 \text{ (orthorhombic)} + 2NaBF_4 + 2H_2O \quad (24)$$

$$H_2WO_4 \text{ (orthorhombic)} \rightarrow WO_3.xH_2O \text{ (monoclinic)} + H_2O \quad (25)$$

$$WO_3.xH_2O \rightarrow WO_3 + xH_2O \quad (26)$$

The value of x is found as 0.5 and is confirmed from the thermogravimetric data presented in Figure 4.10.

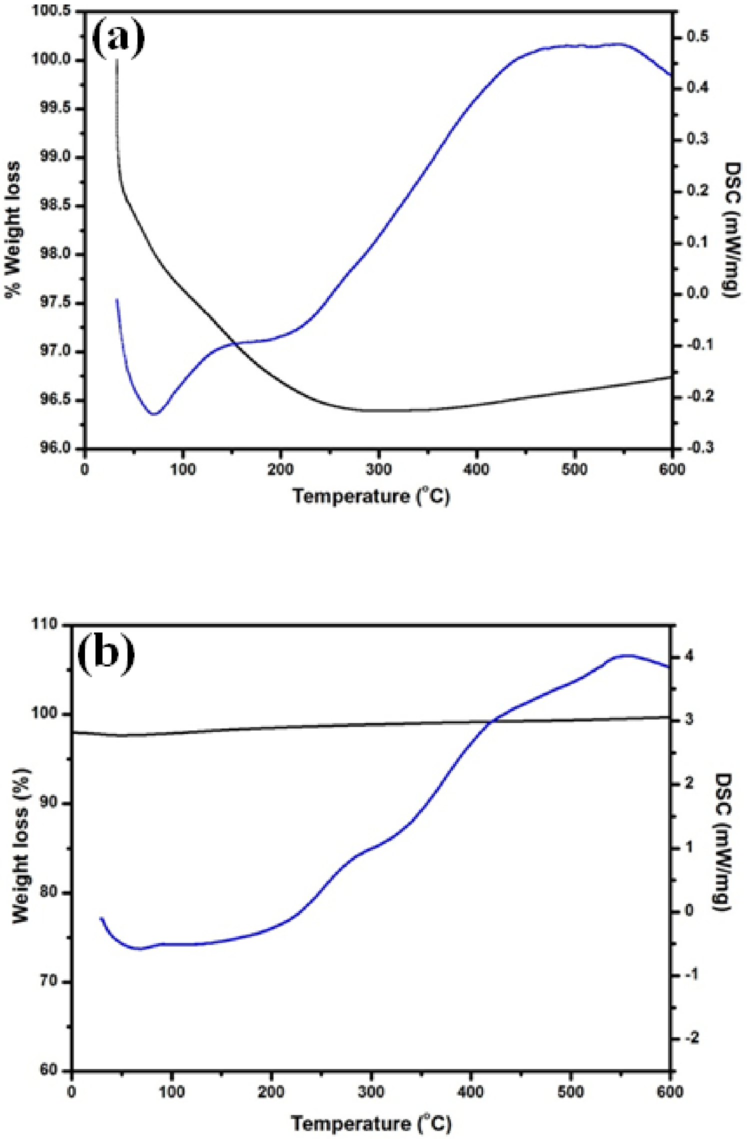

. **Figure 4.10.** TG-DSC plot of WO_3 Nanocuboids at (a) 4 hours and (b) 6 hours.

4.1.2.3. Rietveld Refinement for optimum WO_3 Nanocuboids

In a recent article, Ma et al. [34] started from the aforesaid precursors and reported an identical XRD pattern up to a maximum 2θ value of 50° and concluded the structure to be triclinic as per JCPDS – 321395. In comparison, the present XRD pattern for extended diffraction angle 15–80° (2 θ) consists of broader peaks at higher angles of 53–57°(2θ). This peak in particular matches well with the monoclinic instead of triclinic tungsten oxide crystal structure, as confirmed from the Rietveld profile fitting method

(Figure 4.11). Tungsten oxide is calculated as a pure monoclinic structure (PCR File code: wo3_p21n_80056, a =7.39773, b = 7.49056, c = 7.64700, β = 88.7102° with space group P21/n). The crystal structure model of WO_3 (PCR File code: 80056) is used as a starting point for the refinement. The characteristic reflections of WO_3 are pointed out as (200), (020) and (002). It is observed that the reflections are merged into a broader peak centered at the (020) position, which may be due to the overlap of the strongly broadened peaks. The Rietveld refinement has the lowest indices values, which are recorded as R_p = 23.2, R_{wp} = 29.9 and χ^2 = 1.34, respectively [35].

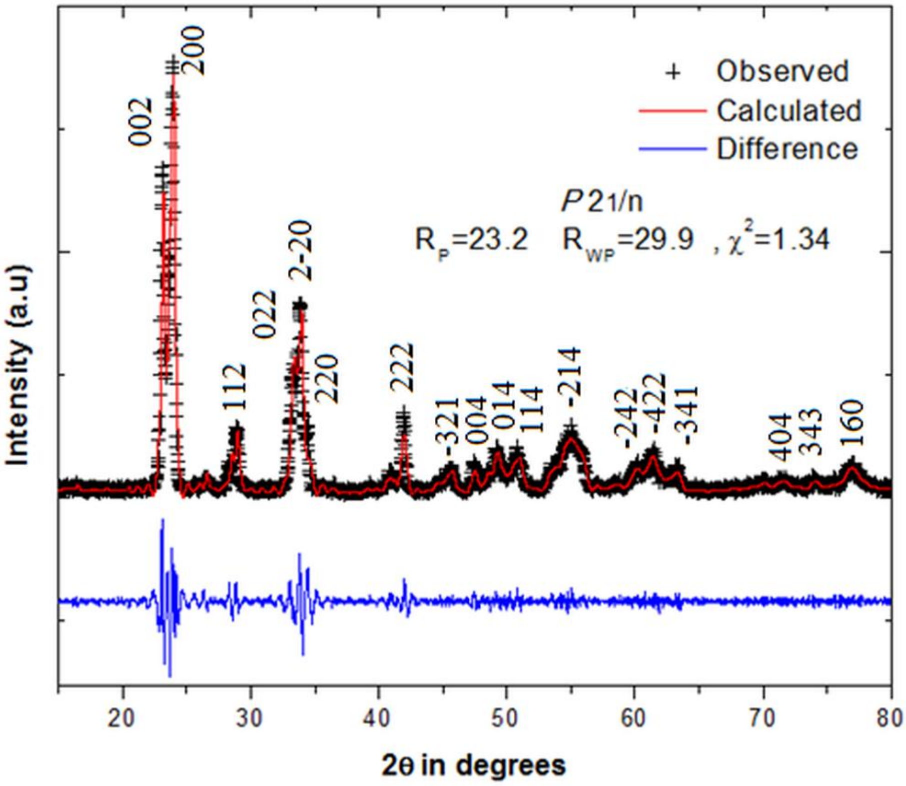

Figure 4.11. Rietveld Refinement of optimized WO_3 Nanocuboids.

4.1.2.4. Morphological Analysis of WO_3 Nanocuboids

The reaction sequence, concentration of HBF_4, temperature and time are varied to obtain different morphologies, which are represented in FESEM images in Figure 4.12 – 4.14. Discrete small dots appear due to gold coating. Detail analysis suggests that the 4M HBF_4 concentration develops an adequate crystal structure, crystallinity and desired morphology. Hence, lower and upper limits such as 3.5 M and 4.5 M HBF_4 concentration have been considered for fine tuning and detailed analysis. Figure 4.12a represents three particles prepared at 3.5 M, 4 M and 4.5 M HBF_4 concentrations, respectively. At low concentration, formation of partially agglomerated spherical particles along with plate shaped particles is preferred instead of formation of nanocuboids. However, at the optimum 4 M concentration, nanocuboid morphology is obtained, as shown in Figure 4.12b. From the image, typical dimensions of the cuboid appear to be ~130 nm length, ~110 nm width and ~85 nm thickness. However, further concentration increment has no distinct influence on the morphology, as shown in Figure 4.12c.

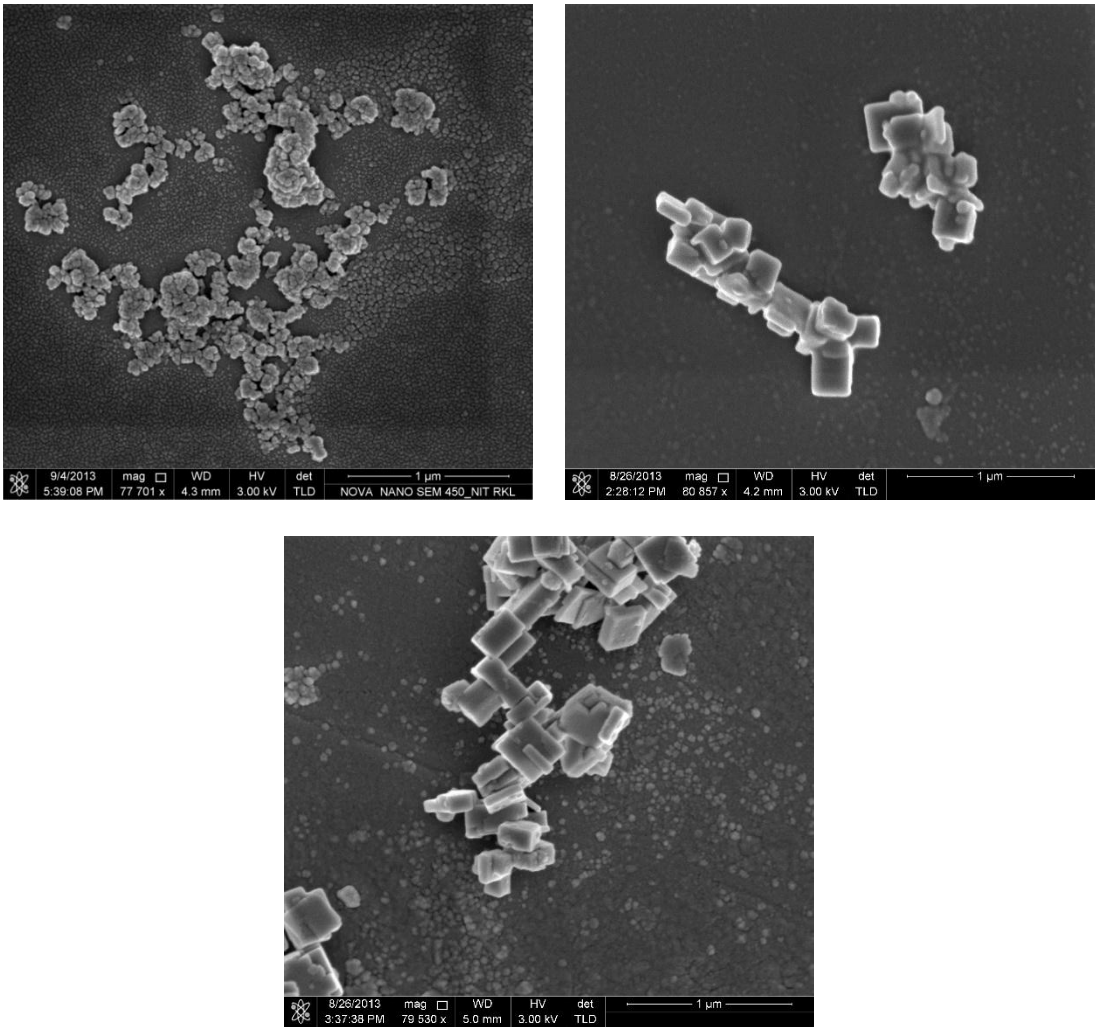

Figure 4.12. FESEM images under experimental conditions of time 6 hours and temperature 180°C at (a) 3.5 M, (b) 4 M and (c) 4.5 M HBF_4 concentrations.

Figure 4.13 shows the effect of hydrothermal duration on the morphology of WO_3 and the plot of specific surface area versus time to determine the growth phenomenon affected by the surface activity. A hydrothermal duration of 2 hours initially develops uniform plate-like morphology with an average particle size of 400 nm and an orthorhombic tungstite crystal structure. Herein, the selected hydrothermal method follows the expected development of WO_3 crystal from aqueous metal salt solutions under critical pressure at a pertinent temperature and solution pH through the structure directing agents. The WO_3 nanoparticle formation mechanism with particular growth direction depends on the solubility of the metal oxides and the reaction kinetics during the synthesis. It significantly alters the critical point of temperature assistance to form high pressure and changes the resultant dielectric properties of aqueous media [36]. At the initial stage, tungstite (H_2WO_4) formation occurs with a structure of layers of WO_6 octahedra sharing four equatorial oxygen atoms which are linked through hydrogen bonds derived from interaction between water molecules and oxygen present in the axial position of the octahedra. Plate-shaped particles are formed due to inhibition of the (010) crystal plane, which is the normal growth direction of the H_2WO_4 structure [34].

It is due to insufficient BF_4^- anion concentration; structural orientation of plates cannot be induced by adding the BF_4^- anion to the hydrogen bond system to occupy the apexes with a boron atom at the center. Thus, the growth axis is not restricted but rather prefers growth of the structure forming cuboids. Moreover, with further time increments up to 4 hours; the cuboid-like WO_3 particles are mixed with a fraction of the plate-like particles. This reveals that the growth mechanism follows a plate- to cuboid-like morphology. Nearly homogeneous cuboid-like morphology has been observed for 6 hours without formation of plates. A gradual decrease in surface area is observed with the time increment because of the agglomeration of particles, which reveals that due to the highly active surface, the particles tend to stabilize themselves following the agglomeration process. Figure 4.14 represents the effects of lower and upper temperature range from the critical temperature of 180°C. Plate-like particles and more agglomerated cuboid-like particles are confirmed at 170°C and 190°C temperatures, respectively.

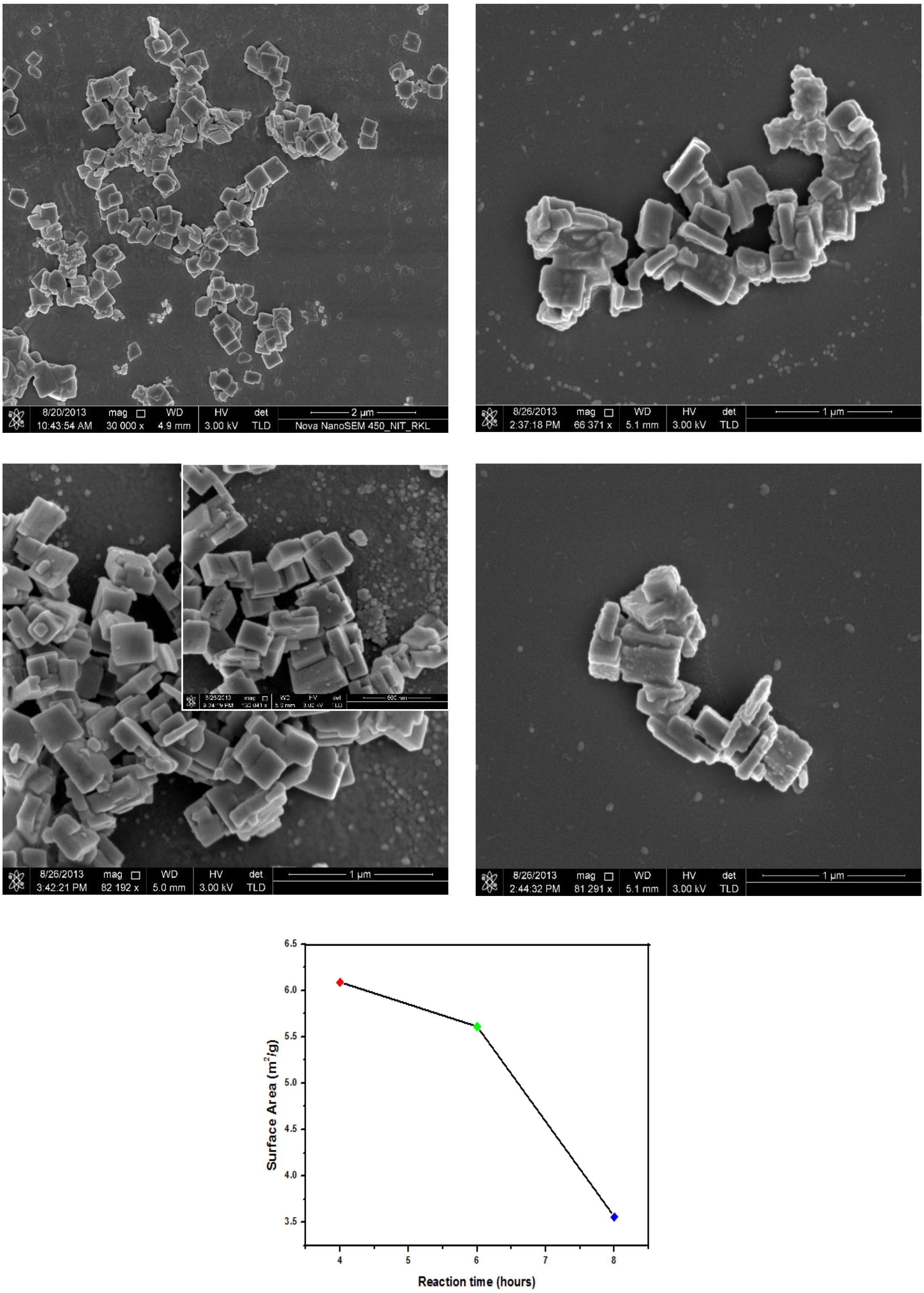

Figure 4.13. FESEM images under experimental conditions of 4M HBF_4 concentration and temperature 180°C for (a) 2hours, (b) 4 hours, (c) 6 hours and (d) 8 hours time duration and (e) BET surface area vs. time plot.

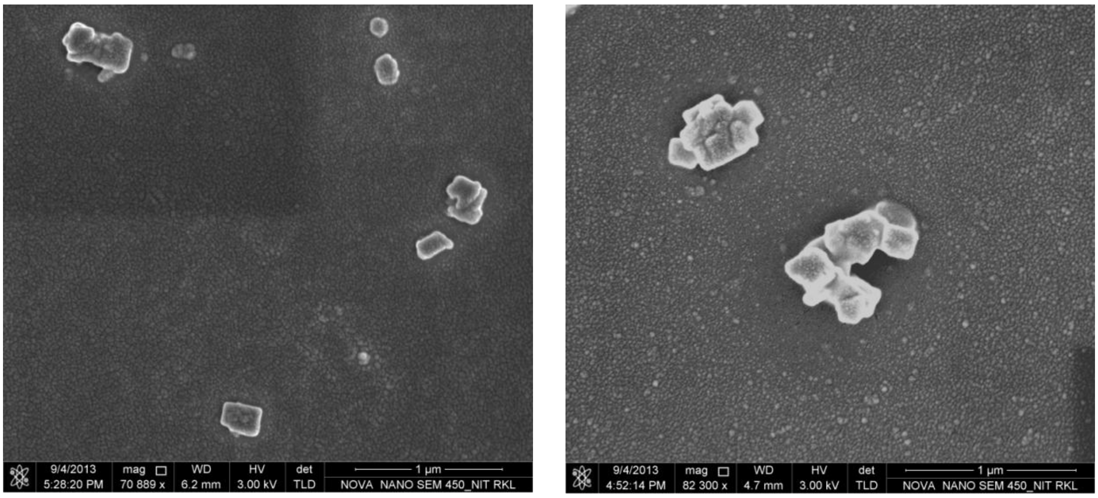

Figure 4.14. FESEM images under experimental conditions of 4M HBF_4 concentration for 6 hours at (a) 170°C and (b) 190°C temperature.

Figure 4.15 represents the TEM micrograph including the HRTEM image and SAED pattern for WO_3 nanocuboids. Figure 4.15a shows soft agglomerated distinct nanocuboid morphology of WO_3 nanoparticles with an average particle length of 140 nm and width of 120 nm. The topographical features reveal that the particle edges are imperfect, which is attributed to the effect of certain tilting angles of individual cuboid particles, whereas the TEM of plate morphology exhibits perfect edges, as reported by Su et al. [37]. Figure 4.15b represents the HR-TEM image of a single nanocuboid. The image clearly shows the resolved lattice fringes in the visible range, indicating its single crystalline nature. The lattice distance is found to be 0.36 nm which can be readily indexed to the (002) plane of monoclinic WO_3 nanocuboids. The value calculated also resembles the value calculated from the X-ray diffraction pattern, which indicates the tentative growth of the particle along this crystal plane. Figure 4.15c shows the selected area electron diffraction (SAED) pattern of a single crystalline WO_3 nanocuboid. In general, h = 0, k = 0 and l = x (where x = 1, 2 or 4) planes restrict the 3D growth pattern and develop 2D plate-shaped morphology [38]. However, the TEM illustration depicts that the highly crystalline WO_3 exhibits an excellent growth phenomenon along the [002] direction to form cuboid morphology.

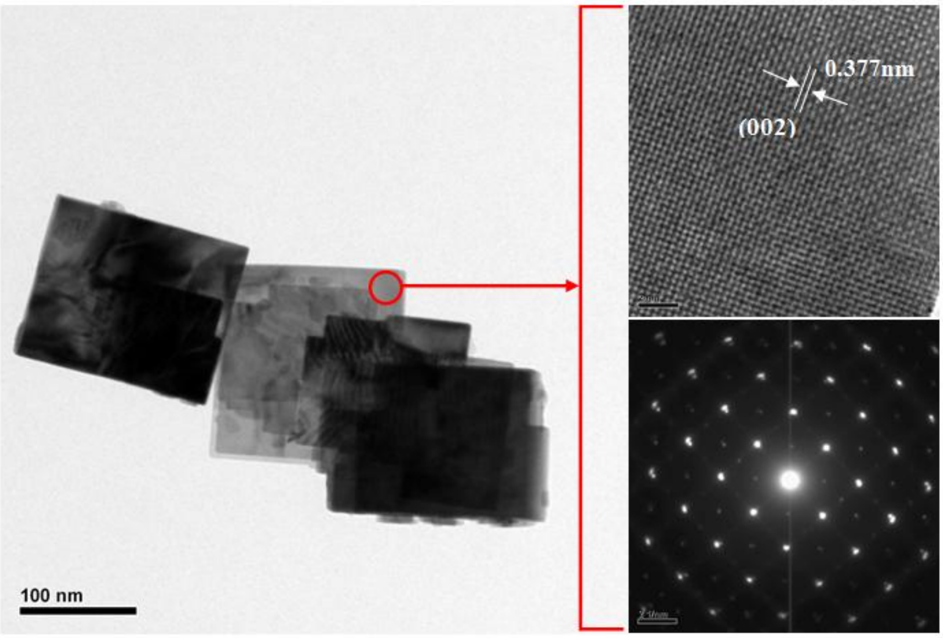

Figure 4.15. TEM analysis of WO_3 Nanocuboids: (a) morphology, (b) d-spacing and (c) SAED pattern.

4.1.2.5. UV-DRS and Band Gap Calculation

Band-gap energy of the selected powder is measured from the UV-vis diffuse reflectance spectra. The measured diffuse reflectance spectra (Figure 4.16) have been used for the estimation of band-gap energy from the Tauc plot. The procedure for calculation is similar to that mentioned in Section 4.1.7. Band gap energy is calculated after synthesis at different conditions. For example, 2 M HBF_4 concentration at 180°C for 4 hours with triclinic WO_3 structure, 3 M HBF_4 concentration at 180°C for 4 hours with hexagonal WO_3 structure, 4 M HBF_4 concentration at 180°C for both 4 and 6 hours with monoclinic WO_3 structure are considered for the band-gap measurements. The band gap energy of triclinic and hexagonal crystal structures is calculated to be 3.25 eV and 2.85 eV, respectively, as illustrated by the 3.09 eV value for a hexagonal structure in previous report [39]. A nearly equal range of band-gap energy of 2.75 eV is found for both 4 and 6 hours treated monoclinic WO_3 nanocuboids without a significant effect of crystalline water.

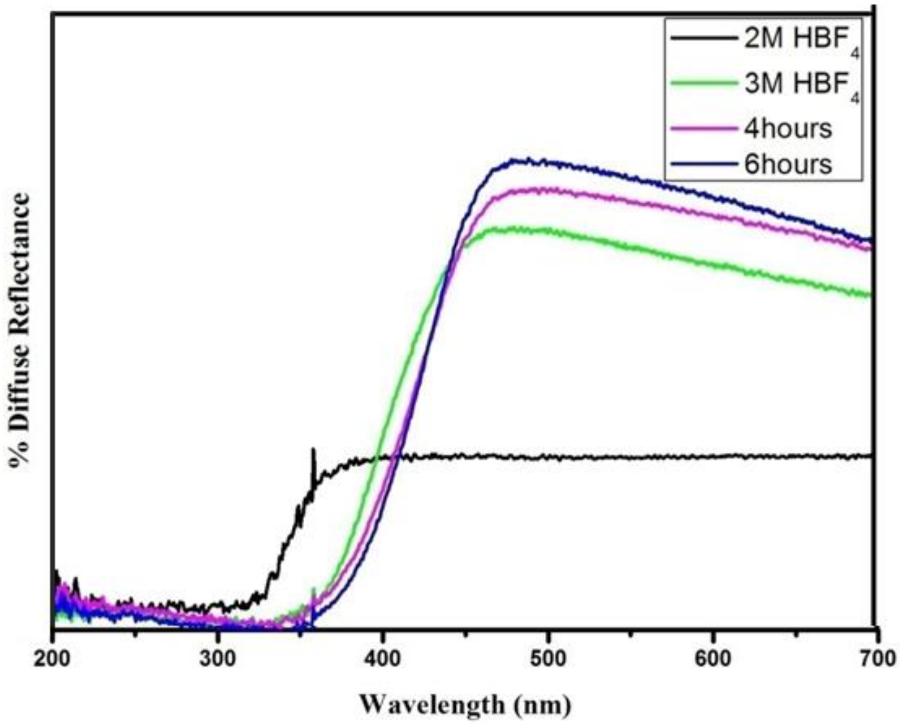

Figure 4.16. UV-DRS of 2 M HBF_4, 3 M HBF_4, 4 hours and 6 hours.
(Inset represents the Tauc Plot)

4.1.2.6. Comparative properties of Monoclinic WO_3 Nanoparticles

The physical properties of the synthesized monoclinic WO_3 nanopowders have been tabulated in Table 4.1. It is well observed that co-precipitation follows a two-step process to achieve final nanopowders without ease of morphological development. Moreover, tuning of material becomes difficult due to high temperature calcination step that leads to compromise with the surface area of the nanoparticles. However, hydrothermal process eases the formation of dimensional WO_3 nanopowders via one step processing. The low temperature processing during hydrothermal reaction makes it a more feasible methodology in perspective of particle size, morphology and surface area. This shows that hydrothermal methodology has certain advantages over co-precipitation method.

Table 4.1. Physical properties of Monoclinic WO_3 Spherical, Rod and Cuboid Nanoparticles

Morphology	**Number of Processing Steps**	**Process Temperature (^oC) & Time**	**Particle size (nm)**	**Surface Area (m^2/g)**
Spherical	2	500^{o}C / 5 min	50 nm	9.91
Rod	2	500^{o}C / 5 min	L=140 nm W = 40 nm	5.16
Cuboid	1	180^{o}C / 6 h	L= 140nm W= 120 nm T = 85 nm	5.41

4.1.2.7. Summary

In this method, hydrothermal method is chosen to develop three-dimensional anisotropic WO_3 nanostructures. Fluoroboric acid has been chosen as an active structure directing reagent for dimensional growth of nanoparticles. Initial variation of HBF_4 concentration at a temperature of 180^{o}C and time of 4 hours follows triclinic WO_3 to hexagonal WO_3 to monoclinic WO_3 phase transformation to obtain WO_3 nanocuboids from sodium tungstate base precursor without stabilization of hexagonal structure. However, single crystal monoclinic and cuboid tungsten trioxide develops through orthorhombic tungstite to monoclinic WO_3 at an optimum fluoroboric acid concentration. Hydrothermal time, temperature and structure directing reagent concentration have significant influence in achieving desired phase and morphology.

4.1.3. Hydrothermal assisted WO_3 Nanofibers

One-dimensional (1D) nanostructures of tungsten trioxide include nanowires, nanotubes, nanofibers, nanorods and nanoribbons which offer the best morphology for most of the electro-functional devices [40, 41]. They have attracted considerable attention due to their dimensional confined transport phenomena. A wide literature review shows that sulfates, chlorides and some organic acids have effective structure directing competence for growth of one-dimensional WO_3 nanostructures [42, 43]. Thus, the basic privilege of this research work is to disclose the synthesis technique of high surface area hexagonal WO_3 nanofiber.

4.1.3.1. Influence of processing conditions on crystal structure

In the beginning the experimental parameter has been chosen to produce WO_3 nanofibers with optimum crystallinity on varying the stoichiometric to high molar concentration of NaCl under constant hydrothermal temperature of 180^{o}C and 12 hours duration. Selection of such duration is to ensure the formation of pure hexagonal WO_3 phase in alkaline halide and optimum hydrothermal condition [40]. All the XRD pattern of the synthesized powders under condition of hydrothermal temperature 180°C and time 12 hours duration and varying concentration (2–5 M) has shown hexagonal crystal structure for all different NaCl molar concentrations. All XRD pattern has been found to match well with the JCPDS Card No. 75-2187 of WO_3 hexagonal crystal structure. Although, all the crystal structures are identical, but there has been a change in the morphology upon varying the concentration. WO_3 nanofiber morphology has been obtained at 4.5 M NaCl concentration; however, agglomeration is attributed to the higher concentration. Since, there is no change in the crystal phase, 4.5 M NaCl concentration becomes the optimum condition to obtain WO_3 nanofibers. The morphological growth phenomenon with varying NaCl concentration has been discussed in a later section. Literature suggests hexagonal WO_3 is a metastable phase, but recent selected process condition reveals the stable hexagonal phase formation with respect to NaCl concentration only. Thermodynamically stable crystal structures are typically close packed, whereas metastable oxide phases have open lattices that promote very high diffusion rates for intercalating ions. In this perspective, time variation 2 to14 hours with increment of 2 hours has also been encountered and kept constant other parameters. Interestingly, just only transparent solution without any solid mass appears after 2 hours hydrothermal treatment of sodium tungstate, 4.5 M NaCl solution at 180°C, but time increment yields hexagonal phase. There has been no change found in the crystal structure with respect to the time variation after 2 hours. All XRD pattern is found to have hexagonal crystal structure matching well with JCPDS Card No. 75-2187. The final processing time has been optimized from their morphology, since, hexagonal WO_3 nanofiber has spacious tunnelling zone for cation intercalation and plausible effective connectivity within nanofibers after coating on the glass substrate. Detailed morphological analysis with respect to different processing conditions revealed the formation of WO_3 nanofibers at 12 hours duration which is discussed in the next section. A targeted reaction is never complete until it overcomes the potential energy barrier required to complete the reaction, and therefore all reactions are carried out at an optimum hydrothermal temperature say 180°C. But, process tuning is needed and hence an additional temperature influenced study has been further carried out to justify the minimum process temperature under 4.5 M NaCl concentrations for 12 hours, and their XRD pattern is shown in Figure 4.17.

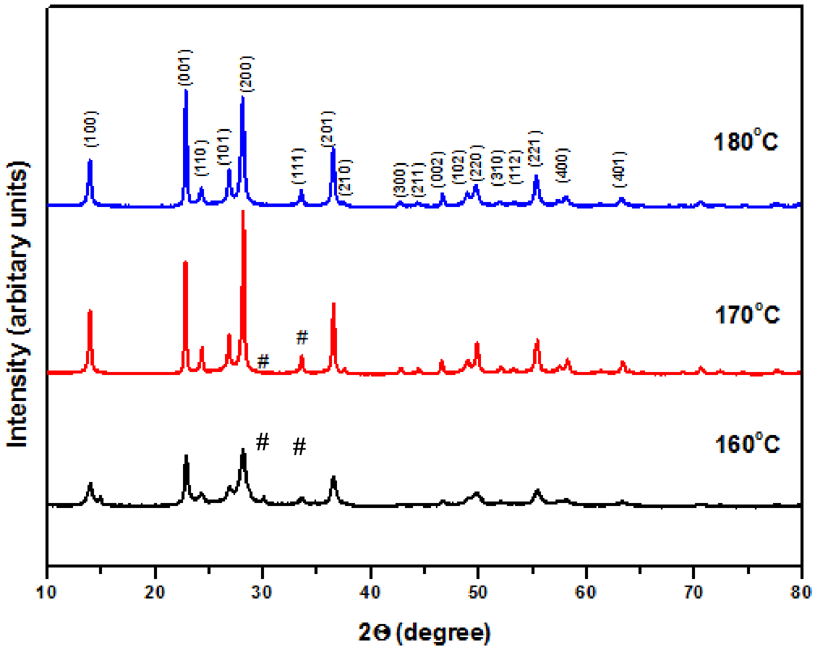

Figure 4.17. XRD patterns on effect of temperature of hydrothermally synthesized WO_3 nanoparticles at 4.5M NaCl concentration for 12 hours.
(# represents anorthic crystal structure)

A difference in the crystal structure is observed at lowest temperature 160°C which develops a mixture of hexagonal and anorthic tungsten oxide; however, pure hexagonal phase is obtained at 170°C and remains constant also at 180°C. The XRD pattern with indexed peak has been shown in the figure. In actual practice, the partial reversible polymorphic phase transformation of WO_3 is also reported in Section 4.3.

4.1.3.2. Rietveld Refinement of optimized WO_3 Nanofibers

Rietveld refinement clarifies the formation of WO_3 hexagonal phase, when synthesized at an optimum condition for 180°C, 4.5 M NaCl concentration for 12 hours. The powders exhibit hexagonal crystal structure as confirmed from Rietveld profile fitting method and found a = 7.298, b = 7.298, c = 3.899Å, $\alpha = 90^o$, $\beta = 90^o$, $\gamma = 120^o$ with space group: P6/mmm according to PCR file code: 1004057 (Figure 4.18) [44]. The refinement gave the residual statistics as follows: $R_p = 9.94$, $R_{wp} = 12.8$ and $\chi^2 = 12.8$, respectively. In the above outlook and choice of interest, the optimized condition for the synthesis of hexagonal WO_3 nanofibers is chosen as 4.5 M NaCl molar concentration at hydrothermal temperature 180°C for the duration of 12 hours. However, characteristic morphological analysis is required to support the synthesis process optimization parameters, since high surface area nanofibers presume to provide more mutual interconnectivity during coating.

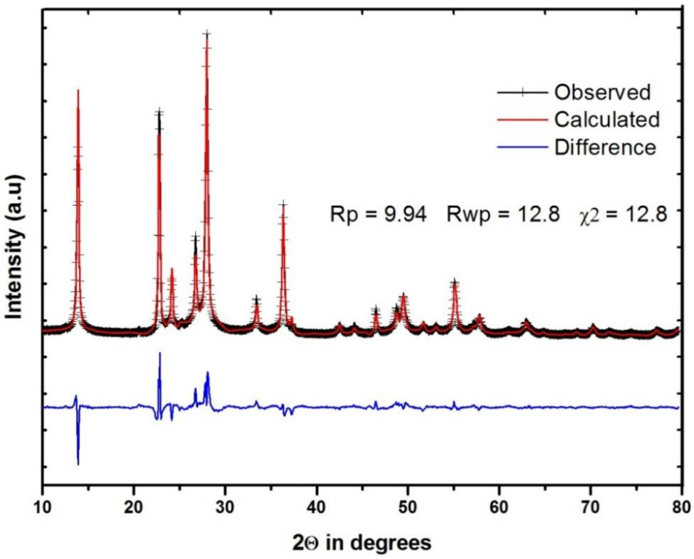

Figure 4.18. Rietveld Refinement of optimized WO_3 Nanofibers at 180°C with 4.5 M NaCl concentration for 12 hours.

4.1.3.3. Effect of process parameters on morphology

Nucleation and growth are simultaneous phenomenon and hence, critical process optimization is worthwhile to control the desired morphology, crystal structure and their crystallinity. In the earlier section, the hexagonal crystal structure and plane growth process has already been explored, herein; a discussion on WO_3 nanofiber (high aspect ratio) starting from nuclei via intermediate less aspect ratio nanorod formation mechanism supports the background of process selection parameters. Thus, influence of NaCl concentration, time and temperature on particle size and geometrical features are represented and discussed chronologically. Low concentration 3.5 M NaCl at 180°C for 12 hours initiates the formation of agglomerated nanorods and thereof bundles, but their dispersibility enhancement is further noticed with sacrificing surface area when NaCl molar concentration is gradually increased from 4 to 5 M (Figure 4.19). An optimum 4.5 M NaCl concentration develops high aspect ratio (c/a ~ 5) nanofibers with surface area $25 m^2/g$, which is lower than the particles obtained at 4 M NaCl, but slight higher than for 5 M concentration. Intermediate concentration develops a discrete nonconforming plate like particles, because of insufficient availability of Na^+ ions, whereas, preferential growth nanofiber is evident when concentration enhancing to 4.5 M. The average particle size is found to be length ~256 nm and thickness ~30 nm, respectively. However, we have found that further concentration increment has no distinct influence on the final morphology of WO_3 nanofibers.

Figure 4.20 shows the effect of the hydrothermal duration on the fibrous morphology of WO_3. Hydrothermal duration of 4 hours and 6 hours initially develops rod like morphology with some non-uniform plates. Although, all the powders have hexagonal crystal phase, but initiation of nanofiber formation started from 8 hours duration, and almost uniform nanorods are seen at 10 hours duration. Growth of the particles to form nanofibers is observed after10 hours only. Uniform but agglomerated bundle of long nanofibers has observed for the duration of 14 hours.

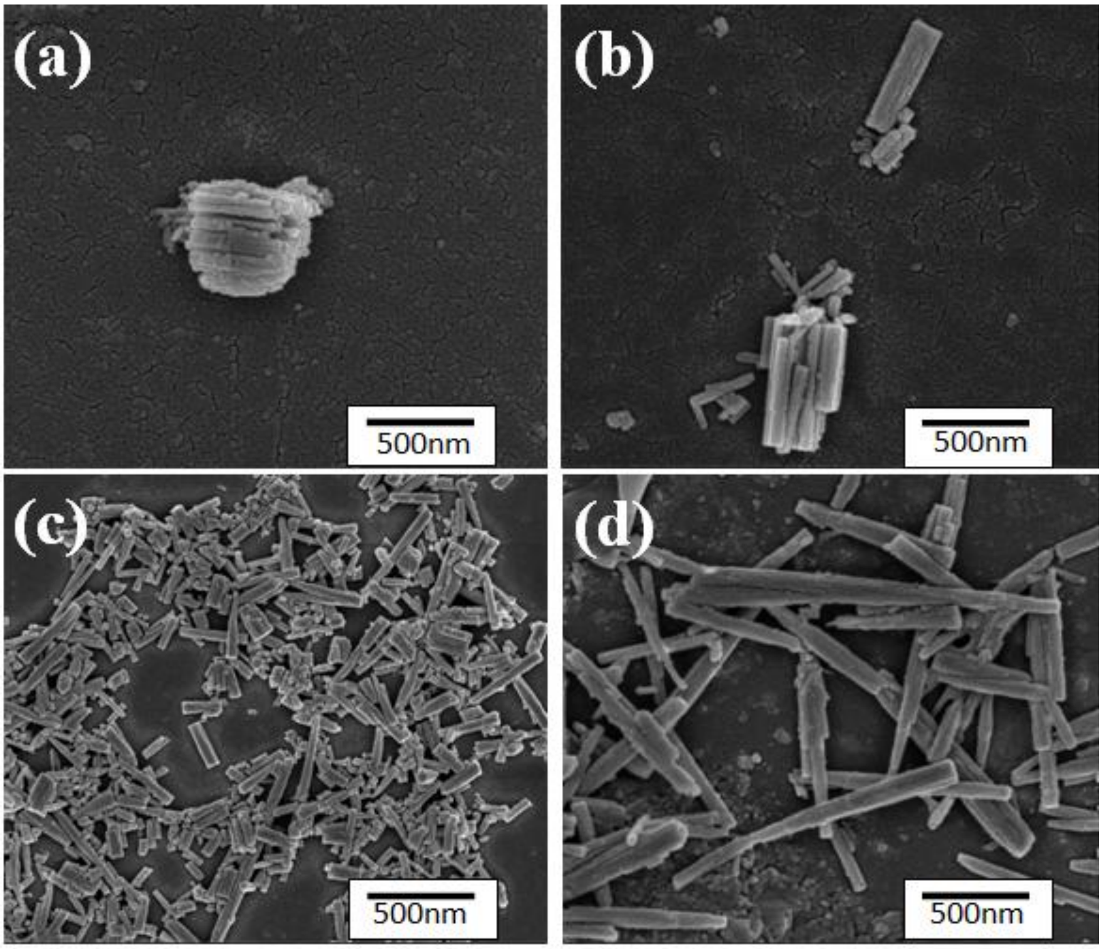

Figure 4.19. FESEM images of WO_3 nanoparticles with variant NaCl molar concentration: (a) 3.5 M, (b) 4 M, (c) 4.5 M and (d) 5 M at 180°C for 12 hours time duration.

Figure 4.21 represents the effect of low temperature range from critical temperature 180°C. A mixture of particles with spherical, plate and rod shaped morphology depicts at 160◦C, whereas agglomerated rod like particle is attributing at temperature of 170°C. This observation reveals that 180°C is the minimum required temperature for the growth of nanofibers.

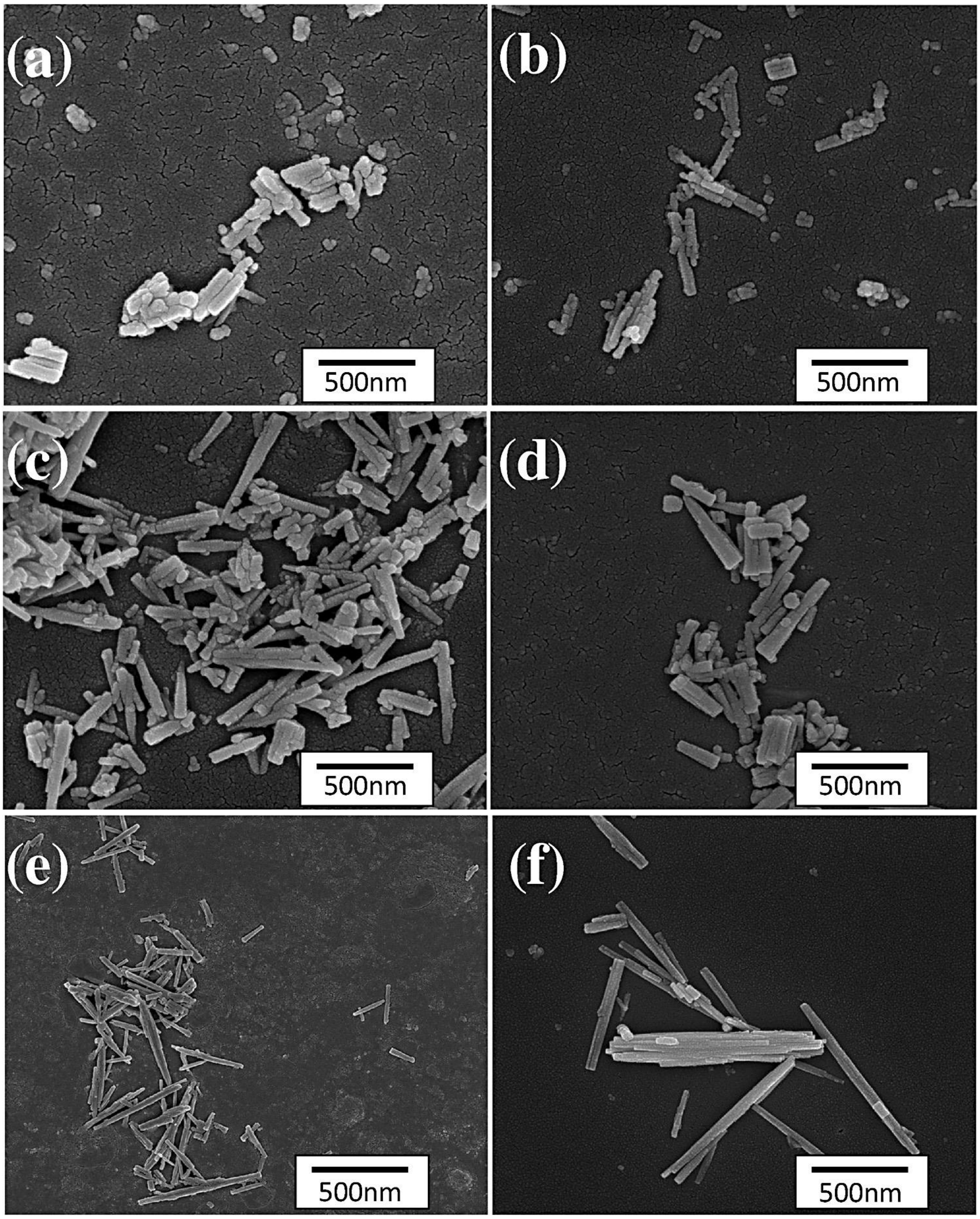

Figure 4.20. FESEM images of WO_3 nanoparticles with variant time duration: (a) 4hours, (b) 6 hours, (c) 8 hours, (d) 10 hours, (e) 12 hours and (f) 14 hours for 4.5 M NaCl concentration at 180^{o}C.

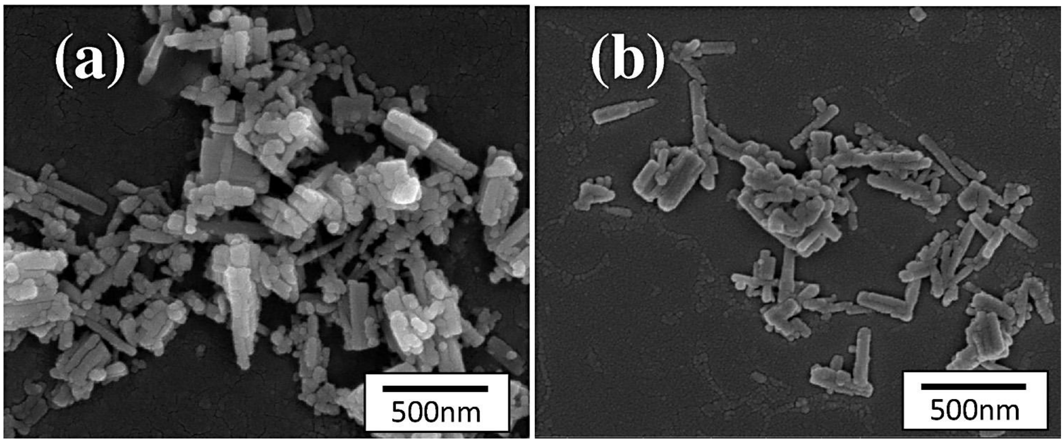

Figure 4.21. FESEM images of WO_3 nanoparticles with variant time temperature: (a) 170^{o}C and (b) 190^{o}C with for 4.5 M NaCl concentration for 12 hours.

4.1.3.4. Morphology formation mechanism

Formation of nanofibers is not a single step process; somewhat it follows sequential formation of spherical nuclei and their formation to plate and rod and finally fibers. Different state has different dispersion efficacy with respect to processing condition. The four-coordinated window structure of WO_3 adsorbs Na^+ ions, but the surface of WO_3 contains many hydroxyls groups which have more interactions with H^+ ions than Na^+ ions due to hydrogen bonding at lower pH. The layered structure of tungsten trioxide is assumed to self-assemble through an electrostatic link between Cl^- ions and H^+ ions with the adsorbed Na^+ ions between the layers. Electrostatic repulsion between Na^+ and H^+ ions occur, which causes folding of the layered structure forming bundle of fibers. Na^+ ions can be presumed to act as a bonding bridge between the growth units to form crystal nuclei. Stabilization of hexagonal WO_3 requires only certain amount of Na^+ ions, but morphology stability is strongly influenced by the number of Na^+ ions. Similar growth mechanism has been found for WO_3 nanowires/nanorods explaining sulphate induced growth mechanism through hydrothermal method [45]. Moreover, high ionic strength of the precursor solution has also an important role to play for the dispersion of the particles. Dispersion of particles increases with an increase in the ionic strength as similarly reported for dispersion of TiO_2 nanoparticles [46].

Transmission electron microscopic technique is employed to gain further insight into the morphology, d-spacing and crystallinity of WO_3 nanofibers (Figure 4.22).

Figure 4.22a shows typical microstructure consists of soft agglomerated distinct nanofibers WO_3 with an average particle length ~ 250 nm, and diameter ~ 25 nm. A clear observation reveals that the orientation of these fibers is from many self organized elongated subunits combining to form ultimate assembled nanofibers. The particles are observed to have partially broken due to the ultrasonication process during sample preparation. Figure 4.22b represents the HRTEM image of a single nanofiber. From the HRTEM image of a nanofiber, it can be seen that the lattice spacing is about 0.384 nm between the adjacent lattice planes of the WO_3 nanofiber, which perfectly matches with the (001) plane of the hexagonal WO_3 crystal structure. These findings suggest that WO_3 nanofiber is a single crystal grown in the direction of [001] crystal plane. Figure 4.22c shows the Selected Area Electron Diffraction SAED) pattern of a single crystalline WO_3 nanofiber. The pattern shows an ordered array of spots along with the concentric circles which depict the crystalline nature of the nanofibers as similar observation noted by XRD pattern.

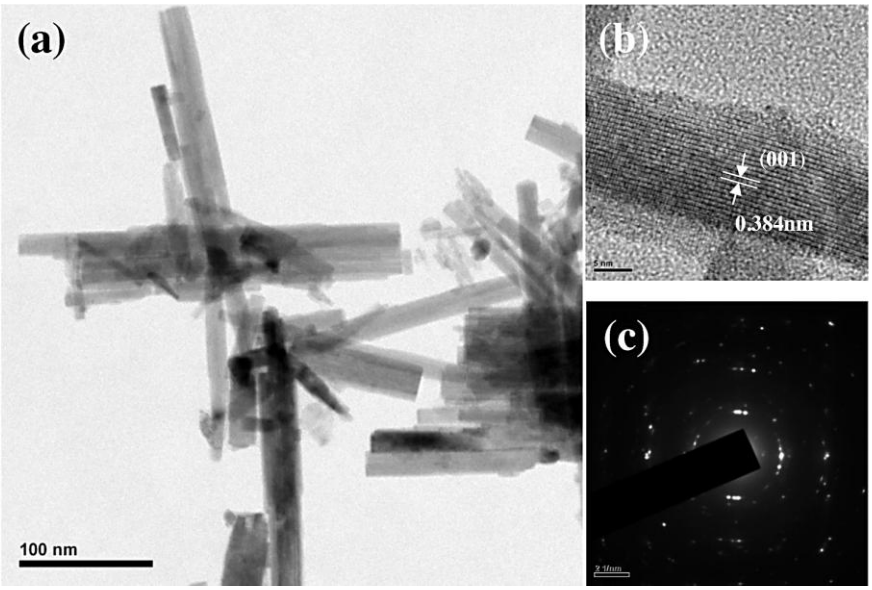

Figure 4.22. TEM analysis of WO_3 nanofibers; (a) morphology, (b) d-spacing from HRTEM and (c) SAED pattern.

4.1.3.5. UV-DRS and Band Gap Calculation

The determination of the band gap energy for the selected nanofibers prepared under different processing condition is measured by UV-Vis diffuse reflectance and represented in Figure 4.23. Different processing conditions such as 4.5 M NaCl at 160°C, 170°C and 180°C for 12 hours are considered for the band gap measurements as other processing conditions showed no difference in the crystal structure upon variation. The representative inset 'Tauc plot' is calculated following similar equations mentioned in Section 4.1.7. The linear slope of the curve in the Tauc plot is extrapolated to zero reflectance and finally obtained the band gap, which varies with respect to processing conditions in the range of 2.75 eV to 2.85 eV; more or less (2.7 to 3.3 eV) similar with reported band gap energy for WO_3 nanoparticulates, films and bulk powders [47]. It is worthwhile to mention that the insufficient thermal energy at the temperature of 160°C is forming anorthic tungsten oxide but has a similar magnitude of band gap energy.

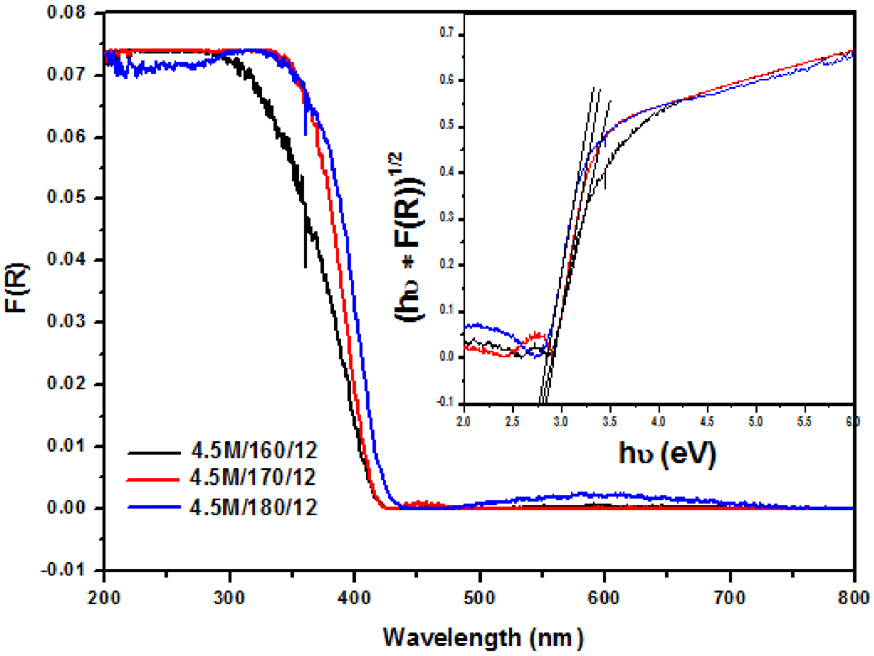

Figure 4.23. UV-DRS of WO_3 nanofibers with respect to temperature effect @ 160°C (4.5 M/160/12), 170°C (4.5 M/170/12) and 180°C (4.5 M/180/12) under 12 hours duration with 4.5M NaCl concentration (Inset represents the Tauc plot)

4.1.3.6. Summary

Growth of anisotropic one dimensional nanostructure with metastable phase of WO_3 has been achieved using sodium chloride as structure directing reagent. One dimensional pure hexagonal WO_3 nanofiber has been successfully grown in the presence of optimum hydrothermal temperature of 180^oC for 12 hours with 4.5 M NaCl concentration. Temperature variation observes the presence of both hexagonal and anorthic crystal phase at lower temperature that stabilizes with pure hexagonal phase at 180^oC. Morphological analysis with respect to above perspectives predicts formation of nanofibers via spherical nuclei to plate to rod to fiber morphology. The metastable hexagonal form of WO_3 requires only certain amount of Na^+ ions, but stability of morphology is strongly influenced by the number of Na^+ ions. Particular directional growth and crystal structure develops hexagonal structure with no significant change in the band gap for different processing conditions.

4.1.4. Process Optimization of ZnO Quasi-fibers

In this section, a discussion on synthesis of ZnO nanocrystals has been carried through a solution combustion method. Optimization of phase and morphology has been done upon varying the oxidizer/fuel ratio, time and temperature.

4.1.4.1. Process Optimization of ZnO Quasi-fibers

Powder X-ray diffraction pattern confirms the crystal structure, crystallinity and phase content of ZnO powders as shown in Figure 4.24. Primarily, experiments are designed to determine the crystal structure and phase purity with respect of varying oxidizer to fuel ratio under constant temperature of 450^{o}C and time of 30 min. All the XRD patterns can be indexed to pure wurtzite crystal phase of ZnO matching well with JCPDS# 79-0206 having space group P63mc with $a = b = 3.2499$ Å, $c = 5.2066$ Å and $\alpha = \beta = 90°$ and $\gamma = 120°$. Fuel deficient ratio (O/F = 4/1), stoichiometric ratio (O/F = 5/1) and fuel excess ratio (O/F = 6/1) shows no change in the crystal phase but a change in crystallinity is observed for the powders, as presented in Figure 4.24a. High crystallinity has been observed for the powders obtained from combustion of stoichiometrically considered reactants. Thus, the stoichiometric ratio of oxidizer/fuel has been optimized for synthesis of ZnO powders. The growth of the particle relies on the time dependent isothermal conditions. Therefore, the optimization of formation of pure phase with respect to time at an interval of 10 min has been carried at temperature 450^{o}C with stoichiometric ratio of reactants (Figure 4.24b). Initially, the reactant solution was retained after first 10 min of combustion reaction but after 20 min brown porous powder is observed. The XRD pattern of powder obtained after 20 min shows peak for wurtzite ZnO along with some impurity peak. The time duration of 30 min produces pure ZnO wurtzite phase with no impurity peaks. Further increasing the time shows no characteristic change in the phase and crystallinity. The impurity peak observed has been indexed as '*' in the XRD pattern corresponding to the presence of oxidizer zinc nitrate hydrate (JCPDS# 19-1464). Similar observation was observed at temperatures below 450^{o}C having other parameters constant time at 30 min and O/F = 5/1 (Figure 4.24c). There is a gradual formation of ZnO phase with decreasing oxidizer content from 300^{o}C to 350^{o}C to 400^{o}C, respectively. The impurity peak of zinc nitrate hydrate depicts the incomplete combustion of the oxidizer during the process. It indicates that the combustion reaction with time and temperature less than 30 min and 450^{o}C do not decompose the oxidizer completely. The final ZnO wurtzite phase is obtained at temperature 450^{o}C. The above result suggests that 30 min and 450^{o}C are the minimum requirements for producing pure phase ZnO powders under stoichiometric ratio. Thus, these parameters are taken as optimized reaction parameters. The following observation is further supported by the FT-IR spectra.

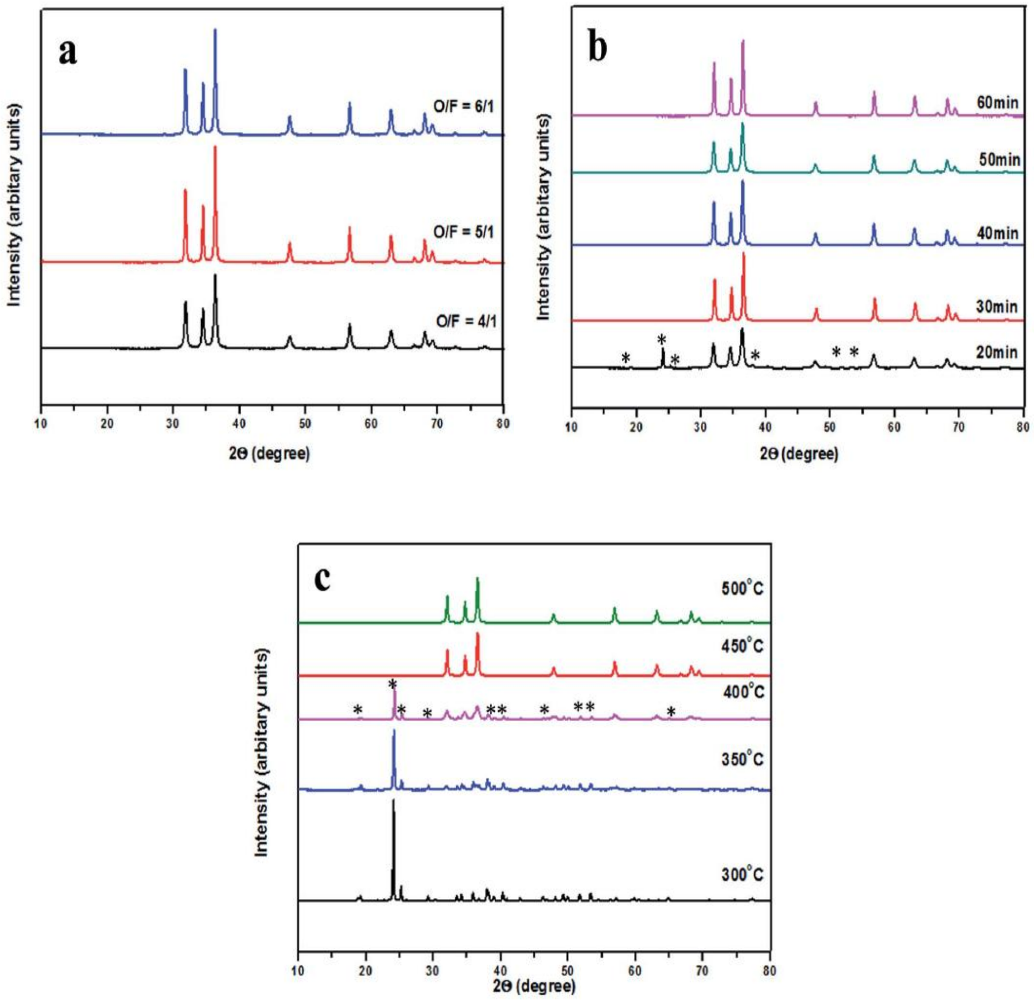

Figure 4.24. Composite XRD patterns: (a) Effect of Oxidizer/Fuel ratio, (b) Effect of time and (c) Effect of temperature.

4.1.4.2. Vibrational Spectral Studies

The presence of functional groups for powders obtained at optimized condition (O/F = 5/1, 30 min, 450°C), at low time/time deficient (O/F = 5/1, 20 min, 450°C) and low temperature/temperature deficient (O/F = 5/1, 30 min, 400°C) has been studied from FT-IR spectroscopy as shown in Figure 4.25. All the powders had one common sharp absorption band at lower wavenumber of 536.86 cm^{-1} corresponding to the vibrations from Zn–O group. The broad absorption peak at about 3396.61 cm^{-1} corresponds to the stretching vibration of O–H mode from chemisorbed or physisorbed water molecules on the powders obtained from deficit of both time and temperature. The sharp absorption peaks observed at 1614.86 cm^{-1} & 1325 cm^{-1} can be attributed to the asymmetric and symmetric stretching from carboxyl group (C=O). The corresponding vibration peak at 818.83 cm^{-1} is assigned to the presence of NO_3^{-1} ions. The presence of NO_3^{-1}, C=O and O–H group confirms the incomplete decomposition of nitrate and carbonaceous matter from organic acid after the combustion reaction. Pure ZnO has no other functional groups present other than Zn–O. This supports the formation of pure ZnO without any impurity content at stoichiometric ratio [48].

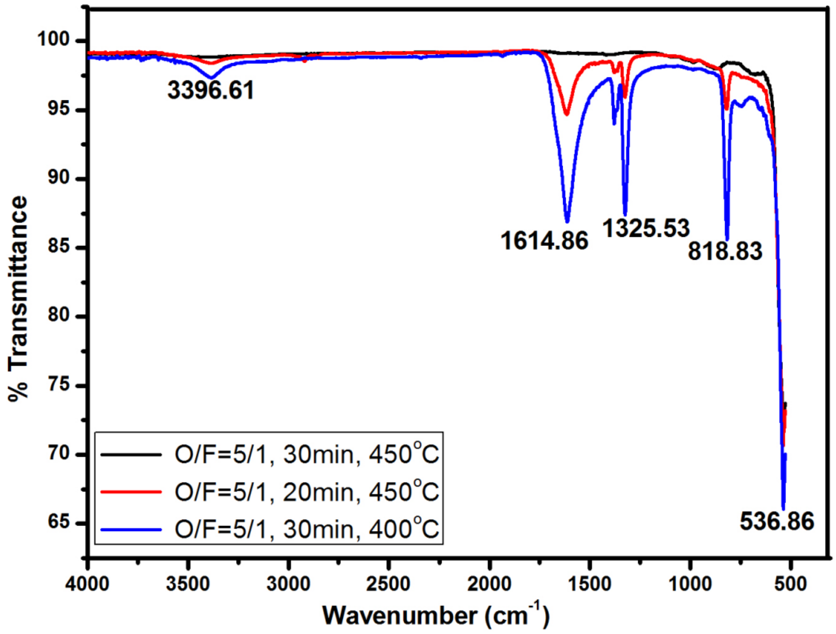

Figure 4.25. Composite FT-IR pattern of ZnO nanocrystals under different conditions.

4.1.4.3. Morphological analysis and Formation mechanism

The morphology optimization of ZnO has been studied by FESEM and TEM imaging. XRD analysis suggests the stoichiometric ratio to be the optimum condition for the development of an adequate and high crystalline crystal structure of ZnO. The FESEM images obtained for powders under the series of varying reaction parameters of oxidizer/fuel ratio, time, and temperature has been presented in Figure 4.26–4.28. Figure 4.26 represents the images of the powders obtained under fuel deficient (Figure 4.26a), stoichiometric (Figure 4.26b) and fuel rich ratio (Figure 4.26c). Unlike any change in the XRD pattern, no major change in the morphology was observed. Combustion reaction produces distinct rod shaped particles with high dispersibility observed for stoichiometrically obtained ZnO powders. However, change in fuel ratio shows some influence on the specific surface area. The surface areas obtained for the fuel deficient, stoichiometric content and fuel rich conditions are 20.19, 17.8 and 16.9 m^2/g, respectively. The highest and lowest surface area value corresponds to small particles for fuel deficient and large agglomerated particles for fuel rich content. The average particle size of stoichiometrically synthesized ZnO quasi-fiber is ~2.8 µm in length and ~0.5 µm in width.

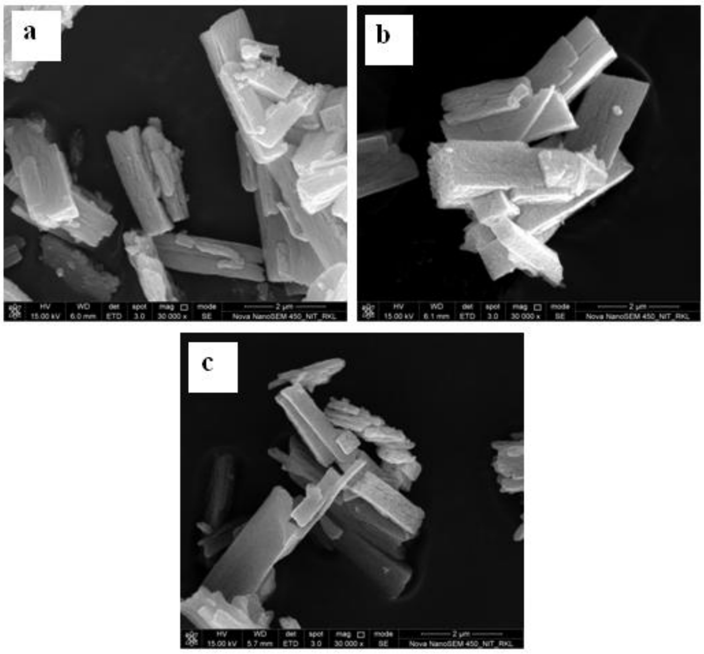

Figure 4.26. FESEM images with respect to Oxidizer/Fuel ratio (a) O/F = 4/1, (b) O/F = 5/1 and (c) O/F = 6/1 at temperature 450°C for 30 min.

Apart from the O/F ratio, growth of particles during combustion process also depends on parameters such as time and temperature. Therefore, particle images corresponding to variation in time has been shown in Figure 4.27. Interestingly, during the first 10 min of reaction, there was only boiling of the solution to form gel. Although rod shaped particles with small spherical and plate shaped particles are observed after 20 min (Figure 4.27a), but impurities are observed in XRD due to incomplete combustion of zinc nitrate. After 30 min of combustion, particles were observed to have soft agglomeration with less uniformity (Figure 4.27b–4.27d). The surface area of particles formed after 30 min with increment of 10 min decreases following the sequence: 15.8 < 11.4 < 9.3 m^2/g, respectively. In accordance to the above result, uniform sized rod particles are formed in minimum time duration of 30 min. Similarly, temperature less than 450°C showed impurity peaks of zinc nitrate but traces of rod shaped ZnO particle is also observed that increases upon the temperature sequence of 300 to 350 to 400°C (Figure 4.28a–4.28c). High temperature led to formation of large agglomerated particles with increased particle size (Figure 4.28d). The surface area of ZnO particles at 500°C drastically decreases to 10.2 m^2/g. Thus, dispersed uniform ZnO quasi fiber particles are formed at 450°C for 30 min with stoichiometric ratio.

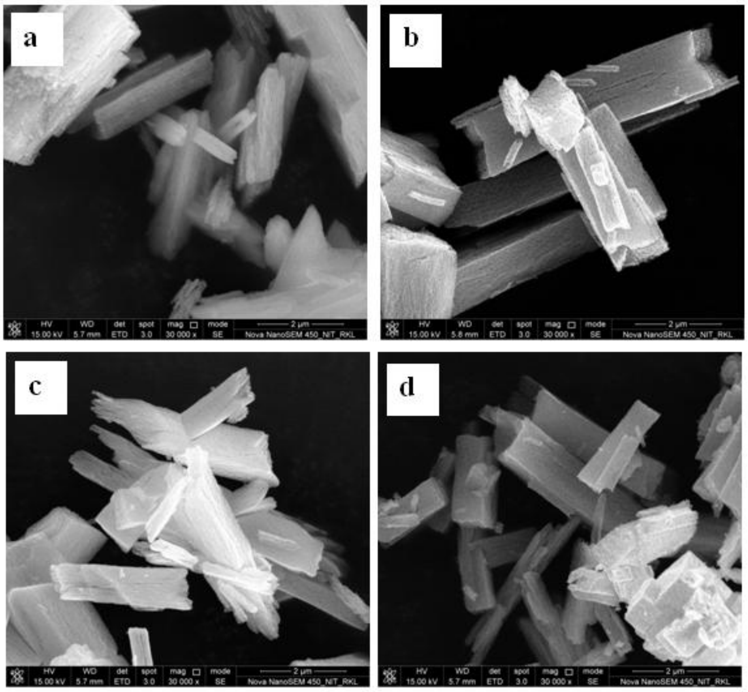

Figure 4.27. FESEM images with respect to time (a) 20min, (b) 40min, (c) 50min and (d) 60min at temperature 450°C with O/F=5/1.

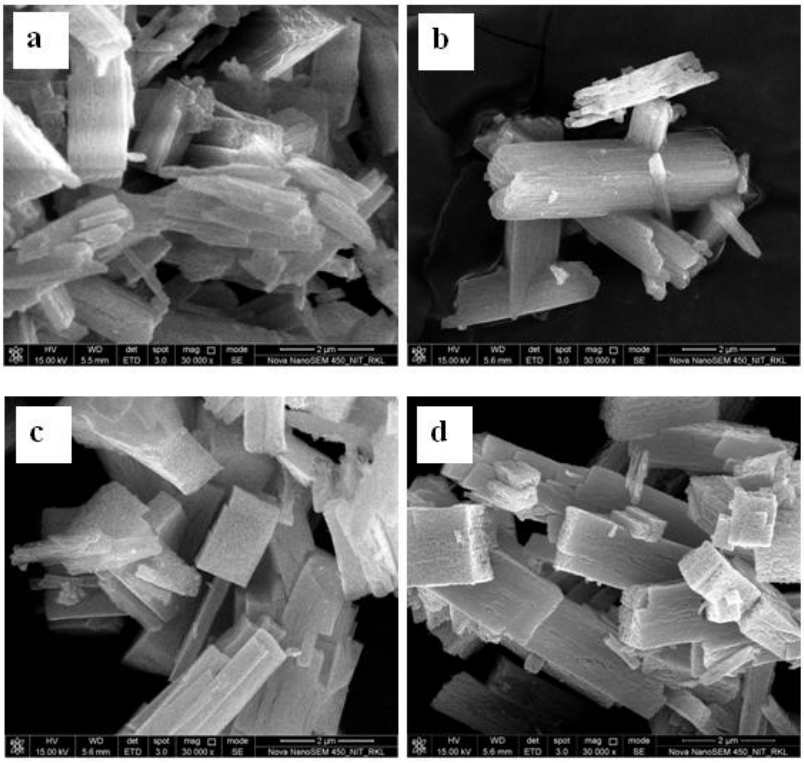

Figure 4.28. FESEM images with respect to temperature (a) 300^{o}C, (b) 350^{o}C, (c) 400^{o}C, and (d) 500^{o}C for 30min with O/F=5/1.

TEM image (Figure 4.29) shows a clear picture of apparent 1-D rod shaped particles that are composed of many small spherical particles forming a quasi-fiber like structure. Low magnification image (Figure 4.29a) shows fiber like particles having average particle size of length ~3 µm and width ~0.5 µm, respectively. High magnification image (Figure 4.29b and 4.29c) shows that individual spherical particles are co-joined to each other during combustion process and aligns to form 1-D structure. The rapid dissolution – recrystallization favors the formation of neck within two particles and thereafter results in the formation of continuous fiber like structure [49]. The spherical particles forming quasi-fiber are found to have average particle size of ~60 nm. The uneven diameter and pore distribution is observed along the longitudinal direction of quasi-fiber ZnO particles. The quasi-fibers are porous in nature as observed from the image. The SAED pattern (Figure 4.29d) shows distinct concentric circles from agglomerated spherical particles depicting high crystallinity of the particles. Similar mechanism has also been illustrated by Sutka et al., whereby formation of 1-D nanostructure is seen through 3D and 2D structures [50].

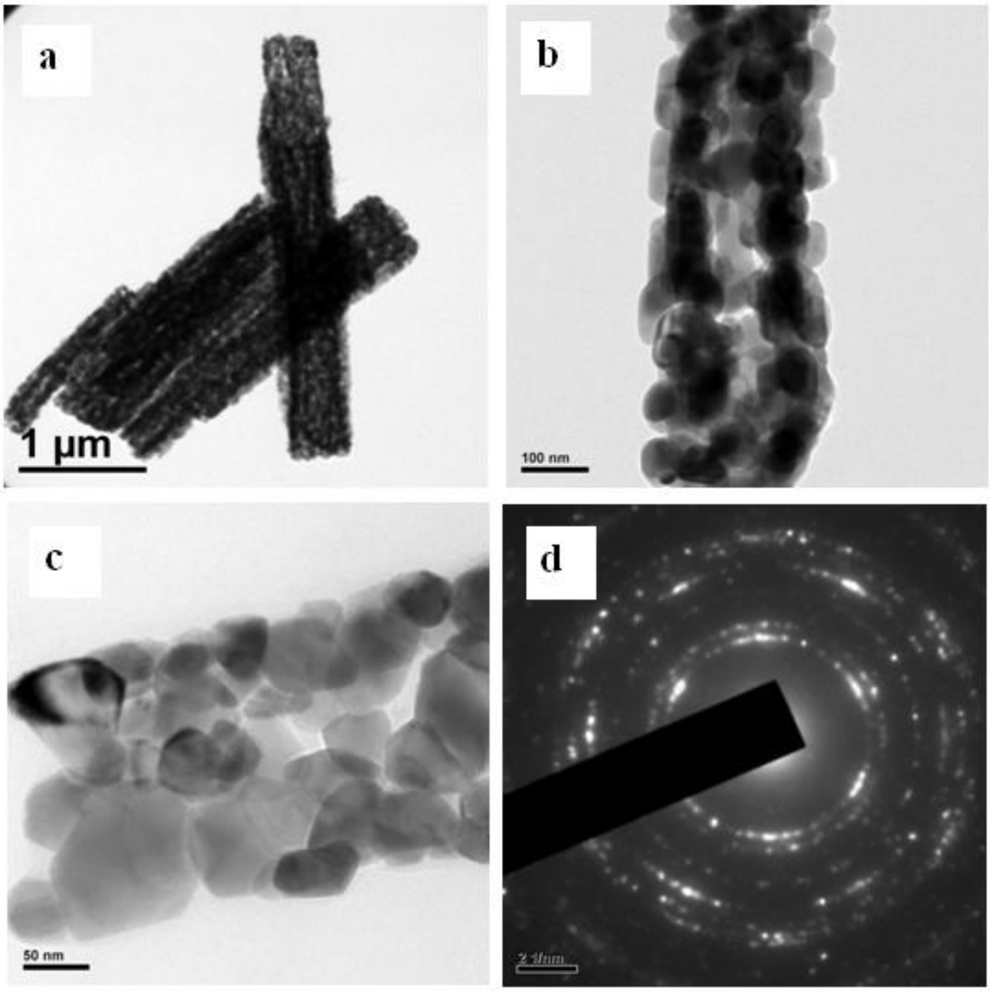

Figure 4.29. TEM images under (a) Low magnification, (b) & (c) High magnification and (d) SAED pattern of optimized ZnO nanocrystals.

4.1.4.4. UV-DRS and Band gap Calculation

The diffuse reflectance spectrum of ZnO has been presented in Figure 4.30 with Tauc plot as the inset representing the energy band gap of quasi fibrous ZnO. Band gap energy is estimated using Tauc plot following similar equation mentioned in Section 4.1.7. The extrapolated linear slope to photon energy gives the band gap energy as shown in inset figure. The band gap energy of ZnO quasi fiber is found to be 2.95 eV, which is consistent with the values reported in the literature [51, 52].

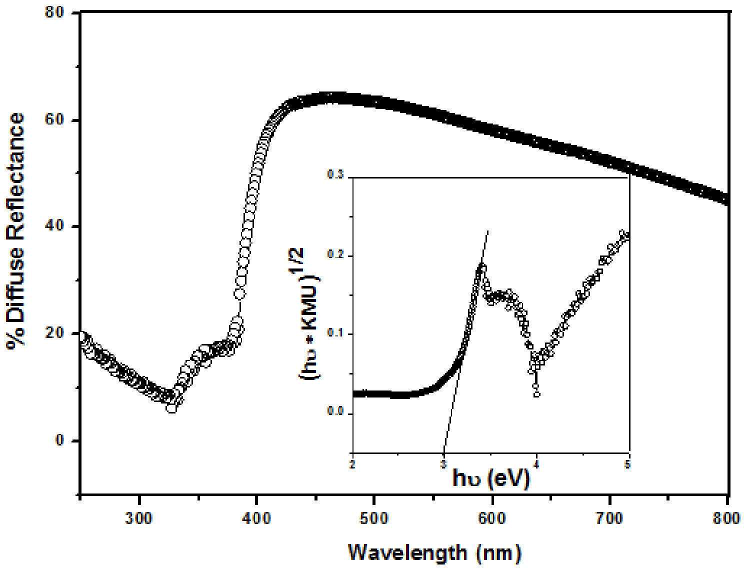

Figure 4.30. UV-Vis Diffuse Reflectance Spectra of optimized ZnO nanocrystals.

4.1.4.5. Summary

Dimensional growth of zinc oxide has been successfully carried by a simple one step solution-combustion method. Highly porous quasi-fibrous zinc oxide is synthesized in presence of zinc nitrate as oxidizer and oxalic acid as fuel. Insufficient combustion time and temperature produces impure zinc oxide due to incomplete combustion of oxidizer. High yield of ZnO photocatalyst is obtained through O/F = 5/1 ratio, 40 min time duration and 450^{o}C temperature during combustion reaction. Pure zinc oxide shows presence of Zn-O bond and no traces of other functional groups from fuel are found.

4.2. Electrochemical Response of WO_3 Nanoparticles

Mostly, the electrochemical measurement has been carried for fabricated WO_3 films prepared via dip/spun coating of peroxo-polytungstic acid on the Indium doped Tin Oxide (ITO) glass substrate and subsequent firing at optimum temperature [53]. Several other strategies like hot wall chemical vapour deposition, thermal evaporation, etc. includes use of sophisticated instrument and operations. Therefore, a great deal of effort has been made for improving the performance of WO_3 films by simple, easy and cost-effective method. It is essential to control the morphology and also surface coating over transparent conducting oxide glass substrate for competent electrochemical response [54].

4.2.1. Electrochromism in Spherical and Rod-shaped WO_3 Nanoparticles

The physicochemical characterization of the synthesized spherical and rod-shaped WO_3 nanopowders has been well discussed in the previous section. In the present section, the influence of morphology on the electrochemical activity of WO_3 nanoparticles drop-coated onto ITO has been reported followed by comparison with dip coated fabricated electrodes.

4.2.1.1. Cyclic Voltammetry of drop coated WO_3/ITO electrodes

The drop coated WO_3/ITO electrodes were prepared for cyclic voltammetry measurements. The optical transparency of spherical WO_3 nanoparticles coated ITO (SWI) glass substrate is found higher than the semitransparent rod-shaped WO_3 nanoparticles coated ITO (RWI) electrode. Cyclic voltammograms (CV) is influenced by the electrochemical response between the range of ±0.5V, scan rate of 50 mV/s and 0.5 M H_2SO_4 electrolyte concentration as shown in Figure 4.31. RWI exhibits high current density of 1.8mA/cm^2 compare to 0.14 mA/cm^2 for SWI films. It is interesting to note that both of the morphologies have near to equal crystallite size and band gap energy but a distinct difference in current density output under identical experimental conditions is observed. Hence, the resultant current density difference can be plausible to (1) adherence efficiency of WO_3 nanoparticles onto ITO surface due to contact geometry and (2) geometrical contact resistance between the film and electrolyte [8, 55].

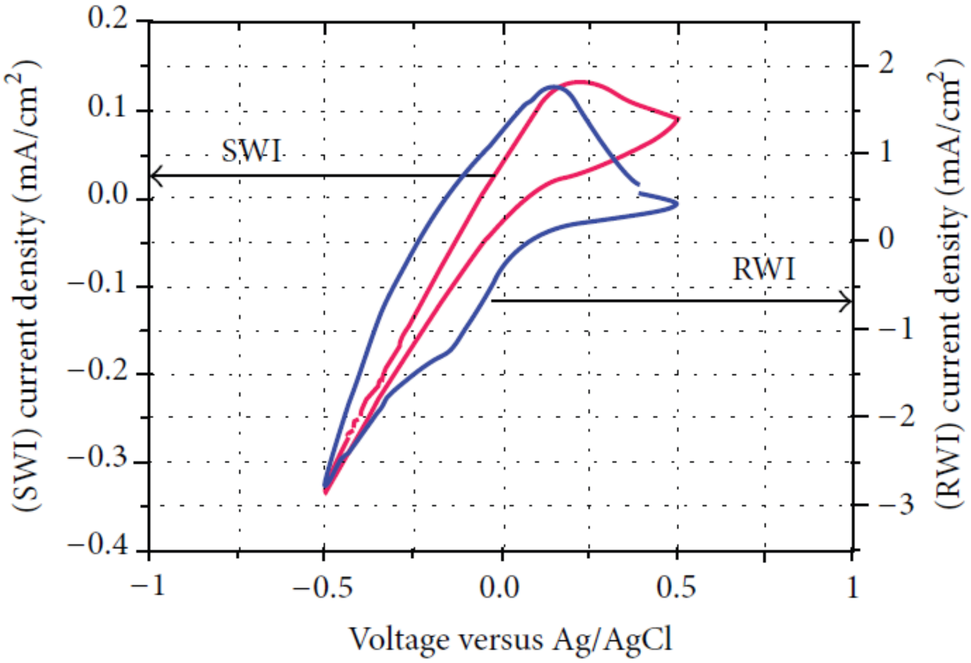

Figure 4.31. Cyclic Voltammograms for drop coated spherical and rod-shaped WO_3 nanoparticles onto ITO substrate under identical voltage and scan rate.

4.2.1.2. Topographical images of drop coated WO_3/ITO electrode

Figures 4.32 represents the top view FESEM images of the SWI and RWI films prepared by drop coating technique to insight the texture and distribution of particles on the surface of ITO glass substrate, respectively. For both the coatings, the morphological texture indicates a rough surface topography. The particles on RWI film is relatively well distributed as compare to SWI film. Particles of SWI film forms island on the surface due to high surface reactivity and their agglomeration tendency, whereas RWI film exhibits continuous structure. And hence the transparency and semi-transparency of SWI and RWI film is quite evident from the images. Hence, the minimum coverage is expected by spherical particles on ITO substrate and at the same time the rod shaped particles favours more contact area and adherence to the substrate than spherical particles, which finally alters the charge transport phenomenon between the film and the electrolyte.

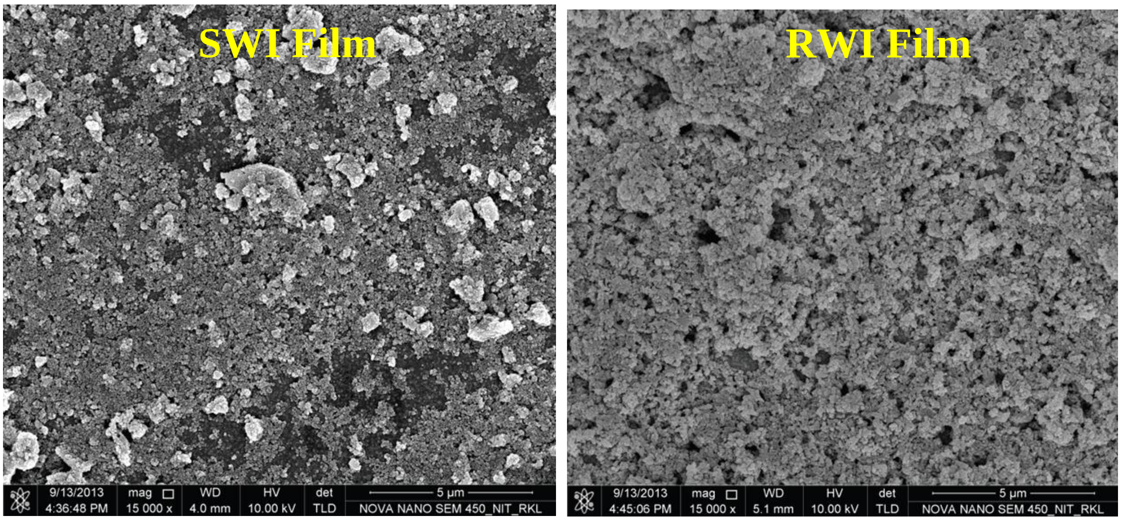

Figure 4.32. Topographical FESEM images of the drop-coated SWI and RWI films.

Furthermore, the geometrical contact resistance, R_c, could be calculated from the slope of anodic and cathodic scans of the film in the electrolyte. Resistance is calculated by applying the equation for (SWI) = (0.2 + 0.5)/(0.14 + 0.33) = 1489 Ω cm^2 and similarly for R_c(RWI) = (0.19 + 0.5)/(1.8 + 0.3) = 280 Ω cm^2 [8]. The contact resistance for RWI is five times less than that of the transparent SWI which enhances the current density. The incomplete RWI current density loop is due to the factors that extraction of hydrogen takes more time than insertion leading to incomplete reversible reactions. On the basis of this observation, the current density raises from initial lower set potential to higher set potential giving high current at saturation potential level [55]. Thus, result suggests that the contact resistance and morphological surface area of film are also important factors for getting fairly good electrochemical response.

Figure 4.33 represents the bare ITO coated glass substrate, rod shaped WO_3 coated ITO (RWI), and electrochromic setup during CV measurement. The colour of the RWI changes from pale yellow to dark blue which attributes to the change from WO_3 to blue tungsten bronze (H_xWO_3) as a result of reduction during the process of proton insertion in acidic medium [56]. The mechanism during electrochemical measurement is as follows:

$$WO_3 \text{ (pale yellow)} + xH^+ + xe^- \longleftrightarrow H_xWO_3 \text{ (dark blue)} \qquad (27)$$

The cathodic peak referred to the extraction of protons and anodic peak insertion of protons. The electrochemical reversibility of the films was observed to be good as its voltammograms were nearly overlapping with each other for repetitive cycles.

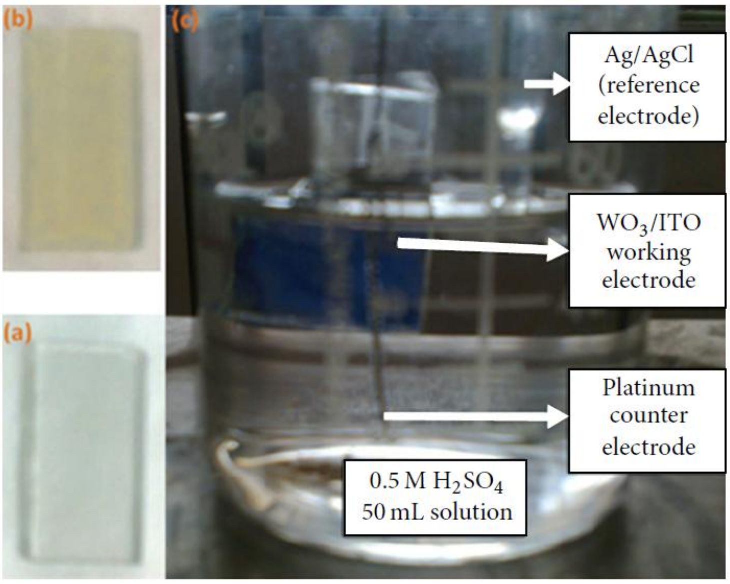

Figure 4.33. Electrochemical setup showing electrochromism during the cyclic voltammetry measurement.

4.2.1.3. Cyclic Voltammetry of dip coated WO_3/ITO electrodes

The dip coated WO_3/ITO electrodes were prepared for comparison. The spherical WO_3 nanoparticles coated onto ITO glass substrate is designated as SWI-D whereas rod-shaped WO_3 nanoparticles coated ITO electrode is designated as RWI-D. Cyclic voltammetry of the fabricated electrode is performed under similar electrochemical conditions as mentioned in section. 4.2.1.1. Cyclic voltammograms (CV) of the dip-coated electrodes are shown in Figure 4.34. A high current density of 2.23 mA/cm^2 is observed for RWI-D compare to 0.39 mA/cm^2 for SWI-D films. The geometrical contact resistances (R_c) of these electrodes were further calculated to understand the conductivity between the electrochromic layer and the electrolyte. The R_c value for SWI-D is calculated to be 972 Ω cm^2 whereas for RWI-D, it is found 272 Ω cm^2. These values are less in comparison to drop-coated fabricated electrodes. A better understanding of the high current density via dip-coating could be explained from topographical images of the dip-coated electrodes.

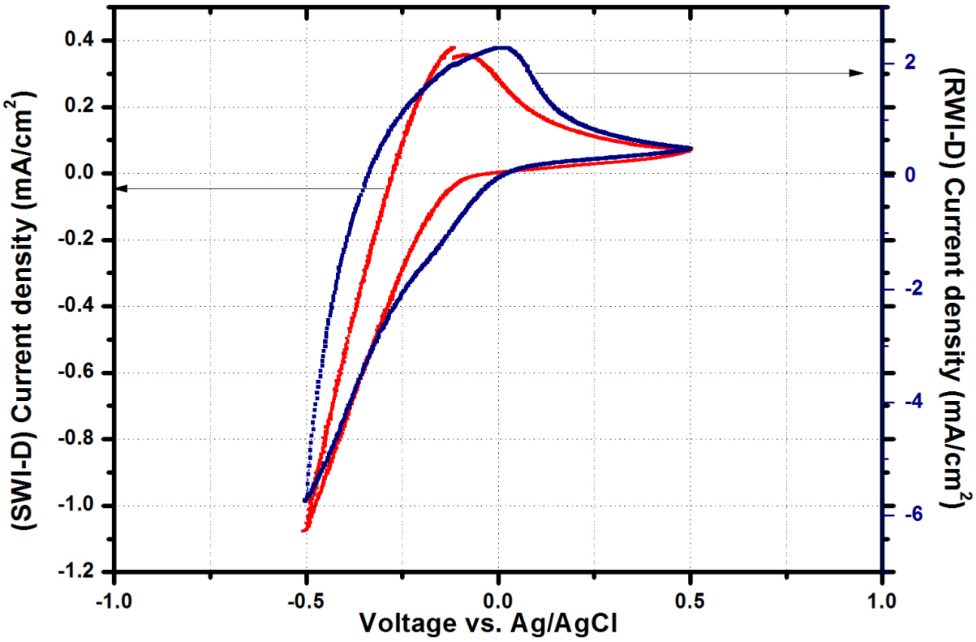

Figure 4.34. Cyclic Voltammograms for dip coated spherical and rod-shaped WO_3 nanoparticles onto ITO substrate.

4.2.1.4. Topographical images of dip coated WO_3/ITO electrode

The surface morphology of the fabricated SWI-D and RWI-D films are shown in Figure 4.35. The dip coated spherical WO_3 nanoparticles onto ITO substrate shows high surface roughage in comparison to rod-shaped WO_3 coated ITO. RWI-D films showed relatively high adherence with homogeneous surface having no cracks. High continuity is observed for RWI-D due to interconnectivity between rod particles; however, washing of particles may occur if the contact area of particle and substrate is less. Thus, it can be predicted that there is high tendency of particle wash out for spherical WO_3 than rod-shaped particles. Another important advantage of dip-coating process is that drying of the films takes place simultaneous with coating. This provides better adhesion of particles in comparison to drop-coating method where drying of coated film becomes another important parameter to be controlled. Moreover, large scale fabrication is another restrictive factor in drop-coating method. Thus, in this perspective dip-coating is a better film fabrication method compare to drop-coating [57]. Table 4.2 represents the physical and electrochemical properties of drop-coated and dip-coated films.

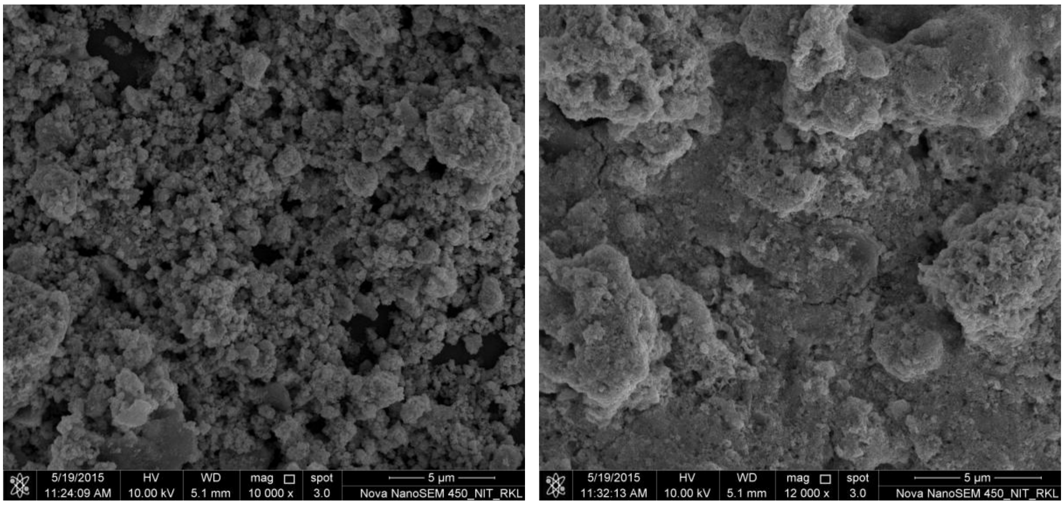

Figure 4.35. Topographical images for dip coated spherical and rod-shaped WO_3 nanoparticles onto ITO substrate.

Table 4.2. Physical and electrochemical properties for drop-coated and dip-coated films.

Sample	Morphology	Transparency	Current density (mA/cm^2)	Contact Resistance ($\Omega\ cm^2$)
SWI	Spherical	Optically Transparent	0.14	1489
RWI	Rod-shaped	Optically Semitransparent	1.8	280
SWI-D	Spherical	Optically Transparent	2.23	972
RWI-D	Rod-shaped	Optically Transparent	0.39	272

4.2.1.5. Summary

A distinct high current density of 2.23 mA/cm^2 is found for dip coated rod-shaped WO_3 nanoparticles onto ITO glass substrate compare to 1.8 mA/cm^2 current density for drop-coated rod shaped WO_3 particles under ± 0.5V and 50mV/s scan rate. In both the coating cases, spherical WO_3 nanoparticles coating shows poor response. Elongated rod shaped nanoparticle preferentially favours more electrochromic response from counterpart spherical particles due to less contact resistance between electrolyte and film and high particle continuity and interconnectivity. The results suggest that anisotropic nanoparticles favour high electrochemical response for dip-coated electrodes.

4.2.2. Electrochromism in WO_3 Nanocuboids

Opto-electrical properties of the optimized WO_3 nanocuboids are evaluated to justify the electrochromic effect of dip-coated WO_3/ITO electrodes.

4.2.2.1. Cyclic Voltammetry & Topographical image of Nanocuboid WO_3/ITO electrode

The optimized WO_3 nanocuboid coated onto the ITO conducting substrate (WO_3/ITO) is used as the working electrode for electrochemical analysis. The fabricated dip-coated WO_3/ITO electrodes are semi-transparent in nature. The direct optical transmittance of the fabricated electrode has a transparency of about 52%. In order to evaluate the electrochromic properties, typical cyclic voltammograms (CV) have been taken between -1.0 and +1.0 V at a scan rate of 100 mV/s using 1 M H_2SO_4 as the working electrolyte. Figure 4.36 shows the cyclic voltammograms recorded for WO_3/ITO electrodes at the 1st, 100th and 500th cycles. It can be seen that the shapes of the CV curves remain unchanged after the 100th and 500th cycles with negligible increased current response, which indicates good cycling stability of the WO_3/ITO electrodes. This is probably due to the good distribution of the particles on the ITO surface after drying of the WO_3 nanocuboid dip-coated ITO electrodes. The topographical FESEM image (Figure 4.37) shows the distribution and texture of particles on the ITO glass surface. It is evident from the image that the particles are relatively well distributed and interconnected. However, the small (~200 nm) pin holes may provide additional ion transportation phenomena and subsequent electrochromic behavior. The electrochromic mechanism of WO_3/ITO electrodes in the H^+ electrolyte is similar to as discussed in Section 4.2.1.2.

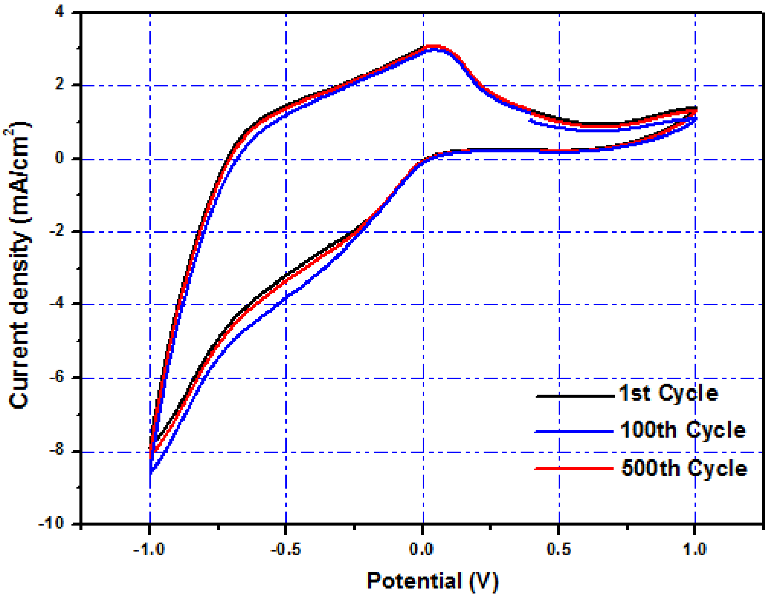

Figure 4.36. Cyclic Voltammograms of WO_3/ITO film at 100mV/s for 1st, 100th & 500th Cycle.

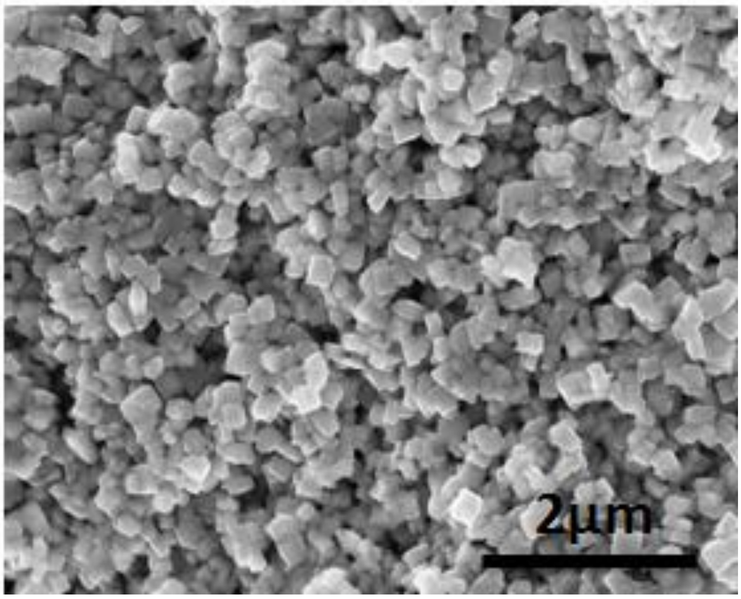

Figure 4.37. Topographical image of dip-coated WO_3 nanocuboids onto ITO glass substrate.

Unique coloration and bleaching processes have been observed for WO_3 nanocuboid coated ITO electrodes during the intercalation and deintercalation of electrons from the WO_3/ITO electrode and H^+ ions from the electrolyte. As shown in the CV curves, the current is found to move negatively with decreasing voltage, corresponding to co-intercalation of electrons and H+ into WO_3 to form hydrogen tungsten bronze [58]. Cathodic and anodic current peaks are observed near -0.25 V and 0.1 V, respectively. The current density observed for the WO_3/ITO electrode is near 3.15 mA/cm^2. Most importantly, a high symmetry of the anodic and cathodic peak is found, which reveals the better electrochromic behavior of WO_3 nanocuboids. A reversible color change of the WO_3/ITO electrodes with varying voltages has been observed. The initial WO_3/ITO electrode is light green in color, but upon application of -0.5 V, the electrode color changes to light blue which then further turns to darker blue at -1.0 V. Bleaching of the electrode occurs at positive voltages of 0.5 V and 1.0 V. Thus, we can conclude that during the deintercalation of H^+ ions, the color of the electrodes bleaches gradually with increasing voltage before the original color is finally recovered. This observation predicts that positive voltage bleaching of the electrodes occurs.

4.2.2.2. Chronoamperometry (CA) of Nanocuboid WO_3/ITO electrode

The estimation of coloration and bleaching time for the WO_3/ITO electrode is known from the current time transients. A typical CA graph is shown in Figure 4.38 for the coloration and bleaching of WO_3/ITO electrodes. During the measurement of CA, experimental increments of voltage are allowed to sweep from the rest potential of 0.0 V to -1 V for a period of 10 s to obtain the coloration phenomenon of the electrodes. Similarly, in reverse, a positive voltage of 1 V is applied for the next 10 seconds, which results in bleaching of electrodes. Interesting coloration and bleaching kinetics are recorded from this analysis. Diffusion of H^+ to the electrolyte (bleaching process) is faster than that from the electrolyte (coloration process) and hence needs 3.18 seconds and 5.05 seconds, respectively. The faster bleaching kinetics than the coloration kinetics is governed possibly by space charge transfer through the electrode and potential barrier at the electrolyte–WO_3 interface, respectively, which controls the two processes diversely.

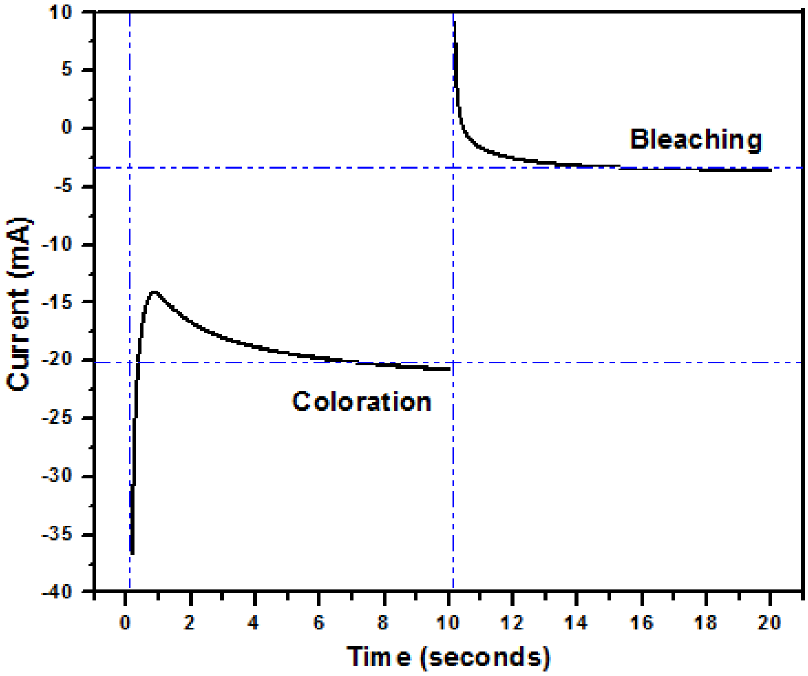

Figure 4.38. Chronoamperometry (CA) measurement for WO_3/ITO film.

4.2.2.3. Chronocoulometry (CC) of Nanocuboid WO_3/ITO electrode

In order to study the amount of charge intercalation of e^- and H^+ ions from an electrolyte with respect to time, chronocoulometry measurement of WO_3/ITO electrode is carried out at voltage sweep range between -1.0 V and +1.0 V. The CC measurement for intercalation and deintercalation process is carried out for the step of 10 seconds each for the forward and backward scan. Figure 4.39 represents a typical CC plot of the WO_3/ITO electrode for the first cycle, and the inset figure represents the CC plot for first 15 cycles. During the forward scan of the WO_3/ITO electrode, the diffusion process leads to the charge intercalation by reducing W^{6+} to W^{5+} states. In the reverse, removal of intercalated charge occurs during the backward bleaching process due to oxidation of W^{5+} to W^{6+} states. The charge intercalation and deintercalation quantified data from the plot have been used to calculate the reversibility of the coloration/bleaching processes. The reversibility of the film can be calculated from the following relation:

$$\text{Reversibility} = \frac{Q_{di}}{Q_i} \qquad (28)$$

where, Q_{di} and Q_i refers to the amount of charge deintercalated and intercalated in the WO_3/ITO films. The percentage of electrochromic reversibility of the WO_3/ITO electrode for first cycle is 72.2%. There is a slight increment in the reversibility after first CC cycle which remains almost constant until the 15th cycle. The reversibility difference between the 1st and 2nd cycle is approximately 5%. From CV, the electrode exhibits high stability until the 500th cycle; therefore, the reversibility obviously remains the same.

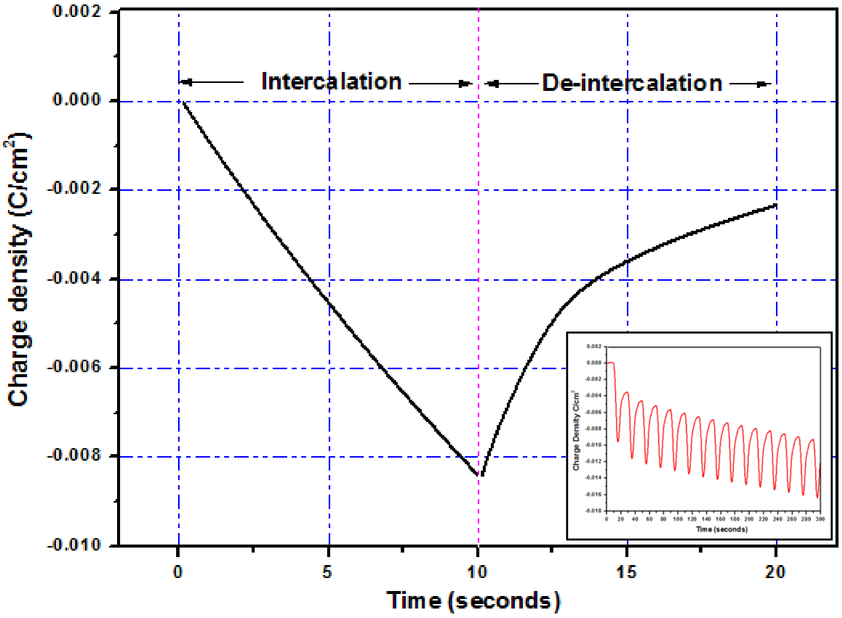

Figure 4.39. Chronocoulometry (CC) measurement for WO_3/ITO film.
(Inset represents the CC for the first 15 cycles)

4.2.2.4. Optical transmittance measurements of Nanocuboid WO_3/ITO electrode

UV-visible transmittance spectroscopy is performed for the WO_3/ITO electrodes in the wavelength range of 200–900 nm after performing the electrochemical analysis. Figure 4.40 shows the room temperature optical transmittance data for WO_3/ITO colored and WO_3/ITO bleached electrodes. The merit of optical performance is to quantify the optical density change (ΔOD) and the coloration efficiency of the WO_3/ITO films. The optical transmittance has been found to decrease with the coloration of the films and then to increase upon the deintercalation process. The transmittance value of WO_3/ITO electrodes at a visible wavelength of 550 nm is utilized for determining the optical density changes. The ΔOD calculation is done as per the following relation [59]:

$$\Delta\text{OD} = log\frac{T_b}{T_c} \qquad (29)$$

Where, T_b and T_c are the transmittance value in the bleached and colored state, respectively. The achieved transmittance efficiency for both bleached and colored monoclinic WO_3 thin film is well comparable with reported data [60].

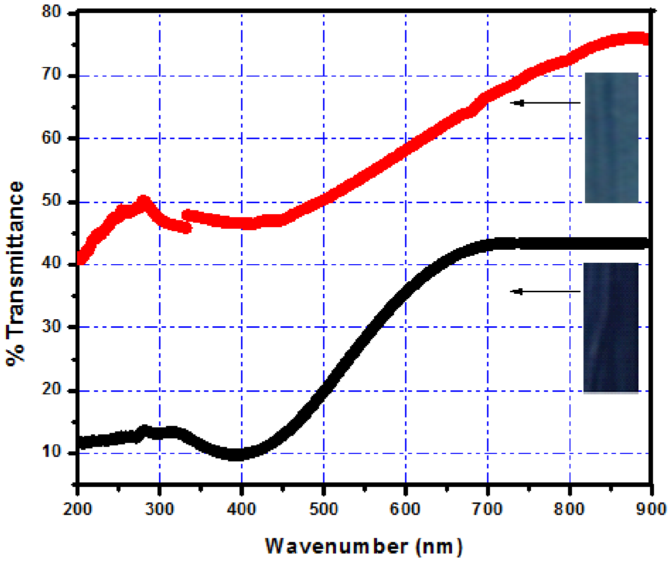

Figure 4.40. Optical transmittance spectra vs. wavelength of colored and bleached films.

The coloration and bleaching of WO_3/ITO electrode is carried out by applying a potential step of -1.0 V to +1.0 V for a fixed time. One of the prime parameter to characterize an electrochromic material is coloration efficiency (CE) of the electrodes. In order to quantify the efficiency during the induction of charge in an electrochromic device, CE is represented as the change in optical density (ΔOD) per unit charge insertion per unit area. It is given by the following relation mentioned below:

$$\text{CE} = \frac{\Delta\text{OD}}{Q_i/A} \qquad (30)$$

where, Q_i is the amount of charge intercalated in the WO_3/ITO electrodes to cause changes in optical density (ΔOD) and A is the area of the electrode. Thus, the coloration efficiency as calculated for the WO_3/ITO electrode has been found to be 60.17 cm^2/C. The result obtained is in accordance with reports by other groups [61, 62].

4.2.2.5. Summary

The nanocuboids exhibit optimum band gap and adherence to develop dip-coated WO_3/ITO electrodes. Tungsten trioxide-coated ITO electrodes have remarkable electrochemical response, electrochromic efficiency, reversibility, and optical switching characteristics in presence of 1M H_2SO_4 electrolyte concentration at 100 mV/s scan rate in the range ±1V. The fabricated electrodes exhibited high electrochemical stability without any significant change in current density and the reversibility of 72.2% is achieved. The electrode coloration and bleaching during electrochromic process took 5.05 and 3.18 s, respectively. The developed process and achievement of the electrochromic response is considerably appreciable, which might have economic viability for fabricating tailor-made smart glass.

4.2.3. Electrochromism in WO_3 Nanofibers

4.2.3.1. Cyclic Voltammetry with respect to coating thickness

In order to evaluate the electrochromic properties of nanofiber WO_3/ITO electrode, cyclic voltammograms (CVs) between scan range -1.0 V to +1.0 V at a scan rate of 100 mV/s are taken in 1 M H_2SO_4 as working electrolyte. The CVs are normalized from constant geometrical effective area 2 cm^2 (dimension 2 cm X 1 cm) of the electrode. The optical transparency of dip coated WO_3/ITO electrode varies from 72% to 27% with respect to number of dip coating, which depicts the semitransparent to near opaque nature. However, transparency does not have significant difference up to ~11 μm thickness. Figure 4.41 represents the CVs with respect to the thickness of the electrodes. Inset depicts the ~8 μm, ~11 μm, ~15 μm, ~18 μm and ~23 μm thickness of WO_3 coating increment for S-1(original), S-2, S-3, S-4 and S-5, respectively. The CV plot reveals that S-5 (~23 μm) film shows higher H^+ intercalation due to high thickness depicting accommodation of more intercalated charges.

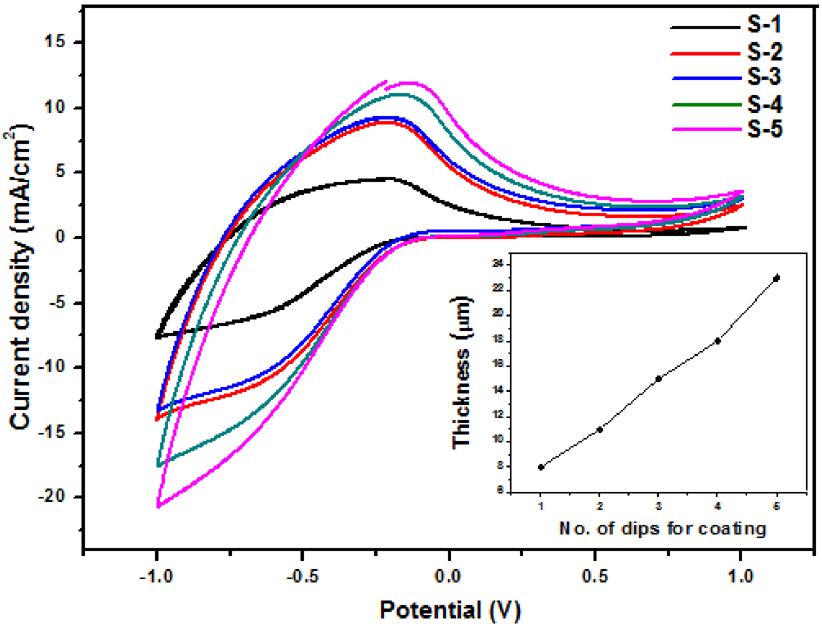

Figure 4.41. CV of WO_3/ITO nanofiber electrode with different coating thickness. (Inset represents the plot of number of dips for coating versus coating thickness)

Moreover, with increment in layer thickness both cathodic and anodic current peak move towards positive potential region. This suggests that there is a reduced charge transfer resistance in the interface during cathodic reaction and de-intercalation during anodic reaction in thinner layer occurs faster at lower voltage. There is not much difference in the current density after ~11 μm (S-2) thickness as observed from CV. Thus, this thickness is chosen to understand the cyclic stability of the fabricated electrode since it has moderate optical transparency also. Furthermore, optical switching characteristics have been shown for this particular electrode.

4.2.3.2. Stability of current density of Nanofiber WO_3/ITO electrode

Figure 4.42a shows the cyclic voltammograms recorded for S-2 (after 2nd dip coating) electrode at the 1st, 100th and 500th cycles. Present study illustrates a stable current response almost well overlapping irrespective of time without any significant change in the shape, which supports the excellent cyclic stability of the S-2 electrode. Figure 4.42b shows the distribution of the WO_3 particles along the interface onto the conducting substrate. Particles appear to be uniformly distributed after drying of dip-coated nanofiber WO_3/ITO electrode. Figure 4.42c illustrates a representative cross-sectional image of the dip coated S-2 electrode which shows the thickness of ~11 μm. In recent, Wei et al. demonstrates that a similar drop-coated nanorod WO_3 exhibits high current density compare to their counterpart nanoplate WO_3 for an unknown coating thickness [54]. A high anodic peak current of 8.9 mA/cm^2 is observed for S-2 (~11 μm) electrode with a difference of 1.9 mA/cm^2 from S-5 (~23 μm) electrode. It is evident that morphology, influenced by tunnelling zone in the hexagonal structure has an important role in the passage of ions in and out from the electrode. The intercalation/deintercalation process is similar to the redox electrochemical reaction mentioned earlier in Section 4.3.6 where the electrode gets colored due to disorder structure forming tungsten bronze. The current is found to increase steadily from negative to a maximum value and then decreases to zero corresponding to the coloration and bleaching of the electrodes at varying voltages. During each of this scan, the electrode undergoes typical reversible color change mechanism from blue to colorless. It is in its reduced state that the electrode appears bluish.

The peak current density of bleaching is much higher than that of coloration, and the current density during bleaching decays faster than coloration. Most importantly, high symmetry of the anodic and cathodic peak is found, which reveals the better electrochromic behavior of WO_3 nanofibers. The enhancement of electrochromism is mainly due to the presence of the active sites and open crystal structure. It is attributed that the hexagonal phase of WO_3 has high structural openness due to its wide-tunnel like structure than the layered structure of other crystal phases of WO_3. According to the reported results, electrochromism in hexagonal WO_3 is more favorable than other layered crystal structures of orthorhombic and monoclinic WO_3. It is mainly due to the presence of vacant sites in the hexagonal structure having possible locations which are trigonal cavity forming tunnel, hexagonal window and the four coordinated square window for occupation of ions in it [63]. The penetration of ions becomes easy with repeated cycles due to the exposure of available active sites for electrochromic reaction resulting in high charge capacity. This may be a probable reason for the high anodic peak current value which is formed due to the de-intercalation of ions during the bleaching out of the samples.

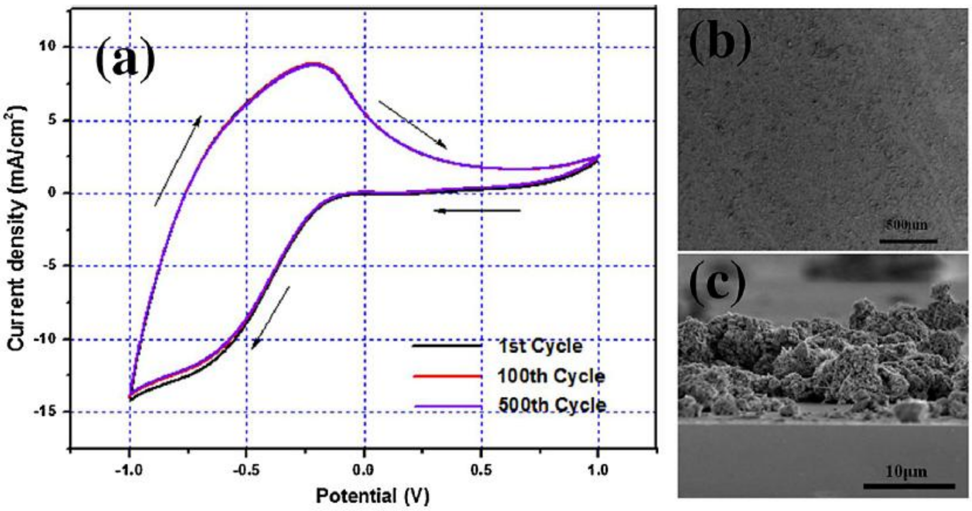

Figure 4.42. (a) CV of 1st, 100th, 500th cycles for nanofiber WO_3/ITO electrode performed at 100mV/s; (b) Topographical images and (c) Cross-section image of fabricated nanofiber WO_3/ITO electrode with coating thickness of ~11 μm.

4.2.3.3. Chronoamperometry of Nanofiber WO_3/ITO electrode

In advance, the coloration and bleaching duration phenomenon of S-2 electrode is further estimated by chronoamperometry (CA) for 10 seconds and represented in

Figure 4.43a. In the beginning, the negative biased voltage (-1.0 V) allows H^+ intercalation from the electrolyte and immediate reversed back to equivalent positive voltage for deintercalation occurrence. Current density increment under negative voltage and subsequent relative faster decay phenomenon are recorded as 6.50 and 4.02 seconds after saturation, respectively. The coloration kinetics under negative voltage is slower than the bleaching kinetics, which is governed possibly due to the interfacial potential barrier generation between electrolyte and WO_3, and the space charge transfer through the electrode and controls the two processes separately. Figure 4.43b shows that the coloration is faster for thick WO_3 coated electrode, but bleaching is faster for thin coated electrode. There is approximately three fold difference observed between the bleaching process of S-1 and S-5, respectively.

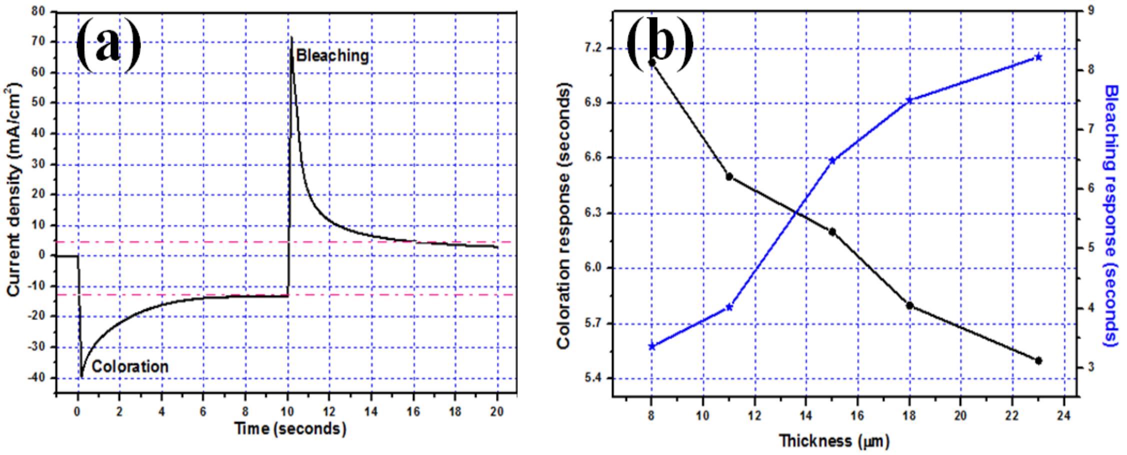

Figure 4.43. (a) Chronoamperometry measurement of WO_3/ITO electrode in 1 M H_2SO_4 under potential sweep of ±1V for 10 seconds each, respectively and (b) Plot of coloration/bleaching with respect to coating thickness.

4.2.3.4. Chronocoulometry of Nanofiber WO_3/ITO electrode

Beyond the scope of the coloration and bleaching activity estimation, an essential charge storage capacity during H^+ ion intercalation/deintercalation of S-2 electrode with respect to identical 10 seconds has been measured by chronocoulometry (CC) and represented in Figure 4.44a. The charge-time transient is reported for 2nd cycle in the figure. The quantified data of charge intercalation and deintercalation from the plot has been used to calculate the reversibility of the intercalation/deintercalation methods. The reversibility of the film can be calculated from Equation 28 in Section 4.2.2.3. The percentage electrochromic reversibility of the S-2 electrode is estimated near to 77.48%. The reversibility with coloration/bleaching response for all the dip coated electrodes has been given in Table 4.3. It has been found that reversibility of the dip–coated electrodes remains between 65 to 80%. Figure 4.44b represents the first 20 charge-time transients taken during cyclic voltammetry. There is difference of 3% in reversibility of first and second cycle. It is clearly seen that the reversibility remains almost constant after the second cycle. As already discussed, cyclic voltammetry shows high stability even after 100th cycle till 500th cycle. Therefore, it is obvious to believe that reversibility of the electrodes also remains stable till 500th cycle.

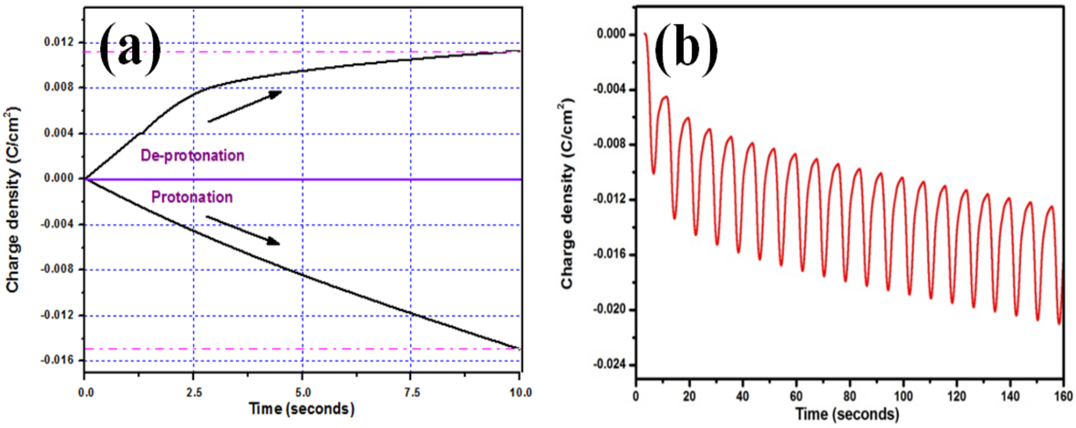

Figure 4.44. (a) Chronocoulometry measurement of WO_3/ITO electrode in 1 M H_2SO_4 under potential sweep of ±1V for 10 seconds each, respectively and (b) Chronocoulometry of first 20 cycles from Cyclic Voltammetry.

Table 4.3. Comparative data of electrochromic hexagonal nanofiber WO_3/TO electrode with respect to number of dip-coatings.

Sample No.	Thickness (µm)	Coloration time (s)	Bleaching time (s)	Reversibility (%)	CE cm^2/C
S-1	~8	7.12	3.36	75	36.1
S-2	~11	6.5	4.02	77.48	63.15
S-3	~15	6.2	6.48	78.30	125.5
S-4	~18	5.8	7.5	80	129.8
S-5	~23	5.5	8.23	66.66	100.3

4.2.3.5. Optical absorption studies for WO_3/ITO electrode

Optical transparency of the proton conducting layer is an important criterion to develop electrochromic devices, and hence transmittance data are taken at room temperature for WO_3/ITO colored and WO_3/ITO bleached electrodes under wavelength range between 200-800 nm for S-2 electrode (Figure 4.45). Both optical density change (ΔOD) and the coloration efficiency depict the optical performance for the colored (T_c) and bleached (T_b) nanofiber WO_3/ITO electrode. The optical transmittance has been found to decrease with the charge intercalation of the electrodes and subsequent increase upon bleaching of the electrodes. Herein, the obtained transmittance values for colored and bleached S-2 electrode at visible wavelength of 550 nm are found as T_c= 22% and T_b = 65%, and utilized for the deter-mination of the optical density following Equation 29 in Section 4.2.2.4.

The coloration efficiency (CE or η) is one of the prime parameters to optimize a fabricated electrode to be well thought-out as an electrochromic material. The quantification of efficiency is calculated following Equation 30 in Section 4.2.2.4. The values calculated for optical density change (0.4704); amount of charge intercalated (Q_i = 0.0149) from CC plot and area of the electrode (2 cm^2) of S-2 electrode are used for CE calculation. The calculated coloration efficiency is found to be 63.15 cm^2/C. Similar transmittance measurement has been carried to obtain a comparative CE result of all the electrodes as shown in Table 4.3. The CE values are 36.1, 63.15, 125.5, 129.8 and 100.3 cm^2/C for S-1(original), S-2, S-3, S-4 and S-5, respectively. There is a steady increase in the CE with respect to the thickness, however, a decrease in the CE is observed for S-5 electrode like that observed in reversibility. Hence, we can conclude that although WO_3 nanofiber has high efficiency to hold ions in its hexagonal crystal structure but its electrochromism sharply depends on the coating thickness also which effectively affects the coloration/bleaching response and coloration efficiency. The obtained value is found in accordance to the reported values by other research group [64].

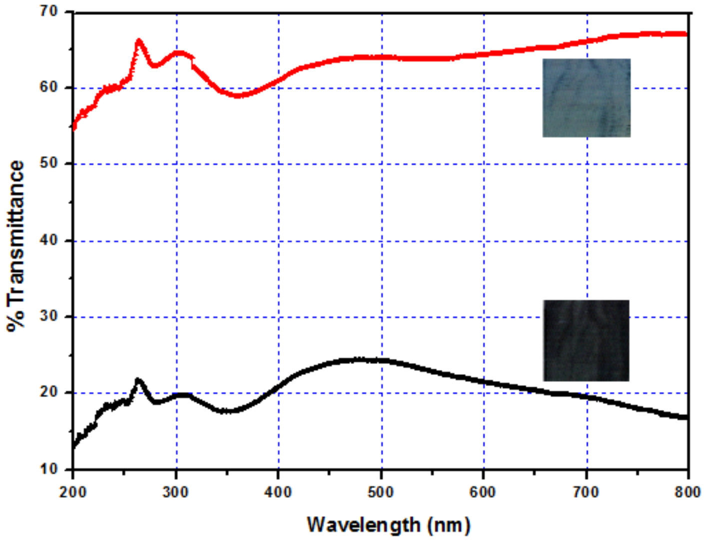

Figure 4.45. Optical transmittance spectra versus wavelength of colored and bleached films

4.2.3.6. Summary

The enhanced electrochromic performance of WO_3/ITO nanofiber electrode is observed in perspective of high current density, the high coloration efficiency with good cyclic reversibility. Moreover, it exhibits an excellent coloration and bleaching characteristics with respect to different coating thickness affecting the response time and CE of the electrodes. The coating thickness of 11 μm exhibits current density of 8.9 mA/cm^2 with reversibility of 77.48% and coloration efficiency 63.15 cm^2/C. The evaluated properties suggest the plausible use of WO_3 nanofibers for high efficient electrochromic device.

4.2.4. Effect of WO_3 crystal structure on Electrochromism

Commercialization of electrochromic device is more sustainable when it follows short switching time, low operation voltage and repeatability under low power consumption. The above factors depend on the electrochemical parameters including scan range, scan rate and corresponding electrolyte concentration that govern the electrochromic mechanism [65, 66]. The studies reveal that the degree of functional application depends on both the morphology and structural deviation. Among the polymorphs of WO_3, regular monoclinic and metastable hexagonal proves to be promising structures for electrochromism due to its proper band gap and ion-intercalation chemistry, respectively [67]. In this context, we would study the cyclic stability, transparency, switching time and coloration efficiency of dip-coated nanocuboid and nanofiber WO_3/ITO electrode under the influence of acid electrolyte concentration, and scan rate with respect to their different crystal structures.

4.2.4.1. Raman Spectroscopy of WO_3 Nanocuboids and Nanofibers

The detail studies on phase, crystal structure, morphology and band gap measurements of WO_3 nanocuboids (nCW) and nanofibers (nFW) has been studied in the previous sections. A deep instinct of structural and bonding behavior has been confirmed by Raman Spectroscopy. Raman spectroscopy illustrates the structural appearance of pure monoclinic nCW and hexagonal nFW as shown in Figure 4.46. For both nCW and nFW, the bands lower than 200 cm^{-1} represents the vibration from lattice modes. The existence of bands between 200 and 600 cm^{-1} attributes to the bending mode of bridging oxygen. On the other hand, region with medium and high frequency corresponds to the deformation and stretching vibration modes. The peak at 699 cm^{-1} resembles the -O-W-O- vibration, whereas, the band at 800 cm^{-1} is the typical peak of monoclinic WO_3 associated with the stretching vibration of bridging oxygen. The obtained peaks in the range 750 – 950 cm^{-1} is characteristic to the asymmetric stretch of -W-O-W- bond or the symmetric stretch of -O-W-O- bond of nCW. Similarly, higher wavenumber bands at 811 cm^{-1} and 672 cm^{-1} describes the -O-W-O- stretching modes of nFW. An additional peak is observed in nFW at 929 cm^{-1} because of the W=O stretching mode of terminal oxygen atoms present on the cluster surface or at the boundaries of the grains [45]. Moreover, existence of the band at 258 cm^{-1} and 349 cm^{-1} in nCW assigns to -O-W-O- bending vibration, which shifts to slight lower region at 241 cm^{-1} and 322 cm^{-1} in nFW. This peak shift is due to local structural changes from a more symmetrical monoclinic crystal system to a less symmetrical hexagonal structure of WO_3 [4].

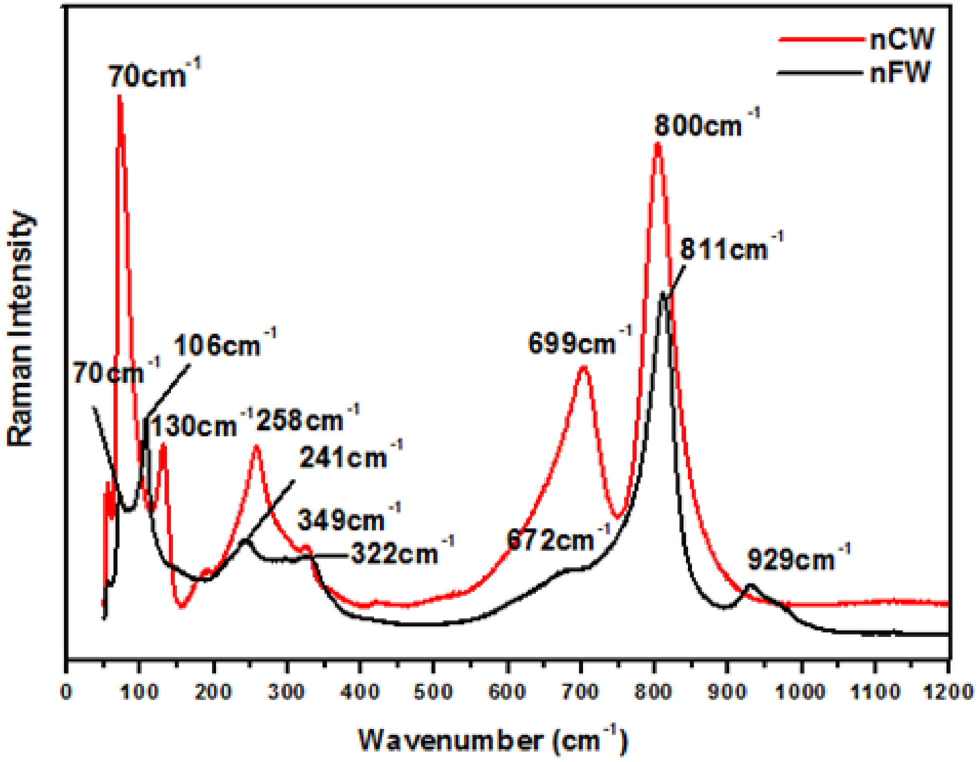

Figure 4.46. Composite Raman spectral pattern of nCW and nFW.

4.2.4.2. Effect of Electrolyte Molar concentration on Cyclic Voltammetry

The dip coated nanocuboid and nanofiber WO_3/ITO electrode are designated as nCW/ITO and nFW/ITO, respectively. Electrochromic mechanism of working electrode (nCW/ITO and nFW/ITO) and Pt counter electrode under ± 0.5V leads to the intercalation of hydrogen (H^+) ions into WO_3 from electrolyte and their simultaneous electro-neutrality through interaction of available equal amount of electrons (e^- s) on WO_3 layer of working electrodes. Aforesaid mechanism promotes the coloring of working electrode. On the contrary, when the polarity of the applied voltages is reversed, de-intercalation of H^+ ions takes place which bleaches the colored electrode [68]. In the beginning, influence of H_2SO_4 acid concentration from 0.5 to 1.5 M with a fixed scan rate say 50 mV/s on CV has been analyzed. Figure 4.47a & 4.47b represents the effect of acid electrolyte concentration on the CVs of nCW/ITO and nFW/ITO electrodes, respectively. High proton concentration enhances the diffusion rate of protons (H^+) into the working electrode and their subsequent current density increment of 0.75 mA/cm^2 and 4.0 mA/cm^2 for nCW/ITO and nFW/ITO electrodes, respectively. However, no significant effect is observed beyond 1 M H_2SO_4 concentration. High mobility of proton eases the insertion, which is leading to high amount proton intercalation during reduction. Conversely, proton de-intercalation slows down due to clustering of protons at the interface of WO_3 and electrolyte during oxidation [69]. The optimized acid concentration is that where easy mode of proton insertion/de-insertion and consistent current density occurs for repeated cycles. In our work, 1 M H_2SO_4 shows better mobility of protons in and out of electrolyte. Therefore, this electrolyte concentration is chosen for further electrochemical studies.

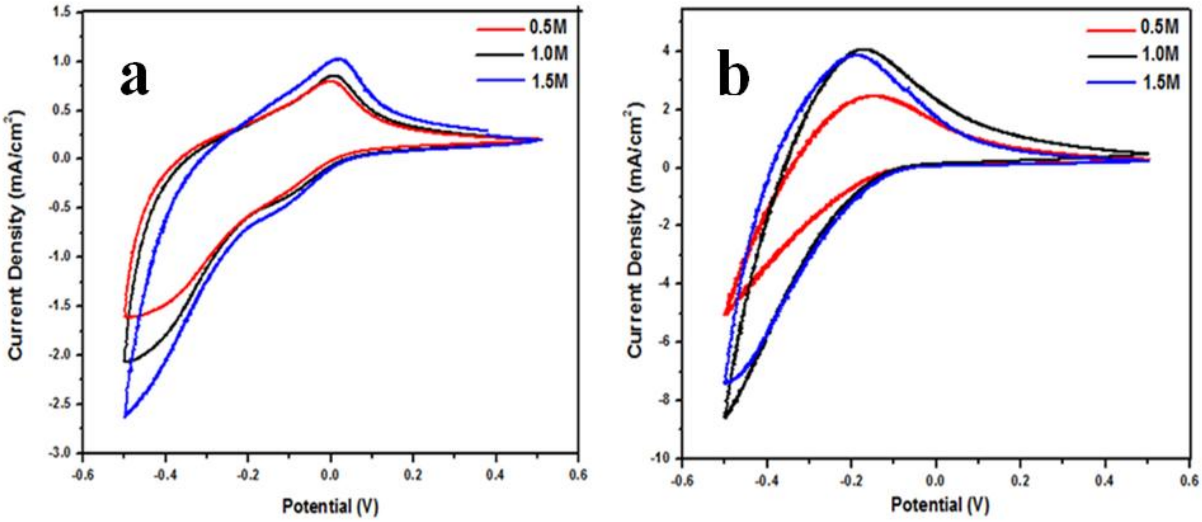

Figure 4.47. Effect of molar concentration of electrolyte (H_2SO_4) on the peak potential for: (a) nCW/ITO and (b) nFW/ITO electrodes.

4.2.4.3. Effect of Scan rate on Cyclic voltammetry

. The characteristic curves in Figure 4.48a & 4.48b shows the CVs measured at different scan rates for a continuous number of cycles at each scan rate in an optimum

1 M H_2SO_4 electrolyte. Increased scan rate in both the cathodic and anodic current peak shifted towards higher potential zone because of rapid evolution of hydrogen and oxidation of inserted hydrogen in WO_3 electrodes, respectively. Low scan rate decreases the diffusion flux to the electrode and their resultant current density [70]. Inset represents the characteristic feature of peak current versus square root of scan rate, where linear behavior is because of the continuous ion diffusion during the electrochemical process. The reversibility for nCW/ITO and nFW/ITO electrodes is well-coordinating till scan rate of 100mV/s.

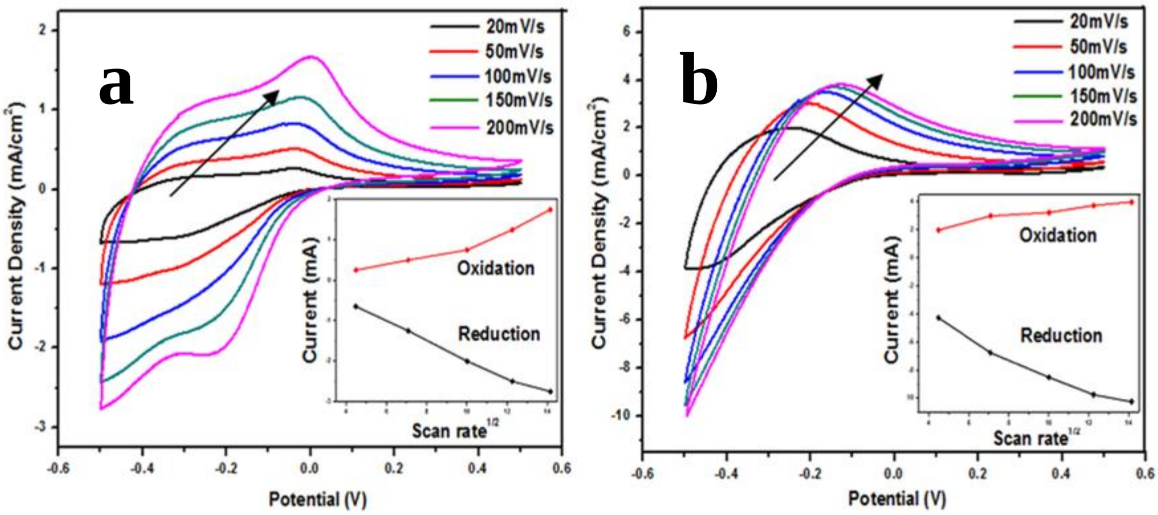

Figure 4.48. Linear potential scan characteristics of current vs. potential recorded in 1M H_2SO_4 at different scan rates (c) nCW/ITO and (d) nFW/ITO electrodes. Inset shows cathodic/anodic peak current vs. square root of scan rate.

4.2.4.4. Cyclic Stability of fabricated electrodes

Figure 4.49a & 4.49b represents the CV for 1st and 1000th cycles recorded for nCW/ITO and nFW/ITO separately in 1M H_2SO_4 with a scan rate of 100 mV/s. Topographical image for the fabricated electrodes is represented in the inset. A stable current response illustrates well overlapped CVs without any significant change in shape. The ion penetration becomes easy due to the exposure of available active sites with repeated cycles for electrochromic reaction resulting in high charge capacity, which indicates excellent cyclic stability of both the electrodes. The distribution of particles on the ITO surface also plays a key role in the ion penetration and charge holding capacity.

Topographical image for the fabricated electrodes is represented in the Figure 4.50a & 4.50b, respectively. Nanocuboids are uniformly distributed; however, the inter-linking between nanofibers exhibits better ion flowing ability in electrolyte for each CV scan. Moreover, hexagonal crystal structure provides an additional advantage of nanofibers to enhance and improve the intercalation that has been discussed later. In this circumstance, the estimated current density for both nCW/ITO and nFW/ITO are found to be 1.2 mA/cm^2 and 3.9 mA/cm^2, respectively. There has been a large difference in current density between both the electrodes as they use different morphology WO_3 with different crystal structures.

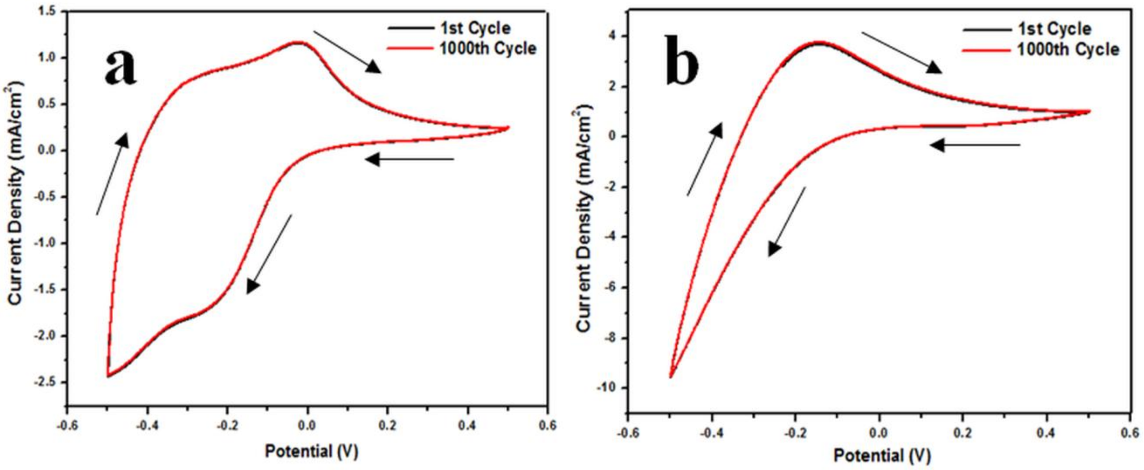

Figure 4.49. CV curves for 1st cycle and 1000th cycles for (a) nCW/ITO and (b) nFW/ITO.

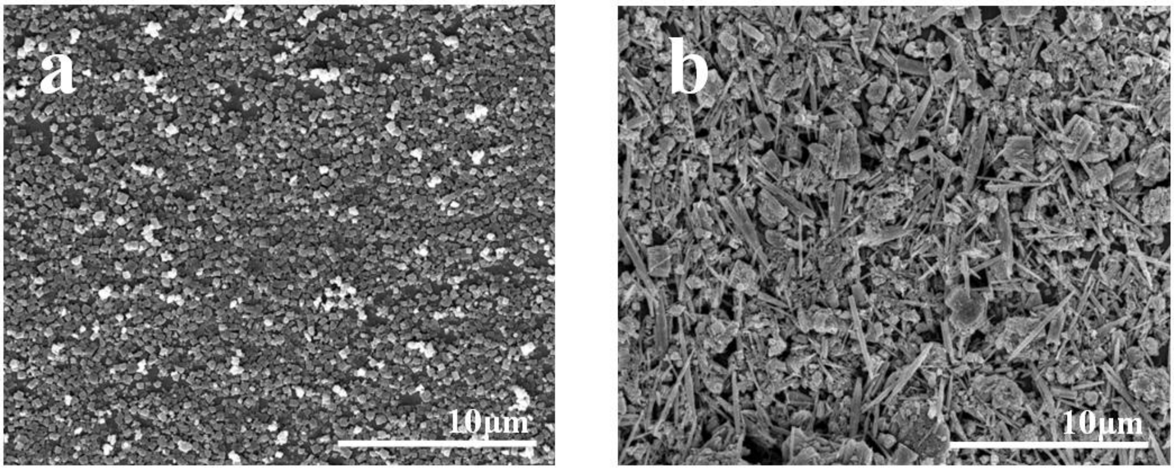

Figure 4.50. FESEM images of dip-coated electrodes (a) nCW/ITO and (b) nFW/ITO.

4.2.4.5. Effect of crystal structure on cyclic voltammetry

Literatures reported that the difference in current density is influenced due to the difference in morphology for same crystal structure [54]. But, limited comparative electrochemical representation of WO_3 is found for different morphology having different crystal structure. The synthesized monoclinic WO_3 has high symmetry and high stability at room temperature, in which small ions can easily travel though the four coordinated tunnels formed upon layering of octahedral that eases the ion transportation and intercalation in the structure (Figure 4.51a). This fundamental electrochemical mechanism is also well acceptable for other orthorhombic crystal structure [71].

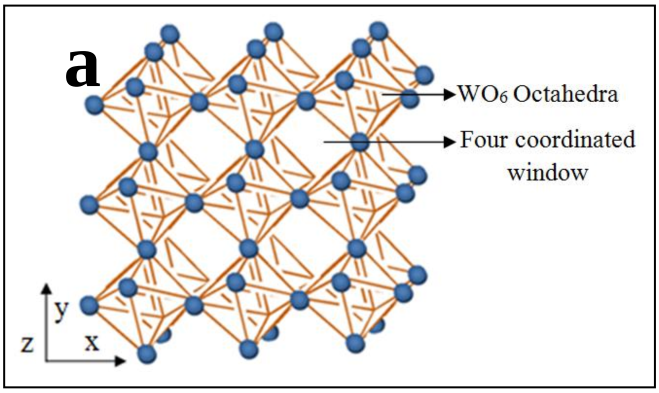

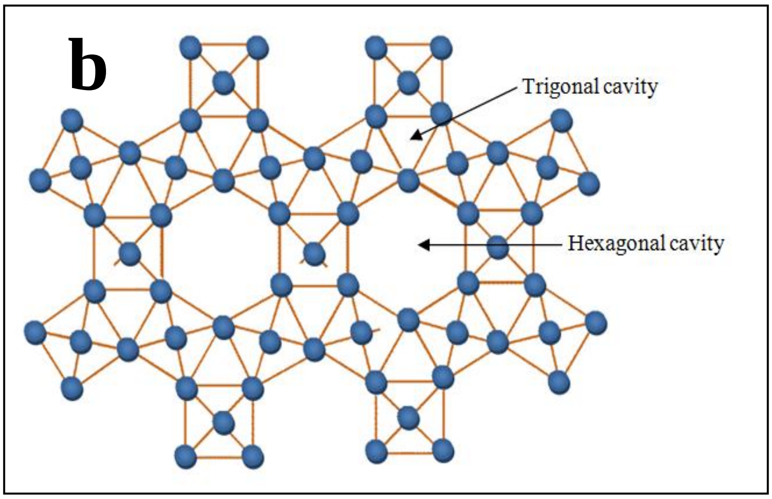

Figure 4.51. Schematic of (a) monoclinic and (b) hexagonal WO_3 crystal structures.

Hexagonal structure (nFW/ITO electrode) has three possible locations for this ion insertion/extraction; they are the hexagonal window, the trigonal cavity and the four coordinated square windows as shown in Figure 4.51b. The degree of openness and ion holding capacity in hexagonal crystal structure is higher than other layered structures of WO_3. The hexagonal WO_3 nanofibers exhibit high current density in comparison to the monoclinic WO_3 nanocuboids. Moreover, interconnectivity and existence of Nanoscale pore have an additional advantage for fibrous morphology.

4.2.4.6. Chronoamperometric studies

The kinetic study of electrochemical redox reaction is carried through the potential step experiments. It determines the switching speed of the fabricated electrode from one state to another state that signifies its application potentiality. Chronoamperometric (CA) measurements quantify the response time required for coloration and bleaching of the nCW/ITO and nFW/ITO electrodes. The current transient for both the electrodes has been taken in 1M H_2SO_4 electrolyte at ±0.5V for a step of 20 sec. The resultant response has been shown in Figure 4.52 for three consecutive cycles for both electrodes. Each cycle is a total run of 40 s. In the first 20 s, current is sweeped due to negative voltage application for proton insertion causing coloration and a positive voltage is immediately applied for proton extraction in last 20 s. It is clearly observed that both the coloration and bleaching current follows smooth stepping and decreases continuously with time. The current decrease with time measures the speed of the electrochromic response. The calculated response values for coloration (t_b) and bleaching (t_c) of nCW/ITO are 11.05s and 7.02s, respectively. Similarly, the current responses for nFW/ITO are 8.09s for coloration (t_b) and 6.82s for bleaching (t_c), respectively. It is evident from the figure that there is not much difference with increasing number of cycles for both the electrodes. The fast color-bleach kinetics compare to coloration is seen for nFW/ITO than nCW/ITO electrode due to its extensive tunnel structure and morphology. It is because the current flow during bleaching is governed by space charge carriers through the electrode, whereas during coloration it is governed by the number of proton insertion through the potential barrier at the interface of WO_3 and electrolyte.

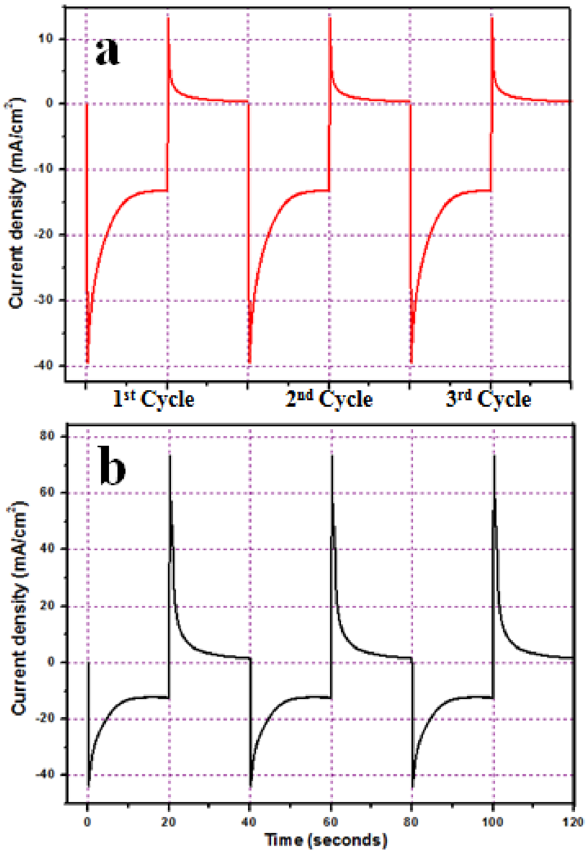

Figure 4.52. Chronoamperometry recorded for (a) nCW/ITO and (b) nFW/ITO electrodes.

4.2.4.7. Chronocoulometric studies

To study the charge intercalation and deintercalation into nCW/ITO and nFW/ITO, chronocoulometric (CC) measurement is carried at ±0.5 V for a step of 20s as shown in Figure 4.53a & 4.53b. The figure shows the charge intercalation/deintercalation for consecutive 3 number of cycles. All the three cycles are performed in identical conditions. It is clearly seen that the charge-time transients for all the cycles of nCW/ITO and nFW/ITO behaves in a similar fashion. There is a negligible difference in charge intercalation/deintercalation in all the cycles of both the electrodes. The amount of charge intercalated (Q_i) and deintercalated (Q_{di}) gives the resultant reversibility of the electrodes. The reversibility is calculated following Equation 28. The electrochromic reversibility of nCW/ITO and nFW/ITO is found to be 38.88% and 78.94%, respectively.

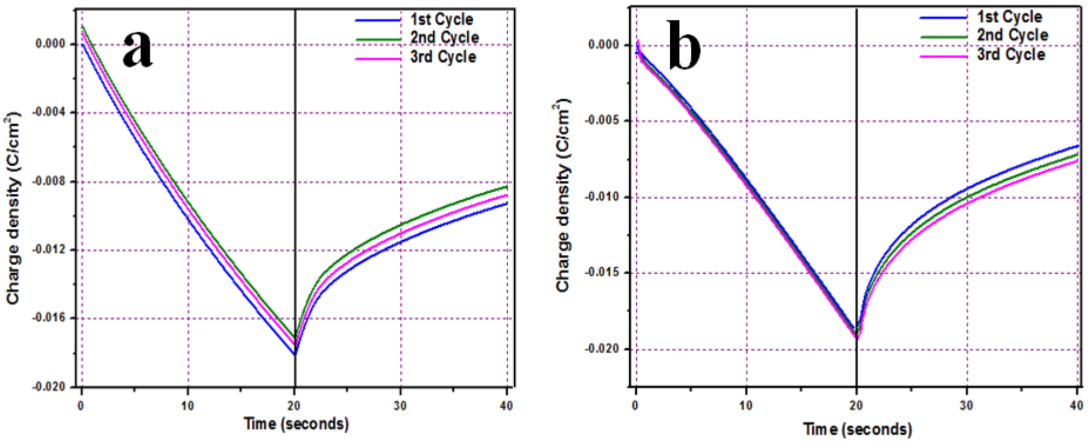

Figure 4.53. Chronocoulometry recorded for (a) nCW/ITO and (b) nFW/ITO electrodes.

4.2.4.8. Optical studies

In order to develop electrochromic devices, the optical transparency is also an important and useful criterion. Hence, direct optical transmittance of the colored and bleached samples has been measured under room temperature in the wavelength range $350 < \lambda < 800$ by UV-Vis spectrophotometry. Figure 4.54a & 4.54b shows the optical transmission data after coloration and bleaching of nCW/ITO and nFW/ITO electrodes, respectively. In both the cases, the transmittance is found to increase upon bleaching than coloration. The optical absorption study of both the electrodes is well described by change in optical density (ΔOD), which is the ratio of T_b (transmittance in bleached state) and T_c (transmittance in the colored state). The coloration efficiency (CE) is given by change in optical density per unit area per unit charge intercalated into the electrode during electrochemical reaction. For calculation of ΔOD and CE, the transmittance values at wavelength 550 nm are considered. The calculated CE values are found to be 36.97 cm^2/C and 54.09 cm^2/C for nCW/ITO and nFW/ITO electrodes, respectively. The values obtained are in accordance with the reported values by other research groups [63, 72]. The details electrochemical parameters comparison has been given in Table 4.4. Finally, the hexagonal WO_3 nanofibers exhibit better electrochromism as compared to the monoclinic WO_3 nanocuboids as evident from all the results.

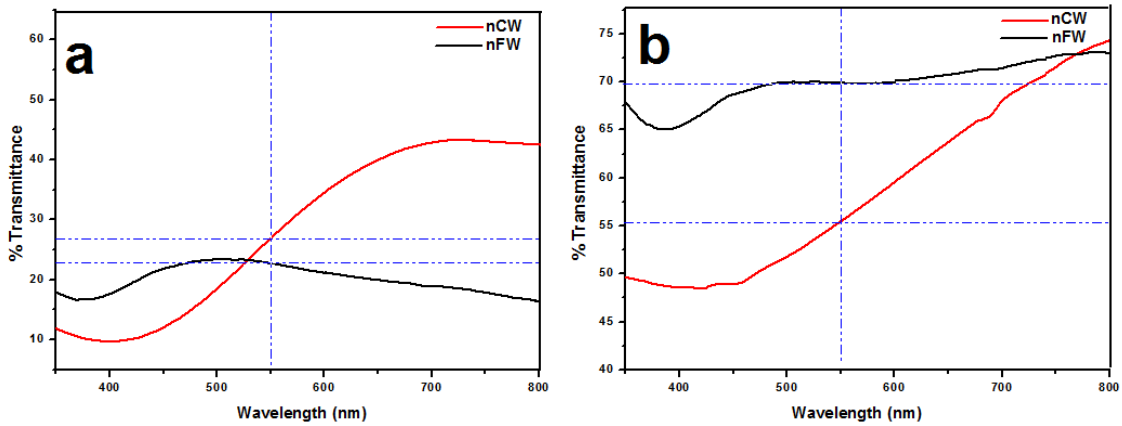

Figure 4.54. Optical transmittance of (a) Colored and (b) bleached of nCW/ITO and nFW/ITO electrodes.

Table 4.4. Comparative electrochemical parameters evaluated for nCW/ITO and nFW/ITO.

Sample Name	Current density (mA/cm^2)	Response time		ΔOD λ=550nm	Coloration efficiency (CE) (cm^2/C)	Reversibility (%)
		t_b (s)	t_c (s)			
nCW/ITO	1.2	11.05	8.09	0.313	36.97	38.88
nFW/ITO	3.9	6.02	5.5	0.486	54.09	78.94

4.2.4.9. Summary

Tungsten oxide nanocuboid and nanofiber has different crystal structure and tunnelling zone to support the ion interaction phenomenon. Surface area, morphology and crystal structure has a significant effect on electrochromic performance. Acid electrolyte concentration and scan rate has been optimized to be 1M H_2SO_4 and 100mV/s, respectively. Electrochemical performance of nFW/ITO electrode under optimized electrolyte concentration and scan rate exhibits fast optical modulation and a high coloration efficiency than nCW/ITO because of hexagonal WO_3 has less symmetrical structure than layered monoclinic WO_3. The obtained data supports that the hexagonal fibrous tungsten oxide has better electrochromic efficacy than monoclinic cuboid tungsten oxide nanoparticles.

4.3. Photocatalytic Studies

In the previous studies, we have discussed the influence of WO_3 crystal structure and morphology on the electrochemical properties high efficient electrochromism. Similar phenomenon can be expected for other radical assisted reaction like photocatalysis [73]. Practically, the photochemical property of WO_3 requires improvement for superior photoactivity. Considering the matter of surface modification, the larger particles say nanocuboids or nanofibers are preferentially forming effective mixed oxide in comparison to counterpart spherical shaped WO_3 nanostructures. Moreover, it is not possible for spherical nanoparticles (~50 nm) to have enough exposed surface, as the particle size is smaller than the primary particle of quasi fiber ZnO (~60 nm) since direct contact between the particles is essential for effective photocatalytic activity (see Table 4.1). Thus, hydrothermally synthesized WO_3 nanostructures are primly used for photocatalytic studies against different dyes.

4.3.1. Effect of WO_3 crystal structure on photocatalytic activity of WO_3-ZnO Nanocomposites

The present study, surface modification of monoclinic WO_3 nanocuboid and hexagonal WO_3 nanofiber is done by coupling with commercial ZnO to form WO_3-ZnO nanocomposites and studied their details crystal structure and particle distribution. Furthermore, optical and photoluminescence spectra of WO_3-ZnO nanocomposites is studied for degradation of methyl orange under both UV and visible light irradiation.

4.3.1.1. Phase Analysis

The powder XRD patterns of the synthesized WO_3 nanocuboids (m-WO_3), WO_3 nanofibers (h-WO_3) and commercial ZnO (C-ZnO) has been shown in Figure 4.55a. As mentioned earlier, WO_3 nanocuboids and nanofibers exhibit monoclinic and hexagonal crystal phase. The commercial ZnO has a regular hexagonal crystal phase. The XRD pattern matches well with the standard JCPDS No. 75-0576 (Space group P63mc, a=b= 3.2427 Å, c= 5.194 Å, $\alpha=\beta= 90.00°$ and $\gamma=120°$). The composite XRD patterns of the optimized 10 wt% m-WO_3/ZnO and 10 wt% h-WO_3/ZnO nanocomposites has been shown in Figure 4.55b. Optimization of weight percentage loading of m-WO_3 and h-WO_3

in ZnO has been done based on the photocatalytic experiments. The clear indexing of the monoclinic and hexagonal phase of WO_3 mixed with ZnO shows the homogenization of the contents present in WO_3/ZnO nanocomposites.

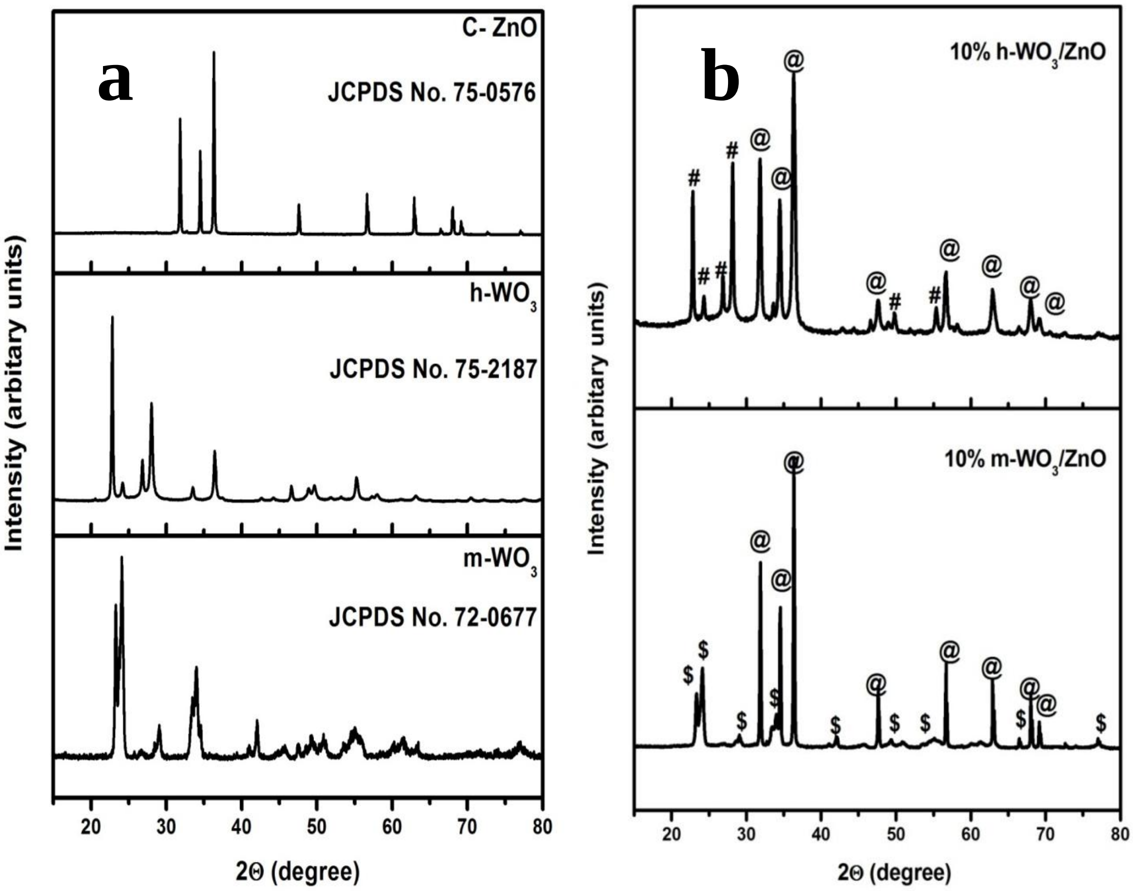

Figure 4.55. Composite XRD patterns of (a) m-WO_3, h-WO_3 and C-ZnO and (b) 10% m-WO_3-ZnO and 10% h-WO_3-ZnO nanocomposites. (@ represents C-ZnO, # represents h-WO_3 and $ represents m-WO_3)

4.3.1.2. Morphological analysis of WO_3-ZnO Nanocomposites

The morphology and dimension of the catalyst particles are very important parameters as they influence the photocatalytic activity under both UV and visible light conditions [74]. The morphological analysis of monoclinic WO_3 nanocuboids and hexagonal WO_3 nanofibers has been described in detail in previous section. Transmission electron microscopy (TEM) image and SAED pattern of C-ZnO has been shown in Figure 4.56a & 4.56b. Near spherical to different aspect ratio particles are seen for C-

ZnO that depicts highly non-homogeneous form of particles. Hard agglomeration of primary particles is seen that forms secondary particles of larger size. The average particle size is found to be 225 nm in diameter. The SAED pattern (Figure 4.56b) of the commercial ZnO shows scattered spots forming concentric circles supporting the range of particles sizes in TEM image. The specific surface area of C-ZnO is 6.19 m^2/g. However, no specific surface area change is observed for 10 wt% loaded C-ZnO nanocomposites with respect to the parent particles.

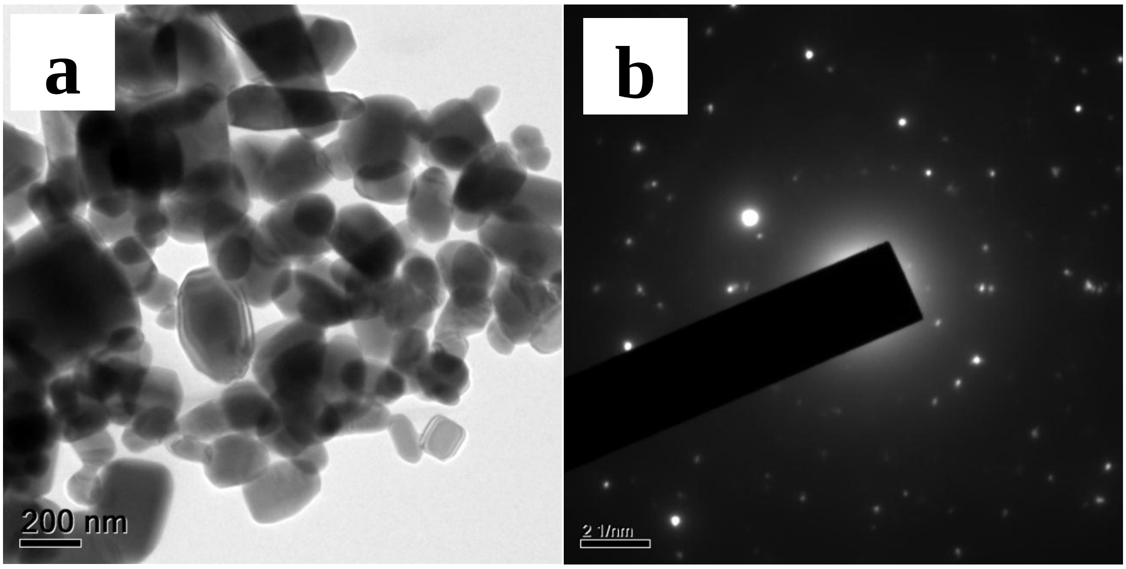

Figure 4.56. (a) TEM image and (b) SAED patterns of C-ZnO.

The SEM-EDS elemental mapping of the optimized 10% m-WO_3/ZnO photocatalyst has been shown in Figure 4.57 to understand the distribution of W, O and Zn in the resultant catalyst mixture. The WO_3 &ZnO nanoparticle in the nanocomposite has intimately attached for better interaction during the photochemical reaction. The SEM image shows well co-ordination of particles which is clearly visualised in the mixed nanocomposite and their individual element EDS maps. A relative uniform distribution of the elements is seen within the oxides, where comparatively high signal of Zn has been obtained than W. W is found to have homogeneous distribution revealing the apposite formation of the nanocomposite to be used as a catalyst.

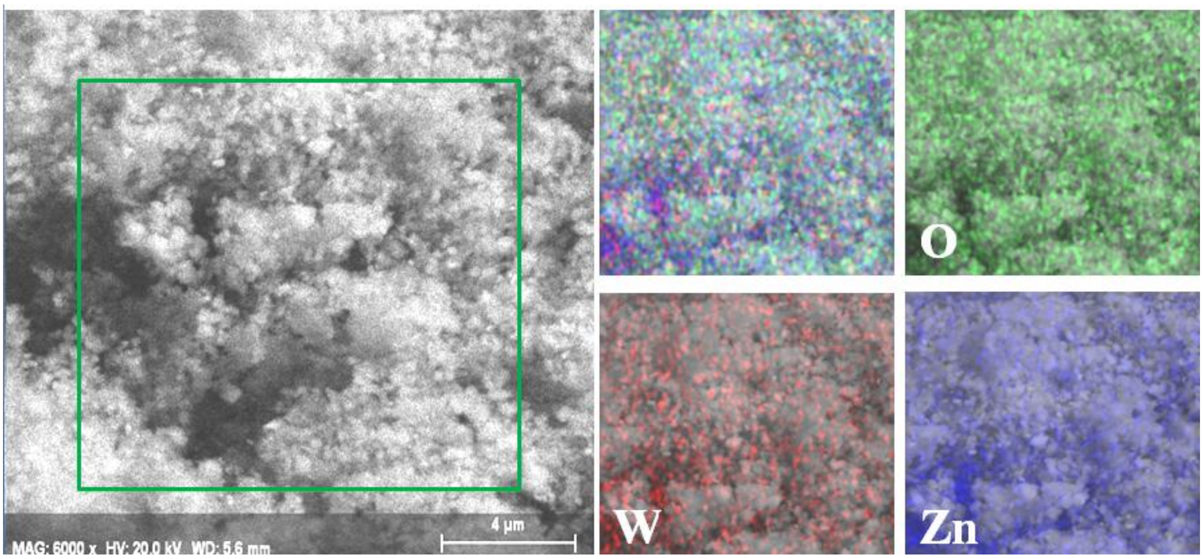

Figure 4.57. SEM elemental distribution of 10% m-WO_3/ZnO mixed oxide.

4.3.1.3. UV-DRS of WO_3-ZnO Nanocomposites

The diffuse reflectance UV-Vis spectra of pure m-WO_3, h-WO_3, C-ZnO and the mixed m-WO_3/ZnO and h-WO_3/ZnO nanocomposite powders has been recorded as shown in Figure 4.58. As seen in the figure, the absorption range of the pure oxides and mixed nanocomposites covers from 200 to 800 nm. To the best of our knowledge, coupling of ZnO with semiconductor of smaller band gap WO_3 is an approach that has extended the absorption light from UV to visible range. The formation of defect energy levels within the forbidden band of ZnO and WO_3 will decrease the band gap energy of WO_3/ZnO nanocomposites resulting to the extension of absorption band [75, 76]. The energy band gap (E_g) for all the nanocomposites and pure powders was determined using the relation $E_g= 1243/\lambda_g$ (eV), where λ_g is the absorption edge [77]. The absorption edge is obtained from the intercept between the tangent of the absorption curve and the abscissa. Figure 4.58a shows the reflectance of C-ZnO, m-WO_3 and m-WO_3/ZnO nanocomposites, and Figure 4.58b shows the reflectance of C-ZnO, h-WO_3 and h-WO_3/ZnO nanocomposites. The commercial ZnO is found to have strong absorption of light from 200 to 390 nm and no absorption in the visible region, whereas WO_3 strongly absorbed under visible region. Among both the crystal structures of WO_3, monoclinic shows high absorption under visible region than counterpart hexagonal structure. The energy band gap of C-ZnO, m-WO_3 and h-WO_3 is calculated to be 3.14, 2.6 and 2.8 eV, respectively. The calculated band gap of WO_3/ZnO nanocomposites formed using both the crystal structures is found to be in the range of 2.4 to 3.14 eV. The presence of WO_3 shifts the absorption edge towards longer wavelengths, which may be due to the formation of the energy level of vacant oxygen for tungsten being doped into the crystal lattice of ZnO [78].

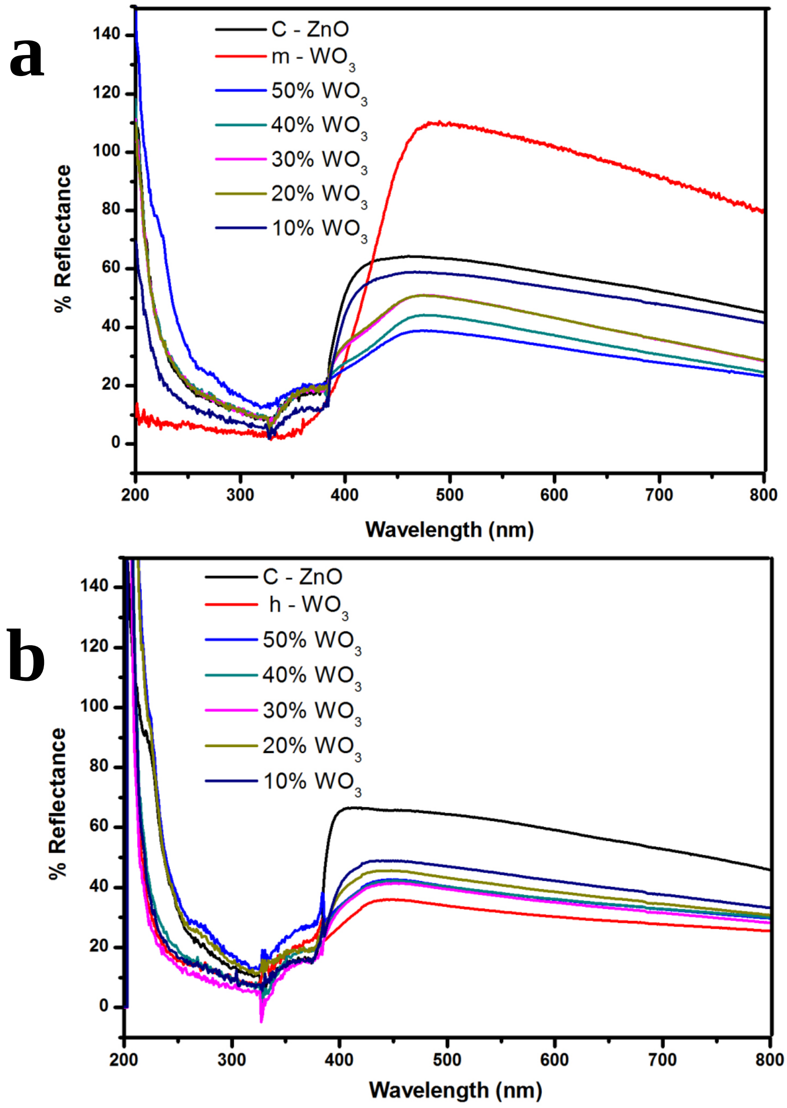

Figure 4.58. UV-Vis absorbance spectra of (a) m-WO_3/ZnO and (b) h-WO_3/ZnO mixed oxide nanocomposites.

4.3.1.4. Photocatalytic degradation of Methyl Orange under UV light

In the present study, the photocatalytic activity of m-WO_3, h-WO_3, C-ZnO and m-WO_3/ZnO and h-WO_3/ZnO mixed nanocomposite (with 10, 20, 30, 40, 50 wt% of WO_3) catalysts were carried out to optimize the most efficient catalyst with optimum WO_3 loading for degradation of common textile dye methyl orange (MO). Methyl orange, an azo-dye is often used as a model dye to probe the photo degradation chemistry that occurs on semiconductor particles. Initially, sensitization of dye towards the UV light is performed. All the photocatalysts showed no adsorption towards the dye during adsorption-desorption equilibrium without light irradiation. Figure 4.59 shows the degradation profile of MO dye under UV light irradiation for 60 min with a difference of 10 min interval. The time dependent degradation curve and kinetic profile of dye with respect to m-WO_3, C-ZnO and their mixed nanocomposite is shown in Figure 4.59a & 4.59b, and h-WO_3, C-ZnO and their mixed composite is shown in Figure 4.59c & 4.59d, respectively. The degradation profile of MO is calculated by C/C_o, where C is the concentration of MO remaining in the solution after irradiation time t and C_o is the initial concentration of the standard MO solution. The self degradation of MO in presence of light is negligible without any catalyst for 60 min duration. The initial concentration is the concentration after adsorption-desorption equilibrium of 60 min. Both m-WO_3 and h-WO_3 showed almost negligible degradation of MO under UV light. The results showed that the best degradation is observed for the catalyst having 10 wt% WO_3 in both monoclinic and hexagonal WO_3/ZnO mixed nanocomposite. The content of WO_3i n the nanocomposite plays a crucial role on the photocatalytic degradation of MO. The increase in WO_3 content beyond 10wt% in the nanocomposite depicts an adverse effect due to more absorption of photons favoring the electron-hole recombination process. The degradation of 99% is obtained with 10% m-WO_3/ZnO composite whereas commercial ZnO (C-ZnO) showed only 78% degradation. In similar fashion, 10% h-WO_3/ZnO composite showed only 95% degradation under UV light as shown in Figure 4.59c. There is not remarkable difference in the photocatalytic efficiency under UV light for mixed oxide nanocomposite with different WO_3 crystal structures.

In order to quantitavely understand the reaction kinetics of the MO degradation in experiments; pseudo first order model is used. The model is expressed as the following equation $-\ln(C/C_o) = kt$, where k is the pseudo first order rate constant [79, 80]. The rate constants are obtained from the linear regression of $-\ln(C/C_o)$ vs. t as shown in Figure 4.59b and 4.59d for m-WO_3/ZnO and h-WO_3/ZnO nanocomposites, respectively. A good correlation for pseudo first order reaction kinetics with $R^2 > 0.95$ is found. The highest reaction rate constant is found to be 3.88 min^{-1} and 3.37 min^{-1} for 10 wt% m-WO_3 and h-WO_3 loaded ZnO nanocomposites, respectively. Since 10 wt% WO_3 showed best results, thus visible light experiments has been carried for pure oxides and 10 wt% and 50 wt% WO_3 loaded ZnO for both the crystal structures.

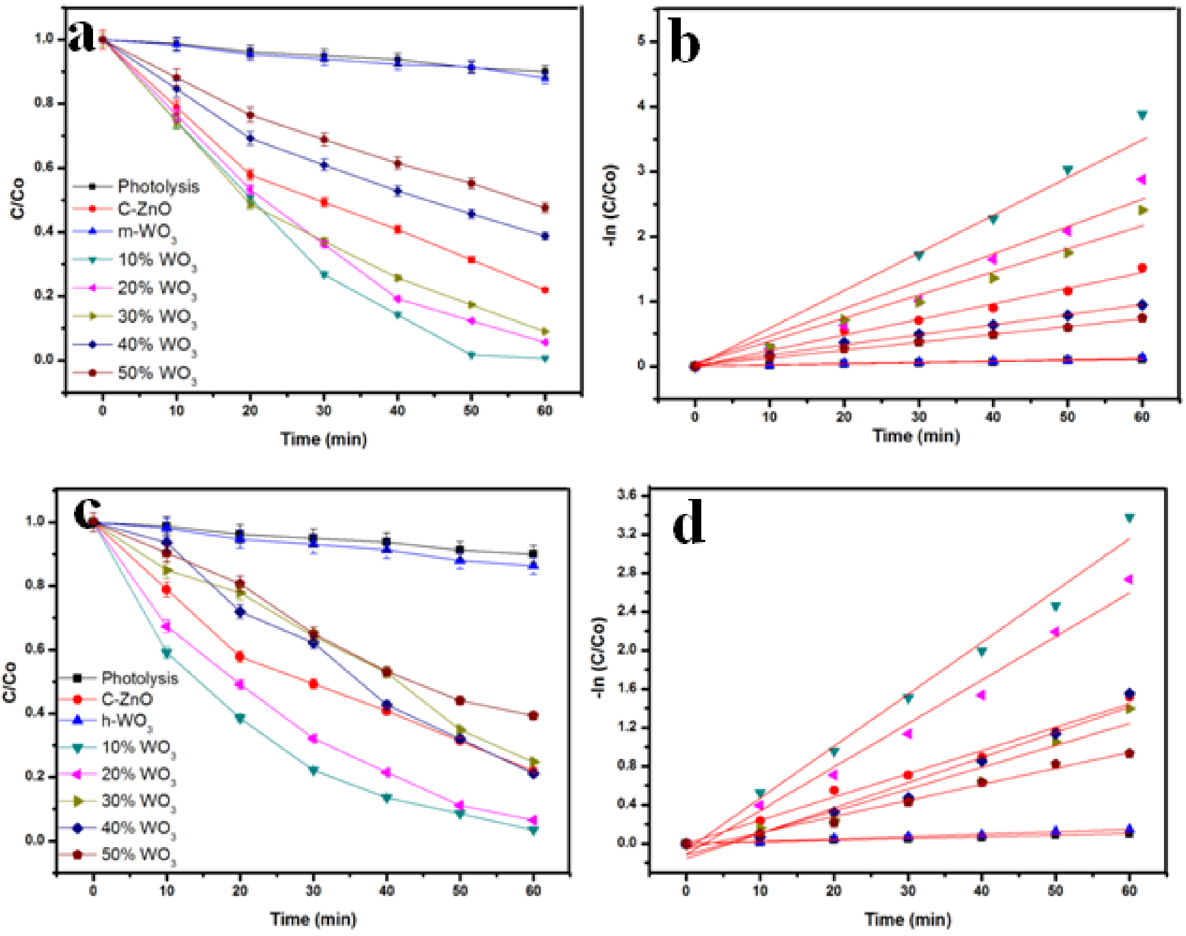

Figure 4.59. Degradation and kinetic profile of MO under UV light for (a) & (b) m-WO_3/ZnO and (c) & (d) h-WO_3/ZnO.

4.3.1.5. Photocatalytic degradation of Methyl Orange under Visible light

Commercial ZnO showed comparatively very less activity of 65% under visible light irradiation than UV irradiation. Pure m-WO_3 and h-WO_3 showed only 20% and 15%

degradation of MO as represented in Figure 4.60a and 4.60c. However, WO_3/ZnO nanocomposite with 10 wt% loading showed enhanced photocatalysis of 85% and 65% for monoclinic and hexagonal form of WO_3. Under visible light, the rate constant for 10% m-WO_3/ZnO is found to be 1.87 min^{-1}which is more than 10% h-WO_3/ZnO (Figure 4.60b and 4.60d). Under UV light irradiation, the efficiency of both monoclinic and hexagonal form is comparable with a difference of 4%. However, irradiations under visible light shows a clear picture on the effect of crystal structure on the photocatalysis of MO dye with a difference of 20% in efficiency. This suggests that WO_3/ZnO nanocomposite is governed by two different mechanisms under UV and visible light which is described in the following section.

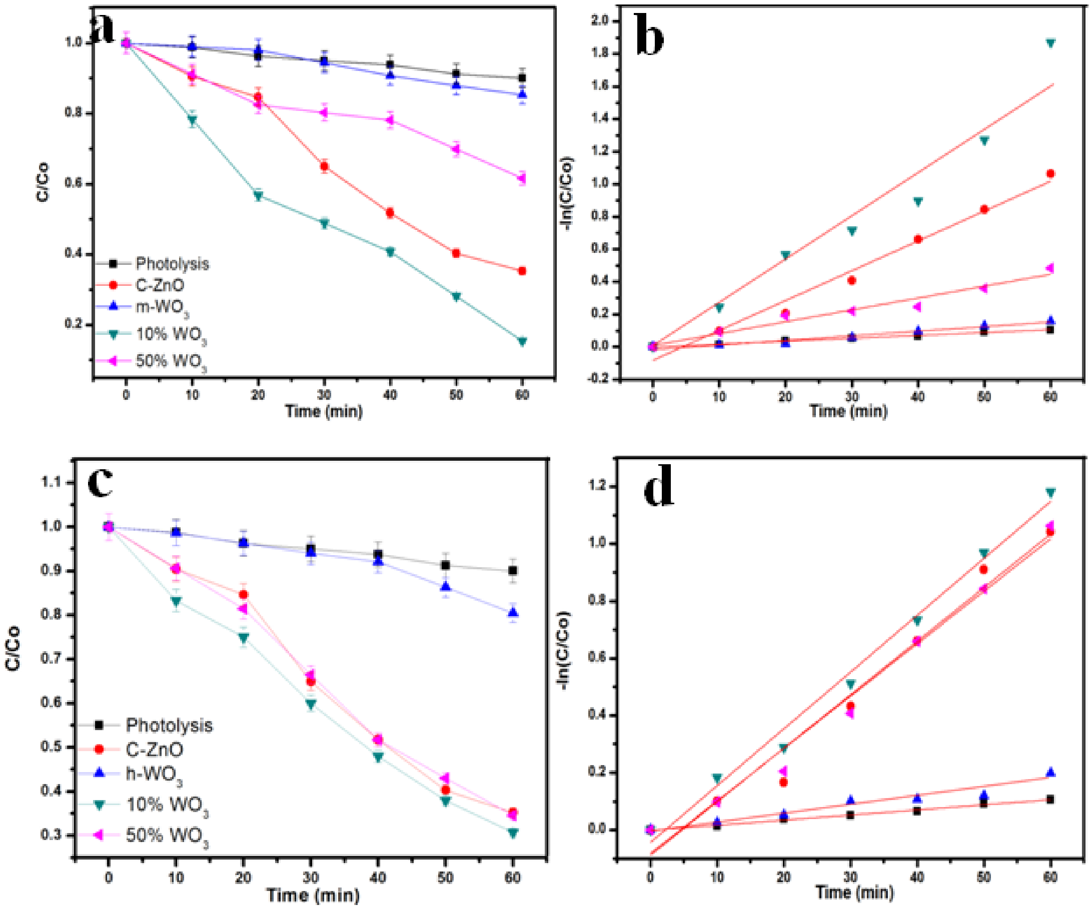

Figure 4.60. Degradation and kinetic profile of MO under Visible light for (a) & (b) m-WO_3/ZnO and (c) & (d) h-WO_3/ZnO.

4.3.1.6. Photocatalytic mechanisms of WO_3-ZnO Nanocomposites

The effect of coupling of WO_3 on the recombination of photogenerated electron and holes in ZnO is investigated through photoluminescence (PL) emission spectra as shown in Figure 4.61. Herein, two emission peaks of pure oxides and mixed nanocomposite are observed, where first emission peak is around 380nm in the UV region which is due to the recombination of photo-generated electrons and holes [81]. Another emission peak is around 470-600 nm that is probably an indirect emission which is related to a surface vacancy on ZnO. Figure 4.61 show that the addition of WO_3 does not change the position of the emission peak in the visible light range. However, a red shift occurred for the emission peak at 380 nm due to the presence of WO_3. Moreover, presence of WO_3 caused a decrease in the intensity of this emission peak, which suggests that the recombination of photo-generated electrons and holes are effectively suppressed by the WO_3. It is seen that among the pure oxides, C-ZnO has less intensity compared to pure m-WO_3 and h-WO_3 under UV region. The lowest intensity is observed for 10% WO_3 loaded oxide nanocomposite.

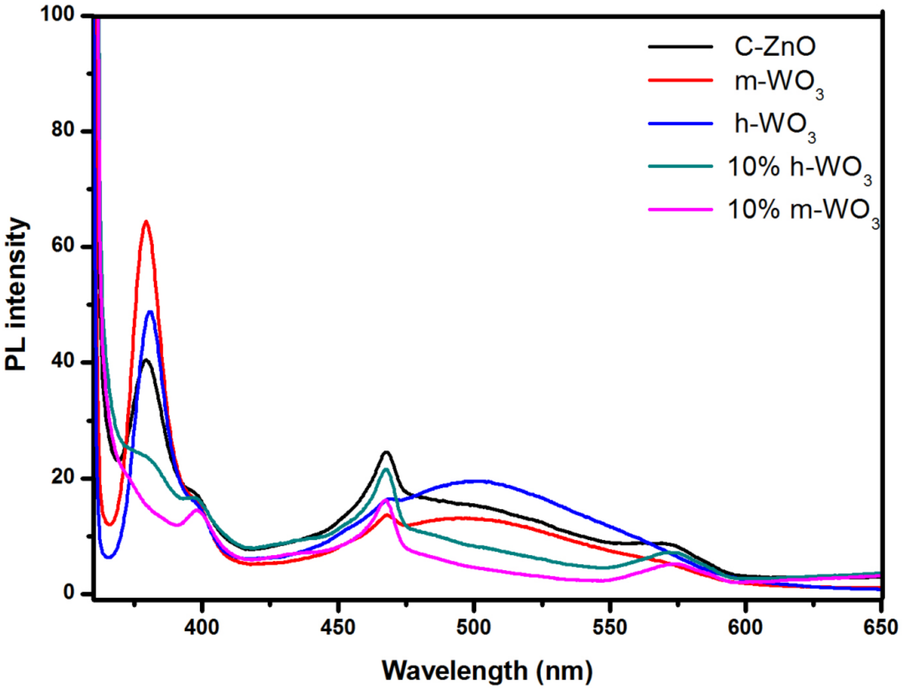

Figure 4.61. Composite photoluminescence spectra of m-WO_3/ZnO and h-WO_3/ZnO mixed oxide nanocomposites.

The photocatalytic mechanism under UV-light irradiation for mixed nanocomposite is probably governed by simultaneous excitation to produce h^+ and e^-. In normal cases, most of electron–hole pairs recombine rapidly; thus the C-ZnO nanoparticles exhibit low photocatalytic activity. The photogenerated electrons easily transfer from the CB of WO_3 to that of ZnO and holes transfer from the VB of ZnO to that of WO_3, suggesting that the photogenerated electrons and holes are efficiently separated. Furthermore, the better separation of photogenerated electrons and holes in the WO_3 and ZnO is confirmed by comparing the PL spectra of the C-ZnO and WO_3/ZnO nanocomposites. The PL spectrum is related to the transfer behavior of the photogenerated electrons and holes; therefore, it can reflect the separation and recombination of photogenerated charge carriers. The lower emission intensity of WO_3/ZnO nanocomposites than C-ZnO indicates that the recombination of the photogenerated charge carrier is inhibited greatly in the presence of WO_3. Thus, the lifetime of the excited electrons and holes can be prolonged in this transfer process, inducing higher quantum efficiency, and therefore, the photocatalytic activity of the as-prepared WO_3/ZnO nanocomposite is enhanced greatly. Subsequently, the photogenerated electrons react with adsorbed O_2 and H_2O on the surface to produce superoxide radical anions such as $\cdot O^{2-}$. The photogenerated holes can be trapped by H_2O and OH^- to further produce ·OH species, which is a strong oxidizing agent. Meanwhile, the O_2 generated from WO_3 loaded photocatalysts promotes the production of the more reactive oxygen species ·OH, which also improves the photocatalytic activity under UV-light irradiation as shown in the schematic Figure 4.62a.

The probable mechanism under visible light could be where WO_3 act as absorber to harvest the visible light energy for photoexcitation of electrons and ZnO as the sink to hold the photogenerated electrons in WO_3/ZnO system until the two systems attain equilibrium. At this equilibrium, the recombination of electron–hole pairs is reduced thereby enhancing the photocatalytic activity of the as-prepared WO_3/ZnO nanocomposites under visible light (Figure 4.62b). In recent similar photocatalytic mechanism of graphite-like C_3N_4 hybridized $ZnWO_4$ nanorods and ZnO/Au &ZnO/Ag under both UV and Visible has been confirmed [82, 83].

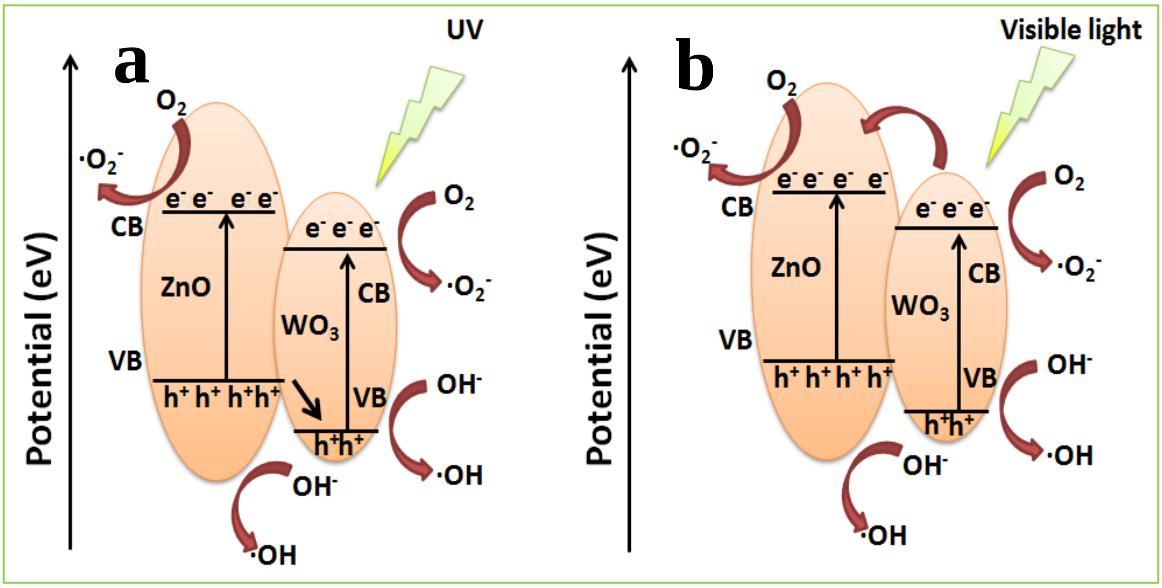

Figure 4.62. Schematic mechanism WO_3-ZnO mixed nanocomposite under (a) UV and (b) Visible light irradiation.

4.3.1.7. Effect of Crystal structure on photocatalysis of WO_3-ZnO Nanocomposites

The different polymorphs of WO_3 affect the efficiency of the photochemical reaction. This effect is better understood under visible light, as observed from the MO degradation profile of the nanocomposites. High rate of reaction has been observed for monoclinic WO_3 than its hexagonal form when composited with ZnO. The hexagonal form of WO_3 has distorted crystal structure with high asymmetry. This distortion attributes to the presence of reduced tungsten as W^{4+} and W^{5+} other than W^{6+} that introduces new discrete energy levels into the band gap. These reduced tungsten atoms are responsible for increased conductance due to small overlapping in the energy levels that eases the hopping of W atoms from one oxidation state to other favouring the easier transport and recombination of electron-hole pairs under visible light energy. But the monoclinic WO_3 is a highly symmetrical and regular structure with no distortion due to reduced tungsten atoms. Thus, it does not produce any discrete energy levels for overlapping, subsequently assists high catalytic efficacy of monoclinic WO_3. The photocatalyst with 10 wt% WO_3/ZnO nanocomposites showed high catalytic efficiency under both UV and visible light. This nanocomposite has high catalytic efficiency due to optimum light absorption that provides enough time for electron trapping as life of reactive species is very short. But nanocomposites with higher content of WO_3 absorb more photons that may lead to low electron accepting efficiency of ZnO due to low ZnO amount in nanocomposites. In consequence, the composites with lower WO_3 content increase the catalytic efficiency and then decreases with higher WO_3.

4.3.1.8. Summary

Surface modification of WO_3 in terms of coupling with ZnO semiconductor is carried out to form WO_3-ZnO nanocomposites. Photodegradation efficiency of methyl orange is influenced by the content of WO_3 in the composite matrix, both crystal structure of WO_3 and source of light energy. Compared to pure ZnO, an optimum 1:9 ratio of WO_3 and ZnO is found fruitful for effective photodegradation due to extension of optical absorption band edge in presence of WO_3 and inhibition of recombination of photoinduced charge carriers as confirmed from UV-DRS and Photoluminescence measurements. Monoclinic WO_3 proves to be a better polymorph for photocatalysis due to high structural symmetry and is a proficient photocatalyst under both UV and visible region. However, WO_3-ZnO composite works differently under these irradiations. Under UV irradiation, WO_3 in the composite acts as hole trapper whereas ZnO under visible light acts as electron trapper to reduce the recombination of these pairs.

4.3.2. Methyl Orange Degradation using Quasi-fibrous ZnO

As discussed in the previous section, optimization of the crystal structure & light energy source has been done through WO_3-ZnO nanocomposites using commercial ZnO. Hence, in this section, combustion synthesized ZnO nanocrystal is investigated for photocatalytic degradation of dye, methyl orange.

4.3.2.1. Photocatalytic Degradation of Methyl Orange

In our study, one step synthesis of ZnO with high yield is achieved through a simple, easy and cost-effective method. Textile industry uses several organic dyes that get released in the water bodies without any prior treatment [84]. Methyl orange (MO) ($C_{14}H_{14}N_3NaO_3S$, Sodium 4-[(4-dimethylamino) phenyldiazenyl] benzenesulfonate) is a typical organic pollutant released from textile industry that has a negative effect on the environment. Therefore, in the present study, combustion synthesized quasi-fibrous ZnO is used for the evaluation of photocatalytic activity against MO dye.

Figure 4.63a shows the degradation profile as C/C_o of MO under dark, UV and visible light conditions, where C is the concentration of MO remaining in the solution after irradiation time t and C_o is the initial concentration. Adsorption – desorption equilibrium is achieved by the stirring the solution in dark for over 90 min. There is no adsorption observed for MO with catalyst for this time period. The degradation percentages of MO under UV and visible light after irradiation of 90 min are 84% and 80%, respectively. Literature reports zinc oxide to be a UV activated photocatalyst because of larger band gap energy (~3.2 eV) with photocatalysis taking place at wavelengths shorter than 400 nm. However, it is observed that the degradation difference between UV and visible light is only 4% for the degradation of MO. This suggests that quasi-fibrous ZnO photocatalyst is more active under UV compared to visible light though the intensity of radiation is different in both cases. Moreover, high crystallinity and BET surface area of particles also play a favorable role to enhance the activity of the photocatalyst [85].

The kinetics of photocatalytic degradation can be described by pseudo first order kinetic rate equation as mentioned in Section 4.6.4. The plot of ln (C/C_o) as a function of irradiation time is shown in Figure 4.63b with correlation coefficient greater than 0.98 supporting the first order rate of reaction. The apparent rate constant for MO degradation under irradiation of UV and visible light is 0.0205 min^{-1} and 0.0183 min^{-1}, respectively. Ma et al. reported similar phenomenon for degradation of methylene blue under UV and visible light using ZnO/Ag_2O heterostructures [86].

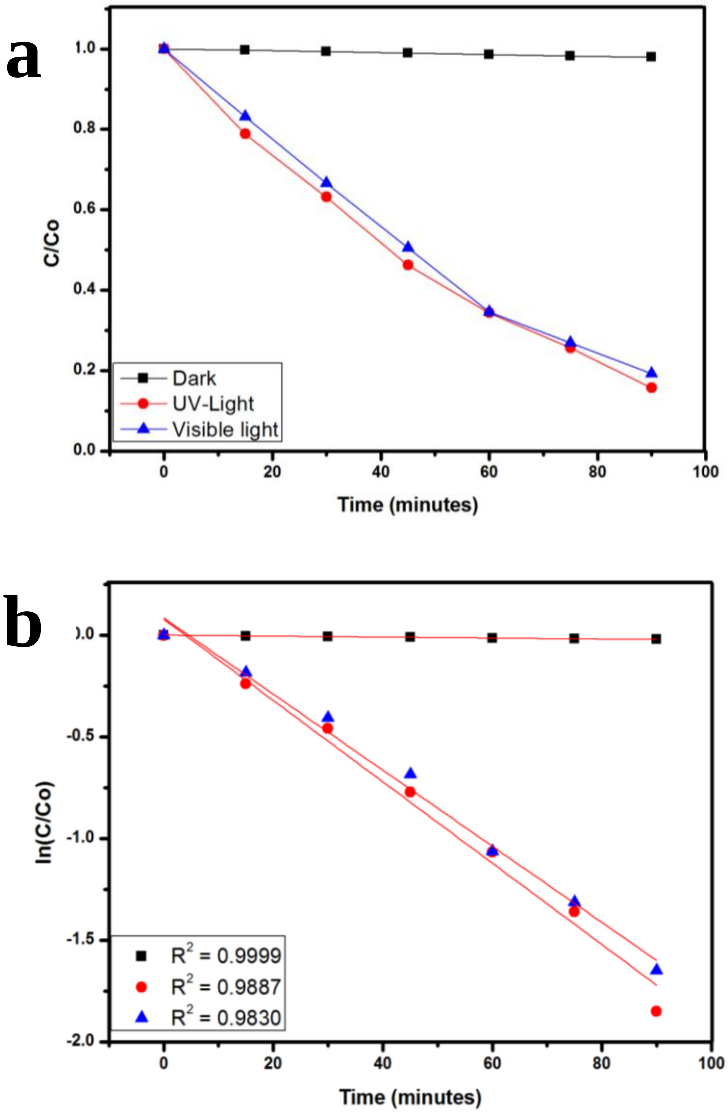

Figure 4.63. (a) Photocatalytic degradation profile and (b) kinetic profile of Methyl Orange.

Recent literature have also depicted similar phenomena where comparatively strong visible activity of ZnO nanocrystals is observed due to anisotropic structures having random pore distribution [87, 88]. Although ZnO shows poor activity under visible light irradiation, the misorientation of lattice planes along the quasi-fiber with random distribution of pore enhances the strain and absorption under visible region. Additionally, the porous nature of the quasi-fiber exposes more sites for photochemical reaction that acts as an added advantage during photocatalysis. Similar porous structures have been observed in an attempt to synthesize hollow structures of ZnO and Pt/ZnO porous nanocages for enhanced photocatalytic activity [89, 90]. Hence, such improved photocatalytic activity can be attributed to the more effective electron-hole separation and larger specific surface area of these specific porous structures. Such improvement of photocatalysis performance implies their potential application in purification of waste water.

4.3.2.2. Reusability and Mechanism of photocatalyst

The reusability of photocatalyst is essential to investigate the stability of photocatalytic performance under both UV and visible region. The synthesized quasi-fibrous ZnO has been used to degrade MO dye for five consecutive cycles, and the results are shown in Figure 4.64a and 4.64b, respectively. Effective photostability is observed for ZnO photocatalyst under visible light irradiation with only a 3.5% decrease in photocatalytic efficiency after five cycles. ZnO after UV irradiation for each cycle shows instability with continuous decrement up to 6% in photocatalytic efficiency at the end of five cycles. This continuous decrease in photocatalytic activity can be attributed to the photocorrosion effect under UV radiation [91]. Photocorrosion of ZnO indicates that in addition to the chemical dissolution process during recycling, photo-assisted dissolution also occurs where both OH^- and hole concentrations at the surface actively take part in the photo-chemical reaction [92]. Thus, a high specific surface area nanoparticle probably favors to adsorb oxygen molecules on the catalyst surface to produce more hydroxyl radicals for faster transport of photogenerated carriers enhancing the photocatalytic activity [93]. These hydroxyl radicals directly trap the organic pollutant for further oxidation. Moreover, the adsorbed oxygen molecules at surface also react with photogenerated electrons to produce superoxide ($\cdot O_2^-$), hydroperoxy ($\cdot OH_2$) and hydroxyl ($\cdot OH^-$) radicals that act as strong oxidizing agents for decomposition of organic dye a shown in Figure 4.65. The excitation of electron to conduction band generates photo-holes that produce hydroxyl radical by trapping the surface hydroxyl group, that also take part in oxidation of dye. However, recombination of electron-hole pair is very difficult to avoid during a photochemical reaction. In our work, ZnO acts as a suitable photocatalyst with good photodegradation efficiency and recycling performance.

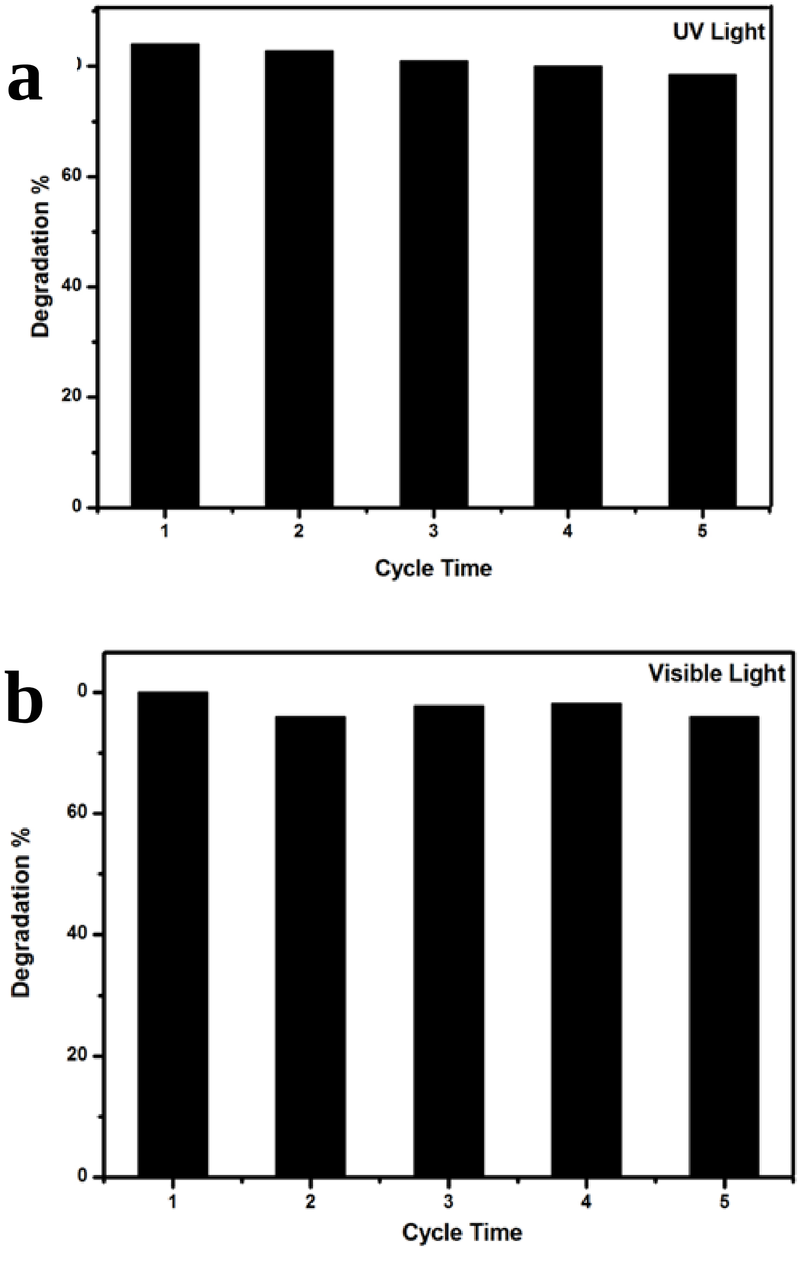

Figure 4.64. Reuse of the photocatalyst under (a) UV light and (b) Visible light.

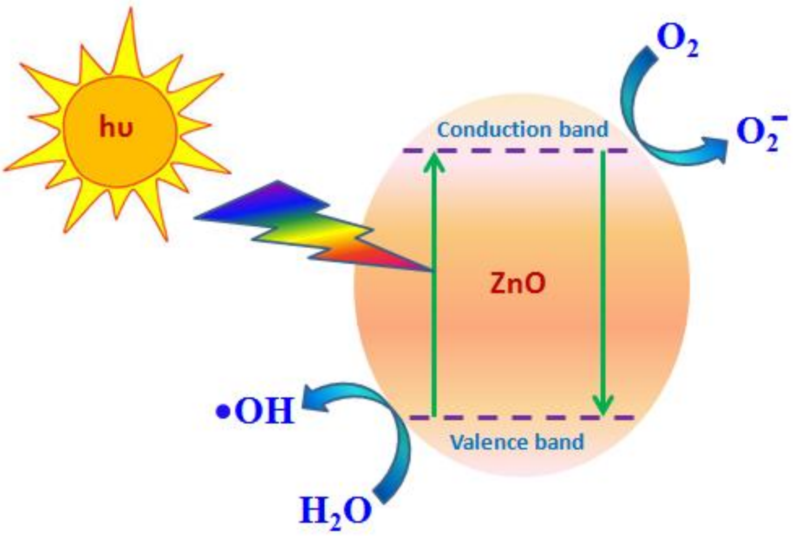

Figure 4.65. Schematic mechanism of ZnO as photocatalyst.

4.3.2.3. Summary

The synthesized quasi-fibrous zinc oxide showed high photocatalytic degradation of the dye (methyl orange) near to 84% and 80% under both UV and visible light irradiation, respectively. While some photocorrosion of quasi-fiber ZnO is observed under UV light, reasonable reuse performance is observed under visible light. MO degradation is found comparable under both UV and visible light irradiation.

4.3.3. Commercial vs. Synthesized Quasi fibrous ZnO in WO_3-ZnO Nanocomposites

In Section 4.3.1, monoclinic WO_3 coupled with ZnO showed high photocatalytic activity comparatively to individual WO_3 and ZnO in degradation of methyl orange. The optimized loading amount of WO_3 in WO_3-ZnO mixed oxide is 10wt%. Furthermore, synthesis of quasi-fibrous ZnO and their comparable methyl orange degradation under UV and visible irradiation is carried in Section 4.3.2. In the present section, a comparison between commercial and combustion synthesized ZnO and their mixed oxide (WO_3-ZnO) is carried to understand the difference in photocatalytic degradation under visible light irradiation taking monoclinic WO_3.

4.3.3.1. Phase & Morphological Analysis

The phase composition, phase structure and morphology of the synthesized WO_3, (Combustion ZnO) CBZ, (Commercial ZnO) CMZ and 10 wt% WO_3-CBZ nanopowders are examined by XRD and FESEM imaging (Figure 4.66). As shown in Figure 4.66a, all of the peaks of WO_3 can be indexed to pure crystalline monoclinic WO_3 (JCPDS card no. 72-0677). All the peaks of CBZ and CMZ are found to well match with the hexagonal wurtzite structure (JCPDS card no. 75-0576) that has been discussed in detail in the previous sections. Since, Section 4.6 concludes 10 wt% WO_3 loading showed best activity with commercial ZnO. Thus, 10wt% WO_3 coupled with combustion synthesized ZnO is used for comparative photocatalytic study. The 10wt % WO_3-CBZ nanocomposite is well indexed for monoclinic WO_3 (*) and hexagonal CBZ (#) that confirms presence of both the phases in the nanocomposite.

Alongside the XRD pattern is given FESEM images of the individual nanopowders and 10% WO_3-CBZ nanocomposites. Figure 4.66b represents the image of 10% WO_3-CBZ where cuboid particles are found embedded into the CBZ matrix that has been described later through SEM element mapping. Commercial ZnO (Figure 4.66c) represents highly agglomerated near spherical and anisotropic particles with average size of ~220nm. However, combustion synthesized ZnO has rod like particles with length ~3μm and width ~0.6μm. Figure 4.66e shows soft agglomerated cuboid like WO_3

nanoparticles with average dimensions 142/118/80 nm[3]. Detail morphological analysis has been discussed in the previous sections.

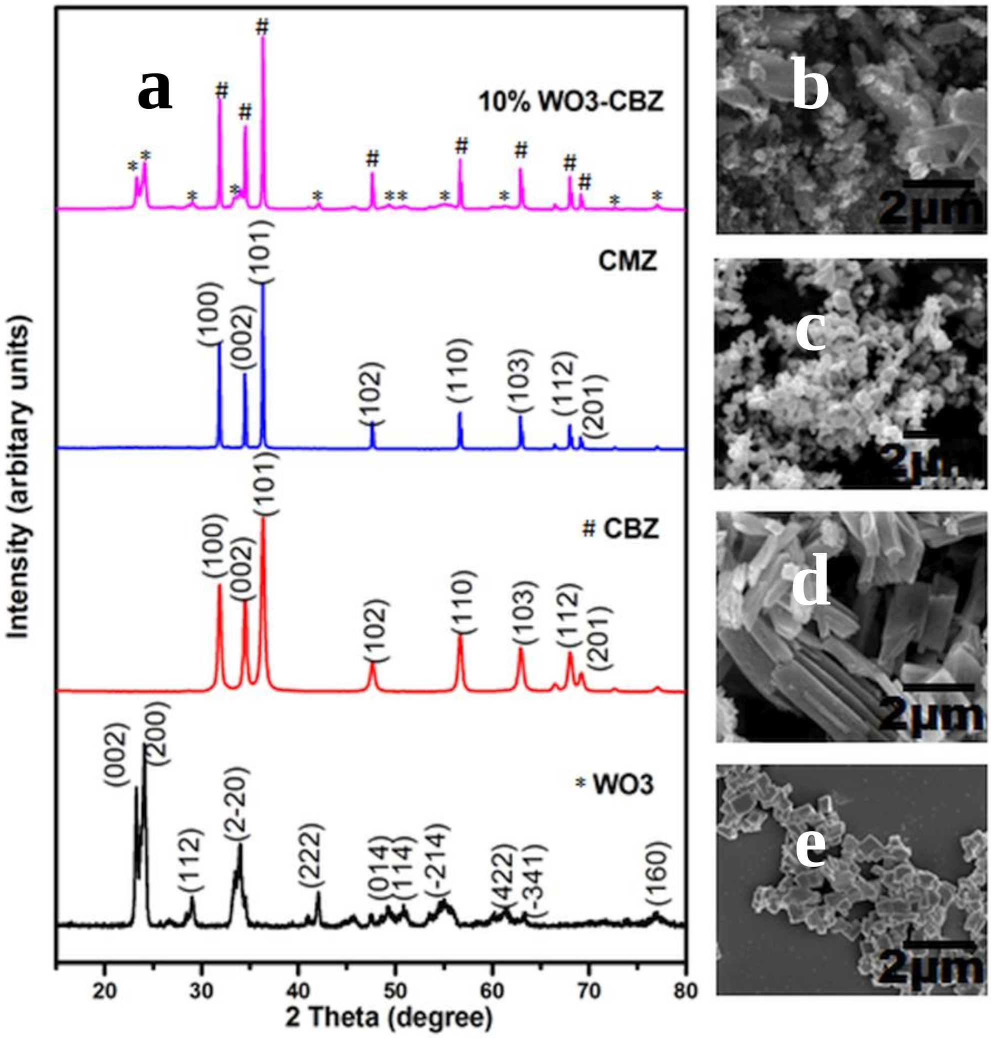

Figure 4.66. (a) Composite XRD pattern and FESEM images of (b) 10% WO_3-CBZ, (c) CMZ, (d) CBZ and (e) WO_3 nanoparticles.

In order to better understand the mixing phenomena and distribution of nanoparticles in the composites, SEM-EDS elemental mapping of 10% WO_3-CBZ and 10% WO_3-CMZ is carried. Figure 4.67a and 4.67b represents the SEM-EDS elemental mapping of 10% WO_3-CBZ and 10% WO_3-CMZ nanocomposites. Although, 10% WO_3-CMZ shows even distribution of W, Zn and O where WO_3 nanocuboids are coated by small CMZ powders but they are seen well adhered on the surface of fibrous ZnO due to interactive mixing and intimate attachment within oxides. It is seen that WO_3 is almost covered by near spherical particles in WO_3-CMZ composite that can affect the photocatalysis.

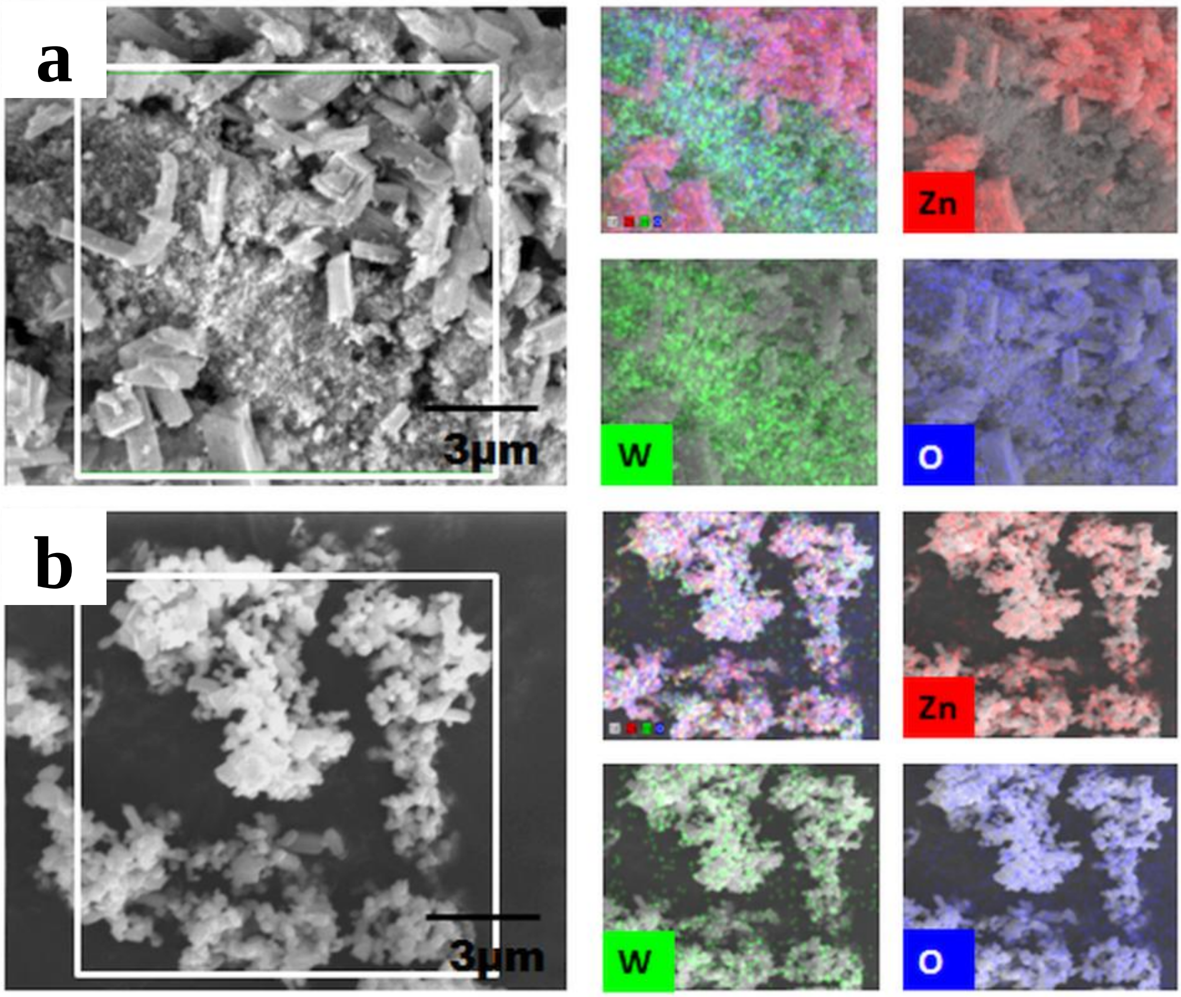

Figure 4.67. FESEM elemental mapping of (a) 10% WO_3-CBZ and (b) 10% WO_3-CMZ.

.

4.3.3.2. Estimation of Band Gap Energy

Figure 4.68 shows the UV-DRS spectra of WO_3, CBZ, 10% WO_3-CBZ and CMZ. Comparing with CBZ, shift in the absorption from approximately 400nm-600nm appeared in the spectrum of 10% WO_3-CBZ nanocomposite, indicating that the as synthesized nanocomposite had the optical ability in the whole range of visible light spectrum [94]. As indicated in figure, the E_g of WO_3, CBZ, 10% WO_3-CBZ and CMZ were calculated as 2.6eV, 2.95eV, 3.05eV and 3.17eV, respectively.

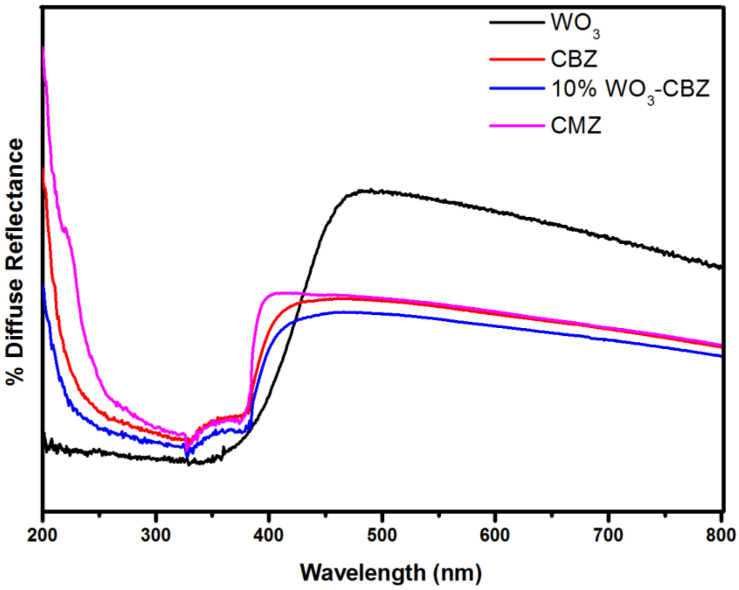

Figure 4.68. Composite UV-DRS plot of WO_3, CBZ, 10% WO_3-CBZ and CMZ.

4.3.3.3. Comparative Photocatalytic Studies

The photocatalytic activity of 10% WO_3-CBZ nanocomposite is studied by degrading methyl orange under visible light irradiation. As a comparison, MO degradation with WO_3, ZnO quasi-fibers, commercial ZnO and 10% WO_3-CMZ are also shown under similar conditions. Figure 4.69a shows degradation profile for MO degradation. As can be seen, only 18% of MO degradation is found with individual WO_3. However, a difference of 12% is observed between CMZ and CBZ that reveals high activity of combustion synthesized ZnO than the commercial ZnO. The dye is 95% degraded in presence of 10% WO_3-CBZ nanocomposites, but, on the other hand, only 85% degradation is observed with 10% WO_3-CMZ.

The kinetic constants of CBZ and 10% WO_3-CBZ is 1.2 and 2.0 times higher than CMZ and 10% WO_3-CMZ. The correlation coefficient (R^2) observed after linear fitting is found > 95 for all the powders that shows photochemical reaction followed first order kinetics (Figure 4.69b). The enhanced photocatalytic performance of 10% WO_3-CBZ nanocomposite can be attributed to effective separation of photogenerated electron-hole pair along with well dispersion of elements in the composite matrix. The possible mechanism for the nanocomposite is harvesting visible light energy through narrow band gap WO_3 present on the surface of quasi fiber ZnO for excitation of electrons. To reduce the recombination of electron-hole pair, the photoexcited electrons gets trapped by ZnO to make the system in equilibrium.

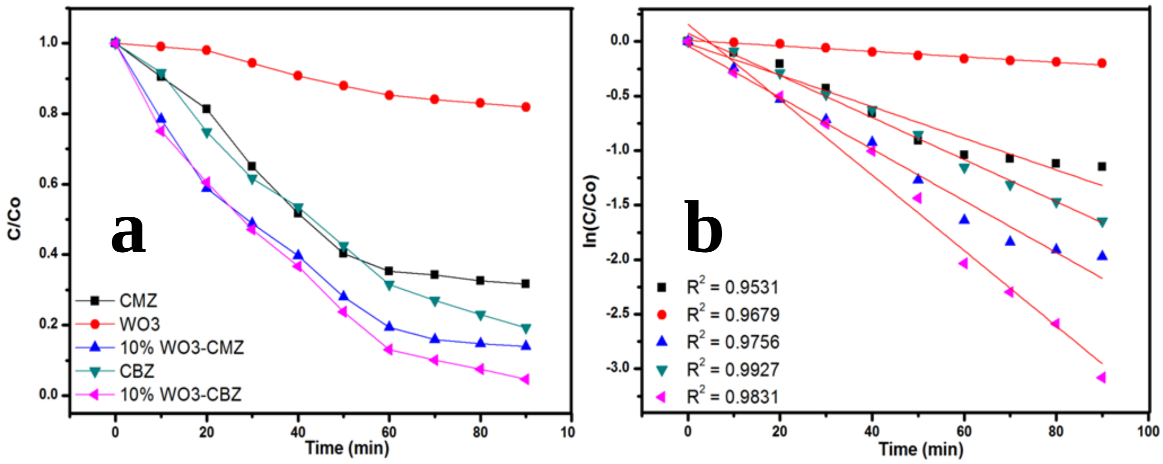

Figure 4.69. (a) Degradation and (b) kinetic profile for methyl orange degradation.

4.3.3.4. Summary

High efficient visible light responsive 10% WO_3-ZnO nanocomposite photocatalyst is prepared by ultrasonic assisted heat treatment method. WO_3 nanocuboids are well dispersed on the surface of ZnO evenly resulting in high degradation of methyl orange than commercial ZnO prepared nanocomposite due to total surface covering of WO_3. The nanocomposite formed from as synthesized WO_3 & ZnO could be an effective photocatalyst for removal of organic pollutants in water.

4.3.4. Highly Efficient WO_3-ZnO Mixed Oxide for Photocatalysis

In the present section, monoclinic WO_3 nanocuboids and combustion synthesized hexagonal ZnO is used to form composites for efficient photodegradation of both the cationic and anionic dyes. Optimization of WO_3 loading has been done based on the photocatalytic experiments following the studies of crystal structure, morphology, surface area and adsorption. Furthermore, band gap and photoluminescence measurement has been performed to understand the photocatalytic activity of optimum WO_3 loaded ZnO for the degradation of both dyes under visible light irradiation.

4.3.4.1. Phase analysis of WO_3-ZnO Mixed Oxides

The indexed diffraction patterns of WO_3 nanocuboids and combustion synthesized ZnO has been shown in Figure 4.66a in previous section. Figure 4.70 represents the XRD pattern of the prepared WO_3-ZnO mixed oxide catalysts through ultrasonic assisted heat treatment method. Constant and clear distinct peak intensity indicates the different percentage content of individual WO_3 and ZnO, respectively.

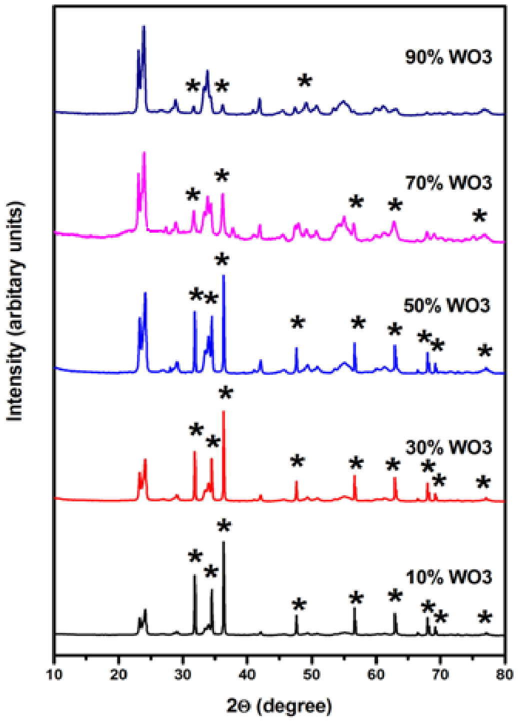

Figure 4.70. Composite XRD pattern of WO_3-ZnO mixed oxide nanocomposites.

4.3.4.2. Morphological analysis of WO_3-ZnO Mixed Oxides

The XRD result depicts the physical content homogenization in the mixture is important that is further confirmed through SEM-EDS elemental mapping in Figure 4.71. A representative FESEM and elemental mapping of an optimum 10% WO_3-ZnO mixed oxide catalyst is shown in Figure 4.71a and 4.71b, respectively. The uniform distribution of elements W, Zn and O predicts the intimate attachment within oxides, where ZnO appears as spherical nature of particles rather than rod shape. Interactive mixing within two different particles is necessary for the effective photocatalytic efficiency, which is further confirmed by TEM analysis after dispersion in liquid media.

More precise particle morphology information is determined from TEM and SAED pattern of the samples as shown in Figure 4.72. TEM and SAED patterns of WO_3 nanocuboids and Quasi-fibrous ZnO are described in detail in Section 4.3 and 4.7, respectively. Figure 4.72a shows the mixture of WO_3 nanocuboid and spherical ZnO particles for an optimum composition of 10% WO_3-ZnO composite oxides.

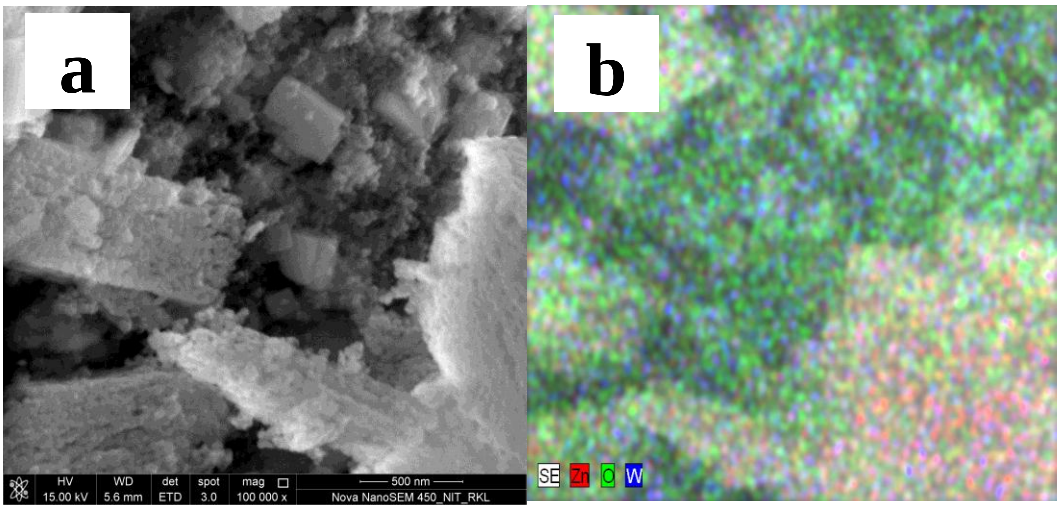

Figure 4.71. (a) FESEM image and (b) FESEM-EDS elemental mapping of 10%WO_3-ZnO.

The particles are well embedded and attached to one another even after well dispersion through ultrasonication, as seen from the TEM image. This embedded system is a favourable accomplishment to achieve high degree of photochemical reaction, which is described later. The corresponding SAED pattern in Figure 4.72b exhibits an ordered pattern from single crystal WO_3 nanocuboid and concentric circles from agglomerated

ZnO spherical particles. The BET surface area of 10% WO_3-ZnO is found to be 15.9 m^2/g. The specific BET surface areas of all the composites have been tabulated in Table 4.4. The surface area of different weight ratio WO_3-ZnO decreases with increasing WO_3 content.

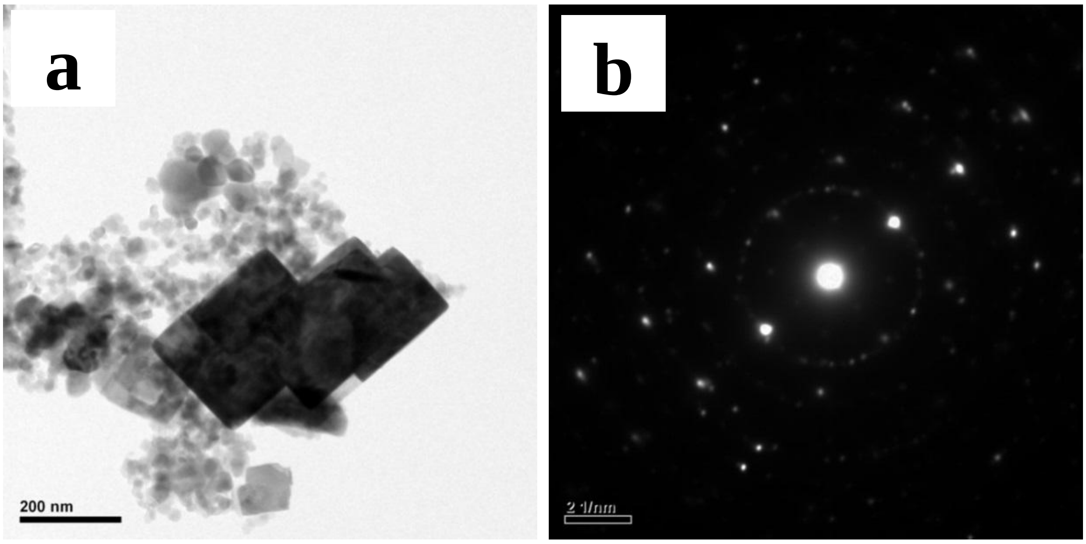

Figure 4.72. (a) TEM image and (b) SAED pattern of 10% WO_3-ZnO nanocomposites.

4.3.4.3. Band Gap Calculation of WO_3-ZnO Mixed Oxides

The Kubelka –Munk (Figure 4.73a) unit of absorption of WO_3, ZnO and WO_3-ZnO mixed oxide composites has been calculated from the following equation: $F(R) = (1–R)^2/2R$ (where R is the reflectance). It is observed that the absorption band is in the wavelength between 380-520 nm for all WO_3, ZnO and WO_3-ZnO mixed oxide composites. Broad tails are observed for WO_3-ZnO mixed oxide samples. The mixed oxide composite shows a slight red shift of band gap absorption in comparison to the pure ZnO. With addition of WO_3 to ZnO, there is the formation of the defect energy levels within the forbidden band that initially increases the band gap energy to 2.98 eV and then decreases with increased loading of the WO_3 in the mixed oxide composites. Band gap energy is estimated using Tauc plot and the extrapolation of the linear slope to photon energy, as shown in Figure 4.73b. The calculated band gap energy has been tabulated in Table 4.5. The band gap of WO_3 and ZnO is found to be 2.78 eV and 2.95 eV, respectively. The energy band gap of 10% WO_3-ZnO mixed oxide composite is almost similar to ZnO that is 2.95 eV but the resultant band gap decreases to 2.25 eV with increasing WO_3 content. However, an optimum content is required to reduce the recombination effect of ZnO.

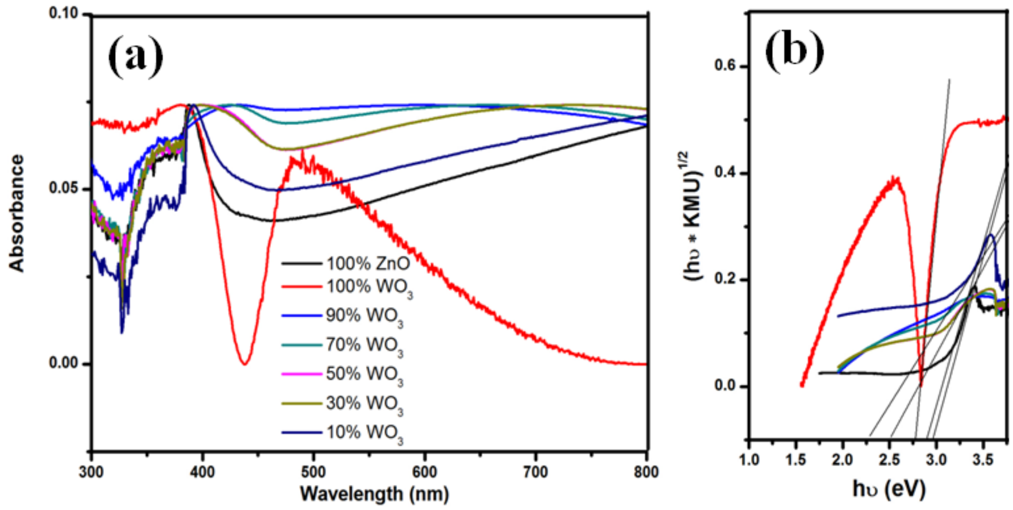

Figure 4.73. (a) UV-Vis absorbance spectra of WO_3, ZnO and WO_3-ZnO mixed oxide composites with different WO_3 loading and (b) Tauc Plot.

Table 4.5. Surface and adsorption properties of WO_3-ZnO mixed oxides.

Catalyst	Surface Area (m^2/g)	Band Gap (eV)	Methylene Blue	Orange G
			% Adsorption	% Adsorption
100% ZnO	17.8	2.95	8%	0%
10%WO_3	15.9	2.98	10%	0%
30%WO_3	14.5	2.52	10%	0%
50%WO_3	11.6	2.55	12%	0%
70%WO_3	9.4	2.25	13%	0%
90%WO_3	6.8	2.25	15%	0%
100% WO_3	5.16	2.78	17%	0%

4.3.4.4. Photocatalytic Studies of WO_3-ZnO Mixed Oxides

The dyes used for photocatalytic studies are Methylene Blue (MB) and Orange G (OG). During the photochemical reaction, adsorption of dye over the catalyst is an important phenomenon to understand the surface reactivity of the catalyst towards dye before photocatalysis. Thus the dye solution along with the catalyst is kept in dark with rigorous stirring for 2 hours to establish adsorption equilibrium. The adsorption of MB in the presence of different mixed oxide has been tabulated in Table 4.5. Maximum and minimum adsorption of 17% and 8% is observed for WO_3 and ZnO, respectively. OG does not show adsorption till 2 hours in the presence of the catalysts. The concentration of the dyes after adsorption is taken as the initial concentration for degradation. The photolysis is carried to understand the photosensitization of dye. In the present experiments, methylene blue and orange G dye is irradiated for 2 hours in the absence of any catalyst but in the presence of light and less than 7% degradation is observed in all cases.

The testing of photocatalytic activity for degradation of MB and OG solution has been carried under metal halide light irradiation. The degradation profile of the MB and OG dye solution with respect to different WO_3 loading (0, 10, 20, 30, 40, 50, and 100 wt%) has been represented in Figure 4.74a & 4.74b, respectively. The zero time in Figure 4.74 and Figure 4.74 corresponds to 2 hours after completion of adsorption equilibrium. Thus, the initial concentration for catalysis is the concentration at the end of the adsorption i.e., after 2 hours. It is clearly evident from the degradation profile (Figure 4.74a and 4.74b) that 10% of WO_3 loading in ZnO shows faster decolourization for both MB and OG under visible light irradiation than ZnO and WO_3. Initially, WO_3 shows very less activity as compared to ZnO but with the decrement of WO_3 loading in ZnO, catalytic activity increases as evident from figure. The composite with 10% WO_3 in ZnO shows 30% higher activity than pure ZnO. High decolourization efficiency of 93% and 89% is observed for MB and OG, respectively.

The photocatalytic performance of the prepared WO_3-ZnO mixed oxide composite is known from the kinetics of the photocatalytic degradation of the MB and OG dye solution, respectively. The kinetic rate constant can be obtained from the linear plot of $-ln(C/C_o)$ with t [95, 96]. The slope obtained gives the rate constant k in min^{-1}. The kinetic plot of both MB and OG with different WO_3 loading is represented in Figure 4.75a and 4.75b, respectively. Both the photodegradation is in accordance with the pseudo first-order kinetic reaction represented by the straight line fitting. The apparent reaction rate constant k (min^{-1}) for different mixed oxide composites for photodegradation of MB and OG has been calculated from the slope of the kinetic plot and shown in

Figure 4.76a and 4.76b, respectively. The obtained rate constant and correlation coefficient from plot is tabulated in Table 4.6.

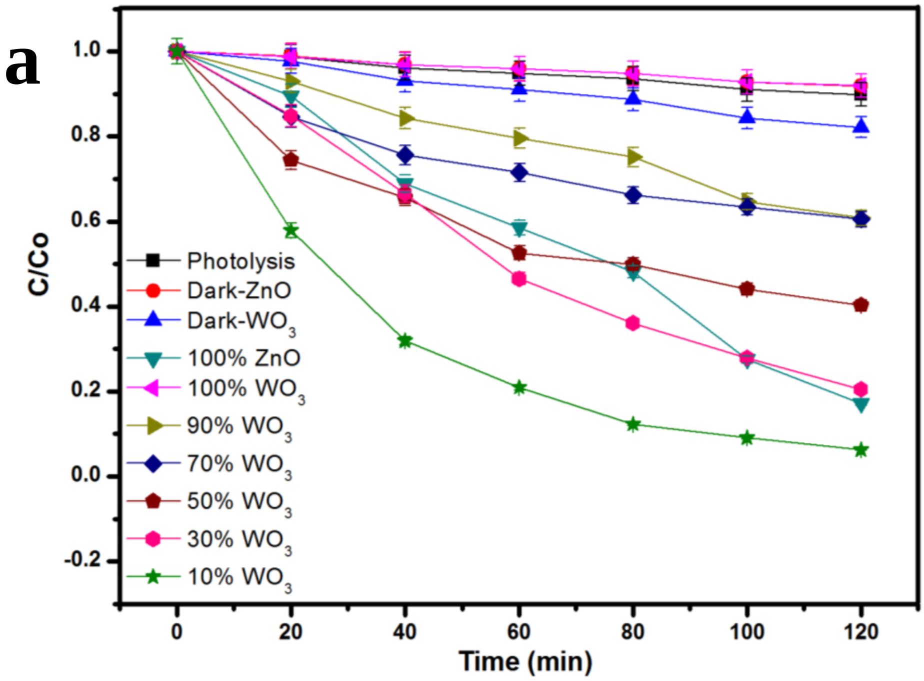

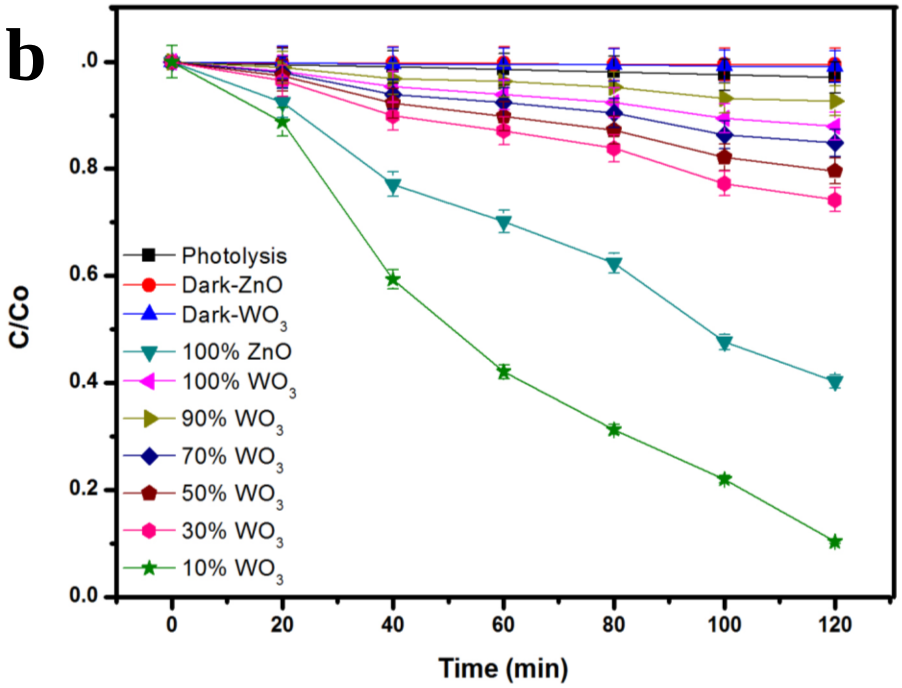

Figure 4.74. Degradation profile of (a) MB and (b) OG with different mixed oxide nanocomposites.

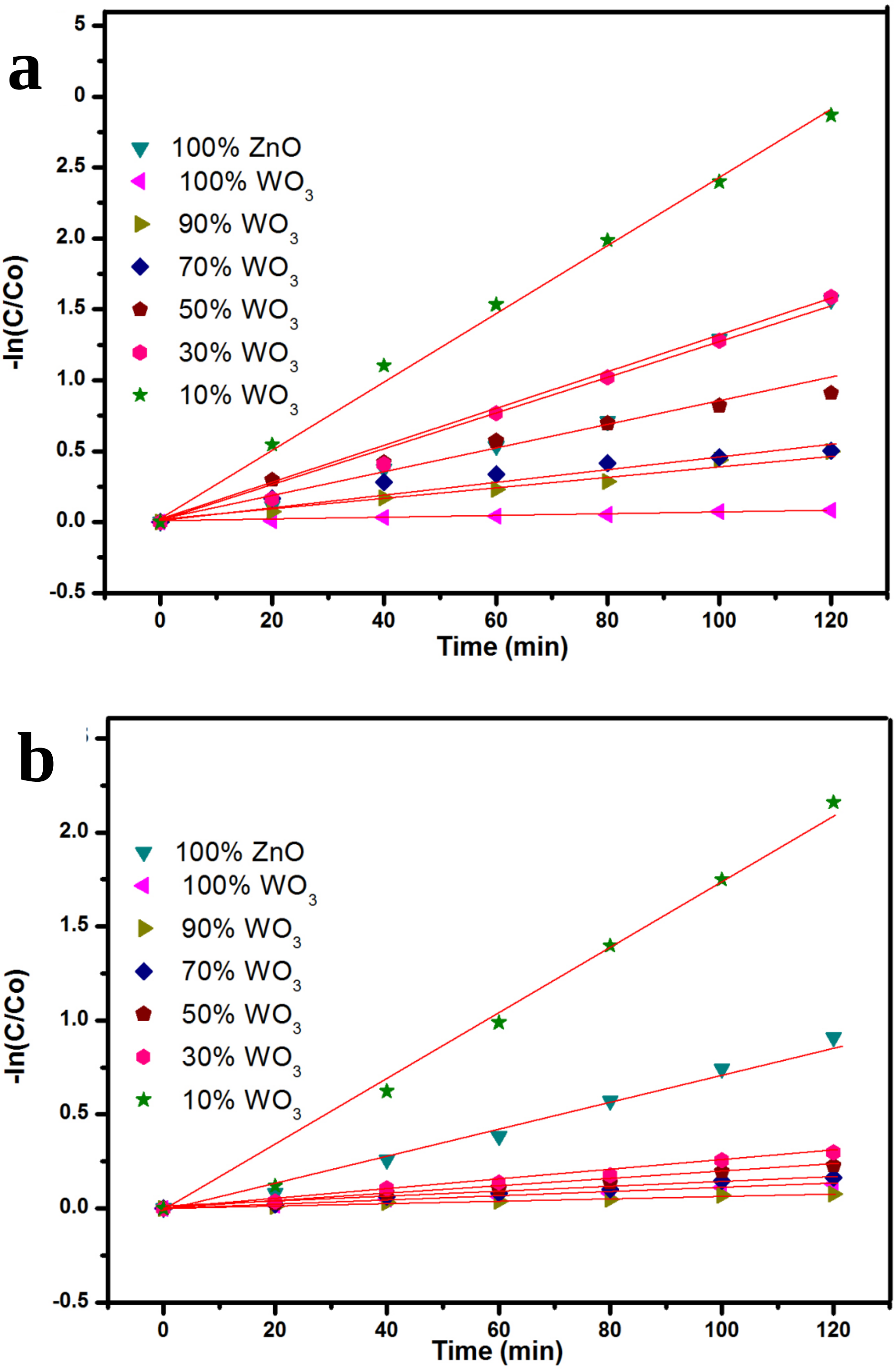

Figure 4.75. Kinetic profile of (a) MB and (b) OG with different mixed oxide nanocomposites.

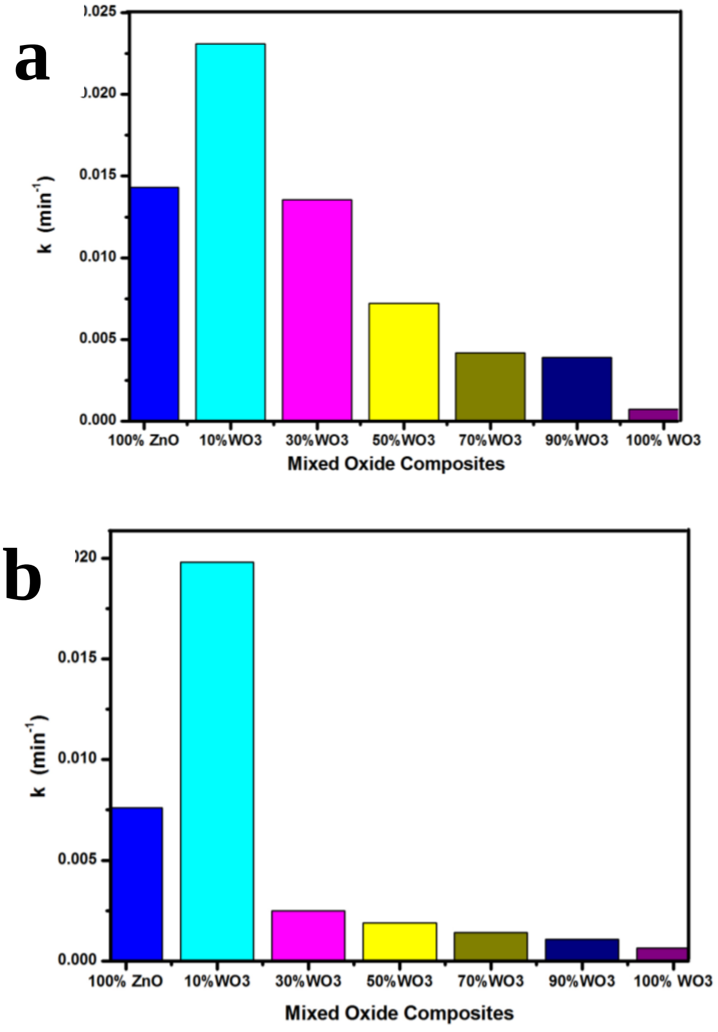

Figure 4.76. Rate constant chart of (a) MB and (b) OG degradation with different mixed oxide nanocomposites.

Table 4.6. Kinetic parameters of MB and OG degradation by WO_3-ZnO mixed oxides nanocomposites.

Catalyst	**Methylene Blue**			**Orange G**		
	% Degradation	**k x 10^2 (min^{-1})**	**R^2**	**% Degradation**	**k x 10^2 (min^{-1})**	**R^2**
100% ZnO	82	1.43	0.9822	59	0.76	0.9862
10%WO_3	93	2.31	0.9878	89	1.98	0.9837
30%WO_3	79	1.35	0.9930	25	0.25	0.9864
50%WO_3	59	0.72	0.9767	20	0.19	0.9886
70%WO_3	39	0.39	0.9797	15	0.14	0.9849
90%WO_3	39	0.41	0.9835	12	0.10	0.9906
100% WO_3	8	0.07	0.9905	7	0.06	0.9877

For comparison, the activity of Degussa P25 TiO_2 for both the dyes is also tested as control experiments under identical conditions and presented in Figure 4.77a & 4.77b. Approximately, 60% and 50% degradation is observed for MB and OG under visible light irradiation, which is less as compared to combustion synthesized ZnO and optimum WO_3-ZnO mixed oxide. This confirms that ZnO absorbs more energy in visible range than standard TiO_2 photocatalyst. It is observed that higher rate constant of 0.0231 min^{-1} and 0.0198 min^{-1} is found with 10% WO_3-ZnO mixed oxide composite for MB and OG, respectively. With decrease in WO_3 content in ZnO, the rate constant value increases thereby increasing the photocatalytic efficiency. The probable reason for increased activity could be attributed to the charge separation mechanism in the WO_3-ZnO mixed composites. The charge separation mechanism has been discussed in the later section. The electron-hole recombination probably reduces with an optimum WO_3 content. The reduction in recombination is further supported by the photoluminescence spectra of the mixed composites as discussed later. Although WO_3 has visible light absorption, lower activity is observed for its narrow band gap resulting in high recombination rate. Therefore, WO_3 can be coupled with other semiconductor materials for charge separation and better photochemical activity.

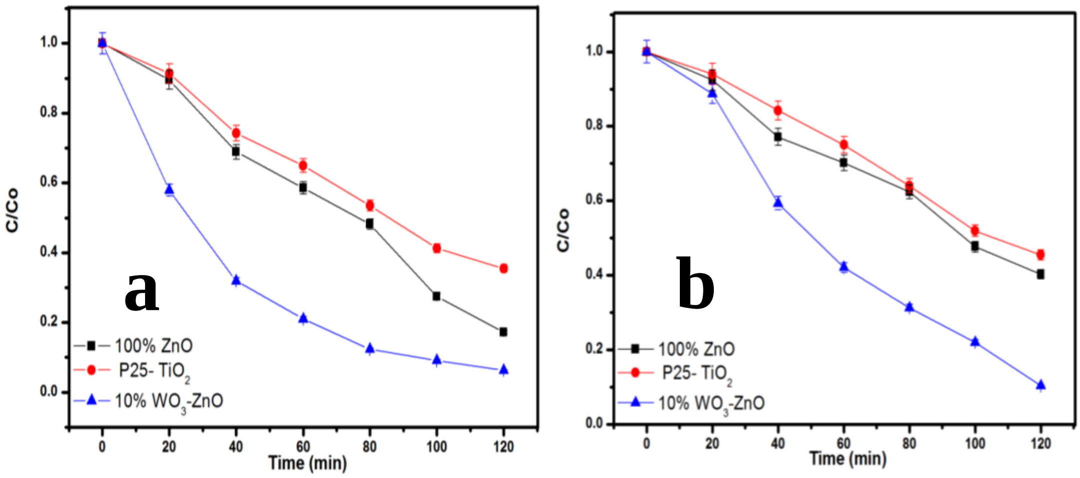

Figure 4.77. (a) MB and (b) OG degradation profile in comparison with Degussa P25 TiO_2.

4.3.4.5. Reuse of the Photocatalyst

Multiple use assessment predicts the long term performance and economic viability of photocatalyst. The reusability of the optimum 10 wt% WO_3 mixed ZnO describes the consecutive photocatalytic degradation efficiency for both MB and OG as shown in Figure 4.78. Each time centrifugation of the catalyst is carried to remove the solid catalyst and the catalyst is dried at 100 ^{o}C for further use. Initially, 93% MB degradation is found in 1st run which decreases as 92%, 90% and 84% in 2nd, 3rd and 4th run, respectively (Figure 4.78a). Similarly, OG degrades as 89%, 88%, 86% and 83% in 1st, 2nd, 3rd and 4th run, respectively (Figure 4.78b). The photocatalytic activity decreases till 10% and 6% for MB and OG, respectively for 4 consecutive cycles, as observed from the figure. Each reusable experiment is carried after proper adsorption-desorption equilibrium. To better understand the material stabilization of the reused catalyst composite XRD pattern of the optimized catalyst and reused catalyst after 4th run is shown in Figure 4.78c.

XRD pattern shows no significant change in the crystal structure after four consecutive cyclic runs of the catalyst. One of the probable reasons for decreasing activity could be leaching of the surface during the photocatalytic reaction attributing to the loss of active support sites. Moreover, the consecutive heat treatment after each cycle decreases the surface area of the catalyst resulting in partial aggregation of catalyst. The organic intermediates that are formed during the catalytic process can also adsorb on the surface, thereby reducing the overall efficiency of the photocatalyst. In addition, loss of catalyst also occurs during repetitive runs resulting in reduced photoreactivity [97]. The above results suggest that the reactivity of the catalyst is completely effective till four consecutive cycles under metal halide irradiation. The working mechanism of the photocatalyst has been discussed in the later section.

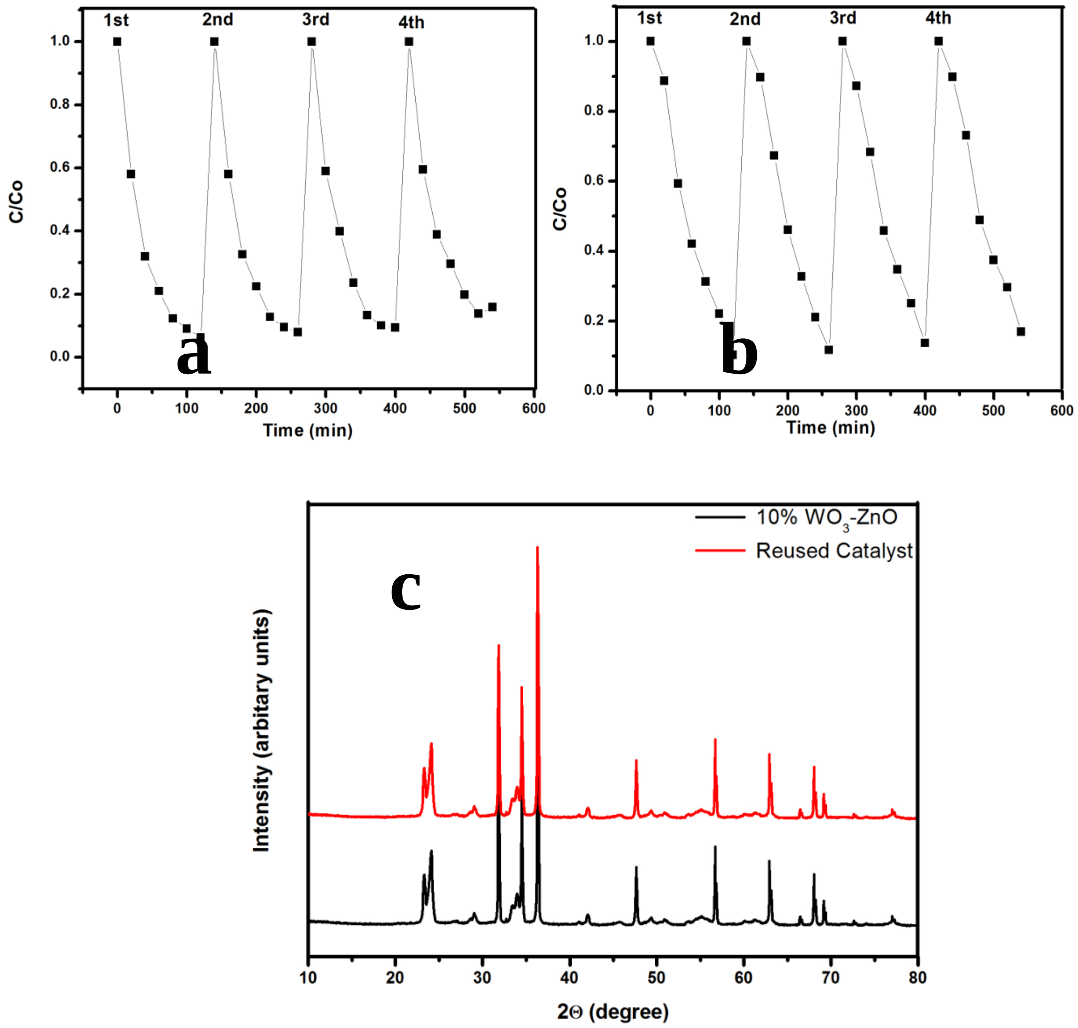

Figure 4.78. Degradation profile on reusability of the 10% WO_3-ZnO mixed oxides (a) MB, (b) OG and (c) Composite XRD pattern of the catalyst and after reuse.

4.3.4.6. Mechanism of Mixed Semiconductor Photocatalyst

WO_3 and ZnO nanoparticles are typical semiconductors. Figure 4.79 shows the possible energy storage mechanism of ZnO in presence of WO_3 when both are irradiated under visible light. The higher photocatalytic activity of the 10% WO_3-ZnO composite attributes to the energy level difference of WO_3 and ZnO that narrows the band gap. In the present system, WO_3 acts as absorber due to its absorption in visible region but narrow band gap (2.7 eV) facilitates the recombination of electron-hole pair through coupling with ZnO. When WO_3-ZnO mixed oxide composite is radiated by visible light, the activation of ZnO to produce the photogenerated electron/hole pairs is not possible due to its large absorption gap, while narrow band gap WO_3 can efficiently absorb the visible light and gets excited to generate electron/hole pairs. The photogenerated electrons generated in WO_3 transfer its electrons to conduction band of ZnO reducing the probability of recombination of photogenerated electron/hole pairs and increasing the number of active species for degradation. Thus, ZnO play as a co-catalyst that traps the electron from further recombination. The photoelectrons easily traps the dissolved O_2 to form superoxide ($\cdot \mathrm{O}_2^-$) anion radical and photoinduced holes trap OH^- to form •OH radical to photodegrade dyes [98]. The reactivity of formed radicals ·OH and $\cdot O_2^-$ are enough to efficiently degrade the organic dye molecules. The charge separation and probable photocatalytic reaction follows the steps given below [99, 100]:

Electron-hole pair generation:

$$WO_3 + hv \rightarrow WO_3\,(e^- \cdots h^+)$$

$$ZnO + hv \rightarrow ZnO\,(e^- \cdots h^+)$$

Charge transfer reaction:

$$WO_3(e^- \cdots h^+)/ZnO\,(e^- \cdots h^+) \rightarrow WO_3\,(e^-)/ZnO\,(h^+)$$

Radical formation:

$$WO_3(e^-) + O_2 \rightarrow WO_3 + \cdot \mathrm{O}_2^-$$

$$ZnO\,(h^+) + OH^- \rightarrow ZnO + \cdot \mathrm{OH}$$

Dye degradation:

$$Dye + \cdot \mathrm{O}_2^- / \cdot \mathrm{OH} \rightarrow \text{Mineral acids} + \mathrm{CO}_2 \uparrow + \mathrm{H}_2\mathrm{O}$$

$$Dye + \cdot \mathrm{OH} \rightarrow \text{Mineral acids} + \mathrm{CO}_2 \uparrow + \mathrm{H}_2\mathrm{O}$$

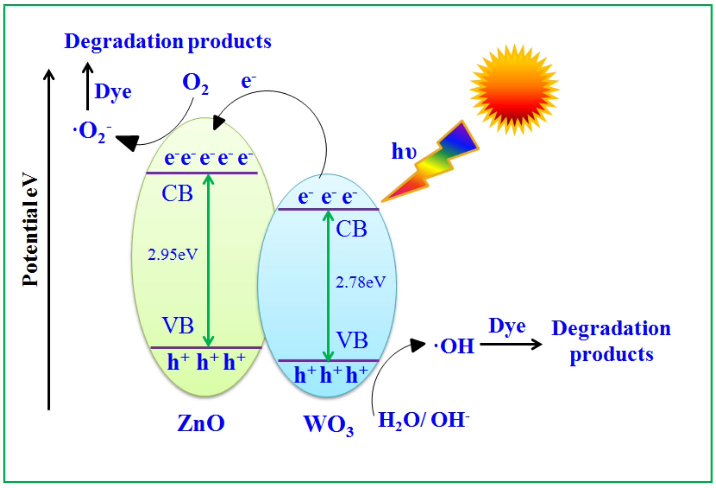

Figure 4.79. Schematic mechanism of degradation by WO_3-ZnO mixed oxide nanocomposite.

4.3.4.7. Photoluminescence Study

The photo-recombination rate of electron-hole pair can be studied from the photoluminescence (PL) spectrum. Figure 4.80 represents the composite PL spectrum of ZnO, WO_3, 70% WO_3, 50% WO_3 and 10% WO_3, respectively. The shift of absorption intensity towards higher wavelength is observed well in the absorption spectra as discussed in earlier (see Figure 4.73a). It depicts the onset of absorption in the visible region from wavelength of nearly 350 nm which is similar to the visible light photocatalyst CdS-ZnS/ZTP, as reported by Biswal et al [47]. When the samples are excited at this particular wavelength, an intense emission peak appears at ~700 nm wavelength for all the samples. Unlike absorption spectra, the PL emission spectra do not shift to higher wavelength but shows change in intensity with respect to WO_3 loading. The change in intensity follows the sequence of 10% WO_3 < ZnO < 50% WO_3 < 70% WO_3 < WO_3, respectively. The PL intensity is suppressed in the presence of 10% WO_3 with ZnO. Pure WO_3 shows the maximum intensity that depicts the highest recombination rate. The reduction in intensity directly relates to the suppression of the electron-hole recombination rate. The reduced recombination rate reveals the efficient charge transfer within the catalyst mixture [101]. This means that more hydroxyl radicals ·OH can be produced in the system containing 10% WO_3-ZnO than that containing pure WO_3, which is advantageous to the visible light photocatalytic activity of WO_3.

Increasing WO_3 content may lead to low electron accepting efficiency of ZnO due to less amount of ZnO in nanocomposites. This can prove as a disadvantage to the visible light photocatalytic activity of the composites. Consequently, the visible light photocatalytic activity of the investigated composites increases at first and then decreases as the WO_3 content increases.

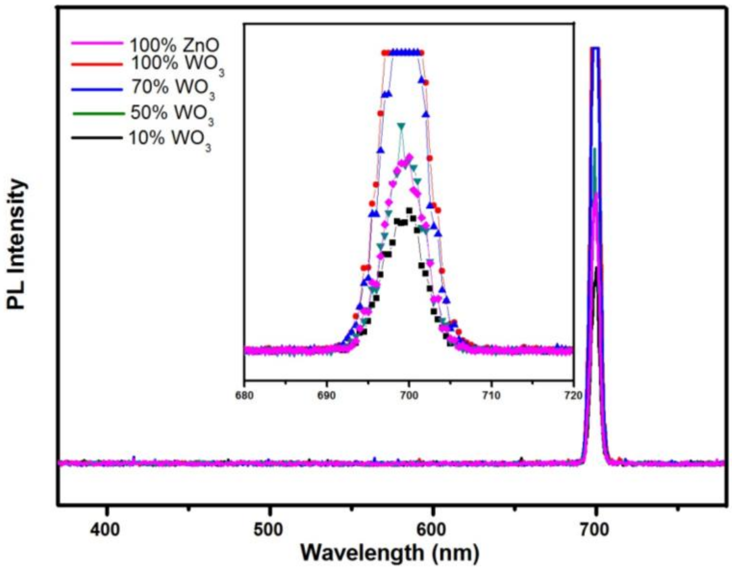

Figure 4.80. Composite photoluminescence spectra of WO_3, ZnO and WO_3-ZnO mixed oxide composites with different WO_3 loading.

4.3.4.8. Summary

An optimum amount 1: 9 of nanocuboid WO_3 and quasi fiber ZnO was found to be an effective mixed oxide mixture for the photocatalytic decomposition of cationic dye methylene blue and anionic dye orange G, respectively. WO_3 acts as absorber of solar energy and ZnO as co-catalyst to reduce the electron-hole recombination. However, higher content of WO_3 beyond 10 wt% decreases the photocatalytic activity due to increasing recombination rate of electron-hole pairs, as supported by the increasing intensity in photoluminescence spectra. The recombination rate is found to reduce in the presence of 10 wt% WO_3. The mixed oxide can be reused effectively though the degree of efficiency slightly decreases with increasing number of cycles.

References:

[193] H. Zheng, J. Z. Ou, M. S. Strano, R. B. Kaner, A. Mitchell, K. Kalantar-zadeh, Nanostructured tungsten oxide-properties, synthesis and applications, Adv Funct Mater, 2011, 21, 2175-2196.

[194] A.R. Kortan, R. Hull, R.L. Opila, M.G. Bawendi, M.L. Steigerwald, P. Carroll, L.E. Brus, Nucleation and growth of cadmium selenide on zinc sulfide quantum crystallite seeds, and vice versa, in inverse micelle media, J Am Chem Soc, 1990, 112, 1327- 1335.

[195] L. Brus, Chemical approaches to semiconductor nanocrystals, J Phys Chem Solids, 1998, 59, 459-465.

[196] C. Santato, M. Odziemkowski, M. Ulmann, J. Augustynski, Crystallographically oriented mesoporous WO_3 films: synthesis, characterization, and applications, J. Am. Chem. Soc., 2001, 123, 10639-10649.

[197] Y. Zhang, Y. Chen, H. Liu, Y. Zhou, R. Li, M. Cai, X. Sun, Three-Dimensional hierarchical structure of single crystalline tungsten oxide nanowires: construction, phase transition, and voltammetric behavior, J Phys Chem C, 2009, 113, 1746-1750.

[198] Z. Wang, X. Hu, Electrochromic properties of TiO_2-doped WO_3 films spin-coated from Ti-stabilized peroxotungstic acid, Electrochim Acta, 2001, 46, 1951-1956.

[199] F. Kleitz, W. Schmidt, F. Schuth, Calcination behavior of different surfactant-templated mesostructured silica materials, Microporous Mesoporous Mater, 2003, 65, 1-29.

[200] B. Yang, Y. Zhang, E. Drabarek, P.R.F. Barnes, V. Luca, Enhanced photoelectrochemical activity of sol−gel tungsten trioxide films through textural control, Mater. Chem., 2007, 19, 5664-5672.

[201] B. Pecquenard, S.C. Garcia, J. Livage, P.Y. Zavalij, M.S. Whittingham, R. Thouvenot, Structure of hydrated tungsten peroxides $[WO_2(O_2)H_2O]\cdot nH_2O$, Chem Mater, 1998, 10, 1882-1888.

[202] Z. Wang, X. Li, Z. Feng, The effect of CTAB on the citrate sol-gel process for the synthesis of sodium beta-alumina nano-powders, Bull. Korean Chem. Soc., 2011, 32, 1310-1314.

[203] K. Harikrishna, O. M. Hussain, C.M. Julien, Electrochromic properties of nanocrystalline WO_3 thin films grown on flexible substrates by plasma-assisted evaporation technique, Appl Phys A, 2010, 99, 921–929.

[204] G.A. de Wijs, R.A. de Groot, Structure and electronic properties of amorphous WO_3, Phys Rev B, 1999, 60, 16463-16474.

[205] K. Bange, Colouration of tungsten oxide films: A model for optically active coatings, Sol Energy Mater Sol C, 1999, 58, 1-131.

[206] E. D. Nikitin, P.A. Pavlov, A.P. Popov, H.E. Nikitina, Critical properties of hydrogen peroxide determined from direct measurements, J Chem Thermodyn, 1995, 27, 945-952.

[207] N. Singh, S. Mittal, K.N. Sood, P.K. Rashmi, K. Gupta, controlling the flow of nascent oxygen using hydrogen peroxide results in controlling the synthesis of ZnO/ZnO_2, Chalcogenide Lett, 2010, 7, 275-281.

[208] L. Zhou, J. Zou, M. Yu, P. Lu, J. Wei, Y. Qian, Y. Wang, C. Yu, Green synthesis of hexagonal-Shaped $WO_3\cdot0._{33}H_2O$ nanodiscs composed of nanosheets, Cryst Growth Des, 2008, 11, 3993-3998.

[209] Y. Choi, G. Sakai, K. Shimanoe, N. Miura, N. Yamazoe, Wet process-prepared thick films of WO_3 for NO_2 sensing, Sens Actuators B, 2003, 95, 258-265.

[210] C.J. Kiely, J. Fink, M. Brust, D. Bethell, D.J. Schiffrin, Spontaneous ordering of bimodal ensembles of nanoscopic gold clusters, Nature, 1998, 396, 444-446.

[211] M. Shen, Y. Du, P. Yang, L.J. Jiang, Morphology control of the fabricated hydrophobic gold nanostructures in W/O microemulsion under microwave irradiation, J Phys Chem Solids, 2005, 66, 1628-1634.

[212] S. J. Kim, I.S. Hwang, J.K. Choi, J.H. Lee, Gas sensing characteristics of WO_3 nanoplates prepared by acidification method, Thin Solid Films, 2011, 519, 2020-2024.

[213] O. Yayapao, T. Thongtem, A. Phuruangrat, S. Thongtem, CTAB-assisted hydrothermal synthesis of tungsten oxide microflowers, J Alloys Comps, 2011, 509, 2294-2299.

[214] M.A. Butler, Photoelectrolysis and physical properties of the semiconducting electrode WO_2 , J Appl Phys, 1977, 84, 1914-1920.

[215] Y. Sun, C.J. Murphy, K.R.R. Gil, E.A.R. Garcia, J.M. Thornton, N.A. Morris, D. Raftery, Photoelectrochemical and structural characterization of carbon-doped WO_3 films prepared via spray pyrolysis, Int J Hydrogen Energy, 2009, 34, 8476-8484.

[216] A. Novinrooz, M. Sharbatdaran, H. Noorkojouri, Structural and optical properties of WO_3 electrochromic layers prepared by the sol-gel method, Central Eur J Phys, 2005, 3, 456.

[217] X. He, C. Hu, Q. Yi, X. Wang, H. Hua and X. Li, Preparation and improved photocatalytic activity of $WO_3 \cdot 0._{33}H_2O$ nanonetworks, Catal Lett, 2012, 142, 637-645.

[218] B. X. Li, G. X. Rong, Y. Xie, L. F. Huang, C. Q. Feng, Low-temperature synthesis of α-MnO_2 hollow urchins and their application in rechargeable Li^+ batteries, Inorg Chem, 2006, 45, 6404-6410.

[219] H. Hassani, E. Marzbanrad, C. Zamani, B. Raissi, Effect of hydrothermal duration on synthesis of WO_3 nanorods, J Mater Sci : Mater Electron, 2011, 22, 1264-1268.

[220] S. H. Baeck, K. S. Choi, T. F. Jaramillo, G. D. Stucky, E. M. McFarland, Enhancement of photocatalytic and electrochromic properties of electrochemically fabricated mesoporous WO_3 thin films, Adv mater, 2003, 15, 1269-1273.

[221] A. G. S. Filho, J. M. Filho, V. N. Freire, A. P. Ayala, J. M. Sasaki, P. T. C. Freire, F. E. A. Melo, J. F. Juliao, U. U. Gomes, Phase transition in WO_3 microcrystals obtained by sintering process, J Raman Spectrosc, 2001, 32, 695-699.

[222] P. Arunkumar, C. Jayajyothi, D. Jeyakumar, N. Lakshminarashimhan, Structure property relations in hexagonal and monoclinic $BiPO_4:Eu^{3+}$ nanoparticles synthesized by polyol mediated method, RSC Adv, 2012, 2, 1477-1485.

[223] D. Sarkar, M. Chu, S. Cho, Y. Kim and B. Basu, Synthesis and morphological analysis of titanium carbide nanopowder, J. Am. Ceram. Soc., 2009, 92, 2877-2882.

[224] P. Reiss, M. Protiere, L. Li, Core/Shell Semiconductor Nanocrystals, Small, 2009, 5, 154-168.

[225] F. Huang, H. Zhang, J. F. Banfield, Two-Stage Crystal-Growth Kinetics Observed during Hydrothermal Coarsening of Nanocrystalline ZnS, Nano Lett., 2003, 3, 373- 378.

[226] J. Ma, J. Zhang, S. Wang, T. Wang, J. Lian, X. Duan, W. Zheng, Topochemical Preparation of WO_3 Nanoplates through Precursor H2WO4 and Their Gas-Sensing Performances, J. Phys. Chem. C, 2011, 115, 18157-18163.

[227] S. Pokhrel, J. Birkenstock, M. Schowalter, A. Rosenauer, L. Madler, Growth of Ultrafine Single Crystalline WO_3 Nanoparticles Using Flame Spray Pyrolysis, Cryst. Growth Des., 2010, 10, 632-639.

[228] H. Hayashi, Y. Hakuta, Hydrothermal Synthesis of Metal Oxide Nanoparticles in Supercritical Water, Materials, 2010, 3, 3794-3817.

[229] X. Su, F. Xiao, Y. Li, J. Jian, Q. Sun, J. Wang, Synthesis of uniform WO_3 square nanoplates via an organic acid-assisted hydrothermal process, Mater. Lett., 2010, 64, 1232-1234.

[230] D. L. Chen, H. Wang, R. Zhang, L. Gao, Y. Sugahara, A. Yasumori, Single-crystalline tungsten oxide nanoplates, J. Ceram. Process. Res., 2008, 9, 596-600.

[231] B. Yang, P. R. F. Barnes, Y. Zhang, V. Luca, Tungsten Trioxide Films with Controlled Morphology and Strong Photocatalytic Activity via a Simple Sol–Gel Route, Catal. Lett., 2007, 118, 280-284.

[232] Z.L. Wang, Splendid one-dimensional nanostructures of zinc oxide: a new nano materials family for nanotechnology, Nano, 2008, 2, 1987–1992.

[233] J. Su, L. Guo, N. Bao, C.A. Grimes, Nanostructured $WO_3/BiVO_4$ heterojunction films for efficient photoelectrochemical water splitting, Nano Lett., 2011, 11, 1928–1993.

[234] M. Boukriba, F. Sediri, N. Gharbi, Hydrothermal synthesis of $WO_3.1/3H_2O$ nanorods and study of their electrical properties, Polyhedron, 2010, 29, 2070–2074.

[235] S. Salmaoui, F. Sediri, N. Gharbi, Characterization of h-WO_3 nanorods synthesized by hydrothermal process, Polyhedron, 2010, 29, 1771–1775.

[236] Y.M. Solonin, O.Y. Khyzhun, E.A. Graivoronskaya, Nonstoichiometric tungsten oxide based on hexagonal WO_3, Cryst. Growth & Design. 2001, 1, 473–477.

[237] J. Li, X. Liu, Q. Han, X. Yao, X. Wang, Formation of WO_3 nanotube based bundles directed by $NaHSO_4$ and its application in water treatment, J. Mater Chem A., 2013, 1, 1246–1253.

[238] K. Suttiponparnit, J. Jiang, M. Sahu, S. Suvachittanont, T. Charinpanitkul, P.Biswas, Role of surface area, particle size and crystal phase on TiO_2 nanoparticle dispersion particles, Nanoscale Res. Lett., 2011, 6, 27–34.

[239] N. Biswal, D. P. Das, S. Martha, K. M. Parida, Efficient hydrogen production by composite photocatalyst CdS-ZnS/Zirconium-titanium phosphate (ZTP) under visible light illumination, Int. J. Hydrogen Energy., 2011, 36, 13452–13460.

[240] N. Rajamanickam, R. N. Mariammal, S. Rajashabala, K. Ramachandran, Effect of (Li, Mn) co-doping on structural, optical and magnetic properties of chunk-shaped nano ZnO, J. Alloys Compd., 2014, 614, 151–164.

[241] P. Pinceloup, C. Courtois, J. Vicens, A. Leriche, B. Thierry, Evidence of a dissolution–precipitation mechanism in hydrothermal synthesis of barium titanate powders, J. Eur. Ceram. Soc., 1999, 19, 973–977.

[242] A. Sutka, G. Mezinskis, Sol-gel auto-combustion synthesis of spinel-type ferrite nanomaterials, Front. Mater. Sci., 2012, 6, 128–141.

[243] L. Song, S. Zhang, X. Wu, Q. Wei, Controllable Synthesis of Hexagonal, Bullet-Like ZnO Microstructures and Nanorod Arrays and Their Photocatalytic Property, Ind. Eng. Chem. Res., 2012, 51, 4922–4926.

[244] P. Cai, D. Zhen, X. Xu, Y. Liu, N. Chen, G. Wei, C. Sui, A novel fiber-optic temperature sensor based on high temperature-dependent optical properties of ZnO film on sapphire fiber-ending, Mater. Sci. Eng. B, 2010, 17, 116–119.

[245] A. Chemseddine, F. Babonneau, J. Livage, Anisotropic $WO_3.nH_2O$ layers deposited from gels, Journal of Non- Crystalline Solids, 1987, 91(2), 271–278.

[246] M. Regraguia, M. Addoua, A. Outzourhitc, E. E. Idrissia, A. Kachouanea, and A. Bougrinea, Electrochromic effect in WO_3 thin films prepared by spray pyrolysis, Sol Energy Mater Sol C, 2003, 77, 341–350.

[247] Q. Mi, R. H. Coridan, B. S. Brunschwig, H. B. Gray, N. S. Lewis, Photoelectrochemical oxidation of anions by WO_3 in aqueous and nonaqueous electrolytes, Energy Environ Sci, 2013, 6, 2646-2653.

[248] X. Chang, S. Sun, L. Dong, Y. Dong, Y. Yin, Large scale production of tungsten trioxide nanoparticles for electrochromic application, RSC Adv, 2014, 4, 8994-9002.

[249] X. Chang, S. Sun, Z. Li, X. Xu, Y. Qui, Assembly of tungsten oxide nanobundles and their electrochromic properties, Appl Surf Sci, 2011, 257, 5726-5730.

[250] D. S. Dalavi, R. S. Devan, R. A. Patil, R. S. Patil, Y. R. Ma, S. B. Sadale, I. Y. Kim, J. H. Kim, P. S. Patil, Efficient electrochromic performance of nanoparticulate WO_3 thin films, J Mater Chem, 2013, 1, 3722-3728.

[251] C. K. Wang, C. K. Lin, C. L. Wu, S. C. Wang, J. L. Huang, Synthesis and characterization of electrochromic plate-like tungsten oxide films by acidic treatment of electrochemical anodized tungsten, Electrochim Acta, 2013, 112, 24-31.

[252] F. Lin, J. Cheng, C. Engtrakul, A. C. Dillon, D. Nordlund, R. G. Moore, T. C. Weng, S. K. R. Williams, R. M. Richards, In situ crystallization of high performing WO3-based electrochromic materials and the importance for durability and switching kinetics, J Mater Chem, 2012, 22, 16817-16823.

[253] M. Deepa, R. Sharma, A. Basu, S. A. Agnihotry, Effect of oxalic acid dihydrate on optical and electrochemical properties of sol–gel derived amorphous electrochromic WO_3 films, Electrochim Acta, 2005, 50, 3545-3555.

[254] R.R. Kharade, K.R. Patil, P.S. Patil, P.N. Bhosale, Novel microwave assisted sol-gel synthesis (MW-SGS) and electrochromic performance of petal like h-WO_3 thin films, Mater Res Bull, 2012, 47, 1787–1793.

[255] C. Fu, C. Foo, P.S. Lee, One step facile electrochemical preparation of WO_3-graphene nanocomposites with improved electrochromic properties, Electrochim Acta, 2014, 117, 139–144.

[256] J. Z. Ou, S. Balendhran, M. R. Field, D. G. McCulloch, A. S. Zoolfakar, R. A. Rani, S. Zhuiykov, A. P. O'Mullane, K. K. Zadeh, The anodized crystalline WO_3 nanoporous network with enhanced electrochromic properties, Nanoscale, 2012, 4, 5980-5988.

[257] G. Sonmez, Polymeric electrochromics, Chem. Commun., 2005, 42, 5251-5259.

[258] D. B. H. Uresti, D. S. Martinez, A. M. L. Cruz, S. S. Guzman, L. M. T. Martinez, Characterization and photocatalytic properties of hexagonal and monoclinic WO_3 prepared via microwave-assisted hydrothermal synthesis, Ceram Int, 2014, 40, 4767-4775.

[259] P. K. Shen, H. T. Huang, A. C. C. Tseung, A study of tungsten trioxide and polyaniline composite films in electrochemical and electrochromic behavior, J Electrochem Soc, 1992, 139, 1840-1845.

[260] H. Karami, A. Yaghoobi, A. Ramazani, Sodium Sulfate Effects on the Electrochemical Behaviors of Nanostructured Lead Dioxide and Commercial Positive Plates of Lead-Acid Batteries, Int J Electrochem Sci, 2010, 5, 1046-1059.

[261] J. H. Ha, P. Muralidharan, D. K. Kim, Hydrothermal synthesis and characterization of self-assembled h-WO_3 nanowires/nanorods using EDTA salts, J Alloys and Compounds, 2009, 475, 446-451.

[262] J. Yang, W. Li, J. Li, D. Sun, Q. Chen, Hydrothermal synthesis and photoelectrochemical properties of vertically aligned tungsten trioxide (hydrate) plate-like arrays fabricated directly on FTO substrates, J Mater Chem, 2012, 22, 17744-17752

[263] J. Zhang, X. L. Wang, X. H. Xia, C. D. Gu, J. P. Tu, Electrochromic behavior of WO_3 nano tree films prepared by hydrothermal oxidation, Sol Energy Mater Sol C, 2011, 95, 2107-2112.

[264] J. Herrmann, Heterogeneous photocatalysis: fundamentals and applications to the removal of various types of aqueous pollutants, Catal Today, 1999, 53, 115-129.

[265] B. Subash, B. Krishnakumar, V. Pandiyan, M. Swaminathan, M. Shanthi, Synthesis and characterization of novel WO_3 loaded Ag-ZnO and its photocatalytic activity, Mater Res Bull, 2013, 48,63-69.

[266] S. Y. Chai, Y.J. Kim, W.I. Lee, Photocatalytic WO_3/TiO_2 nanoparticles working under visible light, J Electroceram, 2006, 17, 909–912.

[267] S. Higashimoto, Y. Ushiroda, M. Azuma, Electrochemically assisted photocatalysis of hybrid WO_3/TiO_2 films: effect of the WO_3 structures on charge separation behavior, Top Catal, 2008, 47, 148–154.

[268] S. M. Lam, J. C. Sin, A. Z. Abdullah, A. R. Mohamed, Transition metal oxide loaded ZnO nanorods: preparation, characterization and their UV–vis photocatalytic activities, Separ Pur Technol, 2014, 132, 378-387.

[269] Y. P. He, Z. Y. Wu, L. M. Fu, C. R. Li, Y. M. Miao, L. Cao, H. M. Fan, B. S. Zou, Photochromism and size effect of WO_3 and WO_3-TiO_2 aqueous sol, Chem Mater, 2003, 15, 4039-4045.

[270] K. Tennakone, O. A. Heperuma, J. M. S. Bandara, W. C. B. Kiridena, TiO_2 and WO_3 semiconductor particles in contact: photochemical reduction of WO_3 to the non-stoichiometric blue form, Semicond Sci Technol, 1992, 7, 423-424.

[271] C. L. Yu, C. F. Fan, J. M. Yu, W. Q. Zhou, K. Yang, Preparation of bismuth oxyiodides and oxides and their photooxidation characteristic under visible/UV light irradiation, Mater Res Bull, 2011, 46, 140-146.

[272] B. Subash, B. Krishnakumar, M. Swaminathan, M. Shanthi, Enhanced photocatalytic performance of WO_3 loaded Ag–ZnO for Acid Black 1 degradation by UV-A light, J Molecular Catalysis A: Chemical, 2013, 366, 54-63.

[273] Y. Wang, Z. Wang, S. Muhammad, J. He, Graphite-like C_3N_4 hybridized $ZnWO_4$ nanorods: Synthesis and its enhanced photocatalysis in visible light, Cryst Engg Comm, 2012, 14, 5065-5070.

[274] P. Fageria, S. Gangopadhyay, S. Panda, Synthesis of ZnO/Au and ZnO/Ag nanoparticles and their photocatalytic application using UV and visible light, RSC Adv, 2014, 4, 24962-24972.

[275] A. Leelavathi, G. Madras, N. Ravishankar, Origin of enhanced photocatalytic activity and photoconduction in high aspect ratio ZnO nanorods, Phys Chem Chem Phys, 2013, 15, 10795-10802.

[276] W. Zhou, F. F. Sun, K. Pan, G. H. Tian, B. J. Jiang, Z. Y. Ren, C. G. Tian, H. G. Fu, Well-ordered large-pore mesoporous anatase TiO_2 with remarkably high thermal stability and improved crystallinity: preparation, characterization, and photocatalytic performance, Adv Funct Mater, 2011, 21, 1922-1930.

[277] S. Ma, J. Xue, Y. Zhou, Z. Zhang, Photochemical synthesis of ZnO/Ag_2O heterostructures with enhanced ultraviolet and visible photocatalytic activity, J Mater Chem A, 2014, 2, 7272-7280.

[278] S. Dhara, P. K. Giri, Enhanced UV photosensitivity from rapid thermal annealed vertically aligned ZnO nanowires, J Nanosci Nanotech, 2011, 11, 1-7.

[279] B. Cao, F. Sun, W. Cai, Electrodeposition-induced highly oriented zinc oxide ordered pore arrays and their ultraviolet emissions, Electrochem and Solid State Lett, 2005, 8, 237-240.

[280] H. Zeng, W. Cai, P. Liu, X. Xu, H. Zhou, C. Klingshim, H. Kalt, ZnO based hollow nanoparticles by selective etching: elimination and reconstruction of metal-semiconductor interface, improvement of blue emission and photocatalysis, ACS Nano, 2008, 2, 1661-1670.

[281] H. Zeng, P. Liu, W. Cai, S. Yang, X. Xu, ZnO-Based hollow nanoparticles by selective etching: elimination and reconstruction of metal−semiconductor interface, improvement of blue emission and photocatalysis, J Phys Chem C, 2008, 112, 19620-19624.

[282] H. Zhang, R. Zong, Y. Zhu, Photocorrosion inhibition and photoactivity enhancement for zinc oxide via hybridization with monolayer polyaniline, J Phys Chem C, 2009, 113, 4605-4611.

[283] X. G. Zhang, Corrosion and Electrochemistry of Zinc, Springer, 1996.

[284] S. Ma, R. Li, C. Lv, W. Xu, X. Gou, Facile synthesis of ZnO nanorod arrays and hierarchical nanostructures for photocatalysis and gas sensor applications, J Hazard Mat, 2011, 192, 730-740.

[285] W. Shouqiang, S. Zhongcai, L. Xudong, L. Ying, C. Linlin, H. Yan, Photocatalytic degradation of methyl orange over ITO/CdS/ZnO interface composite films, J Environ Sci, 2009, 21, 991-6.

[286] Y. J. Li, X.D. Li, J.W. Li, J. Yin, Photocatalytic degradation of methyl orange by TiO_2-coated activated carbon and kinetic study, Water Res, 2006, 40, 1119-1126.

[287] J. Matos, J. Laine, J.M. Hermann, Synergy effect in the photocatalytic degradation of phenol on a suspended mixture of titania and activated carbon, Appl Catal B: Environ, 1998, 18, 281-291.

[288] B. Subash, B. Krishnakumar, M. Swaminathan, M. Shanthi, Highly efficient, solar active, and reusable photocatalyst: Zr-Loaded Ag–ZnO for reactive red 120 dye degradation with synergistic effect and dye-sensitized mechanism, Langmuir, 2013, 29, 939-949.

[289] Y. Yang, T. Zhang, L. Le, X. Ruan, P. Fang, C. Pan, R. Xiong, J. Shi, J. Wei, Quick and facile preparation of visible light-driven TiO_2 photocatalyst with high absorption and photocatalytic activity, Scientific Reports, 2014, 4, DOI: 10.1038/srep07045.

[290] M. T. Uddin, Y. Nicolas, C. Olivier, T. Toupance, L. Servant, M. M. Muller, Nanostructured SnO_2–ZnO heterojunction photocatalysts showing enhanced photocatalytic activity for the degradation of organic dyes, Inorg Chem, 2012, 51, 7764-7773.

[291] Y. J. Wang, R. Shin, J. Lin, Y. F. Zhu, Enhancement of photocurrent and photocatalytic activity of ZnO hybridized with graphite-like C_3N_4, Energy Environ Sci, 2011, 113, 4605-4611.

[292] S. Yang, Q. Yue, F. Wu, N. Huo, Z. Chen, J. Yang, J. Li, Synthesis of the nanostructured Cd_4GeS_6 photocatalysts and their visible-light-driven photocatalytic degradation property, J Alloys and Compounds, 2014, 597, 91-94.

[293] X. Bai, L. Wang, Y. Zhu, Visible photocatalytic activity enhancement of $ZnWO_4$ by graphene Hybridization, ACS Catalysis, 2012, 2, 2769-2778.

Chapter 5

CONCLUSIONS

The present research objective is fulfilled through consideration of several steps and executed to prepare different WO_3 nanostructures using acid co-precipitation and hydrothermal methods; physicochemical and electrochemical characterization; combustion synthesis of ZnO nanoparticles and enhancement of photocatalytic degradation through WO_3-ZnO nanocomposites. The collective findings are summarized as follows:

- Different morphologies of WO_3 nanostructures were developed by acid co-precipitation of precursors namely H_2WO_4 and $Na_2WO_4.2H_2O$ followed by flash heating at 500°C through control over pH, temperature and structure directing agents during synthesis.
- Acid catalyzed reaction (pH~1) of H_2WO_4 in presence of hydrogen peroxide at ~90°C favours formation of isotropic non-confined spherical WO_3 nanoparticles with diameter ~50 nm whereas acid precipitation (pH~3) using CTAB (cetyltrimethylammoniumbromide) as structure directing surfactant develops anisotropic rod shaped WO_3 nanoparticles having length ~140 nm and width ~40 nm, respectively.
- Hydrothermal assisted anisotropic growth of monoclinic WO_3 nanocuboids was carried using fluoroboric acid as structure directing agent. The stable monoclinic phase with nanocuboid morphology was optimized at 4 M HBF_4 concentration for 6 h under 180°C. Morphology stability takes place due to optimum BF_4^- anion.
- Sodium chloride hierarchically grows one-dimensional hexagonal WO_3 nanofibers of length ~256 nm and diameter ~30 nm at 180°C under 12 h of hydrothermal treatment. The metastable hexagonal phase and morphology stabilization takes place under high influence of Na^+ ions in the reaction.
- Solution-combustion method develops one-dimensional ZnO quasi-fiber in presence of oxalic acid as fuel. Quasi-fiber structure of ZnO is formed from partial fusion of near spherical ~60 nm particles.
- Dip-coated rod-shaped WO_3 nanoparticles coated ITO glass electrode shows enhanced current density of 2.23 mA/cm^2 due to less contact resistance, more contact area and high adherence to the ITO substrate in comparison to the spherical WO_3 coated electrodes. High surface discontinuity limits the flow of electrons and ions during electrochemical reaction in drop-coated electrodes.

- High symmetry electrochemical reaction of the dip coated WO_3 nanocuboid dip coated electrode exhibits current density of 3.15 mA/cm^2 with a 72.2% optical electrochromic reversibility.
- High surface area of 25.2 m^2/g and interconnectivity among the fiber particles exhibits high current density of 8.9 mA/cm^2 and 77.4% cyclic reversibility for ~11μm thick coated electrode.
- A correlation between the crystal structures and morphology evaluates the comparative electrochromic performance under 1M H_2SO_4 electrolyte in scan range ±0.5 V and scan rate of 100 mV/s where nanofiber WO_3 exhibits high electrochromic reversibility of 78.94%, fast switching speeds of 6.02s and 5.5s for coloration and bleaching, respectively and high coloration efficiency of 54.09 cm^2 C^{-1} in comparison to the monoclinic WO_3 nanocuboid because of specious intercalation zone and wide open channels in hexagonal crystal structure and interactive fiber morphology.
- Coupling of monoclinic WO_3 nanocuboids with commercial ZnO enhances the photocatalytic degradation of methyl orange than hexagonal WO_3 coupled ZnO nanocomposites where WO_3 act as an electron trapper and absorber under UV and visible light, respectively.
- Quasi-fibrous ZnO imparts better photocatalytic efficiency than commercial ZnO. Only 4% difference in methyl orange degradation is observed between UV and visible light irradiation. The photocatalyst shows efficient reusability under visible light due to negligible photocorrosion.
- Quasi fiber ZnO coupled with 10wt% monoclinic WO_3 nanocuboid exhibits 14% more photocatalytic efficiency than commercial ZnO coupled WO_3 nanopowders.
- Cationic methylene blue (MB) and anionic Orange G (OG) undergoes degradation through charge transfer mechanism in the presence of optimum weight ratio WO_3 – ZnO mixture shows reduction in recombination of photogenerated electron – hole pair with 90% degradation of both dyes in comparison to WO_3 or ZnO individually.

5.1. Future Work

Apart from the brief conclusion on the current research work carried, there are several scopes for further improvement of performance of such with consideration of following future work;

- Detail study of WO_3 nanoparticle growth kinetics and their crystal structures.
- Improved electrode fabrication technique with high uniform coating for enhanced electrochromism.
- Study on effect of different electrolytes (electrolytes based on Li^+ & other H^+ ions) on electrochromism.
- Photocatalytic degradation and kinetics of mixed dyes.
- Photocatalytic degradation of organic pollutants (phenol, acetalydehyde, etc.)

List of publications related to research work

Published (Peer Review International Journal)

1. **S. Adhikari**, D. Sarkar, G. Madras, Highly efficient WO_3-ZnO photocatalyst for Dye Degradation, ***RSC Advances,*** 2015, 5, 11895-11904 (***IF - 3.708***).
2. **S. Adhikari**, D. Sarkar, Synthesis and electrochemical properties of Nanocuboid and Nanofiber WO_3, ***Journal of Electrochemical Society***, 2015, 162, H65-H72. (**IF – 3.266**).
3. **S. Adhikari**, D. Sarkar, G. Madras, Synthesis and photocatalytic performance of quasi-fibrous ZnO, ***RSC Advances***, 2014, 4, 55807-55814 (***IF - 3.708***).
4. **S. Adhikari,** D. Sarkar, High efficient electrochromic WO_3 nanofibers, ***Electrochimica Acta,*** 2014, 138, 115-123 (**IF - 4.504**).
5. **S. Adhikari**, D. Sarkar, Hydrothermal synthesis and Electrochromism of WO_3 nanocuboids, ***RSC Advances***, 2014, 4, 20145–20153 (***IF - 3.708***).
6. **S. Adhikari,** D. Sarkar**,** H. S. Maiti, Synthesis and Characterization of WO_3 Spherical Nanoparticles and Nanorods, ***Materials Research Bulletin,*** 2014, 49, 325-330 (***IF – 1.968***).
7. **S. Adhikari**, D. Sarkar, Electrochemical response of spherical and rod shaped WO_3 nanoparticles, ***ISRN Nanotechnology,*** http://dx.doi.org/10.1155/2013/279398, 2013.

Accepted (Peer Review International Journal)

8. **S. Adhikari**, D. Sarkar, Preparation of Mixed Semiconductors for Methyl Orange Degradation, ***Journal of Nanomaterials*, Accepted (**ID 269019**)**, June-2015 (***IF-1.611***).
9. **S. Adhikari**, D. Sarkar, Metal Oxide Semiconductors for Dye Degradation, ***Materials Research Bulletin,*** **Accepted**, June-2015 (***IF-1.968***).

Conference Proceedings (Peer Review International Journal)

10. **S. Adhikari**, D. Sarkar, Confined Growth of WO_3 for high performance electrochromic Device, **Key Engineering Materials**, 2015, 659, 583-587. (MSAT-8, 2014, Bangkok, Thailand)

Sangeeta Adhikari

M. Sc. (Chemistry)

Date of Birth – 13th May 1989

KEY SKILLS

- **Materials Chemistry**
- **Development of Nanostructures**
- **Functional Applications of Nanostructures**
- **Electrochemical Characterizations**
- **Photocatalysis**

CONTACT DETAILS

Department of Ceramic Engineering
National Institute of Technology
Rourkela – 769008, Odisha, INDIA
Email: adhikari.sangeeta8@gmail.com
Mobile: +919778199019

FIELD OF INTERESTS

Nanomaterials, Electrochromism, Photocatalysis, Electro-Functional Applications

ACADEMIC

Ph.D. **(Ceramic Engineering)**	National Institute of Technology, Rourkela, India **Supervisor:** Prof. Debasish Sarkar **Thesis Title:** Nanostructured WO_3 for Electrochromic and Photocatalytic Applications
M.Sc. **(Chemistry)**	National Institute of Technology, Rourkela, India
B.Sc. **(Chemistry Honours)**	Sambalpur University, Odisha, India
Intermediate (+2 Sc.)	C. H. S. E. Board, Odisha
Matriculation	Indo English School, Rourkela

PROFESSIONAL EXPERIENCE

Research Trainee	Dept. of Chemical Engg., IISc. Bangalore	March 2014-April 2014
Research Trainee	Dept. of Nanoscience & Nanotechnology, Bharathiar University, Coimbatore	May 2012-June 2012
Summer Trainee	Department of Chemistry, BESU, Shibpur	May 2010-July 2010

PROFESSIONAL ACHIEVEMENTS / INVOLVEMENTS

- Publication in Peer Reviewed International Journal – 13; Symposium/Conference – 10
- Regular member of Society of Materials Chemistry
- Department of Science and Technology, India, awarded travel grant for presenting research paper in MSAT-8, Bangkok, Thailand during December 2014 (SB/ITS-Y/04472/2014-2015).
- CSIR, India, awarded Foreign Travel Grant for presenting research paper in MSAT-8, Bangkok, Thailand during December 2014 (TG/8701/14-HRD).

- Best Research Scholar, Department of Ceramic Engineering, NIT Rourkela at RSW-2015.
- Young Scientist Award (Oral) in ICNT-2015 held at Haldia Institute of Technology, Haldia, WB.
- Young Scientist Award (Poster) on SCINO-2013 held at Bharathiar University, Coimbatore.
- Young Scientist Award (Oral) on CCC-2012 held at NIT, Jalandhar.
- Best Paper presentation in Tech Fest-2011 held at NIT, Rourkela.
- Awarded Second prize in Chemistry Quiz in Tech Fest-2010 held at NIT, Rourkela.

PEER REVIEWED INTERNATIONAL JOURNAL PUBLICATION

1. **S. Adhikari**, D. Sarkar, Mixed Oxide Semiconductors for Dye Degradation, **Material Research Bulletin**, **Accepted**, June-2015 (***IF – 1.968***).
2. **S. Adhikari**, D. Sarkar, Preparation of Mixed Semiconductors for Methyl Orange Degradation, **Journal of Nanomaterials, Accepted**, June- 2015 (***IF – 1.611***).
3. **S. Adhikari,** A. Banerjee, N K R Eswar, D. Sarkar, G. Madras, Photocatalytic inactivation of E. Coli by ZnO-Ag nanoparticles **RSC Advances,** 2015, 5, 51067-51077 (***IF - 3.708***).
4. **S. Adhikari**, D. Sarkar, G. Madras, Highly efficient WO_3-ZnO photocatalyst for Dye Degradation, ***RSC Advances,*** 2015, 5, 11895-11904 (***IF - 3.708***).
5. S. Mandal, S. S. Mahapatra, **S. Adhikari**, R. K. Patel, Modeling of Arsenic (III) removal by evolutionary genetic programming g and least square support vector machine models, ***Environmental Processing,*** 2015, 2, 145-172.
6. **S. Adhikari**, D. Sarkar, Synthesis and electrochemical properties of Nanocuboid and Nanofiber WO_3, **Journal of Electrochemical Society**, 2015, DOI: 10.1149/2.0881501jes. (**IF – 2.859**).
7. **S. Adhikari**, D. Sarkar, G. Madras, Synthesis and photocatalytic performance of quasi-fibrous ZnO, ***RSC Advances***, 2014, 4, 55807-55814 (***IF - 3.708***).
8. **S. Adhikari,** D. Sarkar, High efficient electrochromic WO_3 nanofibers, ***Electrochimica Acta,*** *138, 115-123, 2014* (***IF - 4.086***).
9. **S. Adhikari**, D. Sarkar, Hydrothermal synthesis and Electrochromism of WO_3 nanocuboids, ***RSC Advances***, 4, 20145–20153, 2014 (***IF - 3.708***).
10. **S. Adhikari,** D. Sarkar, H. S. Maiti, Synthesis and Characterization of WO_3 Spherical Nanoparticles and Nanorods, ***Materials Research Bulletin,*** 49, 325-330, 2014 (***IF – 1.968***).
11. **S. Adhikari**, D. Sarkar, Electrochemical response of spherical and rod shaped WO_3 nanoparticles, ***ISRN Nanotechnology,*** http://dx.doi.org/10.1155/2013/279398, 2013.
12. D. Sarkar, S. K. Swain, **S. Adhikari**, B. S. Reddy, H.S. Maiti, Synthesis, mechanical properties and bioactivity of nanostructured zirconia, ***Material Science and Engineering – C***, 33 [6] 3413 – 3417, 2013 ***(IF - 2.736).***

UNDER REVIEW / COMMUNICATED

13.S. Adhikari, A. Surin, R. Swain, S. Chakraborty, D. Sarkar, Spongy ZnO for Photocatalytic Degradation of Crystal Violet (**Manuscript Under Preparation**)

INTERNATIONAL CONFERENCE / SYMPOSIUM PROCEEDINGS

14.S. Adhikari, D. Sarkar, Nanostructured WO_3 for electrochromic and photocatalytic applications, **Research Scholar Week - 2015** held at NIT Rourkela.

15.S. Adhikari, D. Sarkar, Photodegradation of methyl orange by WO_3-ZnO nanocomposites, 2nd **International Conference on Nanotechnology (ICNT-2015),** Haldia Institute of Technology, Haldia, India, **2015**.

16.S. Adhikari, D. Sarkar, Confined growth of WO_3 for high performance electrochromism, **Key Engineering Materials, Conference Proceedings, 8th International Conference on Material Science and Technology (MSAT-8),** Bangkok, Thailand, **2014**.

17.S. Adhikari, D. Sarkar, Electrochromic performance of WO_3 Nanocuboids, **INDO-UK International Workshop on AMAN-2014, BITS-PILANI**, KK Birla Campus, Goa, India, **2014**.

18.S. Adhikari, D. Sarkar, Directional Growth of WO_3 Nanostructures, **National Symposium on SCINO-2013**, Bharathiar University, Coimbatore, India, **2013**.

19.S. Adhikari, D. Sarkar, Directional Growth of Nano-WO_3, **National Conference on CMDAYS-2013**, NIT, Rourkela, Odisha, India, 2013.

20.S. Adhikari, D. Sarkar, Synthesis of tungsten trioxide (WO_3) nanorods and its electrochemical studies, **2nd International Science Congress- 2012**, Mathura, India, **2012**.

21.S. Adhikari, D. Sarkar, Synthesis and Characterization of WO_3 Nanopowders**, International Conference on CCC-2012**, NIT, Jalandhar, India, **2012**.

22. Participated in **National Workshop in Materials Chemistry (NWMC-2011)** held at BARC, Mumbai, India, **2011**.

23. Participated in **23rd Annual Conference on National Seminar on Recent Trends in Chemical Science and Technology**, NIT, Rourkela, India, **2009.**